



Study of the viscous interaction with separation at hypersonic regime

Mathieu Lugrin

► To cite this version:

Mathieu Lugrin. Study of the viscous interaction with separation at hypersonic regime. Fluid mechanics [physics.class-ph]. Institut Polytechnique de Paris, 2021. English. NNT : 2021IPPAX098 . tel-03628807

HAL Id: tel-03628807

<https://theses.hal.science/tel-03628807>

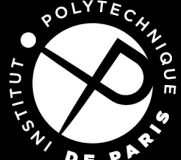
Submitted on 3 Apr 2022

HAL is a multi-disciplinary open access archive for the deposit and dissemination of scientific research documents, whether they are published or not. The documents may come from teaching and research institutions in France or abroad, or from public or private research centers.

L'archive ouverte pluridisciplinaire **HAL**, est destinée au dépôt et à la diffusion de documents scientifiques de niveau recherche, publiés ou non, émanant des établissements d'enseignement et de recherche français ou étrangers, des laboratoires publics ou privés.

Thèse de doctorat

NNT : 2021IPPA098



INSTITUT
POLYTECHNIQUE
DE PARIS



IP PARIS

Study of the viscous interaction with separation in hypersonic regime

Thèse de doctorat de l’Institut Polytechnique de Paris
préparée à l’Ecole polytechnique

École doctorale n°626 Ecole Doctorale de l’Institut Polytechnique de Paris (ED IP
Paris)

Spécialité de doctorat : Mécanique des fluides et des solides, acoustique

Thèse présentée et soutenue à Meudon, le 2 décembre 2021, par

MATHIEU LUGRIN

Composition du Jury :

Paola Cinnella	
Professeure, Sorbonne Université (Institut Jean le Rond d'Alembert)	Présidente
Pierre Dupont	
Chargé de Recherche, Aix-Marseille Université (CNRS/IUSTI)	Rapporteur
Jean Christophe Robinet	
Professeur, Arts et Métiers Paris (Dynfluid)	Rapporteur
Sébastien Esquieu	
Ingénieur de recherche, CEA (CESTA)	Examinateur
Steven Schneider	
Professeur, Purdue University (Aerospace Sciences lab)	Examinateur
Reynald Bur	
Maitre de recherche, ONERA (DAAA/AMES)	Directeur de thèse
Eric Garnier	
Directeur de recherche, ONERA (DAAA/ELV)	Co-directeur de thèse
Samir Beneddine	
Ingénieur de recherche, ONERA (DAAA/MASH)	Invité

Remerciements

J'aurais aimé commencer ces remerciements en affirmant que ceux qui auront le courage d'aller au bout du présent manuscrit se rendront probablement compte qu'il fait partie de ceux qu'on qualifie aisément de "pas infiniment digestes". Cela m'aurait permis de rendre hommage à la fois à Johann Moulin¹, qui me sert d'inspiration dans ce moment difficile et à François Gallaire sans qui je ne me serais jamais orienté vers la mécanique des fluides. Mais, vous aurez probablement compris à la lecture² de ce maigre manuscrit que l'écriture n'est pas mon fort. Exprimer ce que je ressens l'est encore moins³ alors j'espère que vous excuserez la maladresse de ces remerciements.

Ici s'achève ce qui restera probablement la seconde expérience la plus formatrice de ma vie. Yvan, tu avais juste, je ne retrouverai jamais ni l'intensité, ni la technicité des quelques mois passés sur Hector Delta. J'espère que l'on continuera à diverger encore longtemps, et qui sait, la chance finira peut-être par sourire aux piétres hommes d'affaires de la dream team.

Je tiens tout d'abord à remercier Reynald, qui a dirigé cette thèse, ainsi que les membres du jury⁴ qui ont réussi à suivre un pointeur laser fou pendant toute la soutenance.

Sébastien, merci à nouveau d'avoir suivi ce travail, pour ton intérêt et ton enthousiasme, c'est un plaisir de collaborer avec toi, j'attends avec impatience que nos nombreux projets communs se concrétisent.

Samir, merci d'avoir mis autant d'énergie dans l'encadrement et tout particulièrement dans la rédaction des différents papiers, savoir que je pouvais compter sur toi m'a permis de rester motivé même dans les moments creux de cette thèse.

Eric, merci pour ton soutien, notamment quand j'ai voulu me lancer sur des sujets connexes à cette thèse. Merci pour tes précieux conseils et pour ton exigence, qui contribue pour beaucoup à la réussite de ce travail. J'espère qu'on aura de nombreuses occasions de retravailler ensemble. Contrairement à ce que l'on peut penser, cette thèse est loin d'être un travail personnel. Les essais à R2Ch⁵ n'auraient jamais été possibles sans l'intervention de nombreux collègues. Il faut évidemment remercier Nicolas et Jean-Marc qui ont été indispensables au déroulement de la campagne. Merci aussi à François qui en plus de participer à la campagne, s'est investi dans la rédaction du papier expérimental.

Qui de mieux placé pour faire la jonction entre les collègues et les amis que Jean-Pierre, indispensable lors de la conception et réalisation de la maquette et de l'étude des PCB et avec qui j'ai surtout passé de bons moments, autour de bons repas, bonnes bouteilles et discussions passionnantes.

Quelques mots pour ceux qui m'ont supporté au presque quotidien pendant toute cette thèse. Tout d'abord Romain, avec qui j'ai partagé les bons et moins bons moments de ma thèse (et de la sienne aussi). Heureusement qu'on a pu continuer tous les deux le sport national, qui ne se

¹Aussi connu sous le pseudonyme de "Pinpin", [voir ici](#)

²Commentaire purement rhétorique

³Zola quand tu nous tiens !

⁴Et non membres du jury

⁵Soufflerie la plus silencieuse du monde 6 mois par an, capitale de l'instinct et de la spontanéité les 6 autres.

pratique que porte fermé, jusqu'alors réservé à la légendaire pause café du AY-00-21. D'ailleurs, il est hors de question que l'on se dispute la garde des canards, tu es obligé de rester !

Popo, quel plaisir de partager ces pintes et autres bons restaurants avec toi, tu m'as évité d'avoir à raconter ma vie à un Caol Ila, si la décision m'appartenait tu aurais le titre de Popo⁶ à tout jamais.

Un petit clin d'œil à Théodore qui ne lira jamais ces lignes et qui malgré une pratique intensive jusqu'à des heures tardives n'est toujours pas bilingue en espagnol...

Merci au passage aux copains de l'EPFL pour les week-ends⁷ de "reset mental", malheureusement les ordonnances de docteur Lugrin n'aideront probablement pas se coucher tôt le vendredi pour profiter du samedi.

Ce travail n'aurait pas été possible sans l'éducation et le soutien familial, je ne pourrai jamais remercier assez mes parents et grands-parents pour tout ce qu'ils m'ont apporté.

Pour finir, je profite de ces remerciements pour jeter une bouteille à la mer : jeune chercheur recherche 40⁸ millions d'euros pour construire la soufflerie silencieuse de ses rêves⁹.

⁶Ceci est un "un"

⁷Et vacances, à quand le retour en Finlande ?

⁸10 ?

⁹Ou un poste à l'EPFL ?

Contents

1	Introduction	9
2	State of the art	13
2.1	Transition in hypersonic flows	14
2.2	Low frequency dynamics of the shock-bubble system	24
3	Numerical setup	27
3.1	Numerical Simulation	28
3.2	Post-processing tools	35
3.3	Linear Stability Analysis	41
4	Experimental setup	49
4.1	Wind tunnel	50
4.2	Model	52
4.3	Acquisition	53
4.4	Unsteady pressure measurements	55
4.5	Optical measurements	68
4.6	Wind tunnel free stream perturbations measurements	74
5	Numerical study of the bubble dynamics and its impact on transition	77
5.1	Introduction	78
5.2	Large scale, low frequency dynamics of the bubble	79
5.3	Impact of the bubble dynamics on the transition	93
5.4	Conclusion	96
6	Numerical study of the transition scenario	99
6.1	Introduction	100
6.2	Study of the subdomains	103
6.3	Transition scenario	117
6.4	Conclusion	119
7	Numerical study of the effect of compressibility on the transition scenario	121
7.1	Introduction	122
7.2	Flow topology	123
7.3	Boundary layer instabilities	126
7.4	Impact on the transition scenario	133
7.5	Conclusion	135
8	Experimental results	137
8.1	Flow topology	138
8.2	Streaks analysis	140
8.3	Shear-layer oblique modes	145
8.4	Conclusion	146

9 Numerical-experimental comparison	149
9.1 Wind tunnel free-stream fluctuations	150
9.2 Experimental results for the previously studied conditions	152
9.3 Numerical simulation of an experimental run	152
Conclusion	159
Résumé en Français	161

Chapter 1

Introduction

The main challenge for the current development of high-speed flight is to improve the predictability of the thermo-mechanical loads on hypersonic vehicles. This prediction is crucial to design vehicles that can withstand extremely high heat-fluxes while not overprotecting them and keep their weight acceptable. This is particularly important as the heat flux varies depending on the nature of the boundary layer (laminar-transitional-turbulent), and typical flight conditions allow for the 3 regimes. Most of the time, the physical mechanisms behind the thermo-mechanical load variations are complex and multiscale, so they are neither easy to model nor to understand.

This thesis focuses on a particular case, the transitional shock-wave/boundary layer interaction on a compression ramp. Shock-wave/boundary layer interaction (SBLI) is a classical problem of hypersonic flight, since shocks appear in the vicinity of any geometrical discontinuity, such as control surfaces. There are two canonical cases for the study of SBLI at high supersonic/hypersonic speed: impinging oblique shock-boundary layer interaction (OSBLI) and SBLI caused by compression ramps (a schematic of the compression ramp flow can be seen in figure 1.1) on 2D or axisymmetrical geometries. In both cases, a strong adverse pressure gradient imposed by the shock may cause the separation of the boundary layer (BL), creating a recirculation bubble. This separation size, which can vary of several order of magnitude depending on the Reynolds number, may cause serious problems for hypersonic vehicles, as it can lead to drastic changes of control surface efficiency or even to the unstart of an air intake if the separation occurs on a compression ramp upstream from the intake. In addition, the shock-bubble system brings one of the main limitations of SBLI on high-velocity flight: it may initiate low-frequency/large-scale motion in the flow. This can cause unsteady thermal loading and impact the control of the object or the efficiency of the air-inlet.

Another limitation for the current development of hypersonic flight is the understanding and prediction of laminar-turbulent transition. While transitional regime is often encountered in flight, boundary layer transition causes an important rise of wall heat-flux level (more than 20% higher than the turbulent one (Benay et al., 2006)). Thus, predicting its onset is crucial for the correct design of hypersonic vehicles.

Shock-wave/transitional boundary layer interaction combines the complexity of those two subjects in a strongly multiscale problem. On one hand, boundary layer transition in hypersonic regimes commonly appears through the linear development and non-linear breakdown of small-scale instabilities at rather high frequencies. On the other hand, the separated region caused by the shock-boundary layer interaction tends to initiate low frequency/large-scale motion of the flow.

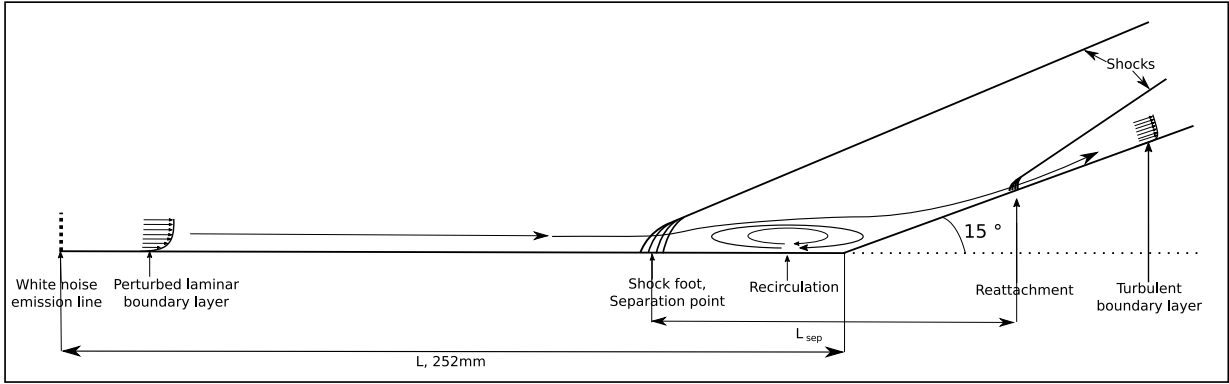


Figure 1.1: Schematic of a compression ramp, showing the topology of the flow with first the attached BL, then the SBLI, followed by the separated region caused by the adverse pressure gradient and finally the reattachment.

This thesis continues previous ONERA studies on the transitional Mach 5 shock-wave/boundary layer interaction conducted on a hollow cylinder-flare geometry by Benay et al., 2006; Bur and Chanetz, 2009; Vandomme, 2004. Those studies, alongside others on more applied geometries such as the PRE-X demonstrator (Bur and Chanetz, 2009), aimed at characterizing the impact of the laminar/turbulent transition on the mean flow and unveiled the need for a better understanding of the transition process through hypersonic SBLI (see for instance figure 1.2). During those experimental studies, the apparition of streaky patterns in the reattachment region has been documented, causing an inhomogeneity in the heat flux distribution.

The goals of the present work are to understand the dynamics and the physical origin of:

- The instabilities in hypersonic SBLI for a transitional flow regime
- The separated region unsteadiness
- The streaks observed in the reattachment region

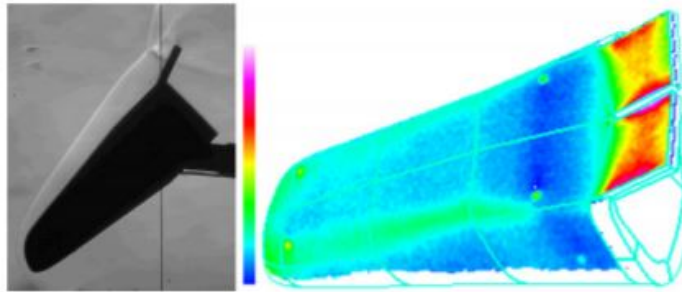


Figure 1.2: Schlieren and infrared imaging from an experiment conducted on the PRE-X model showing the transitional heat flux level at reattachment on the control surface. From Bur and Chanetz (2009).

Given some newly developed experimental methods (such as high bandwidth pressure transducers (Berridge and Schneider, 2012) or high-speed Schlieren imaging (Butler and Laurence, 2021a)) and the recent increase in computing power, more in-depth studies about the dynamics of such interactions are now possible, either focused on the transitional instabilities or the low frequency dynamics of the separated region. The present work aims at studying the instabilities mentioned here-before both experimentally and numerically. First, new experiments will be conducted. The main improvement compared to the previous experiments from ONERA will be the addi-

tion of unsteady pressure sensors and improved optical measurements, for which methodological development are still needed. Secondly, high fidelity numerical studies will be conducted and combined with global stability analyses to unveil the physical mechanism behind the dynamics of the interaction and the transition to turbulence. The geometry and most of the flow parameters used are based on an experimental and numerical database from ONERA that has been studied by Benay et al. (2006) and Bur and Chanetz (2009). The geometry under study is a hollow cylinder-flare.

This study is therefore based on a canonical geometry, from which a deeper understanding will bring new physical insights that provide relevant design information even for more complex geometry and applications. It is co-funded by the CEA, who is interested in canonical ways to explore the physical mechanism present on re-entry vehicles. There is also interest for this case in the NATO community (for example through the NATO-AVT-346 group "Predicting Hypersonic Boundary-Layer Transition on Complex Geometries") as it is a canonical way to study a control surface at high steering angle.

The thesis is organized in the following way:

- A review of the state of the art on both the relevant transitional instabilities in hypersonic flow and the SBLI unsteadiness will be presented.
- Two chapters will be dedicated to the methodology used to qualify, quantify and discuss the physical origin of the instabilities present in the flow :
 - The numerical setup is introduced, including the Navier-Stokes computation, the post-processing and the global stability tools that will be used.
 - The experimental setup is discussed, including the facility, instrumentation, optical measurements and post-processing, with an emphasis on the know-how that was acquired for the use of high-bandwidth pressure transducers needed for hypersonic transition studies.
- The results will then be presented:
 - Starting with a chapter including a numerical study based on high-fidelity simulations and global stability analysis, focussing on the dynamics of the separation bubble. In this chapter, both the bubble large-scale motion and some mechanisms leading to striation in the reattachment region will be discussed. The possible interactions between the bubble motion and the transition to turbulence will also be presented.
 - Another numerical study based on a high-fidelity simulation and a resolvent analysis focussing on the transition scenario in such flow will be presented. A transition scenario, including linear and non-linear mechanisms, which also leads to the creation of streaks in the reattachment region will be proposed.
 - The impact of compressibility on this transition scenario will then be studied, with computations at Mach number of 4,5,6 and 7.
 - A chapter presenting experimental results follows and brings new information on both the shear-layer modes and the heat-flux striation on the flare using innovative post-processing techniques.
 - The last chapter contains a discussion on numerical reproduction of the experiments.
- Finally, conclusions and perspectives will be presented.

Chapter 2

State of the art

This chapter aims at describing the current state of the art on both the recirculation region unsteadiness in super/hypersonic SBLI and the hypersonic laminar-turbulent transition mechanisms. First with a focus on the transitional dynamics, and then on the low-frequency dynamics of the separated region.

Contents

2.1 Transition in hypersonic flows	14
2.1.1 Linear instabilities	14
First mode instabilities	15
Second mode instabilities	15
Mixing layer modes	16
Streaks/Longitudinal vortices/Görtler vortices	19
Remark on the receptivity process	20
Remark on the global stability framework for transition	21
2.1.2 Non-linear mechanisms	22
Second mode fundamental and sub-harmonic breakdown	22
First mode oblique breakdown	22
2.1.3 Relevant mechanisms for hypersonic SBLI	23
2.2 Low frequency dynamics of the shock-bubble system	24
Upstream scenario for weak interaction	24
Upstream scenario: the special case of the transitional boundary layer . .	25
Downstream scenario for strong interaction	25
Bubble global mode for shock-laminar boundary layer interaction	25
Remark on the role of the shock on the unsteadiness	26

2.1 Transition in hypersonic flows

Recently, the interest for the transitional SBLI seems to be growing, for example Hildebrand et al. (2018) conducted a DNS and a global stability analysis on an OSBLI at a transitional Reynolds number, but they focused mainly on the globally unstable mode of the separated region rather than on convective instabilities developing along the geometry. The literature on transition through hypersonic SBLI remains very sparse, most of the interesting results on hypersonic transition published up to this date are attached boundary layer results. This section aims at presenting the main hypersonic transitional instabilities.

2.1.1 Linear instabilities

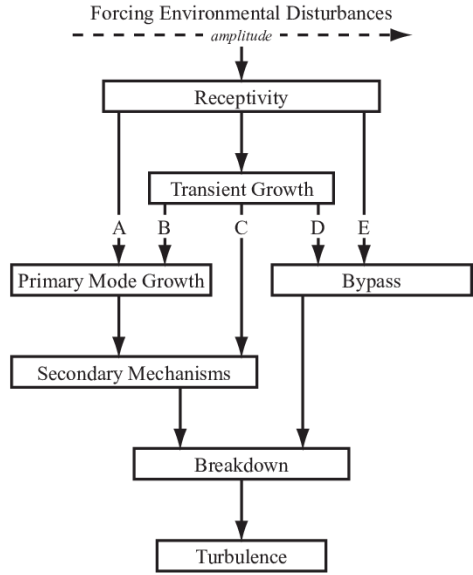


Figure 2.1: Roadmap of the laminar-turbulent boundary layer transition, from Morkovin et al. (1994).

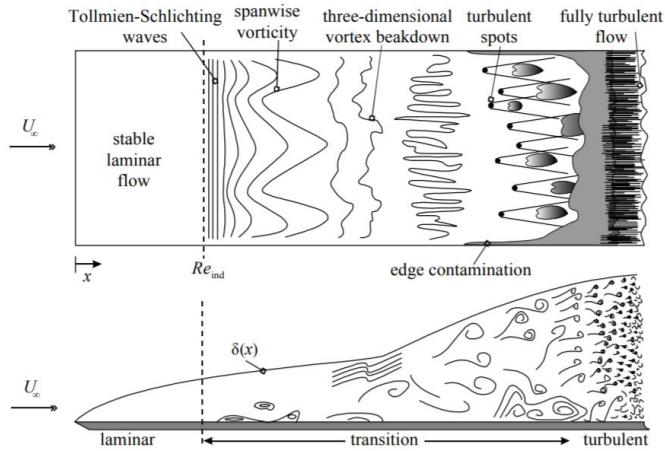


Figure 2.2: Incompressible flat plate boundary layer transition from Simon (2017), original image from Ockendon (2001).

According to the commonly used road to turbulence from Morkovin et al. (1994) (see figure 2.1), the transition process (except for bypass transition) goes through a receptivity process followed by

linear growth, either modal (in the local sense) or transient. This first linear phase is then followed by a secondary phase linked with non-linear interactions that will then lead to the breakdown to turbulence (see figure 2.2). In that context, it is interesting to first look at the literature on linear growth mechanisms and then on the non-linear secondary phase.

First mode instabilities

First mode instabilities are one of the most commonly studied instabilities in the literature as incompressible flat plate boundary layer transition is dominated by the two-dimensional first mode waves (which are viscous instabilities) also known as TS (Tollmien-Schlichting) waves (see figure 2.2). When the compressibility increases, the first mode instability switches from a fully viscous to a viscous-inflexional type. The instability also becomes three-dimensional as it grows at certain angle compared to the streamlines, explaining why the dominant compressible first mode instabilities are called "oblique" first mode (see figure 2.3).

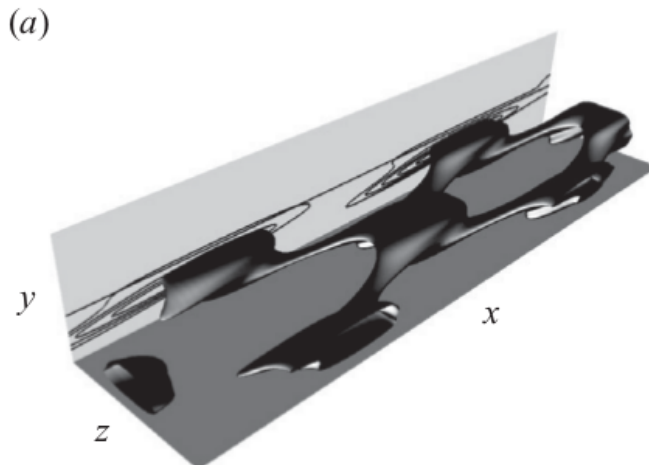


Figure 2.3: Isosurface of Q-criterion from a Mach 3 flat plate DNS showing superposition of two oblique first mode waves. From Mayer et al. (2011).

The angle of the most amplified oblique first mode is known to increase with compressibility up to a saturation at around 65° for a Mach number around 4 (Özgen and KIrcall, 2008). In hypersonic boundary layers, the oblique first mode instabilities are known to have a relatively low maximal amplification rate, especially when compared to second mode instabilities as discussed hereafter (Mack, 1975). They are however still relevant for the transition as their instability domain is larger than that of the second mode (Adams and Kleiser, 1993), leading to important integrated energy levels (*i.e.* high N factor value).

Second mode instabilities

In addition to the first mode which is a viscous instability and to its oblique counterpart which is viscous-inflexional, there is also a fully inviscid instability caused by the generalized inflection point in the boundary layer profile that has initially been documented by Mack (1975) called the second mode instability. The instability is two-dimensional, it appears at higher frequency than the first mode and is considered to be an acoustic mode: the boundary layer acts as a waveguide for acoustic disturbances. Because of its acoustic nature, it has a strong pressure signature at the wall (see figure 2.4) and has thus been extensively studied experimentally using high bandwidth pressure sensors such as PCB 132 sensors (see for example Benitez et al. (2020), Chynoweth et al. (2019), and Estorf et al. (2008) and figure 2.5). Its growth rate becomes locally higher than that of the oblique first mode around Mach 4.5 (see figure 2.6), which makes it the supposedly dominant instability mechanism for hypersonic flow. However, as previously stated, due to its

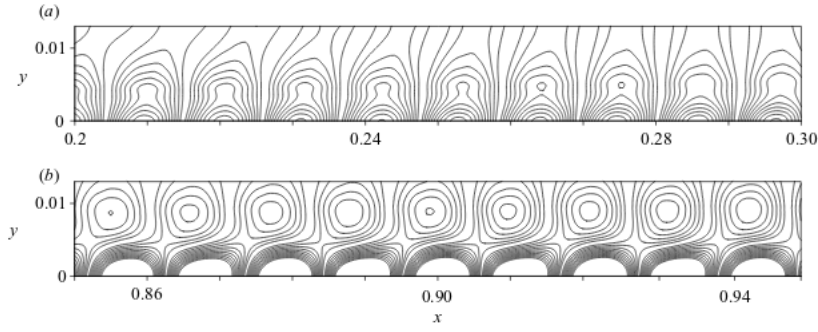


Figure 2.4: Typical pressure fluctuations caused by second mode instabilities on a flat plate at different longitudinal location. From Egorov et al. (2008).

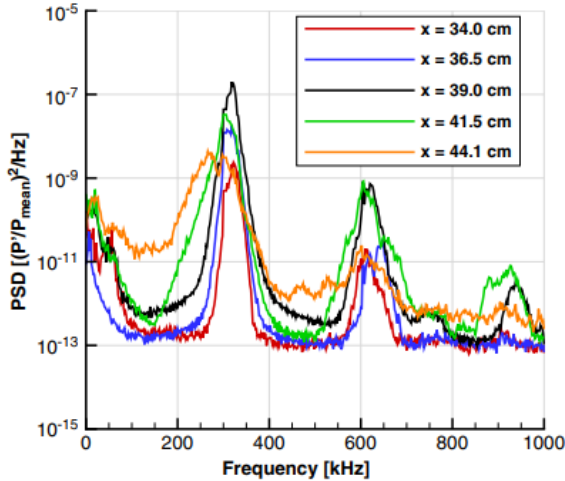


Figure 2.5: Experimentally measured pressure spectra at different station of a flared cone, showing peaks linked with second mode instabilities (around 300kHz) and second mode non-linear harmonics (around 600kHz). From Chynoweth et al. (2019).

smaller instability domain, it may nonetheless be less amplified from an integrated point of view than the oblique first mode, such as documented by Özgen and KIrcalı (2008) for example.

Mixing layer modes

Similarly to what happens in boundary layers, when the compressibility increases, new modes are known to appear in mixing layers (in addition to the well known Kelvin-Helmholtz instabilities). Multiple linear stability analyses and numerical studies (Foysi and Sarkar, 2010; Kudryavtsev and Khotyanovsky, 2005; Sandham and Reynolds, 1990) point towards the fact that three-dimensional obliques waves dominate the high convective Mach number shear-layer.

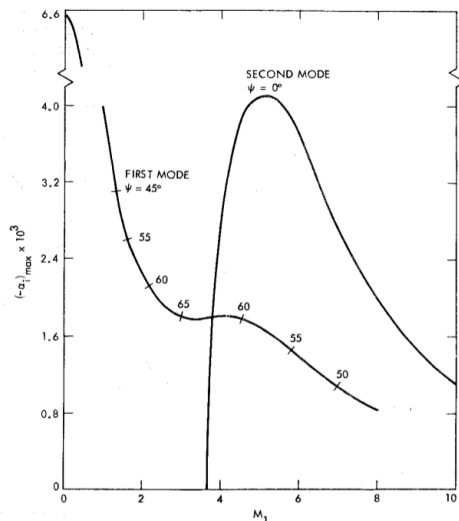


Figure 2.6: Oblique first mode and second mode amplification rate against Mach number, from Mack (1975).

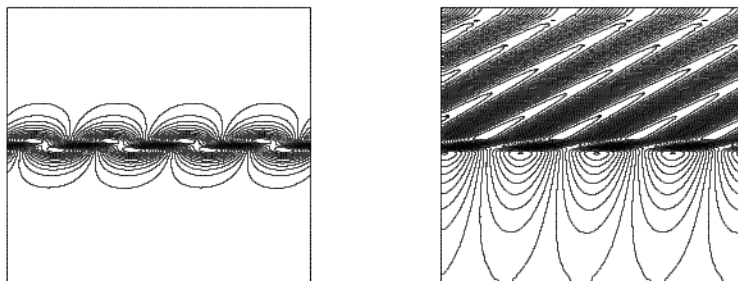


Figure 2.7: Eigenfunction (cross velocity) of the most amplified mode from a linear stability analysis of a low convective Mach number mixing layer (left) and high convective Mach number mixing layer (right) showing the difference between Kelvin-Helmholtz and supersonic shear-layer modes. From Kudryavtsev and Khotyanovsky, 2005.

The difference between Kelvin-Helmholtz and the supersonic shear-layer mode is illustrated in figure 2.7. Figure 2.8 presents the shape of a single and a pair of oblique modes, those modes then create typical flow structures present in transitional high Mach number mixing layer, as illustrated in figure 2.9.

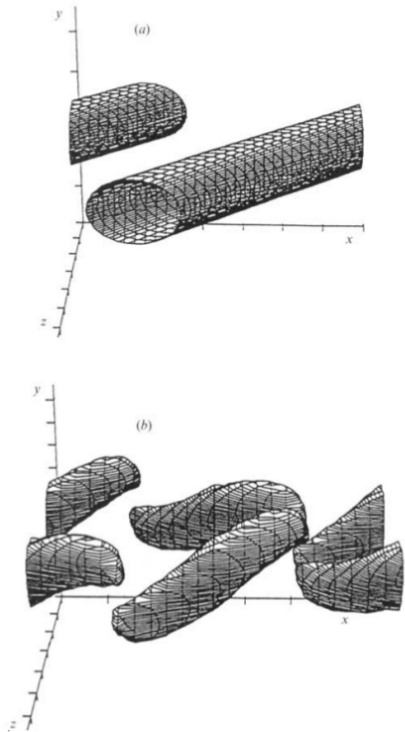


Figure 2.8: Surface of constant pressure from a LES showing a single (top) and a pair of opposed wavenumber (bottom) oblique modes in a high Mach number mixing layer. From Reynolds (1991).

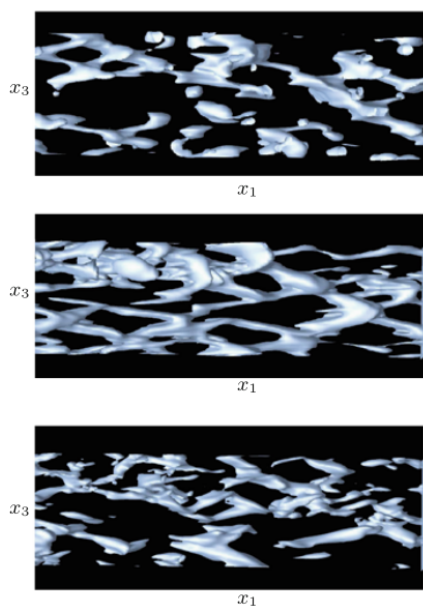


Figure 2.9: Surface of constant pressure from a LES showing oblique modes in a transitional mixing layer at different instant during the transition process. From Foysi and Sarkar (2010).

Streaks/Longitudinal vortices/Görtler vortices

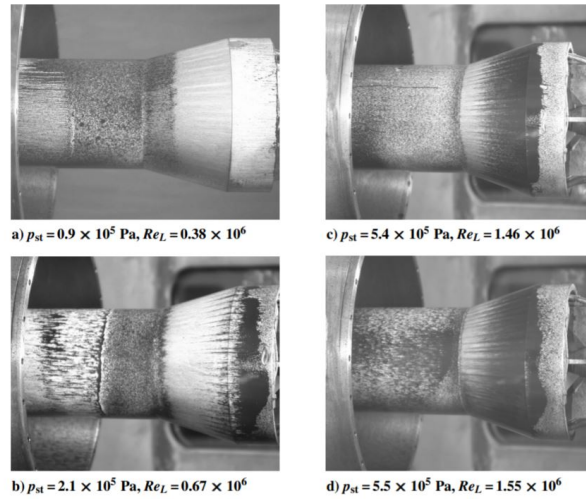


Figure 2.10: Oil-flow visualizations from Benay et al. (2006) showing streaks in the reattachment region.

During the experiments of Benay et al. (2006) at ONERA, an azimuthal striation was discovered at the reattachment point of the SBLI (see figure 2.10). This striation is supposed to be caused by contra-rotating longitudinal vortices: Benay et al. (2006) computed the Görtler number linked with the curvature of the streamlines and concluded that those elongated structures were Görtler vortices due to centrifugal forces.

Numerically, Comte (1999) was the first to document the presence of streamwise vortices in a LES of a turbulent compression ramp interaction that he postulated were Görtler vortices. His work was followed by the DNS of a similar configuration by Adams (2000), who came to the same conclusion. Latter, Navarro-Martinez and Tutty (2005) presented similar results for laminar interactions. Using optical measurement techniques, Zhuang et al. (2018) also showed the presence of elongated vortical structures in an OSBLI case, which they associated with Görtler vortices. Those streaks can also be measured using temperature sensitive paint or infrared thermography as they are known to create strong heat-flux variations due to the upwash (cold) and downwash (hot) region they create (see for instance Roghelia et al. (2017)).

However, the mechanism proposed by Görtler, 1940 is not the only one that can lead to the amplification of steady vortices. Other scenarios can lead to the apparition of that kind of structures. In fact, almost all transition scenarios end up with streaks that break down to turbulence. As we will see later, non-linear mechanisms linked with typical hypersonic boundary layer such as fundamental (second mode non-linear interaction) or oblique (oblique first mode non-linear interaction) breakdown ultimately leads to streaks. For example, heat-flux streaks caused by non-linear mechanisms have been observed on a flared cone case (Chynoweth et al., 2019). Sandham and Reynolds (1990) also found via their numerical work that the oblique modes present in the mixing layer could create those elongated structures via a baroclinic and dilatational mechanisms. Other mechanisms were also recently found to create that kind of structures, Dwivedi et al. (2019) studied a SBLI with input/output analyses (also known as resolvent analyses) and found that a convective mechanism mainly dominated by baroclinic effects could lead to the amplification of streaks too. Sidharth et al. (2018) and Hildebrand et al. (2018) found that the previously discussed laminar global instability of the separated region creates structures similar to those observed by Benay et al. (2006). In addition, Cao et al. (2021) recently showed that the non-linear saturation of those global instabilities could also lead to the apparition of higher wavenumber streaks.

Remark on the receptivity process

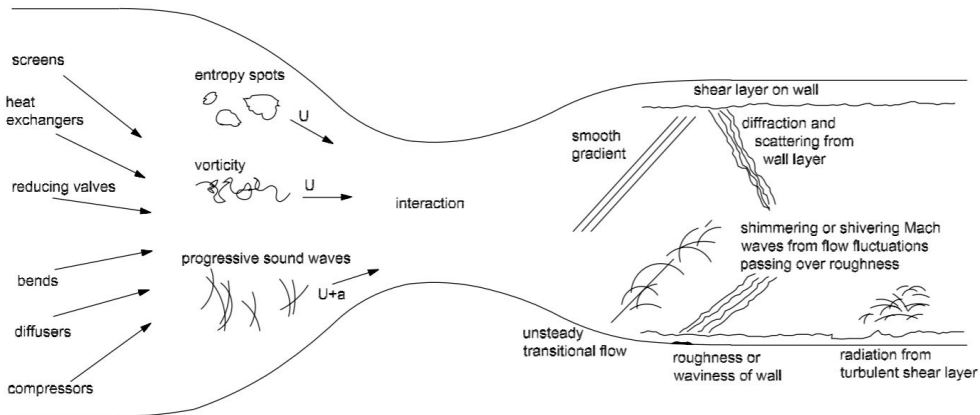


Figure 2.11: Schematic of hypersonic wind tunnel free-stream disturbances. From Schneider (2008).

It is important to note that all the linear instabilities presented above are not created *ex nihilo* in boundary layers, but are dependent on an upstream seeding. While instabilities such as first and second modes are modal from a local point of view (*e.g.* for the second mode, the local momentum profile contains a generalized inflection point and is thus unstable), those modes are convectively unstable, meaning that they cannot be self-sustained. In the global stability framework (see next remark), they are due to the non-normality of the governing linearized operator, which can cause the forcing by a little disturbance to create an important response through the operator. This means that the development of those instabilities is dependent on a triggering excitation. In flight, this can be for example the atmospheric turbulence, disturbances linked to the roughness of a wall, or even the presence of aerosols in the flow. Both the amplitude and the nature of the disturbance will play an important role in the selection of the dominant instability through the receptivity process. This is one of the causes of the uncertainty in the predicted onset of transition for hypersonic flight, as there are only very sparse data on the actual flight conditions. This is also a limitation for the experimental/numerical cross validation, as the free stream disturbances of wind tunnels are very complex and mostly unknown (see figure 2.11). However, the interest for wind tunnel free-stream data seems to be growing in the last decade. One may cite several attempts at measuring free-stream disturbances, such as the work of Masutti et al. (2011) at the VKI H3 wind tunnel, Schilden and Schröder (2017) and Schilden et al. (2016) at the Hypersonic Ludwieg Tube Braunschweig, Gromyko et al. (2013) at the transit-M wind tunnel or Duan et al. (2019) in the BAM6QT and HWT-8 wind tunnels. However, and even if they bring significant improvements to the state of the art, none of those campaigns could bring complete data (*i.e.* information on the fluctuation of the five conservatives variables on the complete relevant temporal frequency/spatial wavenumber spectrum).

Regardless, even with sparse data, recent numerical-experimental cross validations seem to bring promising results; for example the work of Hader and Fasel (2018) with BAM6QT data which shows that, for quiet tunnels, information on pressure fluctuations alone may be enough to accurately reproduce the experiments numerically.

Remark on the global stability framework for transition

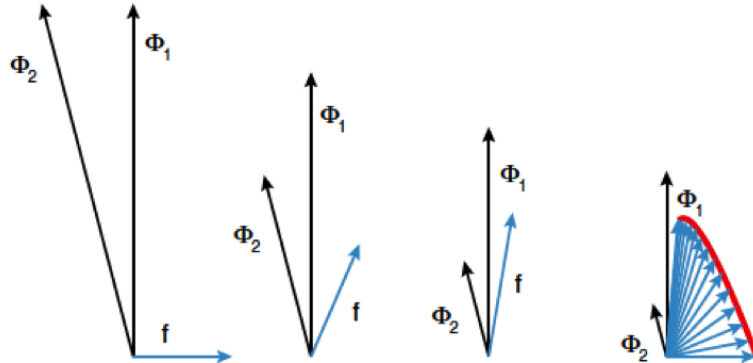


Figure 2.12: Illustration of transient growth from Schmid (2007). An initial forcing \mathbf{f} project on the eigenvectors Φ_1 and Φ_2 . While the eigenvector component decreases, the norm of \mathbf{f} increases.

Global stability analysis is widely used to study the linear dynamics of fluid flows. In many cases, studying the spectrum of the linearized Navier-Stokes operator gives important information on the presence of unstable global modes, which are self-sustained instabilities that will grow exponentially over time. This may explain the origin of unsteady features of some flows. However, Arnal (1989) showed that the transition process in hypersonic regime is highly dependent on receptivity and thus cannot be caused by globally unstable modes. In fact, transitional instabilities are convective, they are able to grow due to the non-normality of the linearized Navier-Stokes operator (*i.e.* its eigenfunctions are non-orthogonal, see Schmid (2007) for instance). Because of that non-normality, initial conditions or external forcing of very low amplitude can trigger high-amplitude fluctuations even when a flow is globally stable (see figure 2.12 which illustrates how the non-normality can lead to transient growth).

The global resolvent analysis (sometimes called input/output analysis) allows to study the impact of the non-normality of the operator on the amplification of such disturbances. Compared to local approaches commonly used to study transition (such as local stability analysis, Parabolized Stability Equation (PSE) analysis, *etc.*), no assumption about the parallelism of the flow is required, which makes it perfectly adapted for the study of convective instabilities in the presence of shocks and separation. Several papers have unveiled the links between resolvent and local stability analyses, and it is now well established that resolvent modes match local stability results in zones where the flow is nearly parallel and dominated by some locally unstable modes (Sipp and Marquet, 2013). As such, resolvent analyses may be viewed as a generalization of the classical local stability approach, with the difference that it may deal with more complex situations that cannot be factored in by a local stability approach or by PSE (see Sipp and Marquet (2013), Beneddine et al. (2016), Bugeat et al. (2019) for instance).

Following the work of Brandt et al. (2011) and Bugeat et al. (2019), we can separate the non-normal mechanisms presented in this work into two categories, the 'convective type non-normalities' and the 'component-type non-normalities'. The former are linked to the advection of perturbations in the mean flow, these are usually referred to as 'modal' instabilities in the LST framework. The latter are linked to the transport of mean-flow momentum by the perturbations (the 'lift-up' effect, for example) that would be referred to as non-normal instabilities in the local framework. Note that the vocabulary from the literature is somewhat ambiguous, as "modal" and "non-modal" terms are used differently in the global stability and the local LST frameworks, sometimes to characterize the same underlying physical mechanism. In the following, we focus on global analysis and use the global stability point of view to refer to the nature of the modes.

2.1.2 Non-linear mechanisms

The linear mechanisms mentioned here-before will not directly lead to turbulence, a secondary phase and breakdown is necessary (see figure 2.1), depending on the flow conditions, instabilities can interact non-linearly in different ways. The most dominant non-linear interaction and breakdown mechanism for hypersonic boundary layer will be presented here after.

Second mode fundamental and sub-harmonic breakdown

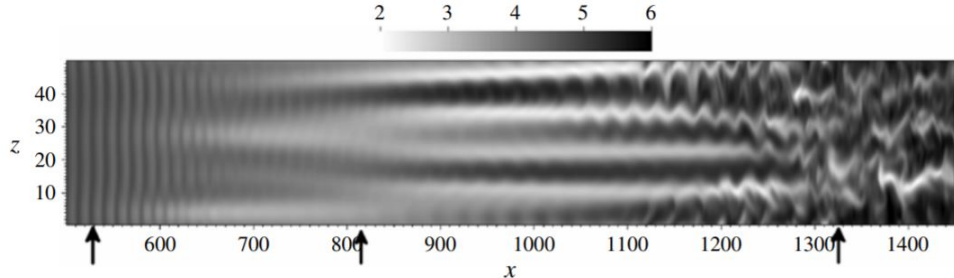


Figure 2.13: Streamwise velocity fluctuations for the second mode fundamental breakdown, the arrows show the beginning of the transition, the saturation of second mode waves and the end of the transition. From Franko and Lele (2013).

When the second mode instabilities reach an amplitude high enough, they start to interact non-linearly to create oblique waves either at the same frequency or a subharmonic one (Adams and Kleiser, 1993; Hader and Fasel, 2018; Sivasubramanian and Fasel, 2011). The growth of the oblique wave creates vorticity, which leads to the apparition of streaks that may be strong enough to breakdown to turbulence (Franko and Lele, 2013).

First mode oblique breakdown

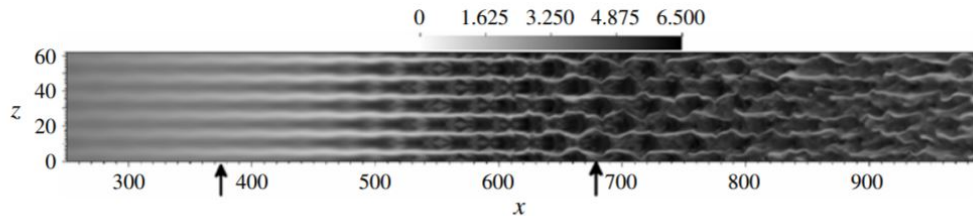


Figure 2.14: Streamwise velocity fluctuations for an oblique breakdown case, the arrows shows the beginning and end of the transition process. From Franko and Lele (2013).

While the second mode is already known to locally dominate the hypersonic flat plate boundary layer, many studies (Chang and Malik, 1994; Fasel et al., 1993a; Franko and Lele, 2014; Franko and Lele, 2013; Mayer et al., 2011) show that its nonlinear evolution is not the only possible cause of transition: oblique breakdown, which is linked to the streaks created by the non-linear interaction of first oblique modes, is also a possible candidate. This mechanism was first discovered by Thumm (1991) (see also Fasel et al. (1993a,b)) for a supersonic (Mach 1.6) boundary layer using DNS. It was shown that the nonlinear interaction of a pair of oblique waves with opposite spanwise wavenumbers generates steady streamwise structures with twice the spanwise wavenumber, which grow rapidly in the streamwise direction (see figure 2.14). Schmid and Henningson (1992) then confirmed for a plane channel flow that this mechanism may also be relevant for incompressible flows. The numerical study of Franko and Lele (2013) shows that oblique breakdown is a relevant way to create turbulence in high-speed boundary layer.

2.1.3 Relevant mechanisms for hypersonic SBLI

Now that the main transition scenarios for hypersonic boundary layer have been presented, it may be interesting to discuss which of those mechanisms could *a priori* play a role in the transition process through a SBLI. Given the results of Franko and Lele (2014) and Franko and Lele (2013), if the transition happens in the attached boundary layer, either oblique or fundamental breakdown should be relevant, with the oblique breakdown being the fastest way to create turbulence. Once the boundary layer encounters the shock and separates, the expected dominant modes changes and the transition should be driven by the supersonic shear layer modes. Finally, in the reattachment region, one could expect streaks (which may be driven by various mechanisms) to be the last structures that may play a role in the transition process.

2.2 Low frequency dynamics of the shock-bubble system

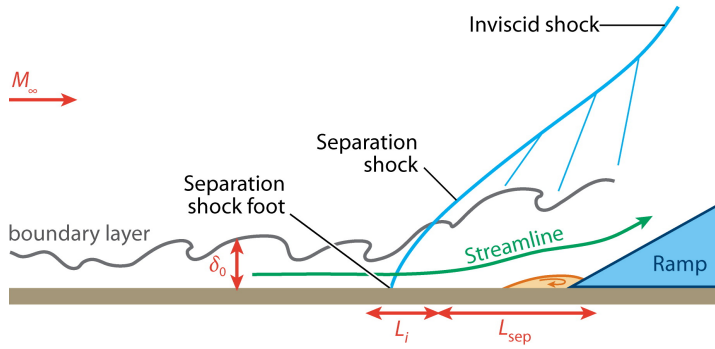


Figure 2.15: Schematic of the compression ramp, incoming boundary layer and SBLI from Clemens and Narayanaswamy (2014).

The shock-bubble system brings one of the main limitations of SBLI on high-velocity flight, as they tend to initiate a low-frequency large-scale motion in the flow called the "breathing of the bubble". This unsteadiness can lead to a variety of problem, either linked to the integrity of the object as the unsteady thermal and mechanical loading can lead to catastrophic failure, or a trajectory default as the effectiveness of control surfaces will be affected.

Multiple studies on shock-wave/turbulent boundary layer interactions allowed the community to draft two dominant scenarios for the origin of the bubble instability. Those scenarios are presented in the annual review of Clemens and Narayanaswamy (2014). Those scenarios are briefly described in the following, and their relevancy for the present study is discussed in further chapters. Several papers on the laminar separation are also available in the literature and tend to show that a global unstable mode may be present in the laminar recirculation region. This section aims at briefly discussing all the known (either turbulent or laminar) mechanisms driving the shock/bubble instability of separated SBLI.

Upstream scenario for weak interaction

The first scenario is dominant in the case of weak or 'incipient' interaction (*i.e.* the shock stands off from the corner, but there is no reversed mean flow) and is specific to turbulent boundary layers. In this scenario, the interaction of incoming turbulent superstructures in the boundary layer with the shock-bubble system is supposed to drive the shock-bubble system unsteadiness (see figure 2.16). For example, Ganapathisubrama et al. (2007) experimentally reported a correlation between large-scale low and high-speed regions in the boundary layer and the unsteadiness of the separation point for a Mach 2 compression ramp using Particle Image Velocimetry and Planar Laser Scattering. Erenbil and Dolling (1993) also showed a correlation between the incoming pressure disturbance and the separation unsteadiness for a Mach 5 compression ramp. Those evidences point toward the idea that the shock-bubble system responds to upstream forcing that are due to the intrinsic structure of the turbulent boundary layer.

Toubal and Sandham (2011) went even further to generalize this idea. They showed that the shock unsteadiness can simply be caused by the broadband upstream excitation of the shock-bubble system by the turbulent boundary layer, even for strong interactions. The interaction acts as a low-pass filter and the unsteadiness may simply be explained as an intrinsic property of the coupled (incoming turbulent BL - interaction) system, without the need of direct correlation with incoming superstructures.

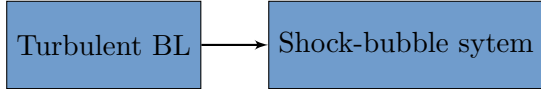


Figure 2.16: Schematic of the mechanisms at stake in the upstream scenario.

Upstream scenario: the special case of the transitional boundary layer

The scenario presented here-before is deemed relevant for turbulent boundary layers and weak interaction. However, as soon as the flow conditions change and the incoming boundary layer is transitional instead of turbulent, the apparition of the superstructures, which are characteristics of turbulent boundary layer, is no longer possible. The continuous broadband excitation of the separation is also not possible anymore as transitional spectrums generally have distinguished peaks at frequencies corresponding to the dominant boundary layer instabilities, or a broader spectrum in the turbulent spots, but not a continuous (in time) broadband spectrum. Because of those characteristics of the transitional boundary layer, the scenario presented here-before seems highly unlikely. However, a comparable scenario can still happen. This time, instead of superstructures, the disturbance can come from the intermittent presence of turbulent spots in the boundary layer. This could lead to a correlation of the incoming spots in the transitional boundary layer with the shock-bubble system unsteadiness. The disturbances may also come from the streaks created in the transitional boundary layer, as similarly to the super-streaks present in the boundary layer, they can lead to an unsteady corrugation of the shock.

Downstream scenario for strong interaction

The second scenario is dominant in the case of a strong interaction with a clearly defined separation (the mean flow presents a reversed flow region downstream from the separation shock). In that case, Debièvre and Dupont (2009) found that there is no correlation between the incoming structures in the boundary layer and the separated region unsteadiness. However, they found a correlation between the pressure signal measured in the separation and the recirculation region. The "breathing" of the bubble is then supposed to drive the unsteadiness of the shock bubble system. This breathing is most probably due to a self-sustained instability mechanism inside the bubble (*i.e.* an unstable global mode, see Nichols et al. (2017) for instance), the downstream oscillation of the bubble being the main driver of the shock oscillation. Piponnaiu et al. (2009) proposed a scenario based on the convection of fluid out of the bubble by the vortical structures in the mixing layer. The undersized bubble then needs to be replenished, which occurs through the reattachment point at a timescale corresponding to the low-frequency oscillation of the shock-bubble system.

It is interesting to note that both the upstream and downstream mechanisms can be present at the same time. For instance, Priebe and Martín (2012) reported correlation of both the downstream part of the bubble and the upstream boundary layer with the shock motion (albeit a stronger one for the downstream part since the separation is important in their case). This hypothesis of both scenarios being present at the same time but with different importance depending on the strength of the interaction is also one of the conclusions in the annual review of Clemens and Narayanaswamy (2014).

Bubble global mode for shock-laminar boundary layer interaction

When the boundary layer is laminar, it is more affected by the pressure gradient caused by the shock than when it is turbulent. This leads to the apparition of a strongly separated region, with bubbles that are significantly larger than those encountered in the turbulent case. The global mode discussed in the downstream scenario presented above may then be linked to other articles about laminar separation unsteadiness. Robinet (2007) was the first to study the global

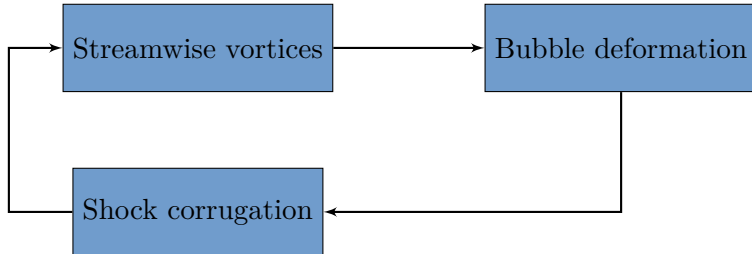


Figure 2.17: Schematic of the mechanisms at stake in the bubble global instability.

unsteadiness of the bubble induced by a shock-laminar boundary layer interaction (an OSBLI in his case). He found that there was a (quasi-)steady three-dimensional unstable mode inside the recirculation region. He proposed a link between this unstable mode and the one already known to happen in incompressible separation (Gallaire et al., 2007; Marquet et al., 2009). More recently, Sidharth et al. (2018) shown that this 3D destabilization of the recirculation bubble was also relevant for hypersonic compression ramp flow. Hildebrand et al. (2018) also found evidence of such an instability in a transitional OSBLI case.

The mechanism behind the self-sustained instability proposed by Hildebrand et al. (2018) relies on the apparition of streamwise vortices in the separated region, those vortices create a spanwise undulation in the reattachment line (through the redistribution of streamwise momentum). This undulation leads to the apparition of corrugation in the base of the shock. Because of this corrugation, streamwise vortices are amplified, closing the loop of the global instability mechanism (see figure 2.17).

Remark on the role of the shock on the unsteadiness

It is interesting to note that although it plays a major role in the definition of the topology of the flow, the shock seems to play little to no driving role in the unsteadiness of the bubble. In most of the recent numerical studies, the shock is supposed to be relatively unimportant, and its resolution is often overlooked. However, recent results from Sawant et al. (2021) using Direct Simulation Monte Carlo (DSMC), which insures a proper physical resolution of the shock-wave, show that it may actually play an important role in laminar SBLI unsteadiness.

Chapter 3

Numerical setup

This chapter presents the numerical tools used in the thesis. First, the numerical strategy is explained alongside characteristics of the Navier-Stokes solver used. Then the post-processing tools used to extract information from the simulations are described. Finally, the linear stability framework employed to gain physical understanding of the mechanisms at stake in the flow is presented.

Contents

3.1	Numerical Simulation	28
3.1.1	Navier-stokes equations and solver	28
3.1.2	High-fidelity simulations	29
3.1.3	Quasi Direct Numerical Simulation (QDNS)	29
3.1.4	Injected noise	32
3.2	Post-processing tools	35
3.2.1	Definition of the fluctuation energy for compressible flow	35
3.2.2	Spectral Proper Orthogonal Decomposition	36
3.2.3	Energy decomposition	37
3.2.4	Low frequency treatment: signal decimation and filtering	38
3.3	Linear Stability Analysis	41
3.3.1	Global stability analysis	41
3.3.2	Resolvent Analysis	42
3.3.3	Jacobian computation	44
3.3.4	Eigenvalues research	45
3.3.5	2.5D formulation for axisymmetric mean flows	45

3.1 Numerical Simulation

3.1.1 Navier-stokes equations and solver

All the computations presented in this thesis are done using the high-performance finite volumes multi-block structured FAST (Flexible Aerodynamic Solver Technology) solver from ONERA (Péron et al., 2017). The FAST solver is solving the compressible Navier-Stokes equations:

The mass conservation writes:

$$\frac{\partial \rho}{\partial t} = \nabla \cdot (\rho \mathbf{u}), \quad (3.1)$$

the momentum equation:

$$\frac{\partial \rho \mathbf{u}}{\partial t} + \nabla \cdot (\rho \mathbf{u} \otimes \mathbf{u}) = -\nabla P + \nabla \cdot \tau, \quad (3.2)$$

and the energy equation (assuming Fourier thermal conductivity):

$$\frac{\partial \rho E}{\partial t} + (\nabla \cdot (\rho E + P)) \mathbf{u} = \nabla \cdot (\tau \cdot \mathbf{u}) + \frac{C_p}{P_r} \nabla \cdot (\mu \nabla T), \quad (3.3)$$

with the flow being described by the conservative variables state vector $\mathbf{q} = (\rho, \rho \mathbf{u}, \rho E)$, where ρ is the density, \mathbf{u} the velocity vector and E the total energy (the state vector can also be described using primitive variables (ρ, \mathbf{u}, T) with T the temperature). $P_r = 0.72$ is the Prandtl number, C_p the specific heat capacity at constant pressure. P is the pressure, which is computed from the state equation for perfect gaz:

$$P = \rho R T, \quad (3.4)$$

with R the universal gas constant.

τ is the viscous stress tensor:

$$\tau = \mu (\nabla \otimes \mathbf{u} + (\nabla \otimes \mathbf{u})^T - \frac{2}{3} (\nabla \cdot \mathbf{u}) \mathbf{I}) \quad (3.5)$$

with μ the molecular viscosity computed according to the Sutherland law:

$$\mu = \mu_s \sqrt{\frac{T}{T_{ref}}} \frac{1 + \frac{T_s}{T_{ref}}}{1 + \frac{T_s}{T}}, \quad (3.6)$$

with $\mu_s = 1.711 \times 10^{-5}$, $T_s = 110.4K$ and $T_{ref} = 273.5$.

Finally, the total energy E is computed as:

$$E = C_p T + \frac{1}{2} |\mathbf{u}|^2. \quad (3.7)$$

The Navier-Stokes equations (3.1), (3.2), (3.3) are then written in vector form:

$$\frac{\partial \mathbf{q}}{\partial t} = \mathbf{F}_c - \mathbf{F}_v + \mathbf{f}. \quad (3.8)$$

Viscous fluxes \mathbf{F}_v are computed using a second-order centered scheme, and convective fluxes \mathbf{F}_c are computed using the second-order upwind AUSM(P) scheme proposed by Mary and Sagaut (2002) with an unlimited third-order MUSCL reconstruction, \mathbf{f} being an eventual source term. The time integration is performed via an explicit third order 3-steps Runge-Kutta scheme. The time step is always set to ensure a CFL number lower than 0.5 in the whole domain. The temperature of the wall is always imposed at 290K to reproduce standard experimental conditions in R2ch (Benay et al., 2006; Bur and Chanetz, 2009). Standard supersonic inflow, outflow and farfield conditions are used for the other boundaries. These are characteristics-based boundary conditions that avoid numerical reflections.

3.1.2 High-fidelity simulations

High-fidelity simulation, and specifically Direct Numerical Simulation (DNS), is a common tool to study transitional flows (Reynolds, 1991; Sandham et al., 2014) and in particular the transition process (Fasel et al., 1993a; Franko and Lele, 2014; Franko and Lele, 2013; Mayer et al., 2011; Schmid and Henningson, 1992).

The idea behind those simulations is to fully resolve all the structures present in the flow, including the smaller scale turbulent structures. This ensures that the computed flow is the exact solution of the posed problem and allows for fine understanding of all the mechanisms present in the flow. Those simulations may appear complex, but in reality they are conceptually simpler than numerically lighter methods like Reynolds Averaged Navier Stokes (RANS) or Large Eddy Simulation (LES), which may involve complex modeling of the physics of the flow. They just rely on the assumption that the numerical parameters are chosen such that all the scale of flow can be completely and accurately resolved by the used numerical schemes. However, two complications arise when one wants to set up that kind of simulation:

1. The cost can quickly become unreachable for applied flow with the current computing resources. This is mainly because of the constraint imposed on the sizing of the mesh due to the need to fully resolve even small turbulent structures (usual mesh sizing for DNS are of the order of $\Delta x_+ = 10$, $\Delta z_+ = 5$, $\Delta y_{+wall} < 1$ in turbulent regions). This can easily lead to meshes of several billions points or more.
2. The simulations are so sensitive to small changes in flow or boundary conditions that the physical interpretation may not be as straightforward as it seems. This is especially true for high-fidelity simulations of transition as the receptivity process will play a paramount role in the selection of the transition scenario. Because of that, the disturbances injected in the simulation will play a central role and the simple fact that the simulation is fully resolved will not be sufficient to get physical results that are, for example, similar to free-flight results as long as the boundary conditions and free-stream conditions of the simulation are not exactly those of free-flight.

3.1.3 Quasi Direct Numerical Simulation (QDNS)

The first drawback of DNS, which is the numerical cost, can easily be tackled in our case. In the present work, we are mainly interested in simulating transition to turbulence through the SBLI. The turbulent dynamics of the reattachment region is not the primary focus of this study, the goal is to capture the mechanisms of transition and shock boundary layer interaction. Therefore, we only need DNS resolution upstream from the reattachment point and LES resolution downstream, provided that the feedback from the downstream region is negligible. This leads to simulations where the mesh sizing is chosen such that the flow upstream of the reattachment point is fully resolved regarding DNS standards. Downstream from the reattachment, where the flow becomes turbulent and the wall-shear-stress is maximum, the sizing of the mesh becomes slightly under-resolved, and corresponds to a highly resolved LES of SBLI (Bonne et al., 2019; Garnier et al., 2002; Teramoto, 2005) rather than a DNS. Therefore, the computation corresponds to a QDNS such as described by Spalart (2000), since the resolution is in between the typical LES and DNS resolution (Garnier et al., 2009; Georgiadis et al., 2009). Spalart (2000) defined the QDNS as similar to most highly resolved LES for 3 reasons:

- All the eddy types in the flow are resolved, including the near wall streaks.
- The eddy viscosity of the LES (from the SubGrid Scale (SGS) model) is of the same order as the molecular viscosity present in the QDNS.
- The spacing of the grid is still very limited (*e.g.* $\Delta x_+ < 50$).

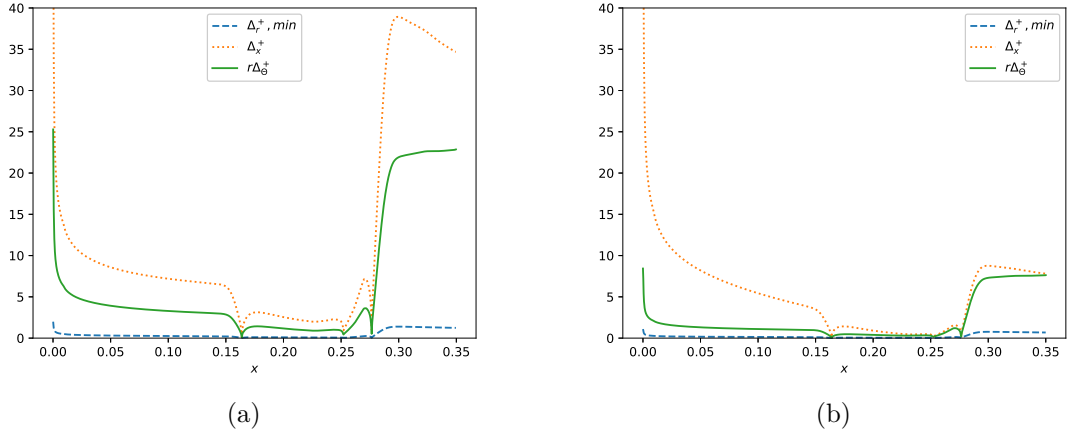


Figure 3.1: Sizing of the mesh in local wall unit for (a) the grid used for the QDNS presented in chapter 6, (b) the grid corresponding to a stricter DNS used for validation purpose.

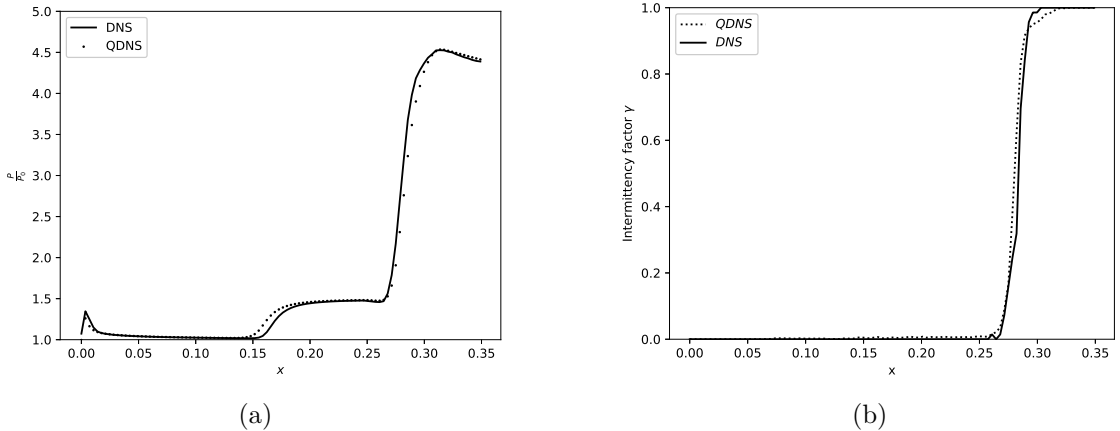


Figure 3.2: Comparison of the results of the DNS and QDNS for (a) the pressure distribution along the geometry and (b) the intermittency factor averaged in time at a given azimuthal position.

Because of that, one can switch from LES with SGS models to Monotonically Integrated Large Eddy Simulation (MILES) where the SGS model is replaced by the dissipation from the numerical scheme. From that point of view, as soon as we consider the feedback from the turbulent zone to be negligible, we can perform computations that are DNS in the pre-transition region and QDNS (or MILES) in the post-transition region just by the design of the mesh and the use of an upwind scheme. The use of an upwind scheme is mandatory in the under-resolved zone of the computation as it maintains the smoothness of the solution by offsetting the energy cascade (Spalart, 2000) (the numerical dissipation replaces the actual dissipation at the end of the cascade) as is commonly done for MILES. The used version of the AUSM(P) scheme was already successfully used by Bonne et al. (2019) in their MILES of an OSBLI case.

Grid size	QDNS	DNS
n_x	1409	3378
n_r	204	249
n_θ	600	1800
n_{pts}	172×10^6	1.514×10^9
Δt	$10^{-8}s$	$5 \times 10^{-9}s$

Table 3.1: Grid and time step for the QDNS and DNS cross validation.

Given that all the studied flows are hypersonic and that at the reattachment point, the boundary layer is compressed in a way that leads to an extremely fine subsonic region, the assumption that the feedback from the downstream region is negligible seems reasonable. The hypothesis that QDNS and DNS gives equivalent results was still checked on the Mach 5 cylinder flare case by performing a full-fledged DNS over a long enough period of time to converge the mean flow and transition point. The DNS have roughly 10 times more grid points (overall) than the QDNS, which brings the total number of cells to around 1.5 billion. A quantitative comparison of the results obtained with the two meshes is presented in this section. Except for the grid and the time step, which are presented in table 3.1, all the numerical parameters are kept the same. The local sizing of the two grids are presented in figure 3.1, showing that the sizing of the fine grid corresponds to the DNS requirement in the reattachment region. Figure 3.2 presents the pressure distribution along the geometry and the intermittency factor for both the QDNS and DNS. The local intermittency value $\gamma(x)$ represents the probability of being in a turbulent spot at a given time (see the work of Narasimha (1990) for more details). It is commonly used to describe the transition process (see for instance Sandham et al. (2014)). An intermittency factor of 0 thus means that the boundary layer is fully laminar, with no turbulent spot, while a factor of 1 means that the flow is fully turbulent. Everything between 0 and 1 is considered transitional. In the present case, the intermittency factor is computed from spectrograms of wall pressure fluctuations along the geometry, following an idea of Arnal and Juillen (1977). First, a range of "laminar" perturbation frequencies is defined. The presence of a turbulent spot is assumed if fluctuations are detected outside this range (at higher frequencies). For this study, it was decided to define the laminar range from 0Hz up to 600kHz. These values have been chosen such that the upper limit is more than twice the highest frequency of the common hypersonic boundary layer instabilities (results have shown that the shape of gamma is not impacted by a change of this threshold toward upper frequencies). This leads to the following definition of γ :

$$\gamma(x) = \frac{1}{T} \int_0^T \eta(x, t) dt, \quad (3.9)$$

with $\eta(x, t)$ the sensor detecting the presence of a turbulent spot, defined as:

$$\eta(x, t) = \begin{cases} 1 & \text{if } S_P^{f>600kHz}(x, t) \geq \epsilon \\ 0 & \text{otherwise,} \end{cases}$$

with S_P the pressure spectral content at a given time from the spectrogram. Figure 3.2 shows that except for a small overestimation of the bubble size, and slight variation in the intermittency (which may be due to the convergence of the spectrograms) the QDNS can predict the right flow topology and transition point, which is an important result given the high sensitivity of the flow topology to the transition location. Results shown here indicate that our quasi-DNS yields an accurate description of both and may therefore be considered appropriate for studying transition, at a fraction of the cost. This conclusion is in line with previous studies (Teramoto, 2005) which already showed that LES may be a satisfactory tool for the study of transition in such flows.

Mesh parameters for all the different computations exploited in this thesis are presented in table 3.2.

Case	Type	M_∞	Span	N_x	N_r	N_θ	N_{tot}	Δt	Chapter
A	QDNS	6	360	1600	220	3600	1.267×10^9	1×10^{-8} s	5
B	QDNS	6	60	1600	220	600	211×10^6	1×10^{-8} s	5
C	QDNS	6	15	1600	220	150	52.8×10^6	1×10^{-8} s	5
E	QDNS	5	60	1409	204	600	172.4×10^6	1×10^{-8} s	6
D	DNS	5	60	3378	249	1800	1.514×10^9	5×10^{-9} s	3
F	QDNS	4-5-6-7	60	1600	220	600	211×10^6	1×10^{-8} s	7
G	QDNS	5	15	1600	220	150	52.8×10^6	1×10^{-8} s	9

Table 3.2: Numerical parameters for the computations.

3.1.4 Injected noise

As mentioned in the previous section, the disturbances injected in the simulations will play a central role in the selection of dominant instabilities. In several papers (Franko and Lele, 2014; Franko and Lele, 2013; Mayer et al., 2011), the inlet disturbance is chosen to excite a particular instability mechanism within the boundary layer. In the present work, it was chosen not to decide *a priori* which mechanism was going to be dominant, and to let all of them compete in the simulation. Consequently, a generic spatio-temporally white perturbation has been injected at the inlet, which excites vortical, acoustic, and entropic modes. This is reminiscent of the work of Hader and Fasel (2018), who injected broadband pressure fluctuations into their numerical simulation to study natural transition mechanisms in hypersonic boundary layers. Note that the injected noise is nonetheless arbitrary, since other choices of generic disturbances may have been considered. Most of the time in this thesis, particular receptivity of the chosen noise is documented.

It is worth mentioning that the injected noise does not aim at accurately reproducing the actual free-stream noise of the hypersonic wind tunnel R2Ch, which is composed of various complex fluctuations (Schneider, 2008, see figure 2.11) with noise radiating from the nozzle and shear layer plus possible perturbations coming from the upstream parts of the blowdown tunnel. Instead, it aims at creating a flow configuration with a generic inlet disturbance, which excites a variety of modes that would develop, compete, and interact together. Because of that, the amplitude of the inlet noise such as presented in figure 3.3 is not comparable to a free-stream turbulence level of the wind tunnel. As the noise is not based on physical insight nor experimental data but is instead purely numerical, there is still strong interaction of the noise with the numerical scheme and the Navier-Stokes operator, leading to important change in the fluctuation level at the beginning of the domain. Figure 3.4 presents the typical longitudinal evolution of the wall pressure fluctuation downstream of the noise injection plane. It shows that the fluctuations decrease quickly at the beginning of the domain and that there is no way to choose a location to get the "converged" free-stream pressure fluctuation level caused by the noise (as the downstream fluctuations may then be linked with physical amplification mechanisms). Thus, the amplitude of the inlet noise is not a free-stream turbulence level and cannot be linked directly to the turbulence level of the R2ch blowdown facility.

However, injecting true spatio-temporally white noise raises numerical difficulties, as spatial schemes are not designed to work with very short wavelength oscillations (of the order of a few cells). Because of that, high-amplitude white-noise injection may require filtering of the small wavelength oscillations to avoid numerical instabilities. This filtering is performed by a convolution of the disturbance signal by a filtering kernel that spans over seven cells in every direction.

To illustrate the sensitivity to the injected noise, five QDNSSs have been performed on the Mach 5 cylinder flare case at $Re_L = 1.9 \times 10^6$ (with $L = 0.252m$ the length of the cylinder, see figure

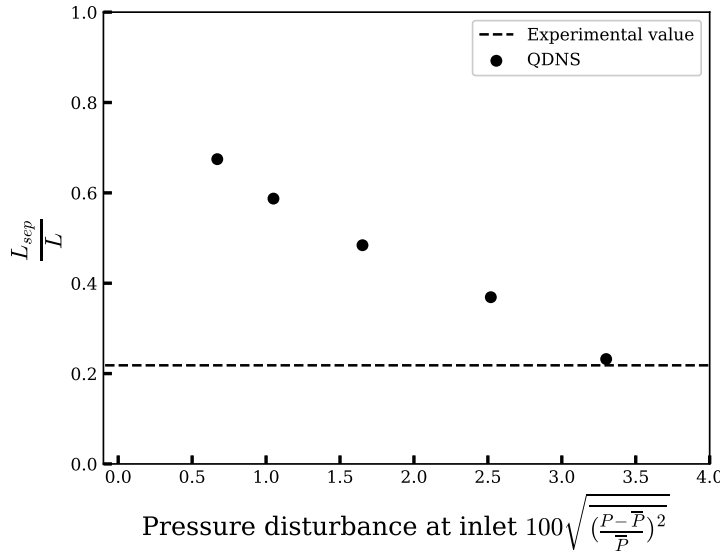


Figure 3.3: Size of the separated region of the mean flow with different levels of filtered noise and experimental value corresponding to the same free-stream conditions from Benay et al. (2006), showing the impact of the disturbances on the topology of the mean flow.

1.1), each with a different level of filtered inlet noise (the noise levels are presented in figure 3.3), yielding five mean flows computed by averaging in time and along the azimuthal direction the simulation results. From these mean flows, a bubble length L_{sep} can be computed, which gives the results presented in figure 3.3. The level of noise impacts the transition location and therefore influences L_{sep} since both the separation and reattachment dynamics strongly depend on the laminar/turbulent nature of the flow. More importantly, these results show that for a given level of inlet perturbation, the QDNS yields results in agreement with the experimental data from Benay et al. (2006), which validates the present computational parameters. But it also reveals how sensitive the flow is to external noise, which raises the question of the level of perturbation to choose for the different studies. The relation between the recirculation bubble topology and the upstream perturbations has also been documented by Marxen and Rist (2010) for incompressible separation. They showed that the transition caused by upstream perturbations leads to the shrinkage of the bubble from both sides. The fact that the mean flow topology is highly dependent on the level of free-stream noise is one of the primary motivations to use the mean flow instead of a base flow (which can greatly differ from the mean flow) for the stability analysis performed in this thesis, as it was already advised by Marxen et al. (2010) and Marxen and Rist (2010).

White noise is injected in the simulations by directly perturbing the density field, the resulting forcing term (through the Navier-Stokes operator) affects all the conservative variables. The injection is realized four cells downstream ($i = 4$) of the inlet boundary condition in order to not interfere with it. The form of this injection is the following:

$$\rho'[j, k] = \rho[j, k](1 + Ar_n[j, k]), \quad (3.10)$$

with A the injected amplitude and r_n a random number normalized such that the root-mean-square on the whole injection plane is 1:

$$r_n[j, k] = \frac{r_r[j, k]}{\sqrt{r_r^2}}, \quad (3.11)$$

r_r being a NumPy generated (numpy.random.random) random number from a continuous uniform distribution between -0.5 and 0.5 which is seeded from the Linux random generator

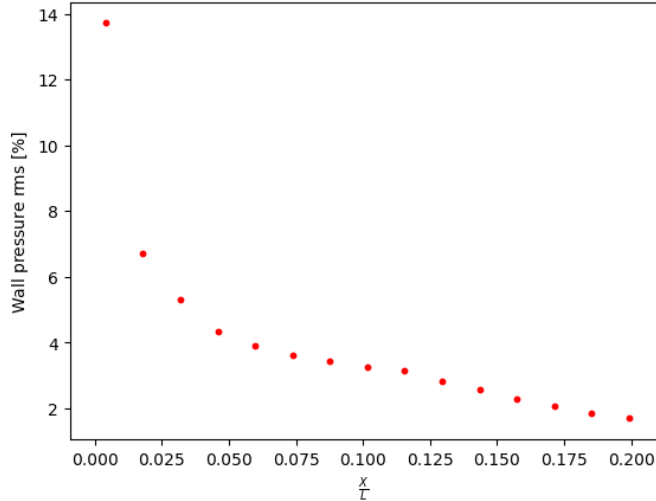


Figure 3.4: Typical longitudinal evolution of the wall pressure fluctuations downstream of the noise injection.

"/dev/urandom" of the cluster, \cdot being for this special case a spatial average and j, k ranging the indices of the cell of the injection plan. In the case of a filtered white noise, the noise is simply fed through a filtering kernel before normalization:

$$r_{filtered} = r_n * K, \quad (3.12)$$

with $*$ denoting the convolution product and K a generic normalized kernel, for instance in the case of a Gaussian filter (5×5):

$$\mathbf{K} = \frac{1}{256} \begin{bmatrix} 1 & 4 & 6 & 4 & 1 \\ 4 & 16 & 24 & 16 & 4 \\ 6 & 24 & 36 & 24 & 6 \\ 4 & 16 & 24 & 16 & 4 \\ 1 & 4 & 6 & 4 & 1 \end{bmatrix}. \quad (3.13)$$

As the time step used in the computation is far less than the convection time through one cell in the streamwise direction, the spatial scheme would be unable to transport a white noise that is updated at every iteration. To address this issue, it was chosen not to update the noise every iteration but to keep it constant for a fixed number of iterations between each update (depending on the streamwise velocity and size of the cells). This ensures that the scheme is able to discretize the noise while the spectral content is still rich enough in the high frequencies for the present study. Typical spectral content of the injected noise is presented in figure 3.5.

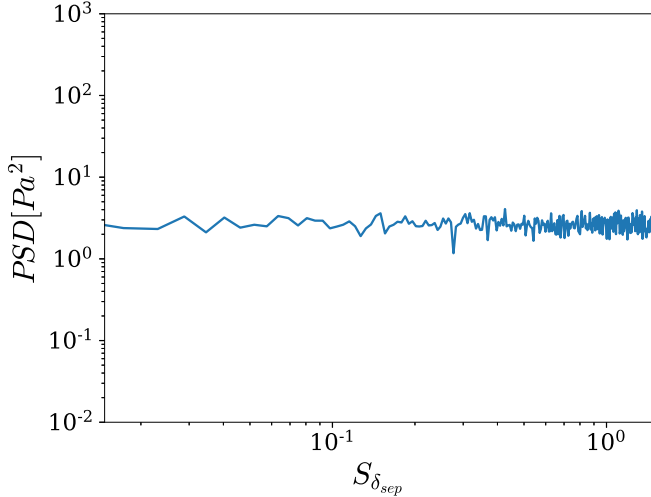


Figure 3.5: Power spectral density of the wall pressure fluctuations, showing the spectral content of the noise 3 cells downstream of the injection.

3.2 Post-processing tools

Once the computations are correctly set up and running, the next challenge is to be able to exploit the huge amount of data that will come out. This section aims at describing the tools that have been used in this thesis to post-process and interpret the simulation data.

It is important to note here that all the tools presented in this chapter are based on a state vector composed of conservative variables: $\mathbf{q} = (\rho, \rho\mathbf{u}, \rho E)$.

3.2.1 Definition of the fluctuation energy for compressible flow

To study fluctuations (*e.g.* transitional instabilities) in the flow, we first need to know which fluctuations are relevant (*i.e.* energetic) and which are not. However, the definition of the mean fluctuation energy for statistically converged compressible flow is not as straightforward as for incompressible flow where the kinetic energy (or "pseudo kinetic energy" as the constant density term is often left out) is indisputably the best norm to use. Multiple articles discussed this subject (Brear et al., 2012; Joseph George and Sujith, 2011; Myers, 1991) and the present consensus points toward the so-called Chu energy norm (Chu, 1965), which has also been independently derived by Hanifi et al. (1996). The Chu energy norm reads (in its continuous form):

$$E_{Chu} = \frac{1}{2} \int_V \bar{\rho} |\mathbf{u}'|^2 + \frac{a^2}{\bar{\rho}\gamma} (\rho')^2 + \frac{\bar{\rho}C_v}{\bar{T}} (T')^2 d\Omega, \quad (3.14)$$

with $a = \sqrt{\gamma RT}$ the local speed of sound and C_v the specific heat at constant volume. As this norm will be mostly used in its discrete form in this work (see equation (3.23) for instance), one needs to define an inner product matrix corresponding to the scalar product associated with this norm $\mathbf{x}^* \mathbf{Q}_e \mathbf{x}$ (\mathbf{x}^* denoting the conjugate transpose of \mathbf{x}), here the matrix is derived from the work of Bugeat et al. (2019):

$$a_1 = \frac{\bar{\rho}}{C_v \bar{T}}, \quad (3.15)$$

$$a_2 = \frac{\frac{|\bar{\mathbf{u}}|^2}{2} - \bar{e}}{\bar{\rho}}, \quad (3.16)$$

$$\mathbf{Q}_e = \Omega \begin{bmatrix} \frac{|\bar{\mathbf{u}}|^2 + R\bar{T}}{\bar{\rho}} + a_1 a_2^2 & -\bar{u}_x(1+a_1 a_2) & -\bar{u}_r(1+a_1 a_2) & -\bar{u}_\theta(1+a_1 a_2) & \frac{a_1 a_2}{\bar{\rho}} \\ -\bar{u}_x(1+a_1 a_2) & \frac{\rho + u_x^2 a_1}{\rho^2} & \frac{\bar{u}_x \bar{u}_r a_1}{\rho^2} & \frac{\bar{u}_x \bar{u}_\theta a_1}{\rho^2} & -\frac{\bar{u}_x a_1}{\rho^2} \\ -\bar{u}_r(1+a_1 a_2) & \frac{\bar{u}_x \bar{u}_r a_1}{\rho^2} & \frac{\rho + u_r^2 a_1}{\rho^2} & \frac{\bar{u}_r \bar{u}_\theta a_1}{\rho^2} & -\frac{\bar{u}_r a_1}{\rho^2} \\ -\bar{u}_\theta(1+a_1 a_2) & \frac{\bar{u}_x \bar{u}_\theta a_1}{\rho^2} & \frac{\bar{u}_r \bar{u}_\theta a_1}{\rho^2} & \frac{\rho + u_\theta^2 a_1}{\rho^2} & -\frac{\bar{u}_\theta a_1}{\rho^2} \\ \frac{a_1 a_2}{\bar{\rho}} & -\frac{\bar{u}_x a_1}{\rho^2} & -\frac{\bar{u}_r a_1}{\rho^2} & -\frac{\bar{u}_\theta a_1}{\rho^2} & \frac{a_1}{\rho^2} \end{bmatrix}, \quad (3.17)$$

with Ω the local cell volume, $\bar{\cdot}$ the temporal average and e the internal energy. Another inner product used in this thesis is the one linked with the standard L_2 norm:

$$\mathbf{Q} = \begin{bmatrix} \Omega & 0 & 0 & 0 & 0 \\ 0 & \Omega & 0 & 0 & 0 \\ 0 & 0 & \Omega & 0 & 0 \\ 0 & 0 & 0 & \Omega & 0 \\ 0 & 0 & 0 & 0 & \Omega \end{bmatrix}. \quad (3.18)$$

It is used in particular for the resolvent analyses as the norm for the forcing terms in the definition of the energy gain (see section 3.3.2).

3.2.2 Spectral Proper Orthogonal Decomposition

Convective amplification mechanisms and global instabilities are known to generate coherent structures (Beneddine et al., 2016), which may be studied through a Spectral Proper Orthogonal Decomposition (SPOD). This variant of the classical Proper Orthogonal Decomposition (POD) was first introduced by Hutchinson (1971) and has been widely used by the turbulence community since then (see for instance Gudmundsson and Colonius (2011)). It has been recently studied from a mathematical point of view by Towne et al. (2018), who showed that it is by construction the optimal decomposition to identify spatio-temporally correlated structures within statistically stationary flow.

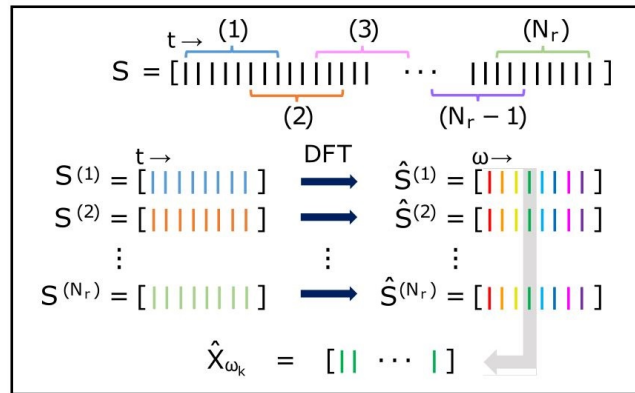


Figure 3.6: Schematic of the temporal treatment for the SPOD, adapted from Towne et al. (2018).

To perform the decomposition, one has to first sample snapshots from the simulation, then gather them in N_r (possibly overlapping) realizations of the flow. Each realization contains a temporal sequence of snapshots vectors $(\mathbf{s}_{t_0}, \mathbf{s}_{t_0+\Delta t}, \dots)$, where the components of \mathbf{s}_t are the values of the 3D flow field at the time t . A Discrete Fourier Transform (DFT) is then applied both in the temporal and azimuthal direction (as all the configurations studied here are axisymmetrical), giving Fourier mode vectors $\hat{\mathbf{S}}^k(\omega, m)$, where k is the realization number, ω the temporal frequency and m the azimuthal wavenumber of the mode. Due to the spectral transformation in the azimuthal direction, the vectors $\hat{\mathbf{S}}^k(\omega, m)$ correspond to bi-dimensional fields: they contain complex values

associated with each flow variables at each pair (x, r) from the mesh. For a given pair (ω, m) of interest, the Fourier modes of all realizations are then stacked in a matrix $\hat{\mathbf{X}}_{\omega, m}$, which reads

$$\hat{\mathbf{X}}_{\omega, m} = [\hat{\mathbf{S}}^0(\omega, m), \hat{\mathbf{S}}^1(\omega, m), \dots, \hat{\mathbf{S}}^{N_r-1}(\omega, m)]. \quad (3.19)$$

This matrix is then processed similarly to a snapshot matrix in a classical space-only POD decomposition: the i -th SPOD mode $\Psi_i^{(\omega, m)}$ can be computed from the i -th left singular vector of $\hat{\mathbf{X}}_{\omega, m}$, which may be computed by solving the eigenproblem associated with the cross spectral density matrix

$$\hat{\mathbf{X}}_{\omega, m} \hat{\mathbf{X}}_{\omega, m}^* \mathbf{Q}_e \Psi_i^{(\omega, m)} = \lambda_i \Psi_i^{(\omega, m)}, \quad (3.20)$$

with \mathbf{Q}_e the inner product associated with the energy norm defined by Chu (1965) which is presented in the section 3.2.1. The SPOD modes are ordered with respect to their contribution to the global dynamics, *i.e.* $\lambda_0 > \lambda_1 > \lambda_2 > \dots$, and for a given pair (ω, m) , the relative contribution of the i -th SPOD mode is measured by the ratio $r_i = \lambda_i / \sum_k \lambda_k$. In the following, we will focus in particular on the leading SPOD mode, and r_0 will be systematically specified to quantify how dominant it is compared to the remaining ones.

In practice, the eigenmodes are computed by using the snapshots' method of Berkooz et al. (1993) which is a less costly but equivalent decomposition based on $\hat{\mathbf{X}}_{\omega, m}^* \mathbf{Q}_e \hat{\mathbf{X}}_{\omega, m}$ rather than (3.20). The reduced eigenproblem to solve becomes:

$$\hat{\mathbf{X}}_{\omega, m}^* \mathbf{Q}_e \hat{\mathbf{X}}_{\omega, m} \mathbf{L}_i^{(\omega, m)} = \lambda_i \mathbf{L}_i^{(\omega, m)}, \quad (3.21)$$

\mathbf{L}_i being the i^{th} right singular vector of $\hat{\mathbf{X}}_{\omega, m}$. The left singular vector (*i.e.* the SPOD mode) can then be retrieved as:

$$\Psi_i^{(\omega, m)} = \frac{\hat{\mathbf{X}}_{\omega, m} \mathbf{L}_i^{(\omega, m)}}{\|\hat{\mathbf{X}}_{\omega, m} \mathbf{L}_i^{(\omega, m)}\|}. \quad (3.22)$$

The resulting i -th singular vector is a discrete 2D field $\Psi_i^{(\omega, m)}$ corresponding to a slice of the SPOD mode in the azimuthal direction. This framework is well-adapted for a spectral study of periodic structures that develop on an axisymmetric geometry, such as streamwise vortices. For visualization purposes, the structure of SPOD modes will be displayed in the present work by showing isocontours of the real part of $\Psi_i^{(\omega, m)} e^{im\theta}$, which will be called SPOD mode in the captions for conciseness.

Note that the spectral resolution in m and ω of the SPOD is set by the azimuthal span of the computational domain, the temporal length of each realization and the sampling frequency of the snapshots, respectively.

The snapshot vector size can also be reduced by down-sampling the mesh, since spatially coherent structures are always significantly larger than the dissipation scale that needs to be resolved in the QDNS.

It is also possible to localize the decomposition to extract coherent structures associated with a given region of the flow, simply by setting all coefficients of \mathbf{Q}_e associated with cells outside this region to zero.

3.2.3 Energy decomposition

The matrix formulation used for the SPOD in section 3.2.2 is convenient to compute the global energy of the fluctuations in the simulation associated to a pair (ω, m) :

$$E_{Chu}(\omega, m) = \frac{Tr(\hat{\mathbf{X}}_{\omega, m}^* \mathbf{Q}_e \hat{\mathbf{X}}_{\omega, m})}{N_r}. \quad (3.23)$$

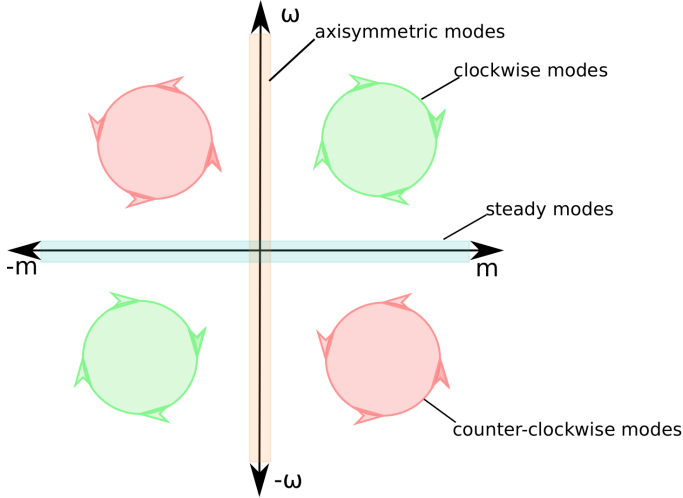


Figure 3.7: Schematic of the fluctuation energy distribution map representing the corresponding structures for each zone.

Equation (3.23) may be used to produce energy distribution maps that reveal regions in the $(\omega-m)$ -domain where fluctuations are particularly energetic. A schematic of such a colormap is presented in figure 3.7, the top right quarter containing the clockwise modes and the bottom right the counter-clockwise modes. Modes along the frequency axis are axisymmetric and modes along the wavenumber axis are steady by construction. As the data from the QDNS are real, the Fourier transformed snapshots display Hermitian symmetry:

$$\hat{X}_{-\omega,-m} = \overline{\hat{X}_{\omega,m}}. \quad (3.24)$$

Because of that, the energy map is symmetric around the origin (*i.e.* the top right/left quarter is the same as the bottom left/right one). Additionally, as the flow is statistically homogeneous in the azimuthal direction, the clockwise and counter-clockwise modes mirror each other as well. Note that for visualization purposes, the energy maps are displayed as continuous colormaps. However, the actual values are only defined in discrete pairs $(\omega-m)$ (that are represented in the background of the maps as dots).

Again, it is possible to localize the decomposition to get energetic levels associated with a given region of the flow, simply by setting all coefficients of \mathbf{Q}_e associated with cells outside this region to zero.

3.2.4 Low frequency treatment: signal decimation and filtering

Computing SPOD modes as described in section 3.2.2 is however out-of-reach for the low-frequency dynamics of the flow, since the required number of snapshots necessary to correctly converge the modes would be too high. As shown later, the large-scale dynamics of the shock-bubble system is associated with frequencies as low as 100Hz or even lower. This may require to simulate at the very least a physical duration of 0.1s (10 periods of the large-scale dynamics) to correctly compute SPOD modes at this frequency, (*i.e.* more than 10 000 000 time steps with the current numerical setup). This would increase by one order of magnitude the cost of the simulations presented in chapter 5 as well as the amount of data to store and process, which are already the main limiting factors.

Therefore, a different strategy is proposed to extract the low-frequency modes based on successive decimation/filtering, which avoids aliasing while yielding a workable amount of data. The data processing is summed up in Fig. 3.9 and consists of the following steps. First, to get a manageable data amount to process, volumic snapshots from the QDNS are sampled every 150 time-step

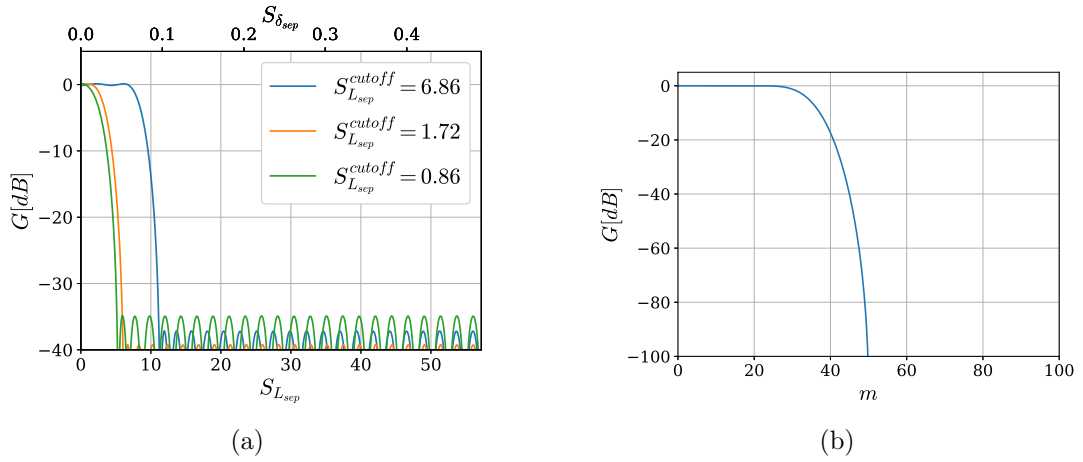


Figure 3.8: (a): Transfer function of the three temporal low pass filters. (b): Transfer function of the azimuthal low pass filter.

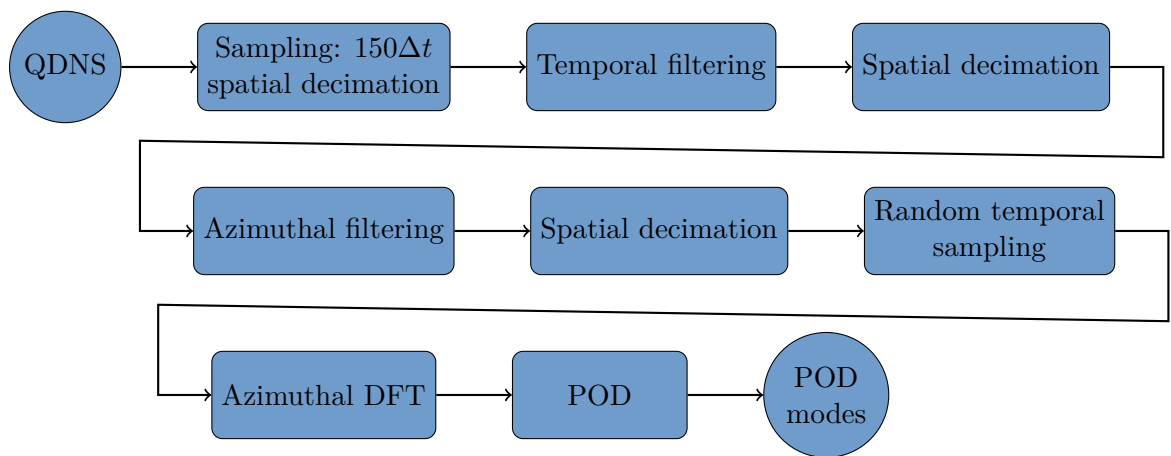


Figure 3.9: Schematic of the treatment applied to data extracted from the QDNS.

$(S_{L_{sep}} = fL_{sep}/U_\infty = 114, S_{\delta_{sep}} = f\delta_{sep}/U_\infty = 1, f = 666\text{kHz})$. They are also decimated in space: every other point in both the streamwise and wall-normal direction and every 4 points azimuthally. This down-sampling is limited enough to avoid aliasing both in time and space. Following this processing, 4000 snapshots are sampled from the full-domain DNS, representing 6ms of sampled signal and around 40 TB of raw data. Then, to isolate the low-frequency dynamics of the recirculation region, transitional and turbulent instabilities are filtered. Three different temporal Finite Impulse Response (FIR) filters have been designed with the Remez algorithm McClellan and Parks, 1973. The frequency response of the filters are presented in figure 3.8. Every filter is of order 50, has a transition region of $S_{L_{sep}} = 4.3$ ($f = 25\text{kHz}$), and has a cutoff Strouhal number of $S_{L_{sep}}^{(c)} = f^{(c)}L_{sep}/U_\infty = 6.86$ ($f^{(c)} = 40\text{kHz}$), 1.72 ($f^{(c)} = 10\text{kHz}$) and 0.86 ($f^{(c)} = 5\text{kHz}$) respectively, with $f^{(c)}$ the cutoff frequency. All of those filters have a cutoff frequency that is relatively low compared to the frequency of transitional instabilities and turbulence. After applying the filter, the spatial resolution in the streamwise direction is divided by two to reduce the memory cost of the following treatment. Since this second decimation is performed after the temporal filtering, it does not cause aliasing because all the small streamwise wavelength instabilities are oscillating at high frequency (and have already been filtered out by the temporal filter). Finally, given the difference in wavelength between the turbulent and transitional instabilities and the large-scale motion of the bubble, an azimuthal low pass filter of order 200, with a cutoff wavenumber of $m = 20$ and a transition region of 30, is applied (figure 3.8b), followed by a last decimation in the azimuthal direction. This yields a total of 100 points in this direction to represent the whole domain.

After those signal pre-processing steps, a procedure similar to the one described in section 3.2.2 can be applied. However, given the already discussed limitations on the temporal resolution, the temporal DFT is not conducted, and the SPOD become a POD analysis with an azimuthal decomposition.

3.3 Linear Stability Analysis

As presented in chapter 2, global stability analysis tools applied to mean flows are powerful to study the origin of either self-sustained unsteadiness (through global stability analysis) or transitional mechanisms (through resolvent analysis).

This section aims at presenting and discussing both the implementation of those methods and the interpretation of the results. First, the mean flow linear stability analysis will be presented. Then, the mean flow resolvent analysis will be described. Finally, the implementation and mathematical simplifications used in this thesis will be discussed.

3.3.1 Global stability analysis

Let us first consider the traditional base flow stability analysis. Starting from $\mathbf{q} = (\rho, \rho\mathbf{u}, \rho E)$ the state vector of the flow and \mathcal{N} the compressible Navier-Stokes operator, the temporal evolution of \mathbf{q} is governed by an equation of the form

$$\frac{\partial \mathbf{q}}{\partial t} = \mathcal{N}(\mathbf{q}), \quad (3.25)$$

By introducing the base flow \mathbf{q}_0 such that $\frac{\partial \mathbf{q}_0}{\partial t} = 0$ and $\mathbf{J} = \left. \frac{\partial \mathcal{N}}{\partial \mathbf{q}} \right|_{\mathbf{q}_0}$ the linearization of \mathcal{N} about \mathbf{q}_0 , the evolution of the fluctuation around the base flow $\mathbf{q}' = \mathbf{q} - \mathbf{q}_0$ in the linear regime is governed by:

$$\frac{\partial \mathbf{q}'}{\partial t} = \mathbf{J}\mathbf{q}'. \quad (3.26)$$

Considering the evolution of a harmonic perturbation of the form:

$$\mathbf{q}' = \hat{\mathbf{q}'} e^{\lambda t}, \quad (3.27)$$

one can rewrite the evolution of the perturbation as:

$$\lambda \hat{\mathbf{q}'} = \mathbf{J} \hat{\mathbf{q}}'. \quad (3.28)$$

One can recognize a standard eigenproblem. Then the imaginary part of the eigenvalue λ is a pulsation and its real part a growth rate. There is a global instability in the flow as soon as one eigenvalue has a positive real part (*i.e.* the perturbation will grow exponentially in time).

However, in transitional and turbulent flows, this analysis around the base flow fails to correctly predict the dynamics of the flow because it cannot account for the strong impact of the non-linearities on the flow. In those cases, and despite the linear nature of the stability analysis, considering the mean flow instead of a steady solution (base flow) is a way to account for some non-linear effects (see McKeon and Sharma (2010) and Beneddine et al. (2016) for instance).

In that case, \mathbf{J} will be defined as $\mathbf{J} = \left. \frac{\partial \mathcal{N}}{\partial \mathbf{q}} \right|_{\bar{\mathbf{q}}_0}$ with $\bar{\mathbf{q}}_0$ a time (and potentially spatial) average of the flow.

In the case of periodic dynamics characterized by a peaked temporal spectrum, the instability developing in the flow is linked to marginally stable/unstable eigenmodes of the linearized Navier-Stokes operator about the mean flow \mathbf{J} , at the frequency of the flow oscillation (Beneddine et al., 2016; Sipp and Lebedev, 2007; Turton et al., 2015). In the more general case where the unsteadiness is broadband, stability modes that describe the oscillations should still exist at a frequency loosely matching the dominant frequency. However, their growth rate may significantly depart from zero (Turton et al., 2015). Therefore, in such a case, one may focus on the least stable/unstable modes in search of relevant modes, as it is likely that the dynamics is not described by marginally stable modes anymore.

However, the sign of the growth rate for those modes is not as easily interpretable as it would be for baseflow-based approaches. Contrary to a stability analysis about a steady solution of the Navier-Stokes equations, the modes about the mean flow (which is not a solution of the governing equations) do not represent the linear stage of the growth of disturbances. Therefore, its sign (*i.e.* the stable/unstable nature of the mode) is not physically relevant. This should be kept in mind when considering a mean flow stability analysis. Thus, this analysis will mainly bring information about the frequency and the spatial shape of some eigenmodes of interest. Note that even in a base flow stability analysis, the growth rate is not an indicator of which mode would be the most energetic within the flow (which is determined by nonlinear saturation effects). For instance, the work of Mettot et al., 2014 is an example where the most energetic disturbances are not associated with the most unstable mode.

Additionally, the recent work from Karban et al., 2020 revealed that the set of variables chosen to describe the dynamical system (*e.g.* primitive versus conservative) moderately affect the eigenspectrum values of the jacobian matrix. This further emphasizes the need not to over-interpret the growth rate values. On the contrary, the spatial structure of the modes, given by the eigenvectors, are almost unaffected by such variable choices. Therefore, they can be analyzed and compared with QDNS results more confidently.

To get more physical insights on the modes, the region in space that is at the origin of the instability (the so-called "wavemaker") can be studied. This is usually done through the structural sensitivity approach developed by Gianetti and Luchini (2007). It involves the computation of adjoint modes (modes of the adjoint linearized operator): the structural sensitivity is computed as the local product of the norms of the direct and adjoint modes (see Gianetti and Luchini (2007), Marquet et al. (2008) or Luchini et al. (2009) for further details). It yields a scalar field that quantifies how an eigenvalue is affected by introducing a localized feedback (Paladini et al., 2019). Therefore, it is useful to identify the spatial zones responsible for the instability mechanism of a mode.

3.3.2 Resolvent Analysis

As stated in chapter 2, stability analysis as presented in the previous section fails to predict the growth of convective instabilities, which are due to the non-normality of the operator. To be able to capture those accurately, one has to focus on the response of the operator to a forcing, via a resolvent analysis.

Again, starting from $\mathbf{q} = (\rho, \rho\mathbf{u}, \rho E)$ the state vector of the flow and \mathcal{N} the compressible Navier-Stokes operator, the temporal evolution of \mathbf{q} is governed by an equation of the form

$$\frac{\partial \mathbf{q}}{\partial t} = \mathcal{N}(\mathbf{q}) + \mathbf{f}_0, \quad (3.29)$$

with \mathbf{f}_0 a forcing term corresponding to the injected noise perturbation. By introducing the mean flow $\bar{\mathbf{q}}_0$ and $\mathbf{J} = \left. \frac{\partial \mathcal{N}}{\partial \mathbf{q}} \right|_{\bar{\mathbf{q}}_0}$ the linearization of \mathcal{N} about $\bar{\mathbf{q}}_0$, the fluctuation around the mean flow $\mathbf{q}' = \mathbf{q} - \bar{\mathbf{q}}_0$ is governed by

$$\frac{\partial \mathbf{q}'}{\partial t} = \mathbf{J}\mathbf{q}' + \mathbf{f}_0 + \mathcal{F}(\mathbf{q}', \bar{\mathbf{q}}_0), \quad (3.30)$$

with $\mathcal{F}(\mathbf{q}', \bar{\mathbf{q}}_0) = \mathcal{N}(\mathbf{q}) - \mathbf{J}\mathbf{q}' - \mathbf{f}_0$ a term gathering the non-linear part of the Navier-Stokes operator. Following the formalism of Beneddine et al. (2016), one may then define $\mathbf{f}' = \mathbf{f}_0 + \mathcal{F}(\mathbf{q}', \bar{\mathbf{q}}_0)$ as a forcing term containing the non-linear forcing and the injected perturbation such that equation ((3.30)) reduces to

$$\frac{\partial \mathbf{q}'}{\partial t} = \mathbf{J}\mathbf{q}' + \mathbf{f}'. \quad (3.31)$$

The Fourier transform of equation ((3.31)) reads

$$\hat{\mathbf{q}'} = \mathcal{R}\hat{\mathbf{f}}', \quad (3.32)$$

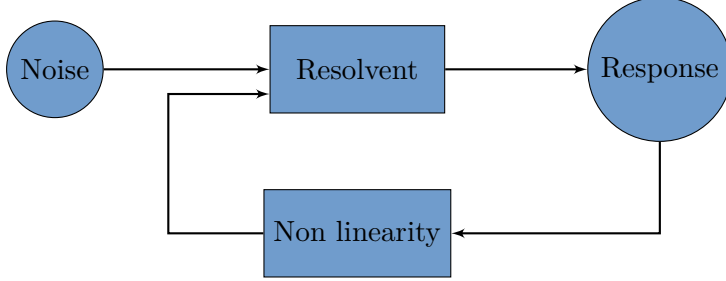


Figure 3.10: Schematic of the input-output form of the mean-flow resolvent analysis.

with \hat{f}' and \hat{q}' the Fourier transform of f' and q' , respectively, and \mathcal{R} the resolvent operator defined as $\mathcal{R} = (i\omega\mathbf{I} - \mathbf{J})^{-1}$. This compact equation shows that the flow may be seen as an input-output system, where a forcing \hat{f}' generates a response \hat{q}' through the resolvent operator.

Then, a resolvent analysis consists in computing for every frequency ω of interest an optimal forcing ϕ_0 which maximizes the gain defined as

$$G(\omega) = \frac{\langle \mathcal{R}\phi, \mathcal{R}\phi \rangle_e}{\langle \phi, \phi \rangle}, \quad (3.33)$$

where $\langle ., . \rangle_e$ represents the energy of the fluctuation as defined in §3.2.1 and $\langle ., . \rangle$ the scalar product associated with the \mathcal{L}_2 norm

$$\langle \phi, \phi \rangle = \phi^* \mathbf{Q} \phi, \quad (3.34)$$

with \mathbf{Q} the weight matrix defined in section 3.2.1. The optimal forcing and the associated gain are given by the dominant right singular vector and dominant singular value of \mathcal{R} , and they may be computed by solving

$$\mathcal{R}^* \mathbf{Q}_e \mathcal{R} \phi_i = \mu_i^2 \mathbf{Q} \phi_i. \quad (3.35)$$

The highest eigenvalue μ_0^2 of equation ((3.35)) is the optimal gain, the corresponding eigenvector ϕ_0 is the optimal forcing. These quantities are functions of the frequency ω . Additionally, as shown in section 3.3.5, one may perform a Fourier transform of equation ((3.30)) in the azimuthal direction such that the gain and optimal forcing are not only functions of ω , but also functions of the azimuthal wavenumber m .

Computing lower-magnitude eigenvalues $\mu_{i \geq 1}^2$ of ((3.35)) gives sub-optimal forcings $\phi_{i \geq 1}$. After normalization, these forcings yield an orthonormal basis of the forcing space, *i.e.* $\langle \phi_i, \phi_j \rangle = \delta_{ij}$. The optimal responses given by $\psi_i = \mathcal{R}\phi_i / \|\mathcal{R}\phi_i\|_e$ gives a similar basis of the response space, and equation ((3.32)) may then be decomposed as

$$\hat{q}' = \psi_0 \mu_0 \langle \phi_0, \hat{f}' \rangle + \sum_{i \geq 1} \psi_i \mu_i \langle \phi_i, \hat{f}' \rangle. \quad (3.36)$$

Physically, when there exists one strong convective instability mechanism within the flow (such as first or second mode instabilities), the optimal gain becomes very high, and the resolvent analysis yields $\mu_0 \gg \mu_{i \geq 1}$ (see Benedidine et al. (2016)). When this occurs, the first term of the right-hand-side of ((3.36)) is expected to be dominant, as long as the noise contained in \hat{f}' does not preferentially excite a suboptimal forcing in a way that shifts the dominance (which was never observed in the present study). Then, \hat{q}' is going to be dominated by the first optimal response ψ_0 as a result of this strong linear amplification mechanism. Therefore, the resolvent analysis may explain the appearance of coherent structures, and as such, it is an important tool to confront with SPOD analyses.

However, $\hat{\mathbf{f}}'$ may project better onto ϕ_0 for some given values of (m, ω) . This may be investigated by introducing the coefficient $c_0 = \mu_0^2 |\langle \phi_0, \hat{\mathbf{f}}' \rangle|^2$, which represents the combination of two mechanisms: the ability of the linear operator to optimally amplify a certain type of structure (through μ_0) and the strength of the excitation of this mechanism by $\hat{\mathbf{f}}'$, which contains both the injected noise and the non-linear terms. Situations where $E_{Chu}(\omega, m)$ is high while the dominant amplification mechanism is weak (*i.e.* $\mu_0^2(\omega, m)$ is small) may be explained by receptivity processes that are accounted for by $c_0(\omega, m)$. In general, in the context of strong nonlinear interaction and no dominant linear instability mechanism, $c_0(\omega, m)$ is not expected to match $E_{Chu}(\omega, m)$ since there is no reason for the forcing term $\hat{\mathbf{f}}'$ to specifically excite a given linear mechanism. However, if $c_0(\omega, m)$ matches $E_{Chu}(\omega, m)$, then for this particular pair (ω, m) , the forcing term projects well onto ϕ_0 such that high-energy structures stem from a weak (but strongly excited) linear mechanism. As shown in the following, such a situation where the non-linearities excite a very specific linear amplification mechanism is central for the transition scenario of the studied flow configuration.

It is also interesting to discriminate the contribution of the injected noise from the contribution of the non-linear terms in the receptivity processes. To do so, one may simply compute c_r , which is defined in the same way as c_0 but with a scalar product spatially restricted to the stencil of the injection plane of the noise (*i.e.* the support of the forcing term). If c_r is close to c_0 , the receptivity is linked to the nature of the noise alone. Otherwise, the receptivity of the non-linear terms also comes into play.

In order to preserve the stochastic framework introduced in section 3.2.2 and to conform with the SPOD approach, the actual computation of c_0 in the following is $c_0 = \mu_0^2 E[|\langle \phi_0, \hat{\mathbf{f}}' \rangle|^2]$, where $E[\cdot]$ is the expected value estimated from an average of values computed for several realizations (using the same time sequences as for the SPOD analysis described in section 3.2.2), $\hat{\mathbf{f}}'$ being computed as $\mathcal{R}^{-1}\hat{\mathbf{q}}'$.

Note that it is possible to localize the resolvent analysis to a given region of the flow by setting all coefficients of \mathbf{Q}_e associated with cells outside this region to zero. The gain is then defined as the maximal energy restrained to this specific zone, and as such, the response is constrained in space (but the forcing is not). This approach is used in the following to study coherent structures in specific domains of the flow.

3.3.3 Jacobian computation

The computation of both the stability spectrum and the resolvent operator requires the jacobian operator \mathbf{J} . Following the procedure described by Beneddine (2017), \mathbf{J} is obtained by a finite-differences linearization of the discrete equations implemented in FASTS. The procedure is the following. We aim at computing $\mathbf{J} = \frac{\partial \mathcal{N}}{\partial \mathbf{q}} \Big|_{\bar{\mathbf{q}}_0}$, in the case of this work, $\bar{\mathbf{q}}_0$ is a mean flow, but this procedure can also be used around base flow. Using a CFD solver (such as FASTS), one can compute $\mathcal{N}(\mathbf{q})$ for any \mathbf{q} . Then, a first order approximation yield the following:

$$\mathbf{J}\mathbf{q}' = \frac{\mathcal{N}(\mathbf{q}_0 + \epsilon\mathbf{q}') - \mathcal{N}(\mathbf{q}_0)}{\epsilon}, \quad (3.37)$$

with \mathbf{q}' being a unitary vector such as $(0, 0, 0, \dots, 0, 1, 0, \dots, 0, 0)^T$. The linear combination of the approximation for every unitary vectors then yields the full operator. However, using only unitary vectors, the computation of the full operator would imply making N_{DOF} calls to the solver. As the stencil of the solver is limited in space, a linear combination of unitary vectors yielding independent response can be used to speed up the process (an example of optimal choice of perturbation points for a bi-dimensional case is shown figure 3.11).

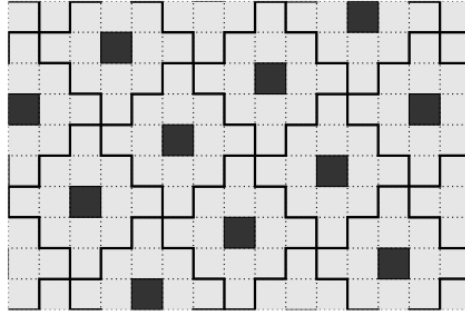


Figure 3.11: Optimal distribution of the perturbed points given a 5 cell stencil for a bi-dimensional case. From [Beneddine \(2017\)](#).

3.3.4 Eigenvalues research

In practice, the different eigenvalue problem encountered in this section (such as (3.35) for instance) are solved using the Arnoldi algorithm via ARPACK ([Lehoucq et al., 2013](#)) coupled with the LU direct solver MUMPS ([Amestoy et al., 2002](#)) for the inversion phase. The actual implementation is done via the PetsC and SlepC libraries ([Hernandez et al., 2005](#)) and their python API, PetsC4py and SlepC4py ([Dalcin et al., 2011](#)).

3.3.5 2.5D formulation for axisymmetric mean flows

Given the size of the matrices involved, the computational cost of the strategy presented in section 3.3.4 is not affordable for 3D cases. Since the mean flow of the studied cases are axisymmetric and the mesh is homogeneous in the azimuthal direction, the Jacobian operator may be rearranged in a block diagonal form as proposed by Schmid et al. ([2017](#)) to make the computation significantly cheaper. This cost-reduction method, which has also been used in Paladini et al. ([2019](#)), is briefly presented below.

Since the solver FAST works internally with Cartesian coordinates, one has to first carry out a transformation to cylindrical coordinates to retrieve the axisymmetry of the flow using the following relation

$$\begin{pmatrix} \rho \\ \rho u_x \\ \rho u_r \\ \rho u_\theta \\ \rho E \end{pmatrix} = \begin{bmatrix} 1 & 0 & 0 & 0 & 0 \\ 0 & 1 & 0 & 0 & 0 \\ 0 & 0 & \cos(\theta) & \sin(\theta) & 0 \\ 0 & 0 & -\sin(\theta) & \cos(\theta) & 0 \\ 0 & 0 & 0 & 0 & 1 \end{bmatrix} \begin{pmatrix} \rho \\ \rho u_x \\ \rho u_y \\ \rho u_z \\ \rho E \end{pmatrix}, \quad (3.38)$$

under appropriate indexing of the degrees of freedom, the Jacobian operator can then be rearranged into the block-circulant form

$$\mathbf{J} = \begin{bmatrix} \mathbf{A}_0 & \mathbf{A}_1 & \dots & \mathbf{A}_{n-2} & \mathbf{A}_{n-1} \\ \mathbf{A}_{n-1} & \mathbf{A}_0 & \dots & \mathbf{A}_{n-3} & \mathbf{A}_{n-2} \\ \mathbf{A}_{n-2} & \mathbf{A}_{n-1} & \dots & \mathbf{A}_{n-4} & \mathbf{A}_{n-3} \\ \vdots & \vdots & \vdots & \vdots & \vdots \\ \mathbf{A}_1 & \mathbf{A}_2 & \dots & \mathbf{A}_{n-1} & \mathbf{A}_0 \end{bmatrix}, \quad (3.39)$$

where each line of blocks corresponds to a given azimuthal slice of the mesh and the block matrices $\mathbf{A}_0, \dots, \mathbf{A}_{n-1}$ have a size corresponding to such a slice (the size of a 2D problem). The block-

circulant nature of the matrix comes from the numerical and physical equivalence of all azimuthal slices of the mean flow, which cannot be distinguished from one another.

As the stencil of the solver is 5 points wide in every direction, there are only interactions between a cell and the next two adjacent cells, simplifying the linear operator to a quasi-block pentadiagonal matrix of the following form:

$$\mathbf{J} = \begin{bmatrix} \mathbf{A}_0 & \mathbf{A}_1 & \mathbf{A}_2 & & & \mathbf{A}_{n-2} & \mathbf{A}_{n-1} \\ \mathbf{A}_{n-1} & \mathbf{A}_0 & \mathbf{A}_1 & \mathbf{A}_2 & & & \mathbf{A}_{n-2} \\ \ddots & \ddots & \ddots & \ddots & \ddots & & \\ \ddots & \ddots & \ddots & \ddots & \ddots & & \\ & \mathbf{A}_{n-2} & \mathbf{A}_{n-1} & \mathbf{A}_0 & \mathbf{A}_1 & \mathbf{A}_2 & \\ & & \mathbf{A}_{n-2} & \mathbf{A}_{n-1} & \mathbf{A}_0 & \mathbf{A}_1 & \mathbf{A}_2 \\ & & & \ddots & \ddots & \ddots & \\ & & & & \ddots & \ddots & \\ \mathbf{A}_2 & & & & & \mathbf{A}_{n-2} & \mathbf{A}_{n-1} & \mathbf{A}_0 & \mathbf{A}_1 \\ \mathbf{A}_1 & \mathbf{A}_2 & & & & \mathbf{A}_{n-2} & \mathbf{A}_{n-1} & \mathbf{A}_0 & \mathbf{A}_1 \end{bmatrix}. \quad (3.40)$$

The format of the operator is very convenient as it allows us to consider only a fraction of the domain containing 5 cells in the periodic direction to reconstruct the full domain information. This method is used for the jacobian computation, greatly reducing the numerical cost of this step.

As shown by Schmid et al. (2017), this block circulant matrix can then be transformed into a block-diagonal matrix

$$\tilde{\mathbf{J}} = \begin{bmatrix} \tilde{\mathbf{A}}_0 & & & \\ & \tilde{\mathbf{A}}_1 & & \\ & & \ddots & \\ & & & \tilde{\mathbf{A}}_{n-1} \end{bmatrix}, \quad (3.41)$$

with

$$\tilde{\mathbf{A}}_m = \mathbf{A}_0 + \rho_m \mathbf{A}_1 + \rho_m^2 \mathbf{A}_2 + \dots + \rho_m^{n-1} \mathbf{A}_{n-1}, \quad (3.42)$$

and $\rho_m = e^{\frac{i2\pi m}{n}}$ corresponding to an m -root of unity.

Given the characteristics of the stencil, this can be reduced to:

$$\tilde{\mathbf{A}}_m = \mathbf{A}_0 + \rho_m \mathbf{A}_1 + \rho_m^2 \mathbf{A}_2 + \rho_m^{n-2} \mathbf{A}_{n-2} + \rho_m^{n-1} \mathbf{A}_{n-1}, \quad (3.43)$$

the spectrum of \mathbf{J} is then the sum of the spectrum of the n smaller submatrix $\tilde{\mathbf{A}}_i$.

The analysis of the global 3D resolvent may also be done by performing n smaller resolvent analyses by successively considering for $m = 0, \dots, n-1$ the operator

$$\tilde{\mathcal{R}}(m, \omega) = (i\mathbf{I}\omega - \tilde{\mathbf{A}}_m)^{-1}. \quad (3.44)$$

For each value of m , the 3D optimal forcing and response, denoted as ϕ_m and ψ_m , respectively, are the singular vectors of $\tilde{\mathcal{R}}$ and can be computed from those of $\tilde{\mathcal{R}}$: $\tilde{\phi}_m, \tilde{\psi}_m$ as

$$\phi_m = \begin{pmatrix} \tilde{\phi}_m \\ \rho_m \tilde{\phi}_m \\ \rho_m^2 \tilde{\phi}_m \\ \vdots \\ \rho_m^{n-1} \tilde{\phi}_m \end{pmatrix}, \quad \psi_m = \begin{pmatrix} \tilde{\psi}_m \\ \rho_m \tilde{\psi}_m \\ \rho_m^2 \tilde{\psi}_m \\ \vdots \\ \rho_m^{n-1} \tilde{\psi}_m \end{pmatrix}. \quad (3.45)$$

This shows that m is actually the azimuthal wavenumber of the resolvent mode. With this formulation, the resolvent operator does not only depend on the frequency, but also m . This leads to an analysis in the (ω, m) -domain that allows direct comparison of the resolvent gain with the energy map (see §3.2.3). For that reason, resolvent analyses are performed for values of m that are consistent with the DNS, and gain values are displayed for a (ω, m) -domain encompassing that of the energy maps (including negative values of m and ω).

This formulation is very convenient as it allows to compare both the stability modes and the resolvent modes with the azimuthally decomposed POD modes and SPOD modes respectively using a projection coefficient defined as:

$$\frac{|\langle \Psi_a, \Psi_b \rangle|}{\sqrt{\langle \Psi_a, \Psi_a \rangle \langle \Psi_b, \Psi_b \rangle}}. \quad (3.46)$$

Chapter 4

Experimental setup

This chapter aims at describing the experimental setup and all the measurements techniques (pressure sensors, infrared imaging, Schlieren visualizations) used in the experimental campaign.

Preliminary work has been conducted on the calibration of broadband pressure transducers and the measurements of the free-stream disturbances present in the wind tunnels. Both of these points are discussed in the following.

Contents

4.1	Wind tunnel	50
4.2	Model	52
4.3	Acquisition	53
4.4	Unsteady pressure measurements	55
4.4.1	Calibration method	55
4.4.2	Calibration results	60
4.4.3	Drawback: heat-flux sensitivity	61
4.4.4	Epoxy layer	64
4.4.5	Conclusion on the use of PCB sensors	67
4.5	Optical measurements	68
4.5.1	IR thermography setup and post-processing	68
4.5.2	Schlieren setup	71
4.6	Wind tunnel free stream perturbations measurements	74

4.1 Wind tunnel



Figure 4.1: R2ch facility

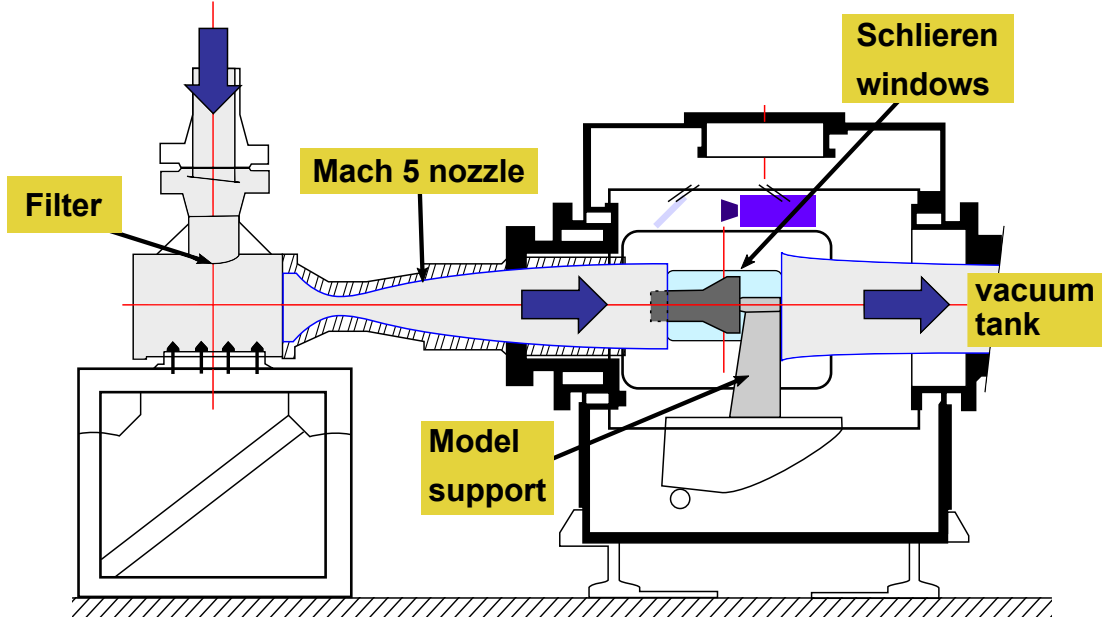


Figure 4.2: Schematic of the R2Ch facility.

The R2Ch facility in the ONERA Meudon site (see figure 4.1) was used for the experiments. The facility is a conventional blow-down wind tunnel (test duration between 15 and 30 seconds) equipped with a set of contoured axisymmetric nozzles covering a Mach number range from 5 to 7 (here, a 0.327m exit diameter Mach 5 nozzle is used). A schematic of the facility is presented in figure 4.2. The R2Ch wind tunnel is a cold hypersonic facility: the stagnation temperature is raised to a level just sufficient to prevent air liquefaction during expansion in the nozzle. Upstream air is heated to a stagnation temperature T_{st} slightly above 500K ($510\text{K} < T_{st} < 550\text{K}$) by streaming through a Joule-effect heater. The stagnation pressure may be controlled to range from laminar/low transitional to fully turbulent Reynolds number. In the present experiments, stagnation pressures P_{st} are chosen in the range $1.3 \times 10^5 \text{ Pa} < P_{st} < 4.1 \times 10^5 \text{ Pa}$. This leads to Reynolds numbers which range from $Re_L = 4 \times 10^5$ to $Re_L = 1.14 \times 10^6$).

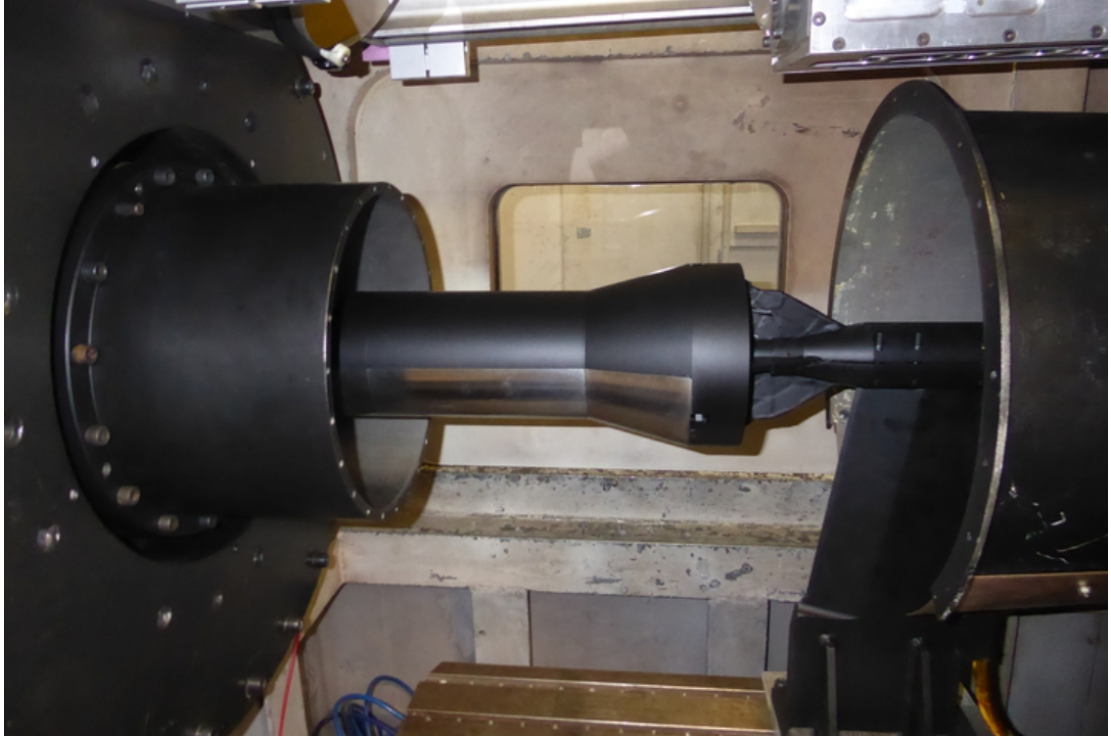


Figure 4.3: Model in the R2Ch blowdown facility.

	M_∞	5	5	5
	Re_L	4×10^5	7×10^5	1.1×10^6
Run 1				
$T_{st}[K]$	504 ± 0.6	524 ± 0.6	547 ± 0.9	
$P_{st}[Pa]$	$1.27 \times 10^5 \pm 480$	$2.41 \times 10^5 \pm 762$	$4.14 \times 10^5 \pm 1157$	
Run 2				
$T_{st}[K]$	503 ± 0.6	525 ± 0.7	553 ± 0.8	
$P_{st}[Pa]$	$1.29 \times 10^5 \pm 459$	$2.25 \times 10^5 \pm 657$	$4.08 \times 10^5 \pm 1266$	

Table 4.1: Mean free-stream conditions and standard deviation computed on a 2-second window during the high-frequency acquisition. The Reynolds number are computed from run 1.

The leading edge of the model is positioned 140 mm upstream from the nozzle exit, at 0° angle of attack and 0° yaw angle. This ensures that the model is entirely located inside the Mach 5 rhombus and that there is no blockage effect. The angle of attack is first set by using an inclinometer. It is then validated using the symmetry of the shock system on the lower and upper part of the model using a dedicated Schlieren setup. The final angle of attack in wind referential is $\alpha = 0 \pm 0.05^\circ$ (the final uncertainty is set by the ability to measure the angles from the Schlieren images). The yaw angle is measured in the nozzle referential using a depth gauge to be $\beta = 0.004 \pm 0.0002^\circ$. However, it may slightly depart from 0° in the true wind referential, which can explain the weak curvature of the reattachment line visible in figure 4.25. While this misalignment may have an effect on the development of the instabilities studied in this article, recent results from Benitez et al. (2021) show that this impact is rather limited in conventional wind tunnel due to the presence of free-stream noise, as they reported similar streaks for angle varying from 0 to 0.3° .

The time evolutions of the stagnation pressure and temperature during a typical run (in this case $Re_L = 1.14 \times 10^6$) are presented in figure 4.4 alongside the time were the different measurements are conducted. The high-speed unsteady data are acquired near the end of the run, when the flow is fully established and the Reynolds number almost constant. Due to constraints intrinsic to the facility, one can never achieve a fully constant stagnation temperature (as the whole system is

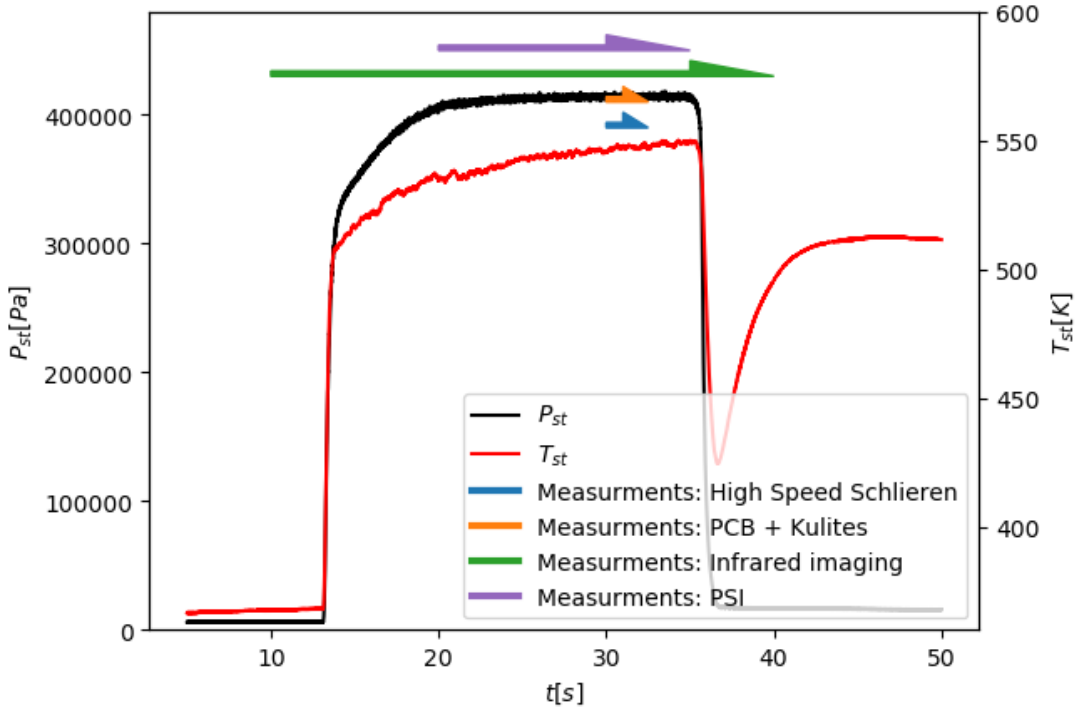


Figure 4.4: Time evolution of stagnation conditions during a run and time acquisitions of several measurements during the run.

slowly heating during the run). Yet, the Reynolds number change during the run is negligible, and the flow conditions can be considered constant over time during the high-speed acquisition. Thus, the operating conditions that are presented in table 4.1 are computed as an average over a 2-second window during the high-speed acquisition. Two runs are presented since two different acquisitions are needed for the infrared imaging (one at full frame, and one at reduced frame, see section 4.5.1). The Reynolds numbers are computed from the first run. One may see that there is an excellent reproducibility of the runs for $Re_L = 4 \times 10^5$ and $Re_L = 1.1 \times 10^6$ (at most 1.5% difference between each run), but a less good one for $Re_L = 7 \times 10^5$ (7% change in P_{st} between run 1 and 2). The difference between the two runs at $Re_L = 7 \times 10^5$ can be attributed to the difficulty to precisely regulate the pressure level upstream of the blow-down wind tunnel. The reproducibility of the unsteady measurements between similar runs is verified by comparing kulite pressure spectrums and is found to be very good, even for the case $Re_L = 7 \times 10^5$.

4.2 Model

The model used for the experiments is a refurbished version of the model from the experiments of Vandomme, 2004. It is a hollow cylinder of outer diameter $D_{out} = 131\text{mm}$, inner diameter $D_{in} = 108\text{mm}$ and length $L = 252\text{mm}$ with a sharp leading edge (measured radius of $27.5 \pm 1\mu\text{m}$), followed by a 15° flare. The total length of interest is 350mm. The flare itself is then followed by a 50-mm-long cylindrical extension to minimize the base flow influence on the interaction region, giving a total model length of 400mm. This model was designed to be able to have a separated flow in transitional conditions. The hollow geometry is a key design feature of this experiment, as it allows a large model to be used in the facility without obstructing the test section by a blockage effect, which would impact the starting phase of the facility. While both the inside and outside structures of the model are reused, the model has been reequipped and resurfaced. The model is made of Isotan, with a Nimonic leading edge, and is half painted in black for infrared imaging. The rugosity of the painted part of the model has been measured using a Marh MarSurf

Table 4.2: PCB132A31 sensors position. Measurement origin is the leading edge of the model.

PCB	1	2	3	4
$\frac{X}{L}$	1.069	1.086	1.102	1.119

Table 4.3: Kulite sensors position. Measurement origin is the leading edge of the model.

Kulite	1	2	3	4	5	6	7
$\frac{X}{L}$	0.793	0.873	1.069	1.086	1.102	1.119	1.25

M 400 and is $Ra < 3.2\mu\text{m}$, while the rugosity of the bare-metal part of the model is $Ra < 1.2\mu\text{m}$. The temperature of the model was measured to vary only slightly during the runs ($< 15\text{K}$ on the flare, $< 2\text{K}$ on the cylinder) and a good approximation for numerical reproduction of the present experiments could be to use an isothermal wall at $\sim 290\text{K}$. A view of the model, including the sensors, can be seen in figure 4.5.

The 52 pressure taps distributed along the model as in previous experiments (Benay et al., 2006; Vandomme, 2004) are kept and provide measurements of the mean pressure distribution along the geometry. Those pressure taps are connected to electronic pressure scanners (ESP32) via stainless-steel tubes prolonged by flexible silicon tubes. Pressure ports are addressed using the digital I/O bank of a NI PXIE 6361 which performs digitization of each sensor signal. The uncertainty on the pressure scanner measurements is estimated to be $\pm 10\%$. The signals of wind tunnel parameters (P_{st} , T_{st} , etc.) are acquired using a NI PXI 6284 multiplexer. The main modification on the model is the presence of 7 Kulite XCQ-093 (1Psi differential range and B type screened) and 4 PCB 132A31 sensors for unsteady pressure fluctuation measurements. Positions of those sensors can be found in tables 4.2 and 4.3. The PCB sensors are conditioned by a 4-channel PCB 482C05 signal conditioner free of any amplification and filtering, the output is then digitized by a NI PXIE-6376 with a sampling frequency set to 3.3MHz. While the acquisition permits very high-frequency measurements with PCB sensors, one has to be careful when interpreting results at frequencies higher than 300kHz as resonance was observed during shock-tube calibration of those sensors (see appendix 1); this resonance is also mentioned in other studies (Butler and Laurence, 2021a; Grossir, 2017). A special model integration technique has been used for PCB sensors and is described in appendix 1. This technique yields both a better flush mount and a thermal protection of the sensor. For the Kulites sensors, signal amplification and galvanic insulation is done through ENS E300 signal amplifier/conditioner (with a low-pass analog filter set to 100kHz), the signal is then digitized by a NI PXIE-6358 (set to a sampling frequency of 1.1MHz). The sensors are connected to a common power supply (ITI QL355) delivering a constant 10V voltage. The PXIE-6376 and PXIE-6358 are in the same PXI rack in order to use a common reference clock. The data obtained with the chosen sampling frequencies (*i.e.*, 1.1 and 3.3MHz) have been compared to data acquired at 40MHz using a Keysight Infinium S-series numerical oscilloscope to ensure the absence of aliasing in the signal. The reference pressure for all the differential measurements (PSI and Kulite sensors) is maintained to a stable value using a vacuum pump connected to a DPI 510 pressure regulator maintaining a buffer tank of approximately 1 liter to the desired pressure (6kPa). The pressure fluctuation amplitude of the reference tank during trial runs has been measured to be less than 10Pa. To distinguish electronic noise from actual signal during the runs, reference measurements are recorded before each run (test section at vacuum pressure, wind-tunnel ready to run). This acquisition provides the noise floor.

4.3 Acquisition

The pressure taps are connected to electronic pressure scanners (ESP32) via stainless-steel tubes prolonged by flexible silicon tubes. Pressure ports are addressed using the digital I/O bank

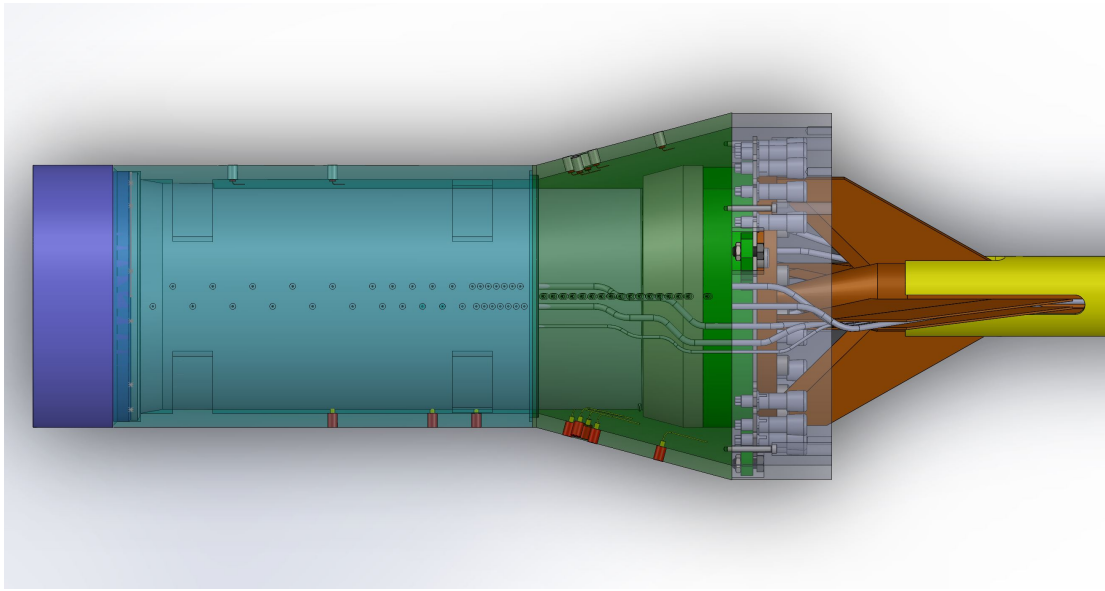


Figure 4.5: 3D view of the model (Kulites in red, PCB in grey).

of a NI PXIe 6361 which performs digitization of each signal sensor. The signals of wind tunnel parameters (P_{st} , T_{st} , etc.) are acquired using a NI PXI 6284 multiplexer. The main modification on the model is the presence of 6 Kulite XCQ-093 (1Psi differential range and B type screened) and 4 PCB 132A31 sensors for unsteady pressure fluctuation measurements. Positions of those sensors can be found in tables 4.2 and 4.3. The PCB sensors are conditioned by a 4-channel PCB 482C05 signal conditioner free of any amplification and filtering, the output is then digitized by a NI PXIe-6376 with a sampling frequency set to 3.3MHz. While the acquisition permits very high-frequency measurements with PCB sensors, one has to be careful when interpreting results at frequencies higher than 300kHz as resonance was observed during shock-tube calibration of those sensors (see appendix 1), this resonance is also mentioned in other studies (Butler and Laurence, 2021a; Grossir, 2017). A special model integration technique has been used for PCB sensors and is described in appendix 1. This technique yields both a better flush mount and a thermal protection of the sensor. For the Kulites sensors, signal amplification and galvanic insulation is done through ENS E300 signal amplifier/conditioner (with a low-pass analog filter set to 100kHz), the signal is then digitized by a NI PXIe-6358 (set to a sampling frequency of 1.1MHz). The sensors are connected to a common power supply (ITI QL355) delivering a constant 10V voltage. The PXIe-6376 and PXIe-6358 are in the same PXI rack in order to use a common reference clock. The data obtained with the chosen sampling frequencies (*i.e.*, 1.1 and 3.3MHz) have been compared to data acquired at 40MHz using a Keysight Infiniium S-series numerical oscilloscope to ensure the absence of aliasing in the signal. The reference pressure for all the differential measurements (PSI and Kulite sensors) is maintained to a stable value using a vacuum pump connected to a DPI 510 pressure regulator, maintaining a buffer tank of approximately 1 liter to the desired pressure (6kPa). The pressure fluctuation amplitude of the reference tank during trial runs has been measured to be less than 10Pa. To distinguish electronic noise from actual signal during the runs, reference measurements are recorded before each run (test section at vacuum pressure, wind-tunnel ready to run). This acquisition provides the noise floor.

4.4 Unsteady pressure measurements

Experimental study of hypersonic transition requires the measurements of high frequency instabilities. Those instabilities create pressure fluctuations at the wall, making measurement via pressure transducer one of the widespread technique. However, sensors that allow measurement in the correct range of frequency (up to 3 – 400kHz or even higher depending on flow conditions) are few and their calibration and limitations are still under debate.

The piezoelectric membrane-based sensors such as the Kulite XCQ093 have historically been used for high-frequency pressure measurements in wind tunnel testing. However, both the cavity, membrane and screen hole resonance frequencies are in the range of hypersonic boundary layer instabilities.

In the recent years, the PCB 132 sensor has been particularly present in hypersonic boundary layer transition literature. This new sensor is a piezoelectric pressure sensor which is announced to be able to accurately capture pressure fluctuations in a range of frequencies from 10kHz (or 100Hz for the 132B39 generation) to up to 1MHz. This possibility to measure high-frequency instabilities is a game changer for hypersonic boundary layer measurements.

Despite all the new experimental results gathered thanks to those sensors (Butler and Laurence, 2021a; Laurence et al., 2016; Zhang et al., 2013), recent studies (Berridge and Schneider, 2012; Butler and Laurence, 2021a; Grossir, 2017) tend to show that a resonance of the sensor in the 300kHz range could be present and that further works need to be done on those sensors.

The precise understanding and know-how on facility use of those sensors is the subject of ongoing projects at ONERA. In the context of this thesis, thorough testing and calibration of PCB132 (mainly A31) sensors have been conducted in house. In addition, and in the scope of the NATO-AVT-346 group on hypersonic transition, a collaboration was initiated between ONERA and Purdue University on the calibration of high-frequency pressure transducers. In that context, beta tests of the PCB 1232-B39 were conducted at the Aerospace Science Lab at Purdue University. Other studies regarding thermal sensitivity and integration problems linked to this sensor were also conducted.

4.4.1 Calibration method

The optimal way to get the full frequency response of the sensor would be to study its impulse response. However, creating a physical pressure impulse is impossible. The most convenient way to get calibration data is to excite the sensor with a Heaviside step and measure its response. Even if the frequency content of a Heaviside is a bit less complete than the one of an impulse, it still allows to compute the transfer functions.

In practice, a pressure step close to a Heaviside step can be created via a shock-wave, as the pressure increase through the shock-wave on a very short distance (in reality the shock-wave is a degenerated Heaviside as it cannot be infinitely thin). Calibration shock-waves are created in shock tubes using a high and low pressure (HP and LP) chamber separated by a membrane. When the membrane is burst (either spontaneously or in a controlled way) a shock-wave is created and start travelling from the high-pressure one to the low-pressure zone.

Other solutions might be used to calibrate those sensors. For example, trials were made at ONERA using a super short duration electrical arc to create a pressure burst. However, this method proved to be less reliable than the shock tube method and lead to new complications linked with very high electromagnetic noise.



Figure 4.6: Meudon calibration shock tube.

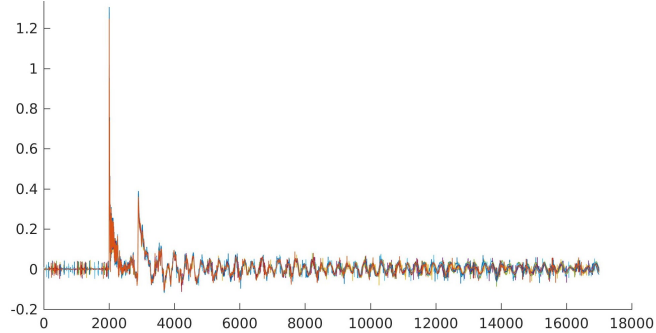


Figure 4.7: Raw PCB signal for 9 superposed runs in the Meudon shock tube, showing the very good reproducibility of the experiments.

Shock-tubes

The results presented in this part of thesis are coming from experiments conducted in two different shock tubes:

- The 3-inch shock tube from the Aerospace sciences lab in Purdue University.
- The metrology shock-tube of ONERA Meudon.

Both tubes are very different in construction but led to overall similar results and conclusions.

The Meudon shock-tube (see Fig 4.6) is a very simple shock tube, it offers no precise control on the pressure in the HP chamber nor is it equipped with a vacuum pump. There is also no triggered burst system. The way the tube work is pretty simple, a carbon paper sheet is added in-between the high and low-pressure chamber. The pressure in the HP chamber is then slowly risen thanks to the 7 bar compressed air network until the diaphragm spontaneously bursts. This method, even if extremely simple, has proven to be highly reliable, leading to perfectly identical burst of the diaphragm (see figure 4.7). Unfortunately, this shock tube does not allow to calibrate the sensor in a pressure environment matching the static pressure of the typical wind tunnel hypersonic flow.

In opposition to the Meudon shock-tube, the 3-inch shock-tube in Purdue (see Fig 4.8) includes a triggered burst system, a vacuum pump and automated valve. All those devices are controlled from a LabView program. This allows to create virtually any pressure step and leads to an advantage for calibration, as one can create different amplitudes of pressure steps and thus get calibration data both in the frequency and amplitude domains. However, one major drawback of the design of the 3-inch shock-tube is that the electrical burst system was retrofitted to the tube. Because of that, the burst system is not properly insulated from the rest of the tube, leading to a somewhat painstaking usage of the tube as a special care is needed in order to be sure that the sensors are properly insulated from the capacitor discharge when the burst is ordered.



Figure 4.8: Purdue calibration shock-tube.

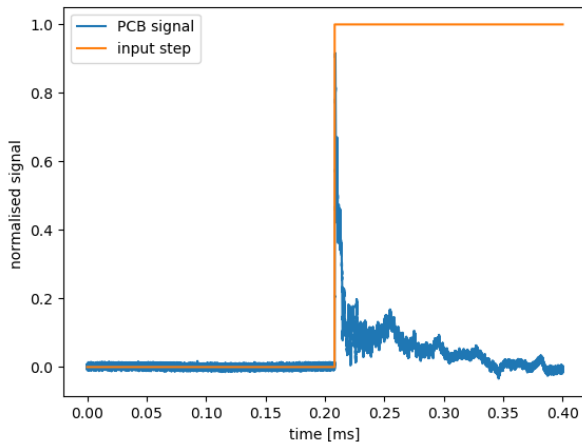


Figure 4.9: Typical normalized response of a PCB sensor to a shock-wave.

Transfer function computation

A transfer function can easily be computed from the shock tube experiment as:

$$T_{xy} = \frac{P_{xy}}{P_{xx}}, \quad (4.1)$$

with:

- T_{xy} transfer function (sensibility of the sensor depending on frequency).
- P_{xy} cross spectral energy: input (pressure step, Pa) output (sensor response, mV).
- P_{xx} power spectral energy: input (pressure step, Pa).

Typical input and output signals used for computing the cross and power spectral energies are presented in figure 4.9.

As the thickness of the shock is not known, it is supposed to be negligible (infinitely thin), the input is then supposed to be a perfect Heaviside function. FLDI measurements from Purdue University may bring more information on the shock thickness in the future.

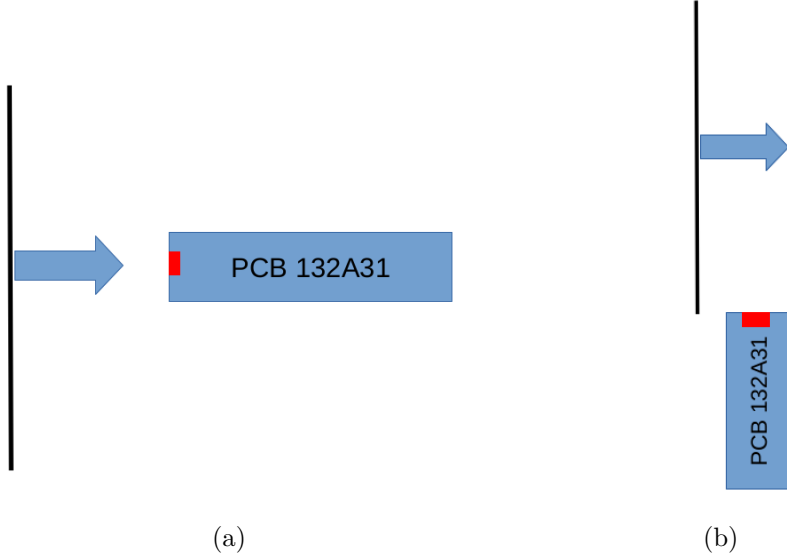


Figure 4.10: Schematic of the sensor and the shock-wave for (a) Pitot mount, (b) flush mount. The sensing element is colored in red.

Pressure rise computation

As shown in the previous section, to be able to compute the transfer function, we need to know the pressure input step. Then, two solutions arise:

- If we can precisely control and measure the pressure in the HP and LP chamber of the shock tube, we can accurately compute the pressure by implicitly solving the following equation to find the pressure step across the shock (this is the solution used for the Purdue shock tube experiments):

$$\frac{P_{HP}}{P_{LP}} = \frac{P_{After}}{P_{LP}} \left(1 - \frac{(\gamma - 1) \left(\frac{P_{After}}{P_{LP}} - 1 \right)}{\sqrt{2\gamma(2\gamma + (\gamma + 1)) \left(\frac{P_{After}}{P_{LP}} - 1 \right)}} \right), \quad (4.2)$$

then, the pressure step is simply:

$$\Delta P_{shock} = P_{After} - P_{LP}. \quad (4.3)$$

- Otherwise, we can simply use a reference absolute sensor to give the pressure step. However, this sensor must have a rise time short enough to get a converged value for the pressure step before any reflected shock-wave (or contact surface) reaches it (this is the solution used in the Meudon shock tube, using a Kulite XCQ-093 5 PSI A sensor).

Pitot and flush mount

As previously stated, the pressure rise time must be short for the input to be close to a Heaviside function. This leads to the question on how to integrate the sensor, which can be either mounted in Pitot position, directly facing the shock-wave displacement direction, or flush to the wall of the tube, the two solutions being illustrated in figure 4.10.

In the first case, the rise time will be extremely short as it scales with the thickness and velocity of the shock. In the second case, the rise time will be way higher, as the scaling length will be the diameter of the sensor (or at least the sensing element length, see figure 4.12), which is several order of magnitude greater. To assess whether or not the rise time is truly significant,

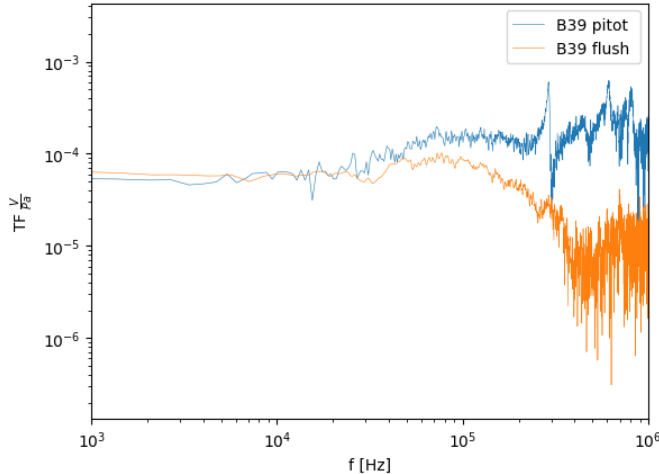


Figure 4.11: Transfer function of the same sensor, for same operating condition with a "Pitot" or a "flush" mount in the Purdue shock tube.



Figure 4.12: Picture of a sanded PCB 132B38 sensor showing the round sensing element in the middle.

test runs were conducted in the Purdue shock tube and are presented in figure 4.11. They show that the spectral content of the Pitot mount is way richer and that it should be preferred. This is particularly true if one is interested in the resonance of the sensor around 300kHz, which is not detectable with the flush mount. Nonetheless, for technical reasons, the runs conducted in the Purdue shock tube were still conducted with the flush mount.

Tube shock calibration limits: need for an acoustic calibration

Shock tube calibration in the Meudon shock tube is limited in terms of low frequency response due to the short time delay between the pressure rise caused by the shock and those caused by the reflected shock or contact surface. A typical way to calibrate unsteady pressure sensors for lower frequencies would be to use methods similar to the one that are used for microphones. Calibrated compression chamber or comparison with measurement made with reference microphones are easy ways to get the sensitivity of the sensor for different frequencies (or even a frequency sweep). It would also be good to be able to verify that the transfer functions given by the shock-tube calibration are actually correct. Several tests can be made with acoustics means at different



Figure 4.13: Ultrasonic validation setup.

frequencies to assess the validity of the computed transfer function. Two protocols were designed at ONERA to validate the transfer functions:

- A single point sinusoidal validation against a calibrated microphone. The sinusoidal excitation is emitted by a compression chamber, which is fed a sinusoidal amplified signal. This validation, even if single point, is extremely cheap and easy to do (the setup is presented in figure 4.13)
- A frequency sweep (0-50kHz) in an anechoic chamber was conducted. A calibrated microphone was used for reference. This was done with the help of acoustics specialists from ONERA. This sweep produced comforting results about the factory calibration of the PCB sensors in this range.

4.4.2 Calibration results

This section is dedicated to the presentation of the results of the calibration runs that were both conducted in Purdue and in Meudon.

Figure 4.14 presents the transfer function computed from experiments in the Purdue shock tube. It shows the difference between typical membrane-based pressure transducer (Kulite) and piezoelectric PCB132 (A31 and B39) sensors: instead of a membrane, the sensing element is a piezoelectric crystal, which has a much higher resonance frequency, leading to less limitation toward high frequency. It also shows the improvement that was made by PCB on the low frequency response of those sensors with the new generation (B39) as the transfer function is flat even for frequencies as low as 1kHz. However, it also shows that the high-frequency part (higher than $\sim 300\text{kHz}$) of the response is chaotic and that precise measurements up to 1MHz are still impossible.

Figure 4.15 presents the calibration results from ONERA, both from the shock tube calibration and the ultrasonic validation. It shows that the factory calibration, the shock tube and the acoustic validation are overall in good accordance. However, the shock tube results seem to show

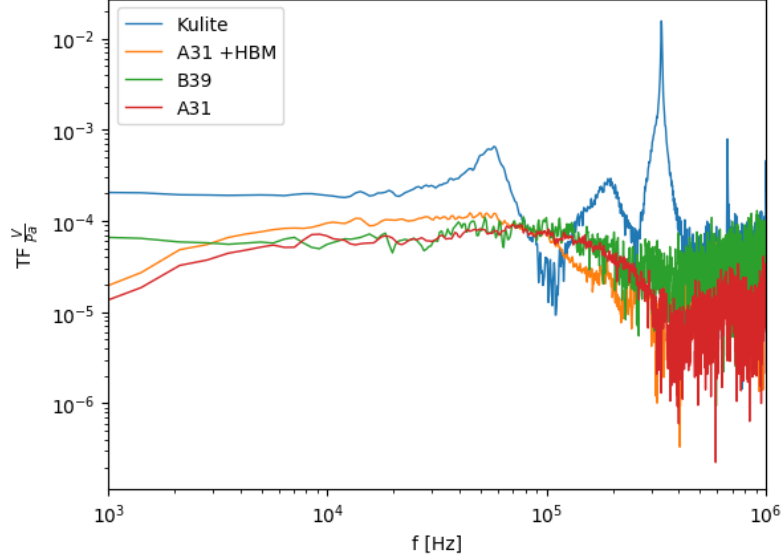


Figure 4.14: Transfer function of different PCB sensors against a Kulite reference sensor (normalized values).

that the sensitivity is not constant on the 11kHz-1MHz range. The most important result is that there seems to be a resonance of the sensor around 300kHz, which is in the middle of the boundary layer instabilities frequency range.

Figure 4.16 presents the transfer function computed from the shock tube experiments (blue) and the sensitivity announced by PCB (orange) for (a) a case with naked sensor and (b) with a thin layer of vacuum grease on top of the sensor, both for the new generation of PCB sensors (132B39). One can see that the computed sensitivity is actually very close to the announced one for frequency lower than 100kHz. The thermal protection given by the thin layer also gives better low-frequency response, this will be discussed in details in the next section.

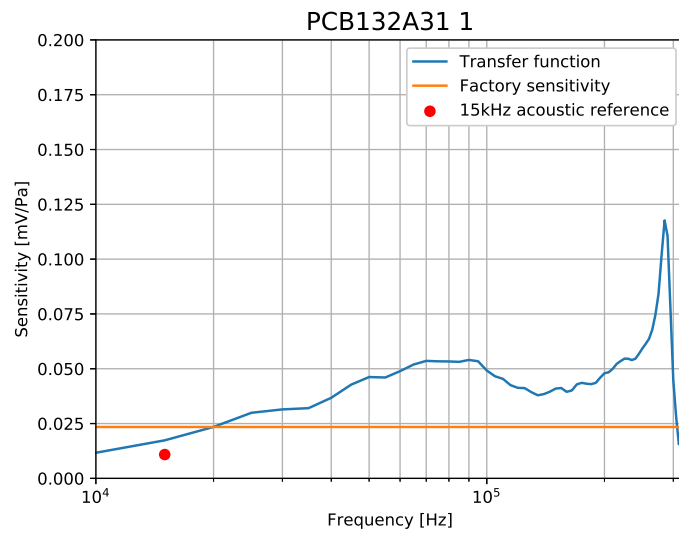
4.4.3 Drawback: heat-flux sensitivity

A main limitation for the use of the PCB132 sensors is that the piezoelectric sensing element is not only sensitive to mechanical constraints (which translate to pressure sensitivity), but also to thermal constraints. Figure 4.17 shows how a PCB132 B39 sensor responds to a flux of hot air. The thermal response is several order of magnitude greater than what the pressure change caused by the flux would generate.

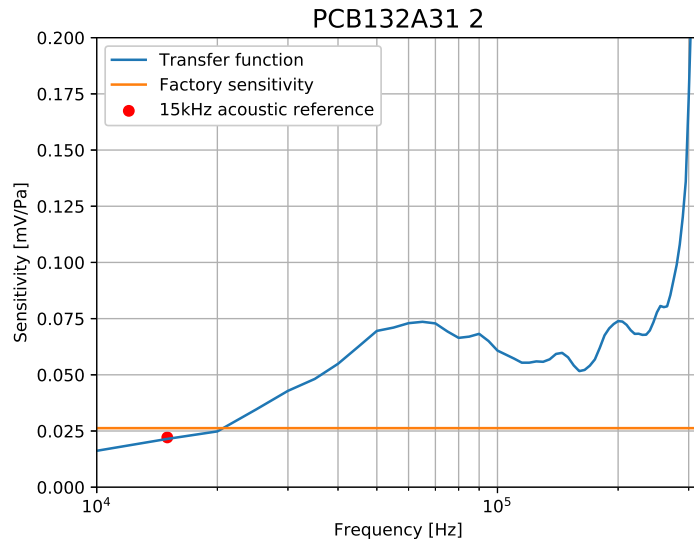
To reduce the impact of thermal variations, an obvious solution is to protect the sensor from heat-flux. This can be easily done by adding protective layers of materials on top of the sensor. However, this may have several impacts on the sensor response. First, adding mass on top of the sensing element will lower the resonant frequency of the sensors. Depending on the property of the added material, the transmission of pressure waves through the added layer may also change the response of the sensor. The solution is then to find the best compromise between protecting the sensing element from heat flux and not changing the measurement properties of the sensor.

One well-known way to protect a pressure transducer is to add a thin layer of grease on top of it. This will reduce the thermal effects and should not change too much the pressure response. Results with a layer of grease on top of the sensor are presented in figure 4.17 for the air flux experiments.

Results presented in figure 4.17, even if not quantitative (the temperature of the air and exposition time of the sensor are not precisely controlled, but are of an order of magnitude that could be



(a)



(b)

Figure 4.15: Calibration results from both the shock tube and acoustic validation for two different PCB132A31 sensors.

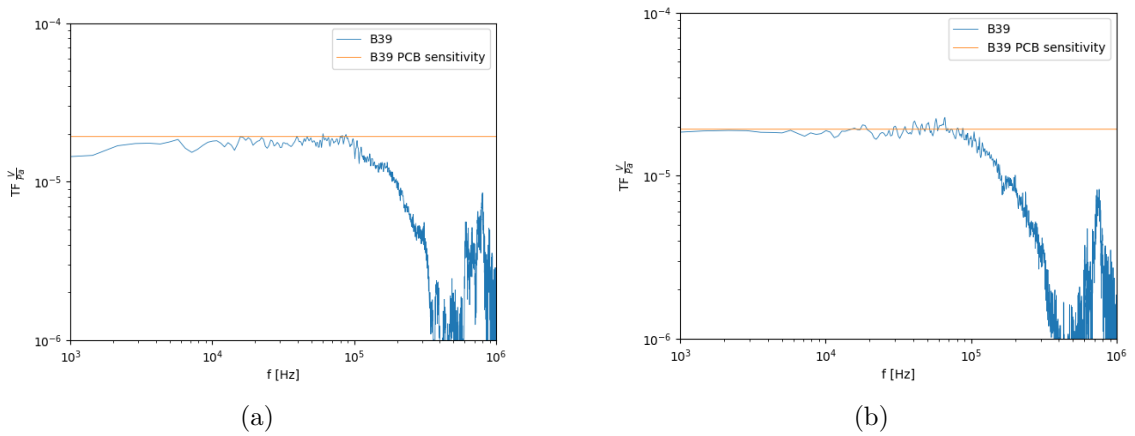


Figure 4.16: Transfer function of different PCB sensors (a) without thermal protection on the 132B39, (b) with thermal protection on the 132B39 (thin layer of vacuum grease).

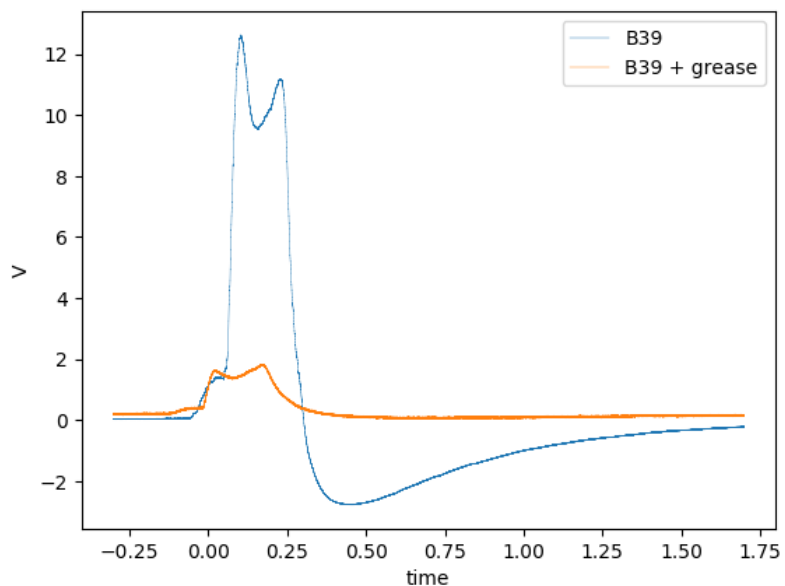


Figure 4.17: Response of the sensor protected by a layer of vacuum grease to a flow of hot air.

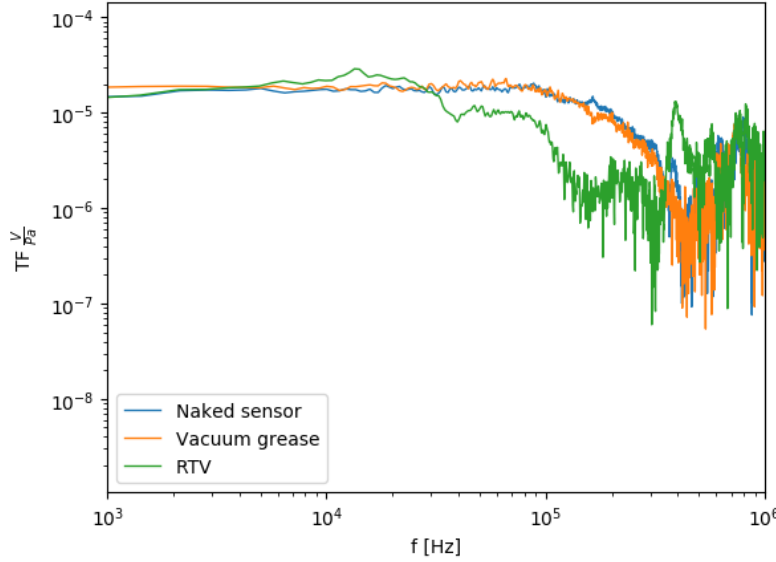


Figure 4.18: Transfer function of PCB sensors with different materials added on top of the sensor to protect it.

encountered during experiments in wind tunnels) show that the added layer of vacuum grease have a huge effect on the sensor response to the flux of hot air, reducing its impact by a factor of more than 6. Another solution would be to add RTV (Room Temperature Vulcanizing) sealant on top of the sensor, as recommended by PCB. RTV sealant has numerous advantages: it is easy to apply and does not stick to the sensor.

However, those methods may have an impact on the response of the sensor to pressure fluctuation and thus the transfer function. To quantify this impact, transfer functions for the same B39 sensor with different means of protection were computed and are presented in figure 4.18. Figure 4.18 confirms that adding material on top of the sensor can have a huge impact on the transfer function. For example, the sensor with RTV has an entirely different transfer function than the naked one, with a degradation of the transfer function for frequency low enough to be in the range of interest for hypersonic boundary layer studies. This may be linked with the thickness and the mechanical properties of the added layer of material. The most interesting results is that despite creating an efficient thermal protection, the thin layer of vacuum grease does not affect much the sensor pressure response and thus seems to be a good way to protect the sensor.

4.4.4 Epoxy layer

Another solution is to add a layer of epoxy on top of the sensing element (which is already drowned in resin), such as presented in figure 4.20. In fact, adding an epoxy layer also answers another major concern about PCB sensors, which is their integration in the model. Most hypersonic wind tunnels currently in operation in the world have a relatively small test section and a huge proportion of the models tested in those wind tunnels are axisymmetric, often conical. This leads to models having small radius of curvature, the integration of a PCB132 sensor can then become problematic as the sensor surface is completely flat while the model is curved, this will inevitably lead to steps at the junction of the sensor and the model such as schematized in figure 4.19. This may or may not actually be a problem for the flow depending on several factors such as the size of the step, the Reynolds number, the thickness of the boundary layer, etc. There is still a risk that that kind of step will influence the flow, and thus it is possible that an alley of sensors will measure self-induced fluctuations rather than fluctuations due to a physical mechanism of the flow.

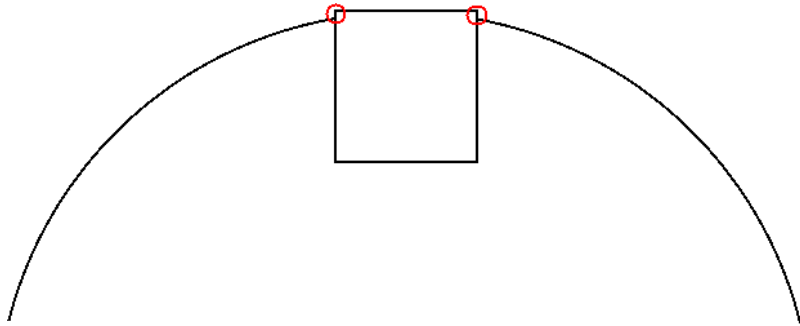


Figure 4.19: Schematic of the integration problem on curved models.



Figure 4.20: PCB sensor with an added layer of epoxy.

Adding an epoxy layer on top of the sensor would be a way to solve this problem, as it could be machined to be perfectly flush to the model without risking the integrity of the sensor.

Effect on the sensor response

To quantify the impact of the added epoxy layer on the sensor, a direct comparison of transfer functions between a PCB sensor with and without an added epoxy layer is presented in figure 4.21. It shows that the epoxy layer is slightly shifting the resonance frequency toward lower frequency (this is expected as the weight added by the layer of epoxy will lower the mechanical resonance frequency), the amplitude of the resonance is also slightly increased. Apart from that, no clear difference can be found between the transfer functions with and without epoxy. The same observations can be made from runs in the R1ch blow down wind tunnel, such as presented in figure 4.22. It is important to note that those results come from $M = 3$ runs and that the peak in the spectrum is not due to a physical instability, but only to the resonance of the sensor.

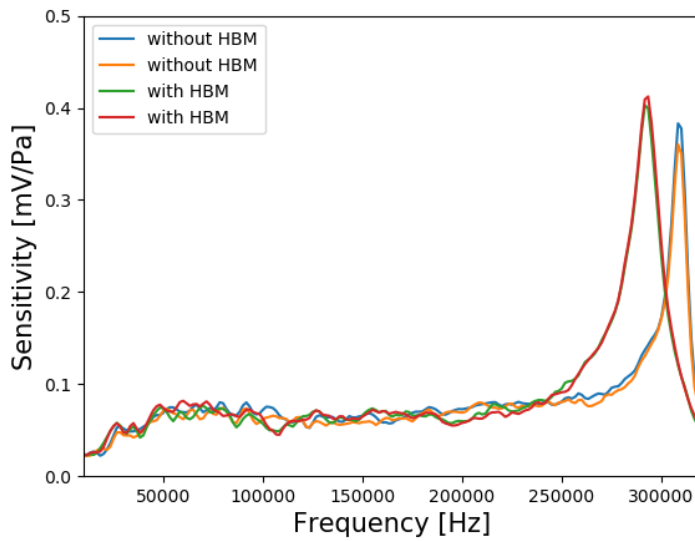


Figure 4.21: Transfer function of the same PCB132A31 sensor with and without epoxy layer, computed from Meudon shock-tube experiments.

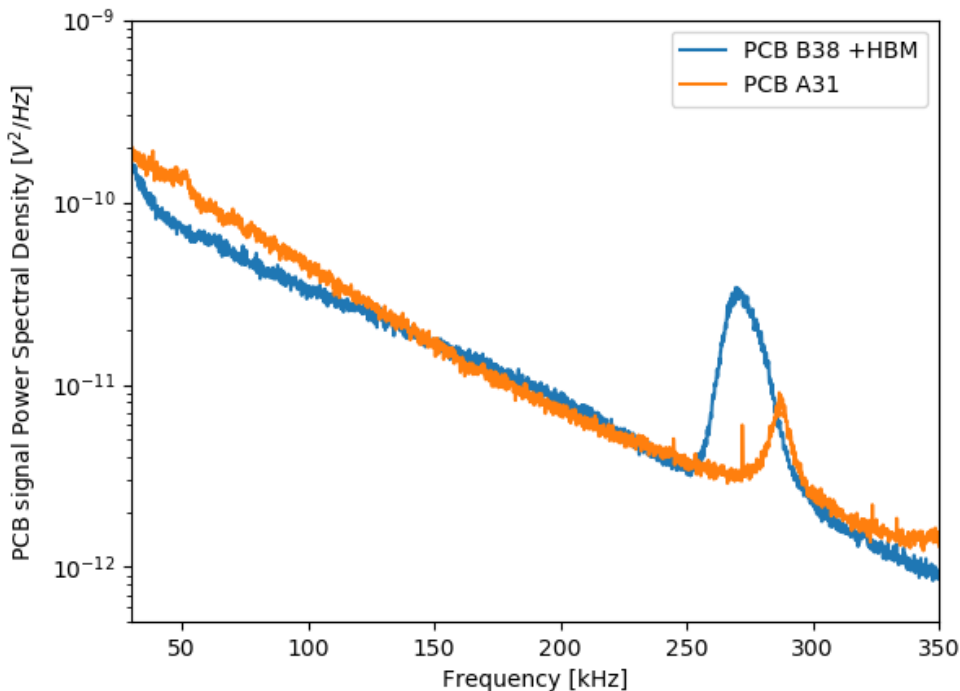


Figure 4.22: Signals from two different PCB sensors, one with an added layer of epoxy and one without in the same flow conditions in the R1Ch facility ($P_i = 2.7 * 10^5 \text{ Pa}$, $T_i = 280 \text{ K}$), mounted on the cone model (see figure 4.23).

Application to wind tunnel testing

The epoxy layer seems to be an efficient solution to solve two of the main limitations to the use of PCB sensors in wind tunnel testing: the heat-flux sensitivity and the model integration.

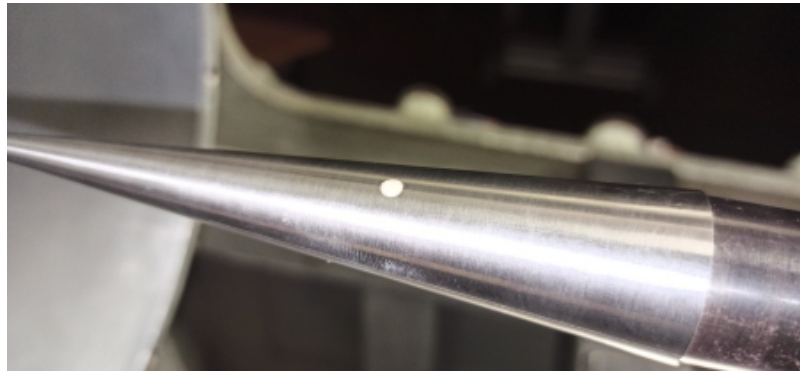


Figure 4.23: PCB 132B38 flush mounted on the 5° cone with the epoxy layer method.

The next question would be how to apply this technique to wind tunnel testing. A typical protocol would be the following:

1. Add a layer of epoxy on top of the sensor (for instance HBM X 60). To facilitate this step, a PTFE (Polytétrafluoroéthylène) mold can be used, the epoxy will stick to the sensor but not to the PTFE mold and thus the layer can be precisely added. It is important that the epoxy is not added while the sensor is mounted on the model as this would lead to the epoxy sticking to the model and this would degrade the response of the sensor.
2. Optional step: calibration of the sensor with the added layer of epoxy in a shock-tube.
3. Mount the sensor on the model, sand the surface to a perfect flush mount.
4. It should be possible to calibrate the sensor mounted on the model with an acoustic method (*i.e.* 1kHz - 10Pa, for example) however this step may require some developments because it supposes to have a device to create precise pressure disturbances. Those devices already exist for microphone calibration, but it is unsure that they can directly be used for 'on-model calibration'.

An example of flush sensor integration using the method described here-before can be seen in figure 4.23.

4.4.5 Conclusion on the use of PCB sensors

PCB sensors offer a way to measure pressure fluctuations in a frequency range that is not achievable using traditional membrane-based pressure transducers, this is illustrated in figure 4.24 (see chapter 9 for more information on that figure), which presents a numerical solution in a turbulent flow compared to the experimental results from a Kulite XCQ093 and a PCB132A31 with an added layer of epoxy. Calibration of PCB sensors can be accurately conducted in shock-tubes, and the sensor can be protected and flush-mounted using an added layer of epoxy. However, the high-frequency response (higher than 300kHz) of the sensor is still problematic.

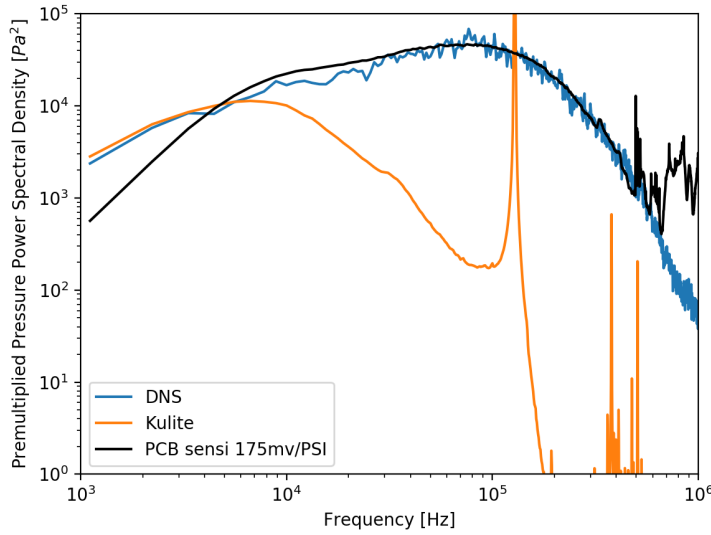


Figure 4.24: Signals from a Kulite XCCQ093 (orange), a PCB with an added layer of epoxy (black) and numerical simulation (blue) for turbulent Mach 5 flow on the flare of the cylinder flare configuration (see chapter 9 for more information).

4.5 Optical measurements

4.5.1 IR thermography setup and post-processing

To perform the heat flux measurements, a mid-wave ($2.5 - 5\mu m$) FLIR SC7600 InSb (640×512 pixels) infrared (IR) camera equipped with a 25mm lens was used. The camera is installed in the wind tunnel test section inside a specific enclosure to maintain it at atmospheric pressure and to provide sufficient cooling of the device through fresh air incoming. The use of a tilted silicon window , with a surface treatment ensuring 95% of transmittivity, eliminates the Narcisse effect. The camera is looking at the model through an aluminum mirror of optical quality as seen in figure 4.25 due to limited space inside the test section. To account for the experimental conditions, and more particularly for the different optics in between the camera and the model, an in-situ calibration was carried out. This operation was performed by placing a thermo-regulated heating plate at the model position and performing camera acquisitions for different temperatures along the dynamic of interest $20 - 75^\circ C$. The derived calibration law is applied to the camera digital levels for the following measurements.

The model made of Isotan is coated with a thin layer of Sacotherm paint. The paint emissivity, together with the material has been characterized by the French National Laboratory of Tests and Metrology (LNE) for different angle of observation. At normal incidence, the paint emissivity is equal to 0.85.

Image registration and heat flux computation are described in more details in Le Sant (2005) and Le Sant et al. (2002) respectively. Therefore, only the main steps of the process will be presented in the following.

First, the model is meshed using a triangular tessellation. The camera point of view is then determined by fitting the mesh to the model contour on the image. This allows to link each pixel to a point on the model and thus to a position in space.

Secondly, camera digital levels are converted to temperature values thanks to Planck's law corrected with the emissivity value. Because each pixel can be related to its 3D coordinates on the model, the observation angle is known. The corresponding emissivity value determined by the

LNE can then be applied as presented in Le Sant, 2005. The paint emissivity not been characterized for angles greater than 60° , it seems preferable not to consider those measurements. Consequently, the corresponding pixels are dismissed in the following.

Then, the heat flux is computed using the temperature history and the FLUX1D approach Le Sant et al., 2002. This method solves the one-dimensional heat equation taking into account the thickness of the model as well as its thermal properties depending on the temperature. The ability to take into account the model thickness is crucial in this experiment as the thermal signal depth penetration ($\sqrt{\alpha t} = 11.7\text{mm}$, with α the thermal diffusivity of the material) is greater than the model thickness (7 mm) during a run. To do so, we consider a zero flux condition on the opposite face of the model. The impact of the curvature has been evaluated to be below 1% and consequently this effect has not been taken into account in the heat flux processing. Finally, because the paint behaves like a thermal resistance, it is assessed in the process by considering a constant heat flux Le Sant et al., 2002. The non-dimensional Stanton number is then computed following the relation:

$$S_t = \frac{\Phi}{\rho_\infty V_\infty C_p (T_{aw} - T_{wall})} \quad (4.4)$$

Where Φ is the heat flux determined from IR measurements, ρ_∞ is the free-stream static density, V_∞ stands for the free-stream velocity, C_p represents the specific heat at constant pressure, T_{aw} represents the instantaneous adiabatic wall temperature and T_{wall} is the model temperature measured by the IR camera. Since we investigate the instantaneous Stanton number evolution in the following, free-stream quantities are computed using the free-stream Mach number and the instantaneous stagnation pressure and temperature measured in the wind tunnel.

Finally, Stanton number distribution maps are re-projected on the 3D model thanks to the image mapping technique. An example of the resulting image is presented in figure 4.26. This image represents the spatial distribution of the mean Stanton number on the model. The red dots correspond to the PCB sensors. Streaky patterns are particularly visible in the reattachment region on the flare. To better recognize this striation pattern, the reader is invited to watch the movie captured by the IR camera provided in the supplementary material. From our analysis, the whole heat flux assessment uncertainties are driven by the uncertainties on the thermal properties of the material and the estimation of the paint factor. However, whereas the paint factor introduces a random error of 5%, the thermal properties induce a bias (8%) which is common to all the runs and therefore does not affect the analysis from run to run.

Unless specified otherwise, no spatial nor temporal averaging or filtering of the IR data is conducted.

Figure 4.26 indicates the two valid areas seen by the IR camera: the IR image represents the low-frequency acquisition (50Hz) which covers both the cylinder part of the model and the full flare; in red, the high-frequency acquisition (972Hz) which focuses on a reduced region at the beginning of the flare. In both cases, the corresponding spatial resolution provided by the camera is 0.4mm/pixel. IR acquisitions were triggered manually to record the full temperature history during the wind tunnel blow-down as indicated in figure 4.4.

A cylindrical coordinate system will be used, as it allows to better represent the axisymmetrical geometry and flow. The cylindrical coordinate system is derived from the Cartesian presented in figure 4.26, x is kept the same with an origin at the leading edge of the model. The radius r is defined as $r = \sqrt{y^2 + z^2}$ (y and z origin are located on the symmetry axis of the model) and the angle θ as $\theta = \tan^{-1}\left(\frac{z}{y}\right) + 90^\circ$, θ is defined in degrees.

To extract information about the azimuthal striation from the IR images, an azimuthal decomposition consisting of the following steps is used. First, the N_i images are interpolated on a regular

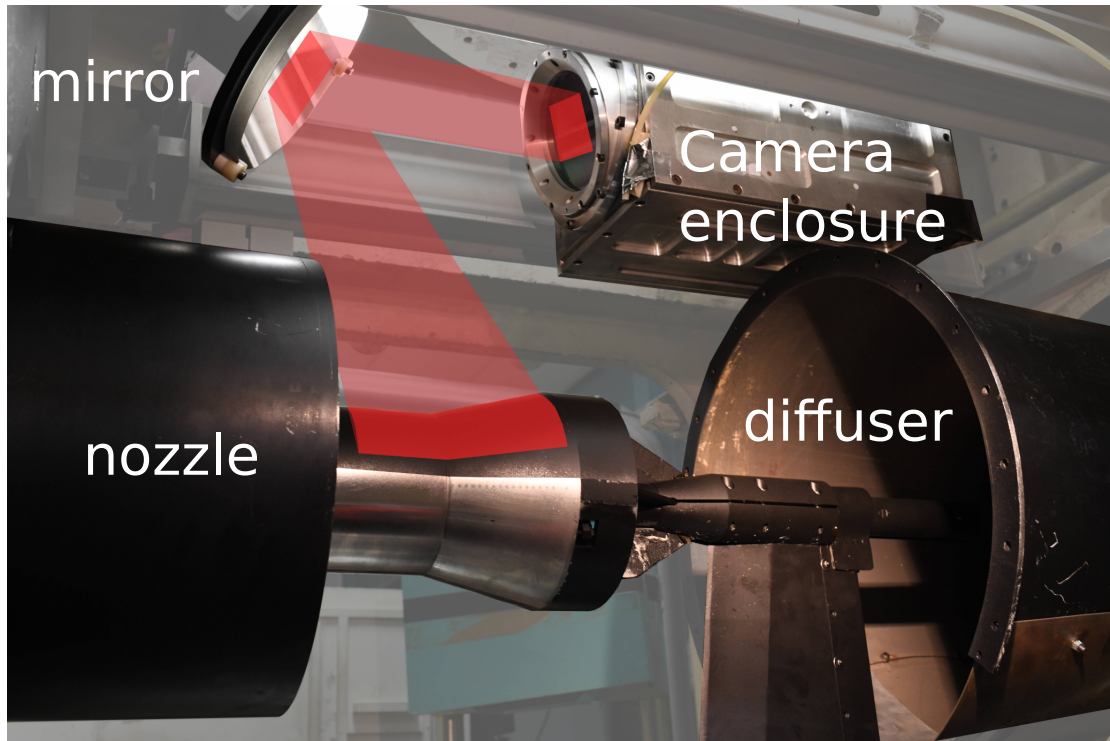


Figure 4.25: Infra-Red imaging setup in the R2Ch facility showing the camera enclosure, the mirror and the optical path.

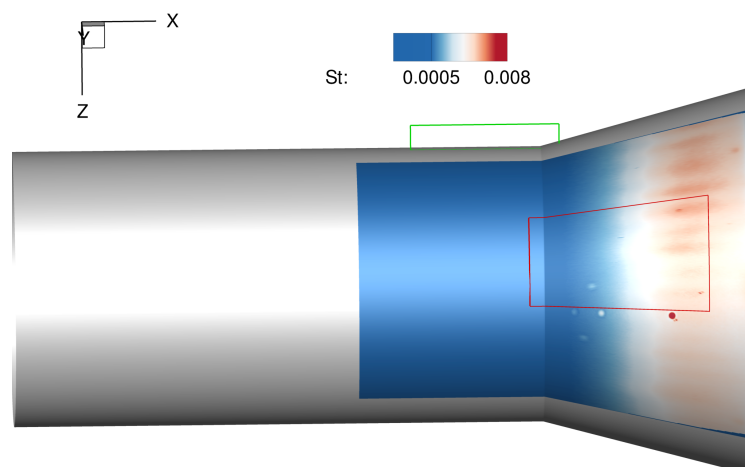


Figure 4.26: Part of the model filmed by the infra-red camera in the 50Hz 640×512 full frame case (image) and 972Hz 208×88 reduced frame case (red line). The green box represent the area filmed by the Schlieren imaging setup (see next section).

(x, θ) grid. Then, a Discrete Fourier Transform (DFT) is applied in the azimuthal direction, giving Fourier mode vectors $\hat{\mathbf{S}}^k(m)$, where k is the image number and m the azimuthal wavenumber of the mode. It is important to note here that the DFT cannot be computed at the longitudinal location of the PCB sensor due to their presence in the IR images. Due to the spectral transformation in the azimuthal direction, the vectors $\hat{\mathbf{S}}^k(m)$ correspond to mono-dimensional vectors of pixels: they contain complex values associated with the pixel intensity at each point (x) from the mesh. For a given wavenumber (m) of interest, the Fourier modes of all the images are then stacked in a matrix $\hat{\mathbf{X}}_m$, which reads

$$\hat{\mathbf{X}}_m = [\hat{\mathbf{S}}^0(m), \hat{\mathbf{S}}^1(m), \dots, \hat{\mathbf{S}}^{N_i-1}(m)]. \quad (4.5)$$

This matrix is then processed similarly to a snapshot matrix in a classical POD decomposition: the i -th POD mode $\phi_i^{(m)}$ can be computed from the i -th left singular vector of $\hat{\mathbf{X}}_m$, which may be computed by solving the eigenproblem associated with the cross-spectral density matrix

$$\hat{\mathbf{X}}_m \hat{\mathbf{X}}_m^* \psi_i^{(m)} = \lambda_i^{(m)} \psi_i^{(m)}, \quad (4.6)$$

For each wavenumber (m) , the associated POD modes are ordered with respect to their contribution to the global dynamics, *i.e.* $\lambda_0^{(m)} > \lambda_1^{(m)} > \lambda_2^{(m)} > \dots$.

In practice, the eigenmodes are computed by using the snapshots method of Sirovich, 1987 which is a less costly but equivalent decomposition based on $\hat{\mathbf{X}}_m^* \hat{\mathbf{X}}_m$ rather than (4.6). This provides the right singular vectors of $\hat{\mathbf{X}}_m$, from which one can easily retrieve the POD modes (see for instance Towne et al., 2018 for details). While for traditional POD, multiple modes are needed to describe the data, here the POD comes after a DFT, giving a different set of modes per wavenumber of interest. In this part of the work, the POD is mainly used to discriminate the correlated physical information at a given frequency from the uncorrelated noise coming from the environment or the acquisition. As such, only the leading mode will be presented and discussed for the wavenumber of interest.

4.5.2 Schlieren setup

Flow visualizations are realized thanks to a classical Z-type schlieren setup as represented on figure 4.27. Due to environmental constraints, the reception side has been folded using a large plane mirror. A HBO arc-lamp and Phantom V2640 high-speed camera are employed to investigate the recirculation region close to the flare junction. The camera was operated at 140kHz, on a reduced region of 596×128 pixels also depicted on figure 4.26. The knife edge was set horizontally to visualize vertical density variations in the shear layer.

Example of images taken with the high-speed camera setup are presented in figure 4.28 for one of the studied Reynolds number. While it clearly displays the density gradient of the mixing layer, it is more difficult to identify structures linked with unsteady features of the flow in this image. One can still note the presence of alternating structures.

To extract information on those potentially spatio-temporally correlated structures, Spectral Proper Orthogonal Decomposition (SPOD) is used. Recently, it has been used with great success to post-process high-speed Schlieren images in hypersonic wind tunnel experiments (Butler and Laurence, 2021a,b).

The actual treatment is done following a procedure that is close to the one used for the IR post-processing, but including a temporal Fourier transform instead of a spatial one. It is also very close to the one described in section 3.2.2: first, the images are regrouped in N_r overlapping realizations of the flow. Each realization contains a temporal sequence of vectors representing the images $(\mathbf{s}_{t_0}, \mathbf{s}_{t_0+\Delta t}, \dots)$, where the components of \mathbf{s}_t are the intensity of the pixels of the 2D image at the time t . A Discrete Fourier Transform (DFT) is then applied in the temporal

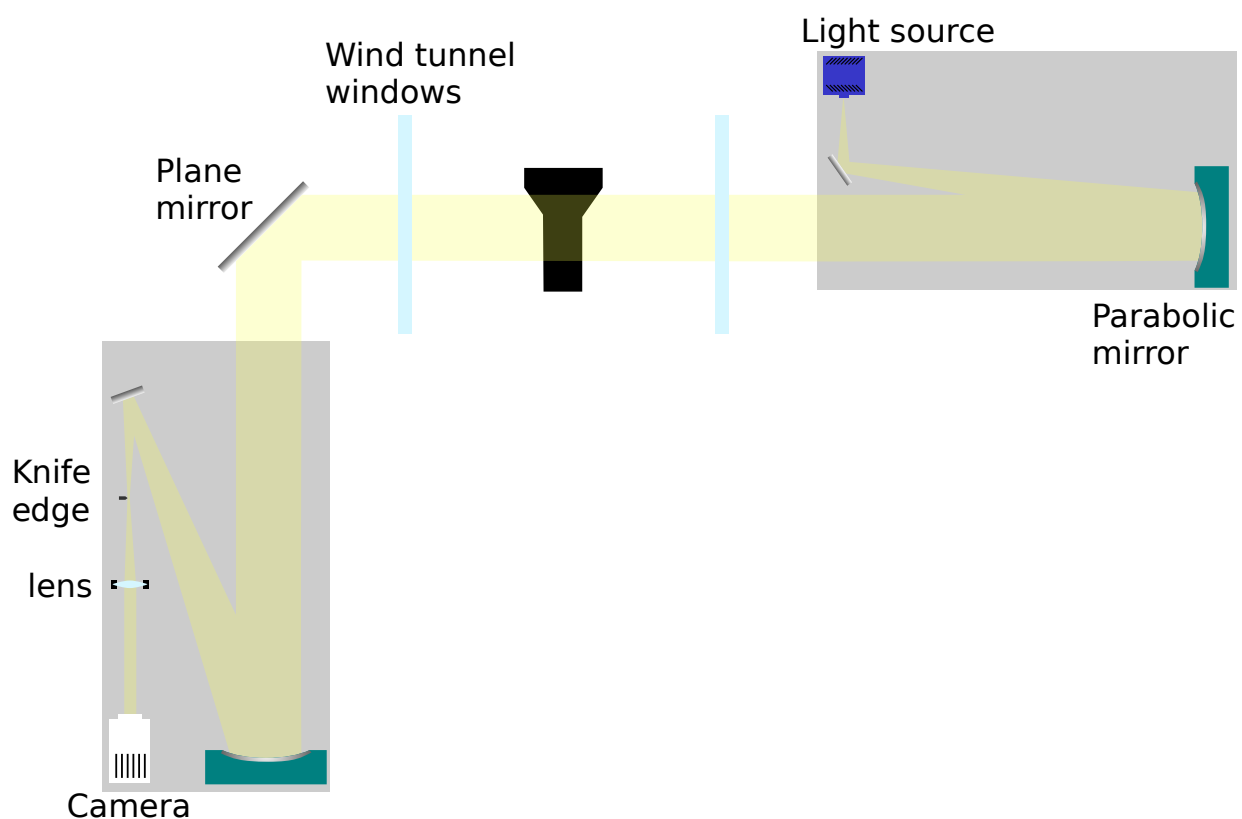


Figure 4.27: Z-type schlieren setup. Due to environmental constraints, the reception side has been folded using a large plane mirror.

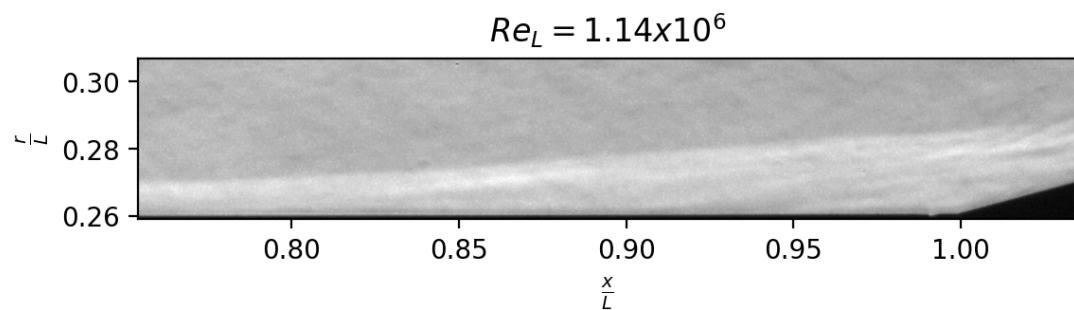


Figure 4.28: Example of instantaneous Schlieren images from the movies used for the SPOD.

Sampling rate	140kHz
Number of images	83324
Number of images in each realization	2048
Frequency resolution	68Hz
N_r	80

Table 4.4: Numerical parameters for the SPOD.

direction, giving Fourier mode vectors $\hat{\mathbf{S}}^k(\omega)$, where k is the realization number, ω the temporal frequency. For a given frequency ω of interest, the Fourier modes of all realizations are then stacked in a matrix $\hat{\mathbf{X}}_\omega$, which is then treated following the same procedure described here-before for $\hat{\mathbf{X}}_m$ in the case of the IR post-processing. The numerical parameters such as the number of images, the realization size and the number of realizations are presented table 4.4.

4.6 Wind tunnel free stream perturbations measurements

As pointed out in section 2.1.1 and 3.1.4, numerical simulations of experimental results of hyper-sonic transitional flows is challenging since we have very sparse information about the free stream perturbations in the R1Ch and R2Ch blowdown facilities.

To get some information on those perturbations, a pilot experiment was designed using an existing conical model which was equipped with a Kulite XCQ093 (5 PSI-D) and a PCB132A31 sensor. This experiment was designed following the encouraging results provided by Hader and Fasel, 2018 which could numerically recreate experimental results with a good accuracy by introducing pressure fluctuations measured in the BAM6QT. Even if their method may not work for noisy tunnels such as R2Ch given the higher fluctuations levels compared to a quiet tunnel, measuring the pressure fluctuation spectra and root-mean-square (rms) levels are good starting points to qualify the wind tunnel free-stream noise.

The chosen cone is convenient for that kind of measurement as it is designed to have as little impact as possible on the flow: the half angle (5°) is chosen such that the shock is attached and weak (at Mach 5). Moreover, the cone is not long enough for impactful instabilities to develop in the boundary layer.

However, this experiment is still a suboptimal solution for the measurement of free-stream fluctuations, as they still have to go through the shock and then penetrate the boundary layer before reaching the sensor. Moreover, the transfer function of the shock and the boundary layer is not known at the present time. In addition, only pressure measurements can be accomplished, giving only incomplete information about the fluctuations.

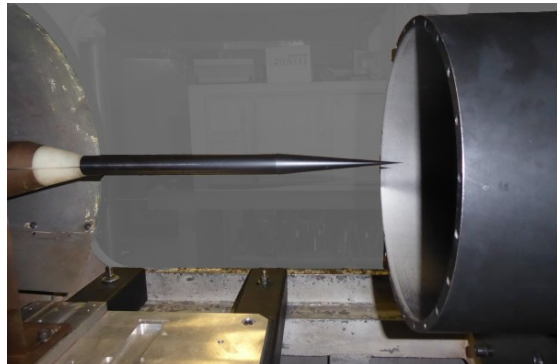


Figure 4.29: Measurement cone in the R2ch facility.

As the retrofitted cone was damaged during pre-measurement runs, a new cone has been designed, a 3D model is presented in figure 4.30. Its geometry is globally very close to the old one (same half angle and same length). It is made of RAMAX HH steel and is finished by surface grinding to ensure a good surface roughness ($R_a < 0.4\mu\text{m}$) and sharpness of the tip. The main difference with the retrofitted cone is that the sensors are mounted much closer to the tip, leading to a lower risk of instabilities developing upstream of the sensors and reducing the boundary layer thickness at the sensing location. The new cone is also designed such that the sensors are easier to access. The model is fitted with a PCB132A31/B38/B39 (depending on the run, the cone is also used as a convenient way to test PCB sensors in blowdown tunnels) and a Kulite XCQ093 (1/5 PSI-D) sensor for pressure fluctuations measurements.

The acquisition system and reference pressure used are similar to those described before (see section 4.3).

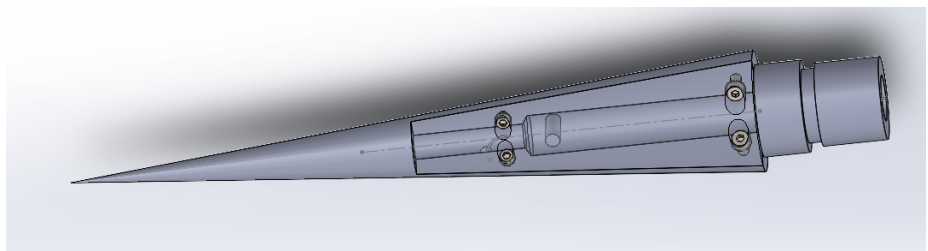


Figure 4.30: 3D model of the new cone.

Chapter 5

Numerical study of the bubble dynamics and its impact on transition

This chapter aims at describing the low frequency shock-bubble unsteadiness and understanding both its physical origins and its impact on the transition process. A high-fidelity simulation of the massively separated shock/transitional boundary layer interaction is performed at a free stream Mach number of 6 and for a transitional Reynolds number. The chosen configuration yields a strongly multiscale dynamics of the flow as the separated region naturally oscillates at low-frequency, and high-frequency transitional instabilities are triggered by the injection of a generic noise at the inlet of the simulation. The simulation is post-processed using Proper Orthogonal Decomposition to extract the large scale low-frequency dynamics of the recirculation region. The bubble dynamics from the simulation is then compared to the one stemming from the instability of the global Navier-Stokes operator linearized about the mean flow. A critical interpretation of the eigenspectrum of this operator is presented. The impact of the large-scale dynamics on the transitional one is then assessed through the numerical filtering of the low wavenumber modes. The content of this chapter largely comes from a published article in the Theoretical and Computational Fluid Dynamics journal (Lugrin et al., 2021a).

Contents

5.1	Introduction	78
5.2	Large scale, low frequency dynamics of the bubble	79
5.2.1	Extraction of the dominant bubble modes from the QDNS data	79
5.2.2	Spatio-temporal characterization of mode B	84
5.2.3	Physical mechanism driving mode B	88
5.2.4	Spatio-temporal characterization of mode R	90
5.2.5	Physical mechanism driving mode R	91
5.2.6	Partial conclusions on the large scale dynamics	93
5.3	Impact of the bubble dynamics on the transition	93
5.4	Conclusion	96

5.1 Introduction

The goals of the study presented in this chapter are the following. First, a full description of the low-frequency low-wavenumber dynamics of the separated region is still missing for the studied configuration and will be presented in this chapter alongside an in-depth study of their underlying physical mechanisms. To do so, results from QDNS A (see 3.2) are exploited. The domain used for this simulation span over 360 degrees, which allows for large scale modes to grow without constraints. Proper Orthogonal Decomposition (POD) is used to extract large-scale coherent structures from the simulations. The QDNS analysis is then coupled with a linear stability analysis about the mean flow to get insights on the underlying physical mechanisms. This leads to the second point of the study: the use of the mean-flow stability results to characterize the spatio-temporal behavior of the large scale structures, which could not be fully addressed by the QDNS alone due to the (too) slow timescale involved.

After characterizing the dynamics of the bubble, the final question of this chapter comes naturally: what are the interactions between the large scale dynamics and the transitional one ? It is particularly important to know how far one can go in reducing the azimuthal domain size before the flow topology and transition process are significantly affected. This is also linked with the question of which mechanisms (*i.e.* convective mechanism alone (Dwivedi et al., 2019), convective mechanism excited by non-linear interaction or absolutely unstable mechanisms (Cao et al., 2021; Sidharth et al., 2018)) creating streaks play an important role in the transition process in this case where free-stream perturbations are present. To address this last point, two more QDNSs (cases B and C) are exploited, covering reduced spans of the domain in order to select the wavenumbers of the mode that will be able to grow in each simulation. This allows to have simulations without the dominant bubble mode, and thus to study their impact on both the topology of the flow and the transition process.

The numerical simulations that will be exploited in this chapter are the case A, B and C of table 3.2. Computations of the flow of cases A and B were performed on the OCCIGEN supercomputer at CINES under the GENCI allocation A0072A11041. The three simulations are the following: one unfiltered 360° computation (a schematic of the computational domain is presented figure 5.1 along a numerical schlieren of the mean flow), and two spatially-filtered simulations where only certain azimuthal wavenumbers m are retained. By confronting the unfiltered dynamics to those spatially filtered, we aim at assessing the impact of the small wavenumber dynamics (*i.e.* the large scale bubble dynamic) on the larger wavenumber structures (smaller scale). The filtering is performed by restricting the azimuthal extent of the computational domain and imposing periodicity conditions on the azimuthal boundaries. The azimuthal extent and number of points in each mesh of the different simulations are presented in table 3.2. Contrary to the full (360°) domain, where every integer wavenumber up to the mesh size is resolved, the QDNSs labeled B and C in table 3.2 are such that only m values multiple of 6 and 24 can develop, respectively. This restriction results from the reduced size of the domain and the imposed periodicity: only an integer number of wavelengths can exist in the spanwise direction, otherwise the periodicity conditions would lead to discontinuities in the flow fields. For instance, for the domain used in QDNS C, the span of 15° (1/24th of the full domain) only allows structures with wavenumber 0, 24, 48, 72, 96, . . . to develop.

The free-stream conditions chosen for this study are presented in table 5.1, the flow conditions are chosen in order to maximize the importance of the separation dynamics. The Mach number is set to 6 and the free-stream conditions are chosen to attain a transitional Reynolds number value. The free-stream is perturbed by a random white noise ($A = 1\%$ see appendix 1) in order to trigger convective instabilities through their receptivity process. The perturbation level is chosen such that the boundary layer is laminar when interacting with the separation shock, causing a stronger separation. However, the flow is fully turbulent before the end of the domain, which

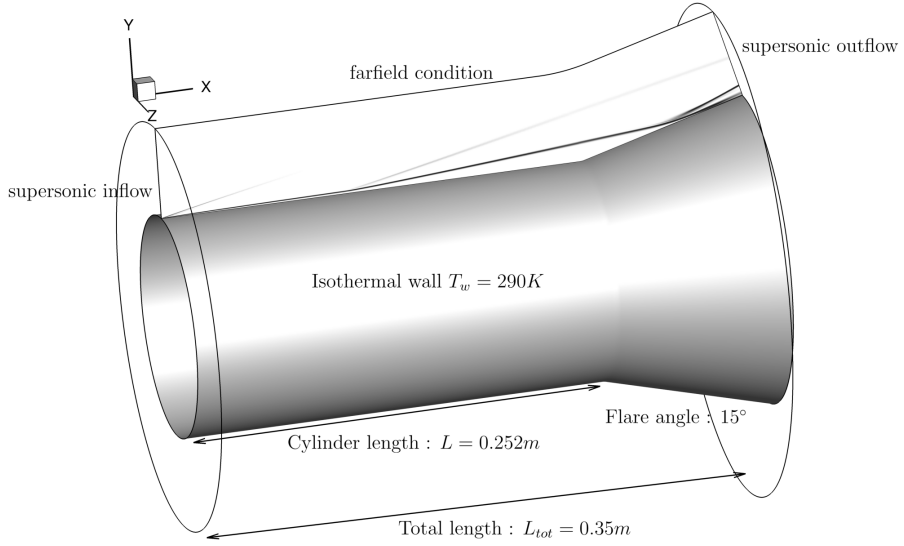


Figure 5.1: Computational domain used in the full domain simulation showing boundary conditions and characteristics length. A numerical Schlieren of the mean flow is also shown.

Table 5.1: Free stream conditions and characteristic values for the simulation.

M_∞	T_∞	P_∞	U_∞	T_i
6	86.6 K	1023 Pa	1119 m/s	710 K
T_{wall}	Re_L	δ_{sep}	L_{sep}	L
290 K	1.95×10^6	0.00165 m	0.192 m	0.252 m

encompass the totality of the transition process. The free-stream conditions are presented in table 5.1. The conditions lead to a massive separation such as visible figure 5.1

The chapter is organized as follows. First, the low frequency dynamics of the recirculation bubble is characterized through the study of POD modes from the QDNS. The physical mechanisms underlying the characterized modes are investigated through the study of the linearized Navier Stokes operator. The impact of the bubble dynamics on the transitional process is then assessed before concluding on the overall impact of the bubble modes on the flow.

5.2 Large scale, low frequency dynamics of the bubble

5.2.1 Extraction of the dominant bubble modes from the QDNS data

This section is dedicated to the study of the shock-bubble system dynamics. As stated before, this dynamic is supposed to be of large spatial scale and low frequency (most studies pointing towards the existence of quasi-steady modes (Hildebrand et al., 2018; Robinet, 2007; Sidharth et al., 2018)). Thus, it is studied by processing filtered snapshots of the flow, such as described in section 3.2.2. This section aims to characterize the dominant modes.

The first interesting result is that the dominant POD modes (and their energetic content λ_0) computed from data filtered with the three different filters presented in section 3.2.2 are very similar. Fig 5.2 presents the differences between the leading POD modes when using filtered data with two different cutoff frequencies: $S_{L_{sep}}^{(c)} = 6.86$ versus $S_{L_{sep}}^{(c)} = 0.86$. First, figure 5.2 (a) shows that the energetic content of the leading POD for each studied wavenumber is only slightly affected by the change of cutoff frequency. Additionally, the spatial organization of the

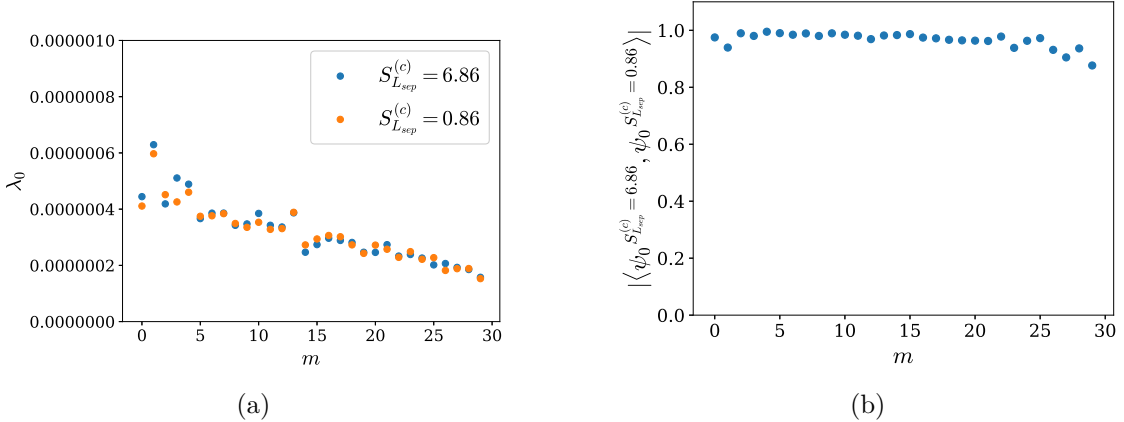


Figure 5.2: Difference between the leading POD modes extracted from data filtered at $S_{Lsep}^{(c)} = 0.86$ and $S_{Lsep}^{(c)} = 6.86$: (a) present the relative change in energetic content, (b) the alignment coefficient between the two modes.

modes is nearly not affected. This last statement may be quantified by computing an alignment coefficient (Pickering et al., 2020), which is defined for two modes Ψ_a and Ψ_b as the normalized scalar product:

$$\frac{|\langle \Psi_a, \Psi_b \rangle|}{\sqrt{\langle \Psi_a, \Psi_a \rangle \langle \Psi_b, \Psi_b \rangle}}, \quad (5.1)$$

this coefficient is equal to 1 for perfectly aligned modes and 0 if they are orthogonal. Figure 5.2 (b) shows that the alignment coefficient between two corresponding modes with different cutoff frequencies is close to one for all the wavenumbers of interest. Therefore, the POD modes are virtually unaffected by the change in temporal filters. Besides proving that the bubble dynamics is, as expected, dominated by very low-frequency modes (*i.e.* at or below $S_{Lsep} = 0.86$), it shows that the study of the shock-bubble system dynamics may safely be conducted using the ($S_{Lsep}^{(c)} = 0.86$)-filtered data only. Indeed, no new modes nor important changes in the energetic content appear with the increase of $S_{Lsep}^{(c)}$ from 0.86 to 1.72 or 6.86.

Figure 5.3 (a) presents the energy in the leading POD modes for a wide range of wavenumbers extracted from the entire domain. It shows that a mode at $m = 1$ dominates the flow, and other modes display decreasing yet significant amounts of energy for higher wavenumbers. As known from previous numerical results (Cao et al., 2021; Hildebrand et al., 2018; Sidharth et al., 2018), some bubble modes are linked to strong fluctuations in the reattachment region. To assess whether the modes relate to such reattachment dynamics, one may analyze how the POD modes are affected when the POD is bounded to the region upstream from the reattachment point ($x/L < 1.11$). Figure 5.3 (b) presents the energy of the leading POD modes for each wavenumber when such a spatial restriction is applied. When compared to figure 5.3 (a), one sees that only the energetic content of the ($m = 1$)-mode remains nearly unchanged by this spatial restriction. This observation hints that the dominant ($m = 1$)-mode is mainly localized before reattachment in the separated region, which can be confirmed by computing the alignment coefficients of the leading modes computed with and without spatial restriction. This coefficient is close to one (0.970), confirming that the dominant ($m = 1$)-mode from the full domain is the same as the dominant one for the domain upstream of reattachment. The dynamics of this mode being mainly present in the separated region, it will be called mode B (bubble).

For higher wavenumbers ($m > 1$), the energy level of the dominant modes drastically decreases when switching from the spatially unbounded POD to the spatially bounded one, showing that their dynamics differs from mode B. Their energy content is mainly localized in the reattachment

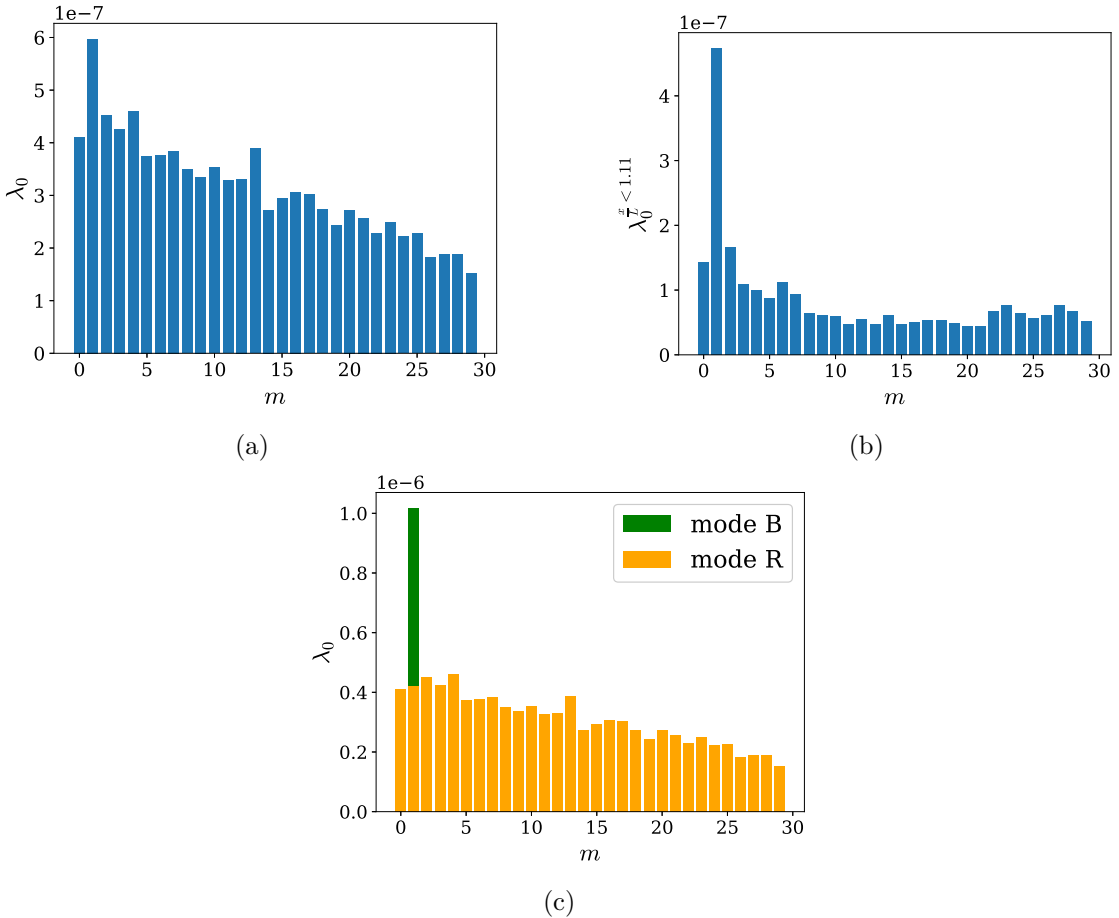


Figure 5.3: Energy contained in the leading POD mode. (a): when the optimization is conducted on the full domain, (b): restrained on the region upstream from the reattachment point. (c): for the full domain but showing the contribution of the two most energetic modes for $m = 1$.

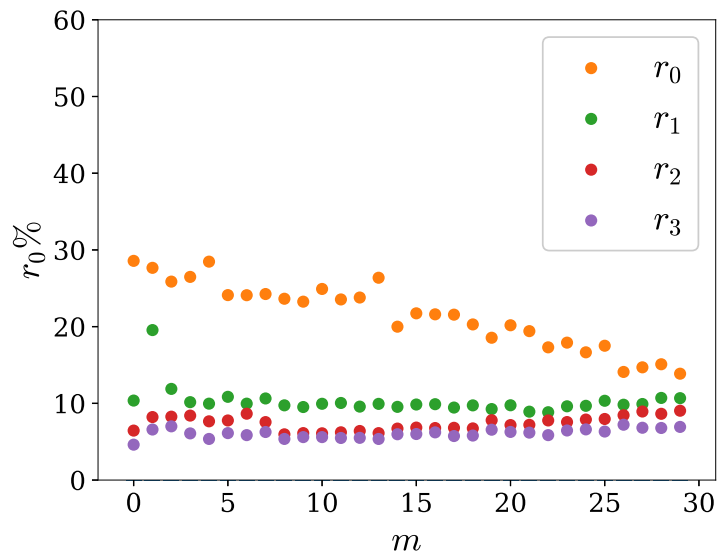


Figure 5.4: Percentage of energy contained in the first 4 POD modes against the wavenumber (POD modes computed from the full domain).

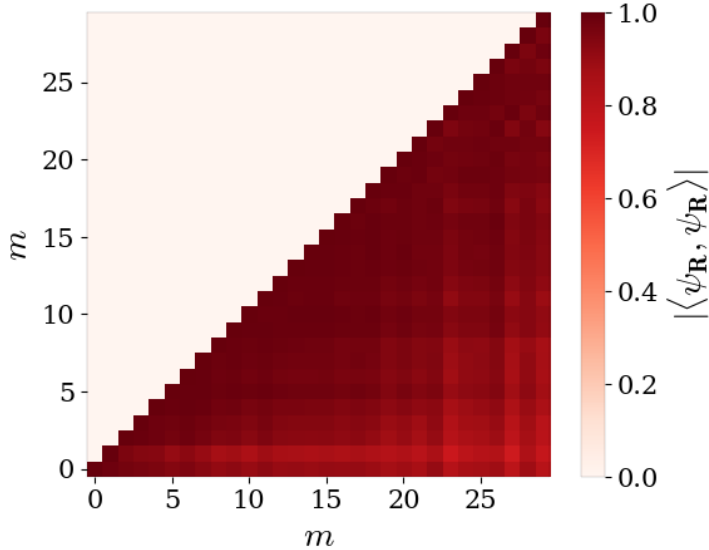


Figure 5.5: Alignment coefficient between the POD modes identified as mode R for different wavenumbers. Due to the symmetry $|\langle \Psi_R^{m=a}, \Psi_R^{m=b} \rangle| = |\langle \Psi_R^{m=b}, \Psi_R^{m=a} \rangle|$, only half of the map is displayed.

region, explaining the drop of energy when only considering the region $x/L < 1.11$. Moreover, apart from their azimuthal periodicity, all these ($m > 1$)-modes are extremely similar. This statement may be assessed by computing alignment coefficient between $\Psi_0^{(m)}$ and $\Psi_0^{(m')}$ for different wavenumbers $m > 1$ and $m' > 1$. An alignment coefficient matrix is presented in figure 5.5. The close-to-one value in the whole matrix confirms that all the modes have a very similar spatial organization in the (x, r) domain; they are all linked with the same physics. As such, these modes belong to a common group called modes R (reattachment) in the following.

On a side note, one has to be careful when interpreting the results at wavenumbers higher than 22 since the azimuthal filter starts to significantly affect their energetic content (see the characteristics of the azimuthal filter presented in figure 3.8 (b)). This is true for all the figures presented in this section.

Nevertheless, the previously discussed figures only represent the energetic level of the leading POD mode and ignore the lower-ranked modes that may still significantly contribute to the dynamics. Figure 5.4 presents the percentage of energy contained by the four dominant POD modes for each wavenumber. Overall, there is a clear separation between the leading POD mode and lesser-ranked modes for all wavenumbers except $m = 1$, where the second mode also contains significant level of energy (it contains more than 22% of the energy at $m = 1$ while it is less than 10% for most of the higher wavenumber). This second POD mode at $m = 1$ aligns well with other R-modes at higher wavenumber (see figure 5.5), indicating the coexistence of mode B and R at $m = 1$. At higher wavenumbers, the flow is clearly dominated by a single mode, identified as mode R. Lesser rank modes are clustered to significantly lower energetic level and are therefore not studied here. To summarize those findings, the energetic content of modes B and R against wavenumber is presented in figure 5.3 (c).

Figure 5.6 presents the spatial shape of modes R and B. Mode B displays strong field variations in the separation shock and mixing layer. Then, the interpretation of its energetic content is not straightforward: the displacement of the shock causes a strong variation in most of the fields because of both the amplitude of the motion, which is a feature of the mode, and the jump relation across the shock, which is not. Thus, the energetic content of the mode may not be fully attributed to its dynamic and is somewhat difficult to compare with the one of other modes.

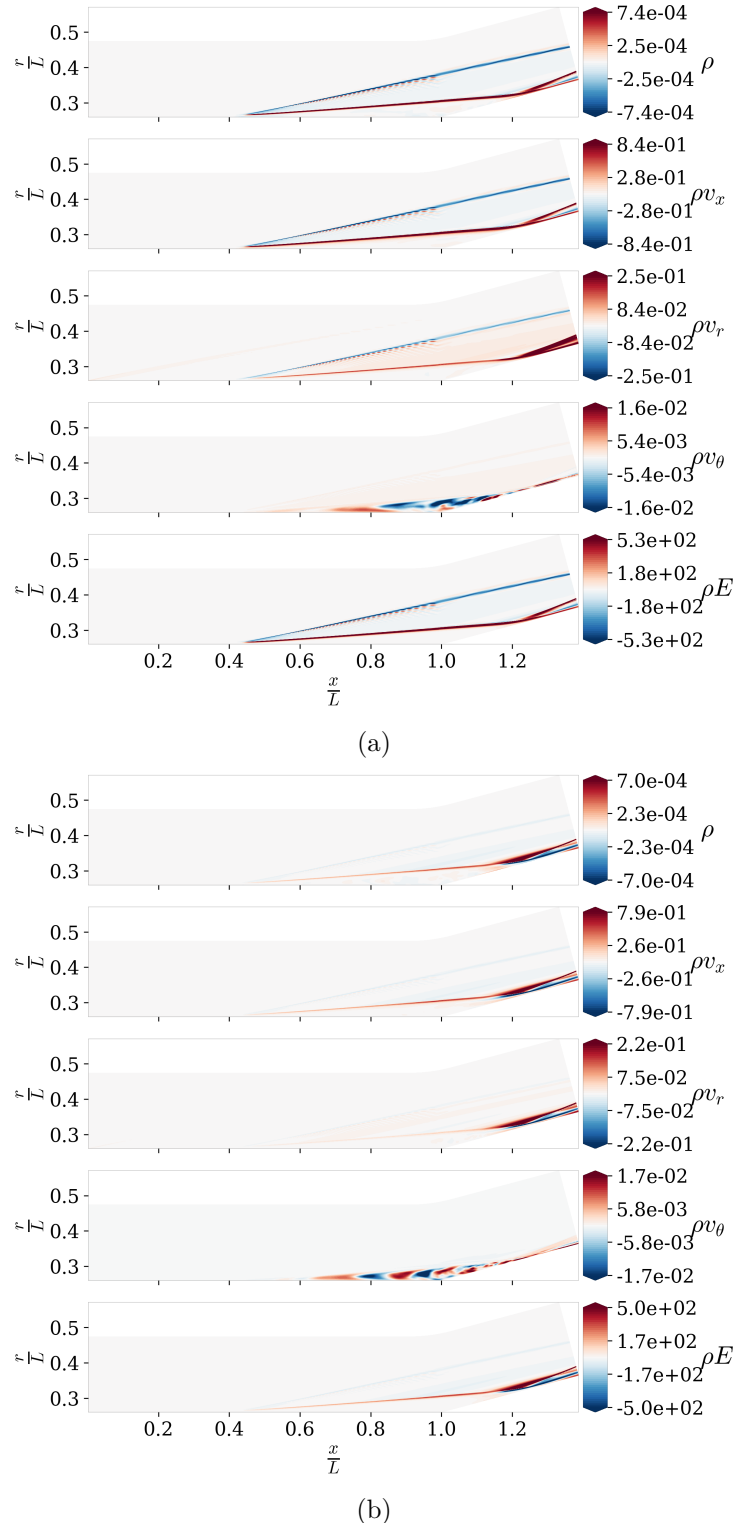


Figure 5.6: (a): leading POD mode at $m = 1$, the mode corresponds to the identified mode B, (b): second-ranked POD mode at $m = 1$, the mode corresponds to the identified mode R. The modes are extracted from the full domain.

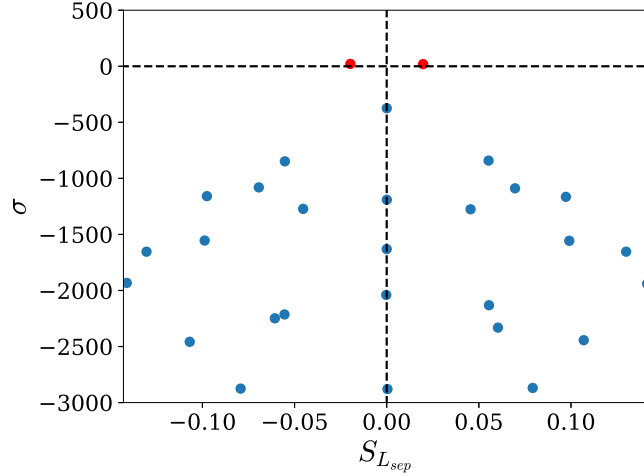


Figure 5.7: Eigenvalues of the linearized operator for $m = 1$, the red dots are the two conjugate eigenvalues linked with mode B.

Note that since the modes are computed by solving an eigenvalue problem, they are defined up to a complex multiplicative constant, and therefore their phase is arbitrary. The spatial shape of the modes confirms the results obtained from figure 5.3: mode B is located mainly in the mixing layer and the separation shock, while mode R is strong in the reattachment region (even if it is still present in the recirculation region, mostly for ρv_θ).

In the present study, the main drawback of this POD-based analysis is that it provides very little information on the temporal frequency (which is only known to be lower than $S_{sep} = 0.86$). It is impossible to assess if the modes are steady or not. If they oscillate, their frequency is likely too low to be properly characterized from the available high-fidelity data. It is worthy to note that this is not a drawback of the POD method itself, but a limitation stemming from the available data of the present study. The physical time that has been computed is too short with regard to the mode frequency to allow for a correct interpretation of the temporal evolution of the mode.

Fortunately, one may obtain that information from the linearized Navier-Stokes operator. As discussed in section 3.3.1, and supposing that modes R and B are self-sustained (*i.e.* absolute) instabilities of the flow, the operator should display eigenmodes whose spatial structure would match that of the POD modes. Once such modes are found, the stability analysis directly provides their frequency. As said in section 3.3.1, the modes are likely to have a growth rate near zero (but they can be stable or unstable). Therefore, we focus on the least stable/unstable modes in the following.

5.2.2 Spatio-temporal characterization of mode B

This section aims at characterizing the dynamics of mode B by analyzing the linearized Navier-Stokes operator about the mean flow. The study will be conducted for $m = 1$. As explained in section 3.3.1, if mode B is a self-sustained instability of the flow, the stability eigenspectrum should display a mode with a near-zero growth rate and a spatial structure matching that of figure 5.6 (a). Then, the results of the stability analysis should provide information about the temporal behavior of this unsteadiness.

Figure 5.7 presents the eigenspectrum of the linearized operator for $m = 1$, showing a marginally unstable unsteady mode (and its complex conjugate). We will show that this mode corresponds to mode B identified previously. The mode pulsates at $S_{L_{sep}} = 0.019$ (110Hz). This result should, however, be taken with caution, as the averaging time of the mean flow used for this

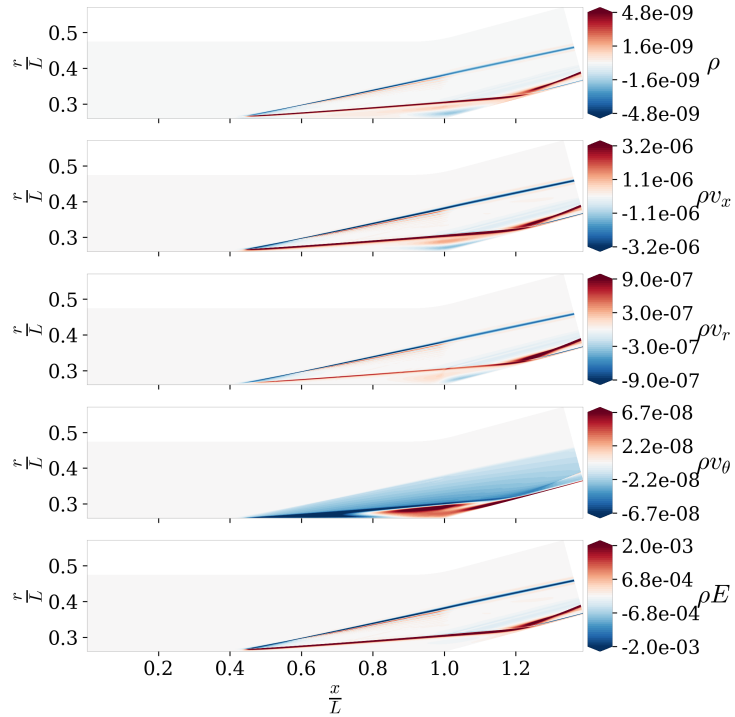
stability analysis is of the same order of magnitude than the pulsation of the mode. In the following, we still investigate the physics of the mode, as interesting parallel can be made with the existing literature. A parallel can already be made here with the reviews of Clemens and Narayanaswamy (2014) and Piponnai et al. (2009) for shock wave-turbulent boundary layer interaction. The Strouhal numbers in those reviews are very close to the one found here: they report a value $S_{L_{sep}} = 0.025$ for a Mach 5 compression ramp point, and for high-supersonic interactions (Mach 3), a range from 0.02 to 0.05 (Clemens and Narayanaswamy, 2014). Values around $S_{L_{sep}} = 0.03$ seem to be typical for shock unsteadiness in turbulent SBLI (Nichols et al., 2017; Piponnai et al., 2009; Touber and Sandham, 2009). Regarding mode B, this may point toward a common phenomenon between the present paper and these previous studies. Piponnai et al. (2009) and Wu and Martín (2008) have proposed a physical scenario that drives the shock unsteadiness for shock wave-turbulent boundary layer interactions. This scenario involves a self-sustained instability driven by the advection of mass from the bubble by the mixing layer, which is then replenished at a much slower time-scale in the reattachment region. This mode is also documented to create a bubble breathing (expansion/contraction motion) where the separation and reattachment points move in opposite directions Clemens and Narayanaswamy, 2014.

However, the consistency between the Strouhal number from Clemens and Narayanaswamy (2014), Piponnai et al. (2009), and the present numerical study may appear somewhat surprising since shock-turbulent BL interaction and shock-transitional BL interactions lead to entirely different bubble aspect ratios, especially for the recirculation length. Despite these drastically different conditions, the characteristic time of the unsteadiness scales with the bubble length, which confirms that L_{sep} is indeed the correct length scale involved in the physical mechanism at play. Explanations on this good match, despite the very different nature of the flow, are provided in section 5.2.3.

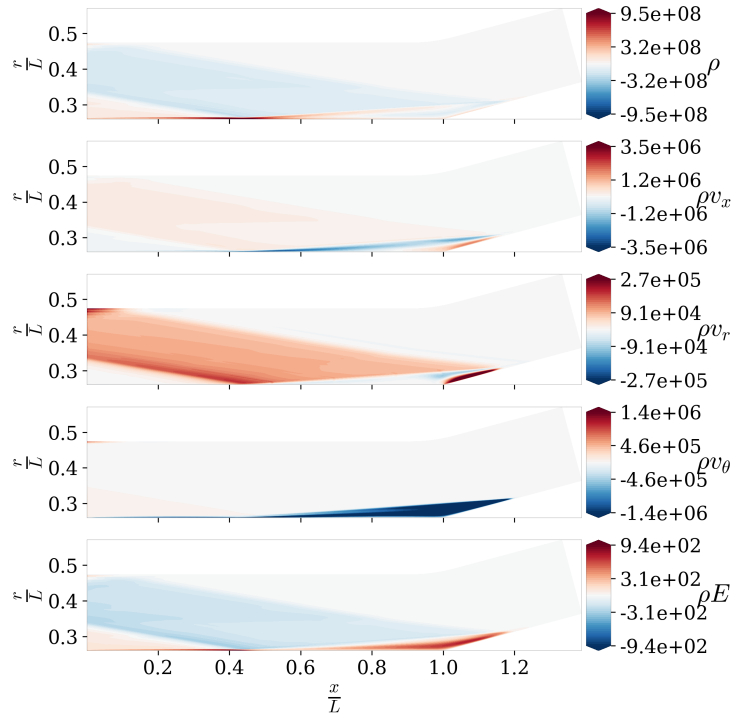
Figure 5.8 presents both the direct and adjoint mode linked to the marginally unstable eigenvalue. The direct mode can be compared to the dominant POD mode at $m = 1$ (see figure 5.6 (a)) to see that their spatial structure is very similar. The modes are mainly present in the separation shock, the mixing layer and the reattachment region, the separation shock being in phase opposition compared to the mixing layer and reattachment. The agreement with mode B is confirmed by the value of the alignment coefficient between the POD and stability mode (see equation ((5.1))) restricted to the relevant zone (*i.e.*, the bubble upstream of the reattachment, here $0.4 < \frac{x}{L} < 1.11$). Here, the value obtained is 0.91. This good alignment confirms the link between the stability mode and the POD mode. Then, the adjoint mode represents the optimal perturbation that would excite mode B. In the following, it will be used to compute the wavemaker, *i.e.* the spatial zones responsible for the unsteadiness, through a structural sensitivity analysis (Luchini et al., 2009).

Figure 5.9 presents the near-wall signature of the unstable mode B (at $m = 1$). It shows that the induced deformation of the separation and reattachment lines (obtained by superimposing the mode to the base flow) are in opposed directions, such that the mode corresponds to a "breathing" of the bubble. This is further illustrated by figure 5.10, which presents the temporal evolution of the separation and reattachment locations for a given azimuthal position, and shows that the bubble is successively expanding and shrinking. This result is reminiscent of the work of Nichols et al. (2017), who already established a link between the "breathing" motion of the recirculation region and a global stability mode for turbulent SBLI through a mean flow stability analysis conducted on LES data.

The streamlines from figure 5.9 also shows that the mode is responsible for fluxes of mass in and out of the bubble near the reattachment point. There are also signs that the separation and reattachment line undulations are linked with streamwise momentum benefit or deficit, pushing them upstream or downstream depending on the position. When animated in time, mode B is found to be rotating in the azimuthal direction.



(a)



(b)

Figure 5.8: (a): Unstable mode (eigenvector) linked with the marginally unstable eigenvalue at $m = 1$ for the direct operator. (b): same figure as (a) but for the adjoint operator.

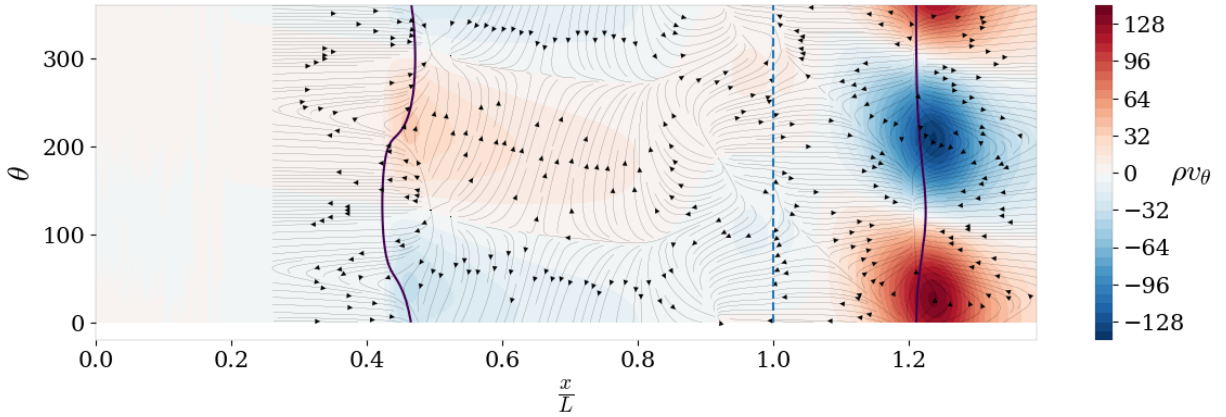


Figure 5.9: Impact of the mode B at $m = 1$ on the limit of the recirculation region (black line), azimuthal momentum (colormap) and unstable mode streamlines (arrows) in the first cell above the wall. The dashed line represents the limit between the cylinder and the flare.

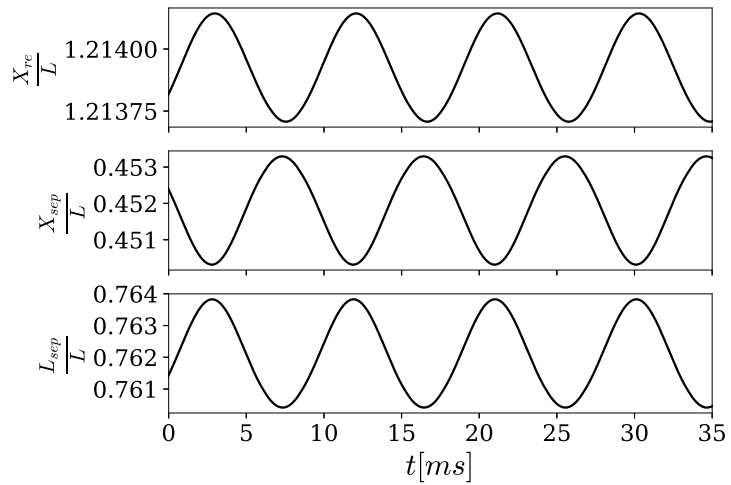


Figure 5.10: Temporal evolution of the reattachment position (up), separation position (middle) and separation length (down) for a given azimuthal position. The amplitude and phase of the mode are coherent between the sub-figures but are arbitrary.

5.2.3 Physical mechanism driving mode B

The previous stability results point to a physical scenario for mode B that is somewhat comparable to that of Piponnai et al. (2009), where the mixing layer advects information downstream, and the bubble advects information upstream in the near-wall region at a slower rate. The structural sensitivity of the mode (see section 3.3.1) provides insights on the underlying physical mechanism by revealing the locations responsible for the instability (*i.e.* the wavemaker). Figure 5.11 shows that the mode displays high sensitivity values in the mixing layer, in the near-wall region, near the separation point, and in the shock. On the contrary, the sensitivity values are low near the reattachment point. Interestingly, the local sensitivity maxima clearly draw a loop in the recirculation region, which follows streamlines of the mean flow. This loop is highlighted in figure 5.11 by a blue path of arrows for the downstream convection by the mixing layer, and a red path of arrows for the near-wall upstream convection by the recirculation region. The travel time of the fluid along the loop is approximately 4.4ms (0.2 ms for the blue path, 4.2ms for the red path), corresponding to a dimensionless frequency of $S_{L_{sep}} = 0.039$. As such, the temporal period of the mode corresponds almost exactly to twice the time for the flow to go through this loop.

In the following, we propose a hypothetical instability scenario that may explain the factor 2 between the recirculating time and the period of the mode. First, let us start from an infinitesimal oscillating perturbation in the separation region (as it is the most sensitive region) at a frequency of $S_{L_{sep}} = 0.019$. Let us assume, for instance, that this disturbance is initiated by an upstream motion of the separation shock. Due to this motion, the boundary layer separation occurs earlier along the body, causing an increase in the separation length. In addition to that, the separation angle, defined as the angle between the dividing streamline and the cylinder at the separation point (see figure 5.12), increases as shown in figure 5.13. Thus, the separation shock becomes stronger, causing an increase in the adverse pressure gradient, making the separation of the boundary-layer stronger. This change in separation length and strength causes the bubble to be oversized compared to its equilibrium size (the mean separation size). The timescale associated with this change of flow topology corresponds to the advection time along the blue downstream path (*i.e.* 0.2ms).

As proposed by Piponnai et al. (2009), the change in recirculation bubble topology leads to a change in upstream mass flow from the reattachment region to sustain the mean separation size. However, in the present case, the initial change in topology is not caused by the vortex shedding in the mixing layer (as it is still laminar) but by a motion of the shock. From Piponnai et al. (2009), a physical hypothesis for the change in incoming mass flux in the reattachment region is linked with the flapping of the mixing layer. An analogy could be made here by looking at the impact of the mode on the reattachment angle α_{re} between the dividing streamline and the flare at the reattachment point (see figure 5.12). One may expect that when the mixing layer impacts the flare with a lower reattachment angle, more flow is directed downstream towards the reattachment region and less flow is recirculated upstream (in the extreme case where this angle is null, all the flow goes downstream). As shown in figure 5.13, the reattachment angle indeed varies with the size of the bubble.

Therefore, one may propose the following instability scenario. When the bubble size increases, the reattachment angle decreases. Consequently, a deficit in upstream mass flow appears near the reattachment, which is eventually convected up to the separation point along the red path. Given the 4.2ms travel time along this path, the mass flow deficit reaches the separation point after half a period of the initial oscillation, during the downstream-motion phase of the shock. This reinforces the motion of the initial disturbance by pulling the shock even further downstream. The same holds for an initial downstream motion of the shock, except that it leads to a shrinking of the bubble, an increase in the reattachment angle and a mass surplus going upstream. This process will then continuously amplify the motion of the separation point until non-linear saturation stops it.

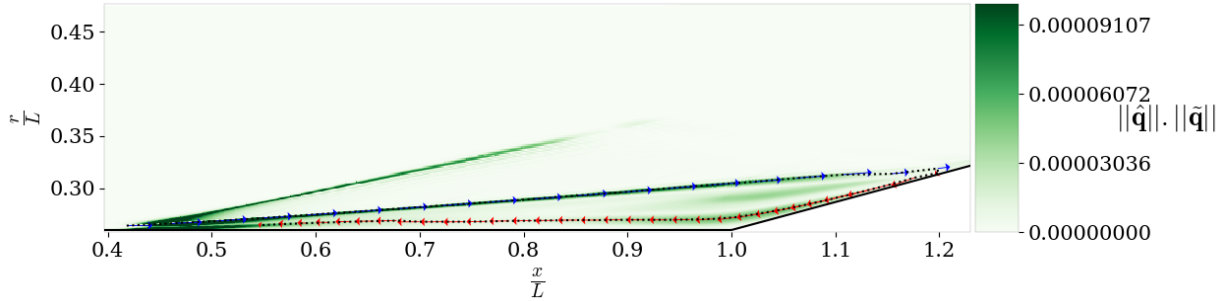


Figure 5.11: Structural sensitivity of mode B for $m = 1$ along with the two information paths for the global mode deduced from local maxima of the structural sensitivity. Velocity vectors are represented along these paths (the arrows have different scales for the upper and lower paths), showing that the paths follows local mean trajectories of the flow.

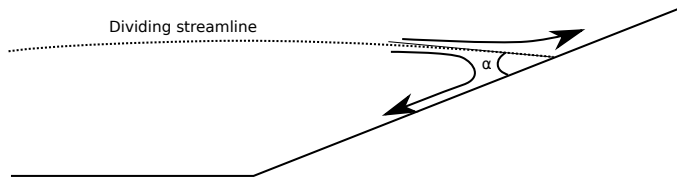


Figure 5.12: Schematic showing the definition of the reattachment angle.

Several links exist between this hypothetical scenario and observations of Debièvre and Dupont (2009), who experimentally studied the dynamics of a separated turbulent SBLI. First, they noted a phase shift of π (*i.e.* half a period) between the pressure signal in the shock foot and the reattachment region, which is also the case in our scenario since an upstream motion of the separation shock causes an increase and decrease in pressure at separation and reattachment, respectively, because of the smaller reattachment angle. This out-of-phase relationship between the separation and reattachment region is also described in the work of Agostini et al. (2015). They also reported a negligible time delay between the shock motion and the bubble motion compared to the "shock timescale". In the present scenario, while this delay is not "faster than an acoustic propagation or convection in the streamwise direction" as they propose, the downstream advection time is still less than a twentieth of the mode period. They also documented the absence of correlation of the shock motion with upstream perturbations coming from the boundary layer, which is supported in the present study by the negligible structural sensitivity values in the boundary layer.

It is important to highlight that, contrary to what most of the existing papers propose, this bubble instability appears inherently three-dimensional as there are no marginally stable nor unstable modes corresponding to mode B in the linearized operator spectrum for $m = 0$. Two hypotheses can be made to explain this three-dimensionality. First, the three-dimensionality of the perturbation may be a condition on its unsteadiness (and thus on its self-sustainability): as soon as the shock perturbation is 3D, there is an azimuthal unbalance in the pressure distribution, leading to an azimuthal motion of the separation shock perturbation. Then, the azimuthal travel of the shock-wave perturbation just has to synchronize with the bubble retro-action (*i.e.* to be of period T) to yield amplification of the shock motion. A second possibility is that the unstable mode may require mass transfer inside the bubble to exist. It could be a reason why this instability does not exist for $m = 0$, where no azimuthal mass transfer would be possible. However, further work is required to conclude whether this instability could exist in a two-dimensional form.

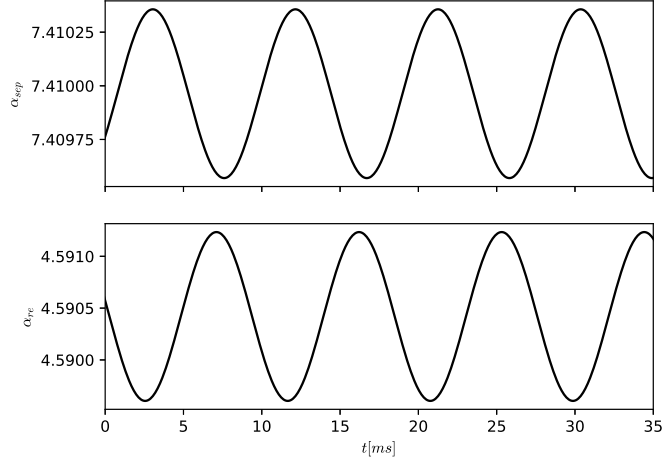


Figure 5.13: Temporal evolution of the separation angle α_{sep} in degrees (up) and the reattachment angle α_{re} in degrees (down), which is defined as the angle between the dividing streamline and flare at the reattachment point computed from the superposition of the mode to the mean flow. The amplitude and phase of the mode are coherent between the sub-figures and with figure 5.10 but are arbitrary.

5.2.4 Spatio-temporal characterization of mode R

This section aims at using a global stability analysis to characterize the mode identified as mode R. It focuses on $m = 5$ to discuss the results, since it is one of the wavenumbers where a mode of type R strongly dominates the dynamics. But the observations/conclusions below hold for all wavenumbers for $m \in [4, 17]$. The existence of mode R for $m < 4$ and $m > 17$ is discussed in section 5.2.5.

Figure 5.14 (a) presents the eigenspectrum of the linearized operator for $m = 5$. Contrary to the spectrum for $m = 1$, there is neither unstable nor marginally stable pair of unsteady eigenvalues. Instead, there are two eigenvalues near the real axis, both quasi-steady, one displayed as a red dot and the other shown as a green dot. They will be called in the following mode R-1 and mode R-2, respectively.

A priori, mode R could stem from both of those eigenvalues. However, a study of their spatial structure shows that they significantly differ from the POD mode: the alignment coefficients with the POD mode in the full domain are 0.15 and 0.32 for R-1 and R-2 eigenmodes, respectively. Figures 5.15 and 5.16 illustrates these differences by comparing the spatial shape of the eigenmodes to the POD mode. Even if figures 5.15 (a) and (b) show that both modes R-1 and R-2 are mainly present in the reattachment region, there are still some significant discrepancies between them and the POD mode, especially for the fluctuations inside the bubble, which strongly differs.

A hypothesis could then be that these two stability modes are present in the simulation and that the POD mode is the result of their interaction. A way to check this assumption is to investigate the low-amplitude region of the modes. In this region (*i.e.* in the recirculation region), non-linear interactions of the stability modes should be weak, such that the resulting mode R should appear as a linear combination of modes R-1 and R-2. However, this is not true in the reattachment region, since non-linear terms will dominate this high-amplitude region. To confirm that hypothesis, one can check if the POD mode belongs to the linear span of the two stability modes. This may be done by using a least-square method to find the best linear combination of R-1 and R-2 modes matching the POD mode in the recirculation region ($0.4 < \frac{x}{L} < 1.11$):

$$(\alpha, \beta) = \text{argmin}(\|\alpha \hat{q}_{R-1} + \beta \hat{q}_{R-2} - \Psi\|), \quad (5.2)$$

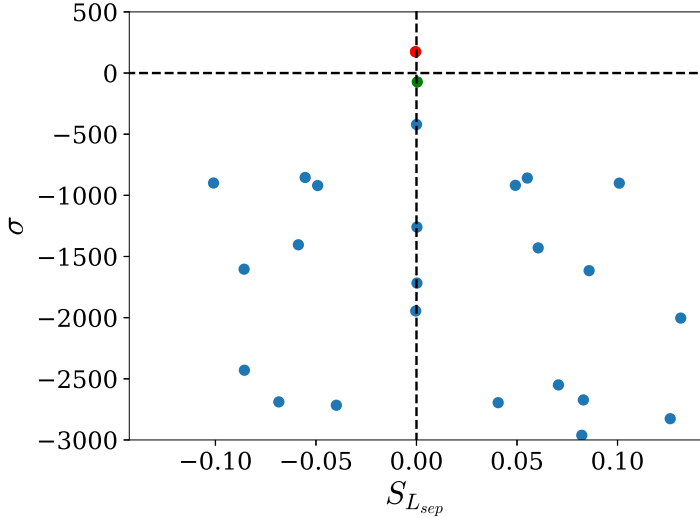


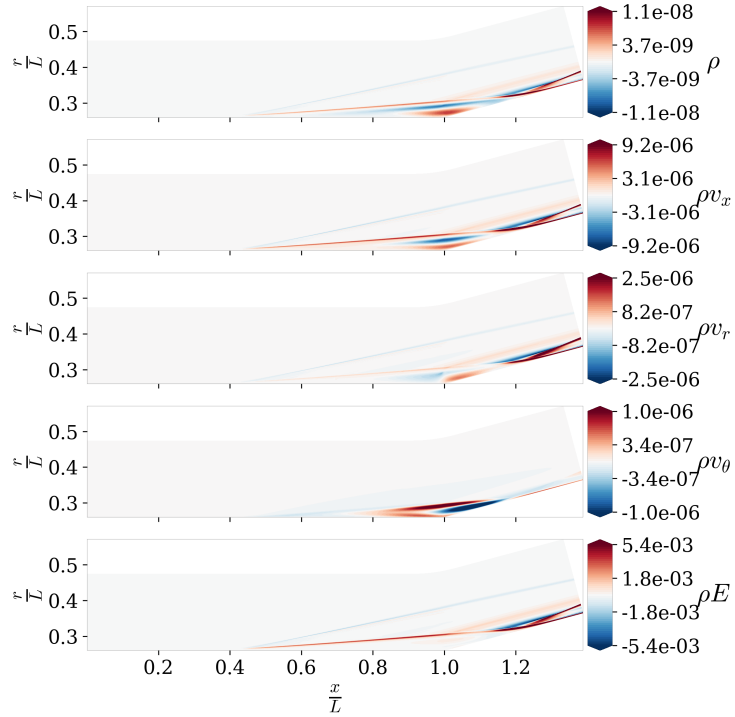
Figure 5.14: Eigenvalues of the linearized operator for $m = 5$, the red and green dot are the eigenvalues linked with mode R (R-1 and R-2 respectively).

this optimized combination $\hat{q}_{R-1+R-2} = \alpha\hat{q}_{R-1} + \beta\hat{q}_{R-2}$ has an alignment coefficient (see equation (5.1)) with the POD mode of 0.95 (against 0.62 for mode R-1 alone and 0.2 for mode R-2 alone). This means that while the POD mode is not aligned with either of the stability modes, it belongs to the subspace spanned by these two modes. This confirms that mode R is due to the interaction of the linear global modes R-1 and R-2.

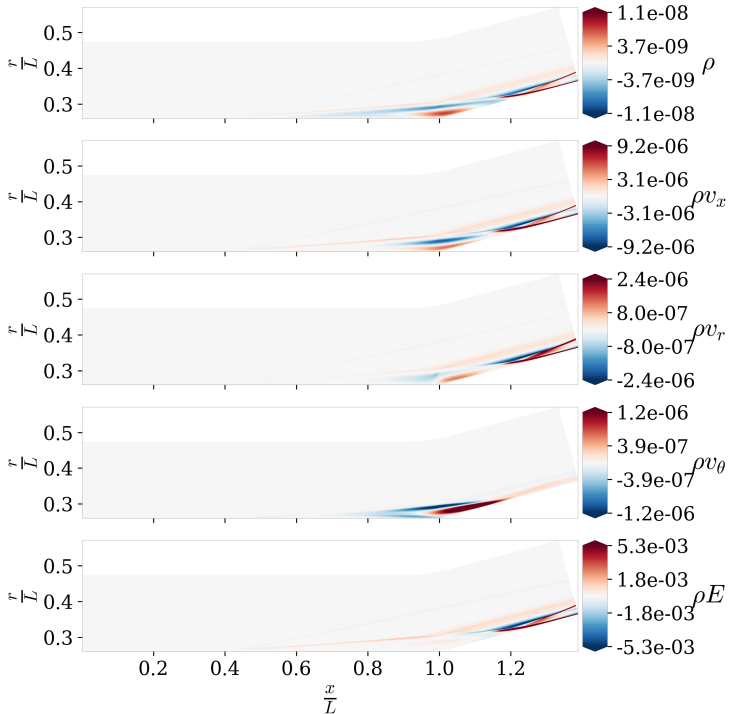
5.2.5 Physical mechanism driving mode R

Now that mode R is characterized as a quasi-steady mode due to the interaction of two global instabilities, the question of its physical origin remains. Figure 5.18 presents the evolution of the growth rate and frequency of mode R-1 and R-2 against the wavenumber. For R-1, it shows a destabilization (increase in growth rate) of the mode for increasing wavenumbers up to 10, followed by a growth rate decrease. While keeping in mind the limitations of the interpretation of the growth rate that were mentioned in section 3.3.1, it is still interesting to note that an extremely similar quasi-steady unstable branch is already documented in the literature (albeit for a base flow stability analysis) Hildebrand et al., 2018; Sidharth et al., 2018. The present study confirms that this mode exists in transitional flows and can be found by a mean flow stability analysis. The behavior of mode R-2 mirrors that of mode R-1, with first a decrease in growth rate until $m = 13$ then an increase until $m = 17$. It is interesting to point out that the frequency of both mode R-1 and R-2 are equal at every wavenumber and is slightly increasing with wavenumber, indicating that they may relate to a similar physical mechanism. It is also worth mentioning that while mode R-2 has a negative growth rate, it is almost always closer to the real axis than mode R-1. Therefore, it has no reason to be less relevant (see section 3.3.1). Both of the branches disappear for wavenumbers $m > 17$ and $m < 4$. The presence of mode R for $m < 4$ in the QDNS that was presented in section 5.2.1 cannot be explained by the linear growth and interaction of modes R-1 and R-2. Therefore, it may be due to the non-linear interaction of several of those modes at higher wavenumbers ($m > 4$) which can redistribute energy toward smaller wavenumbers. The same holds for $m > 17$.

Let us now discuss the mechanism leading to the self-sustained instability proposed by Hildebrand et al. Hildebrand et al., 2018, which may be relevant for R-1 and R-2 modes. Their scenario relies on the apparition of streamwise vortices in the separated region, which then creates a spanwise undulation in the reattachment line (through the redistribution of streamwise momentum). Because of the feedback through the recirculation region, this undulation leads to the apparition



(a)



(b)

Figure 5.15: (a): Unstable mode R-1 (eigenvector) for the marginally unstable eigenvalue at $m = 5$. (b): Stable mode R-2 for the marginally stable eigenvalue at $m = 5$.

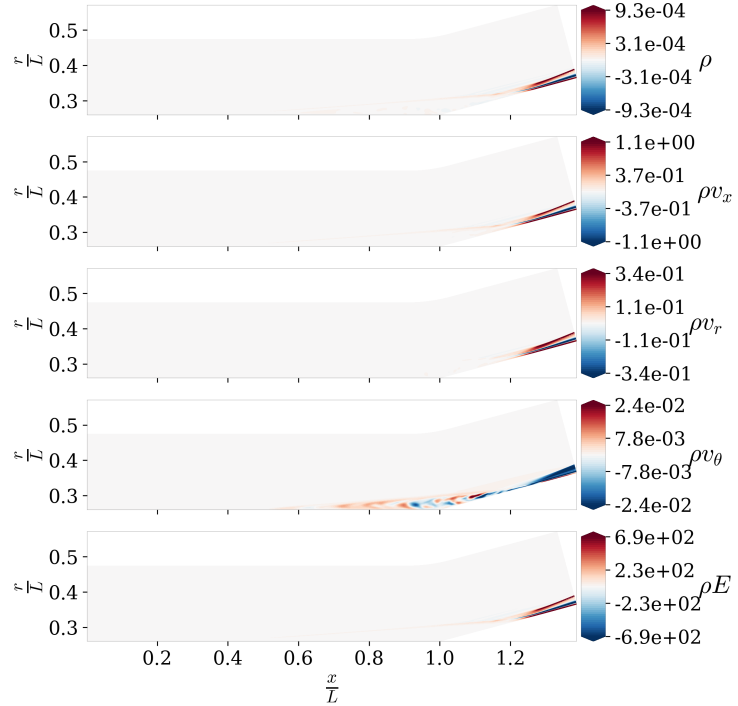


Figure 5.16: Leading POD mode at $m = 5$ extracted from the full domain.

of corrugation in the base of the separation shock. Then, this amplifies the streamwise vortices, closing the feedback loop of the global instability mechanism.

The results presented in figures 5.17 (a) and (b) show that this scenario is also happening here, not only for mode R-1, but also for mode R-2. Both modes display a parietal azimuthal (spanwise) momentum signature very close to that presented by Hildebrand *et al.* Hildebrand et al., 2018, reminiscent of the presence of streamwise vortices in the recirculation and reattachment region. Because of the near-wall streamwise momentum deficit induced by those vortices, the reattachment line undulates. This causes the corrugation of the separation line, leading to the amplification of the streamwise vortices. The fact that both mode R-1 and R-2 seem to be caused by the same underlying mechanism may explain the frequency similitude observed in figure 5.18.

5.2.6 Partial conclusions on the large scale dynamics

To conclude, two large-scale modes dominate the bubble dynamics: First, a quasi-steady mode (mode R) that causes a striation in the reattachment region and which stems from the interaction of two quasi-steady self-sustained modes, Then, an unsteady mode (mode B) that causes a breathing motion of the bubble, also linked to a global instability.

A scenario leading to a self-sustained instability has been discussed for both modes. The unsteady mode may correspond to the shock unsteadiness already documented in several shockwave-turbulent boundary layer interactions cases.

5.3 Impact of the bubble dynamics on the transition

The previous section has unveiled the low frequency, low wavenumber modes dominating the recirculation region. First, there is a scale separation between the previously discussed dynamics and the convective instabilities leading to transition. Thus, the hypothesis that the recirculation region modes are the cause for transition is unlikely. However, this scale separation does not

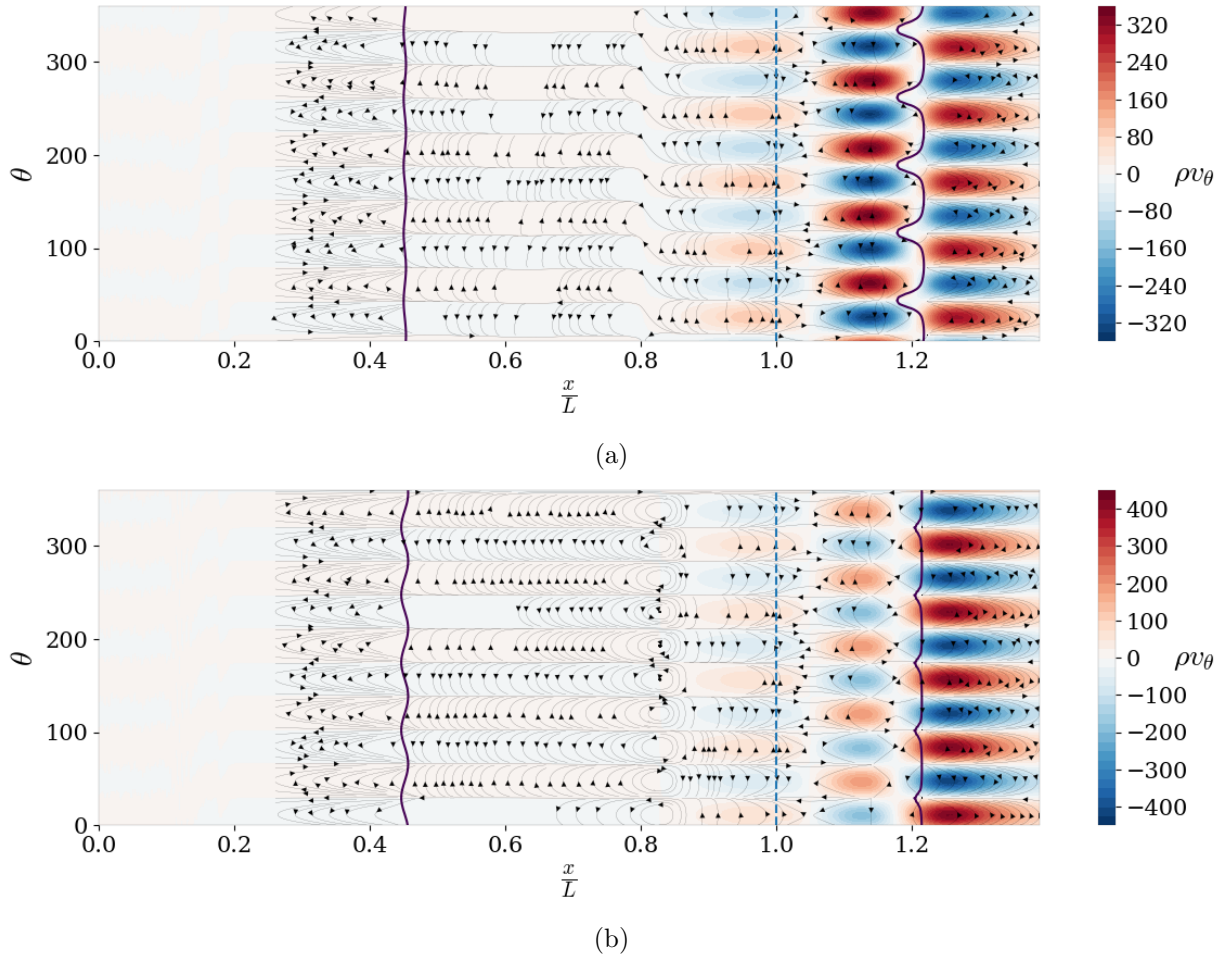


Figure 5.17: (a): Impact of the mode R-1 at $m = 5$ on the limit of the recirculation region (black line), azimuthal momentum (colormap) and mode streamlines (arrows) in the first cell above the wall. (b): same figure as (a) but for the mode R-2 at $m = 5$. The dashed line represents the limit between the cylinder and the flare.

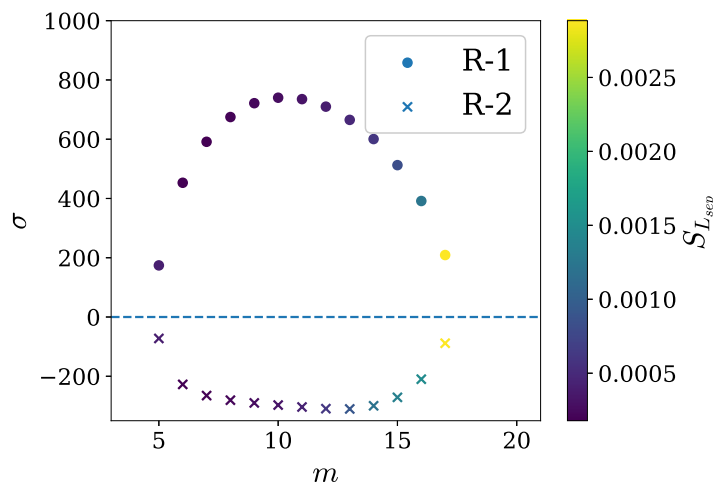


Figure 5.18: Evolution of the growth rate and frequency of mode R-1 (o) and R-2 (x) against wavenumber.

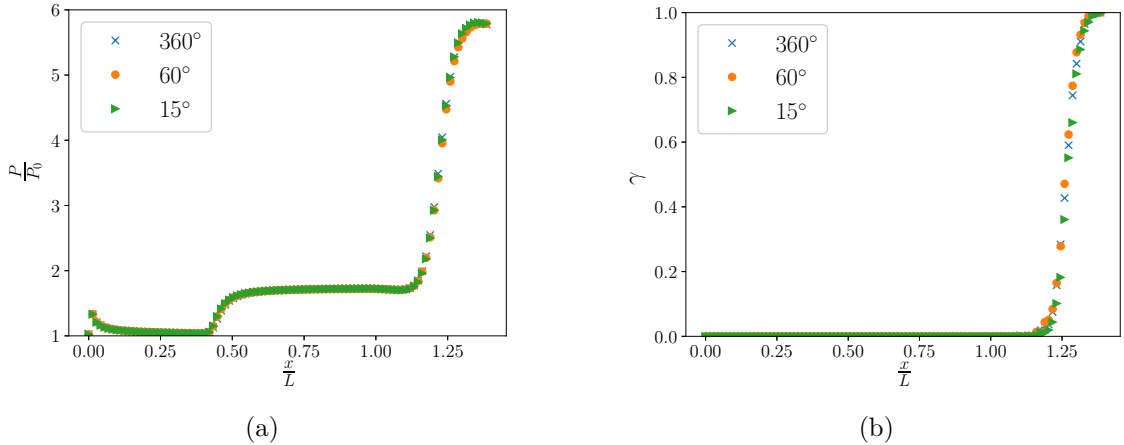


Figure 5.19: Mean wall pressure distribution (a) and intermittency function (b) for the 3 different azimuthal spans of the computational domain.

allow to conclude if the bubble dynamics has an impact on the transition through the modification of the mean flow, which may affect the linear amplification mechanisms of the convective instabilities.

The impact of the bubble dynamics on the transitional one can be assessed by comparing the three different simulations (QDNS A, B, and C, see table 3.2). As previously explained, the reduction of the domain azimuthal span leads to a periodic filtering of the wavenumbers that develop in the simulations. This yields three simulations containing different global modes. First, the full domain simulation (QDNS A) contains every mode. Thus, it serves as a reference to study the impact of those modes on the flow topology and convective instabilities. Then, the simulation on the 60 degrees domain (QDNS B) can only contain modes R, as modes of type B are energetic for low wavenumbers that are filtered by the span of the domain (modes of wavenumber smaller than six cannot develop). Finally, the 15-degrees-simulation (QDNS C) contains no unstable recirculation modes, since the smallest non-zero wavenumber that can develop is 24, effectively filtering mode B and mode R.

This section focuses on the difference of flow topology and transition caused by the presence, or absence, of the two unstable modes of the separated region.

First, and as presented through the wall pressure distribution in figure 5.19 (a), all three simulations predict the same mean-flow topology with no difference neither in the separation nor in the reattachment point location. This is an important result given the already discussed dependence of recirculation region length on the transition to turbulence, hinting that the suppression of the bubble modes has no impact on transition. This assumption can be confirmed by computing an intermittency function (see chapter 3). The intermittency distribution is displayed in figure 5.19 (b) for the three simulations. It confirms that the transition onset and the point where the flow reaches completely developed turbulence are the same for all cases.

To go further in the comparison between the three simulations, figure 5.20 presents wall pressure power spectral densities at different longitudinal locations; (a) is situated in the boundary layer, (b) and (c) in the separated region and (d) after the reattachment point. Those four figures give a good overview of the complete transitional dynamics of the flow. They all show that there is no noticeable difference between the three simulations. Without going into deeper details about the transition scenario of the flow, which is very similar to that presented at Mach 5 in the next chapter, mainly two different transitional instabilities can be spotted in figure 5.20 (a) and (b): a peak at frequencies around $S_{\delta_{sep}} = 0.4 - 0.5$ which is linked to second mode instabilities and another broad peak at lower frequencies (especially visible in figure 5.20 (b))

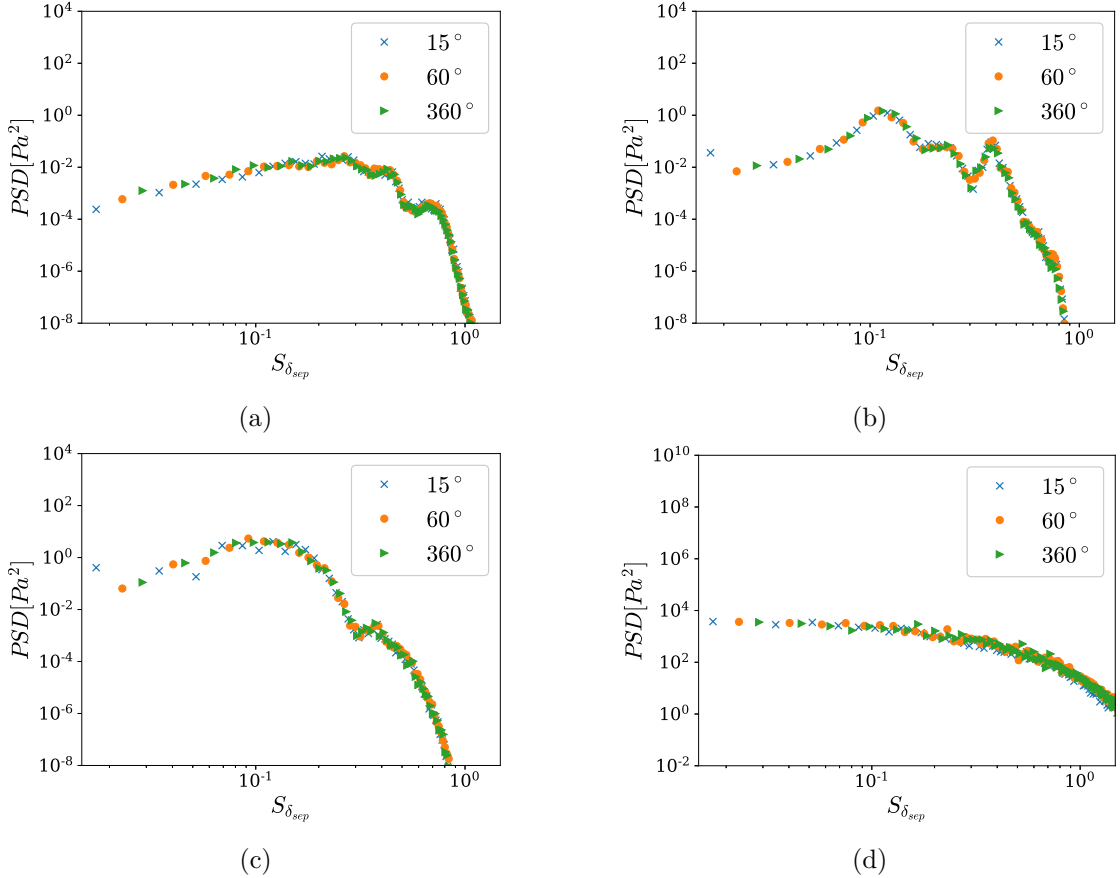


Figure 5.20: Pre-multiplied wall pressure power spectral density at station: boundary layer at $\frac{x}{L} = 0.28$ (a), separated region at $\frac{x}{L} = 0.56$ (b) and $\frac{x}{L} = 0.91$ (c), reattached region at $\frac{x}{L} = 1.33$ (d) for the 3 different azimuthal span of the computational domain.

which is linked to oblique first mode instabilities. Both of those instabilities have the same wall pressure fluctuation signature for all three QDNSs. Thus, they are completely unaffected by the bubble dynamics.

From the results presented in this section, one can conclude that the low-frequency/large-scale motion of the recirculation region, albeit present in this flow, has no impact on the transitional instabilities and the overall transition process. This also imply that transition scenario based on absolute instabilities of the bubble such as proposed by Cao et al. (2021) become irrelevant in cases with significant free-stream perturbations such as studied here. For that kind of flow, computation on reduced domains (at least down to 15 degrees) are fully able to predict the correct flow topology and high-frequency dynamics.

5.4 Conclusion

To conclude this chapter, the flow is found to be mainly dominated by two coexistent coherent modes. First, a quasi-steady one that mainly exists in the reattachment region. This mode is linked to an already documented scenario (Hildebrand et al., 2018) that relies on the apparition of streamwise vortices in the recirculation region, which are able to amplify themselves through the deformation of the bubble. Secondly, an unsteady mode that causes the breathing of the bubble through a back-and-forth motion of both the separation and reattachment points. A new self-sustained instability scenario for the shock unsteadiness has been proposed. This inherently three-dimensional scenario is linked with a feedback loop inside the recirculation bubble, with

information being convected downstream by the mixing layer and upstream by the near wall region of the recirculation region.

Then, the impact of the bubble dynamics on the transitional mechanism has been studied through two other QDNSs with spatial filtering of the bubble modes. Those simulations showed that the bubble dynamics has no impact on the transitional instabilities. This is an important result as it means that key design parameters such as heat-flux, transition onset and separation size can be accurately simulated on a reduced domain, leading to a significant decrease in the computational cost.

Chapter 6

Numerical study of the transition scenario

This chapter aims at drafting a dominant transition scenario in a Mach 5 compression ramp flow through the study of numerical simulations and resolvent analysis of the mean flow. A high-fidelity simulation at a free stream Mach number of 5 and a transitional Reynolds number is conducted. The inlet of the computational domain is perturbed with a white noise to excite convective instabilities. Coherent structures are extracted using Spectral Proper Orthogonal Decomposition (SPOD), which gives a mathematically optimal decomposition of spatio-temporally correlated structures within the flow. The mean flow is used to perform a resolvent analysis to study non-normal linear amplification mechanisms. The comparison between the resolvent analysis and the SPOD results provides insight on both the linear and non-linear mechanisms at play in the flow. To carry out the analysis, the flow is separated into three main regions of interest: the attached boundary layer, the mixing layer and the reattachment region. The content of this chapter largely come from a published article in the Journal of Fluid Mechanics (Lugrin et al., 2021b).

Contents

6.1	Introduction	100
6.1.1	Methodology for the study of subdomains	100
6.2	Study of the subdomains	103
6.2.1	Attached boundary layer	103
6.2.2	Mixing layer	108
6.2.3	Reattachment region	113
6.3	Transition scenario	117
6.4	Conclusion	119

6.1 Introduction

This chapter is dedicated to the study of the transitional mechanisms that develop in the studied configuration. It aims at drafting a general dominant scenario for low hypersonic SBLI on compression ramp.

Given the conclusion of chapter 5, the computations presented in this chapter are conducted on a reduced domain of 60° (Case E of table 3.2) to limit the computational cost of the study.

The chosen free stream conditions are presented in table 6.1 and correspond to an experimental study point. As this computation was performed before any experimental campaign, the chosen inlet perturbation involves a lower level of noise than the one in the R2ch blowdown facility, which corresponds to $A = 1.5\%$ and yields $L_{\text{sep}} \approx 0.5L$ (see figure 3.3). This is mainly because the available experimental results from Benay et al. (2006) only contain time-averaged data and do not bring any unsteady information on the dynamic of the flow that could be used for comparison. Also, reproducing the free-stream fluctuations from R2ch without any experimental data was too challenging at that time. Quantitative characterization of the white noise actually injected is given in figure 6.2: the red curve ($X = 0.028L$) displays the temporal spectrum of the wall pressure fluctuations a few millimeters downstream from the inlet, showing that the PSD is flat as expected.

To get an insight on the flow created by those conditions, an isosurface of the Q criterion ($Q = 9 \times 10^{-6} U^2 / \delta^2$) coupled to a numerical Schlieren visualization of one snapshot from the DNS is presented in figure 6.1. It shows the three main regions of interest of the study: the attached boundary layer upstream from the interaction, then the mixing layer between the separation shock and the reattachment point, and finally the reattachment region. It also shows that the transition point is located at the reattachment: the incoming boundary layer upstream of the interaction is laminar (incompressible shape factor around 2.7) when at reattachment, the incompressible shape factor is close to 1.5, characteristic of a turbulent boundary layer. Figure 6.1 qualitatively shows how the transition process is increasing in intensity as it goes through each studied zone, eventually creating turbulent structures on the flare. To confirm the assumption that the flow is transitioning at reattachment, figure 6.3 presents both the intermittency factor (see section 3.1.3) and the wall pressure distribution along the geometry. The results presented in figure 6.3 shows that the intermittency is strictly 0 in the whole attached boundary layer and really close to 0 for most of the separated region (which is characterised by the pressure plateau at $P/P_0 = 1.6$). In the final part of the mixing layer, the intermittency first slightly increases and then brutally reaches 1 at the reattachment (which is characterized by a steep increase in pressure). The goal of the chapter is then to understand what mechanisms are causing the flow to transition around the reattachment point and to draft a transition scenario.

This chapter will mainly focus on the interpretation of numerical and resolvent analysis results. In particular, the three regions of interest (attached boundary layer, mixing layer, and reattachment region) are studied in different subsections, following a methodology explained at the beginning of the next section. The results are then summarized in section 6.3, where we also provide an overall view of the proposed scenario for the transition process.

6.1.1 Methodology for the study of subdomains

In the next three sections, which correspond to the study of the subdomains of interest defined in section 6.1, the physical analysis follows the methodology below:

1. the flow structure is qualitatively discussed based on the observation of the instantaneous vortical structures within the flow, visualised with an isosurface of constant Q-criterion extracted from the QDNS,

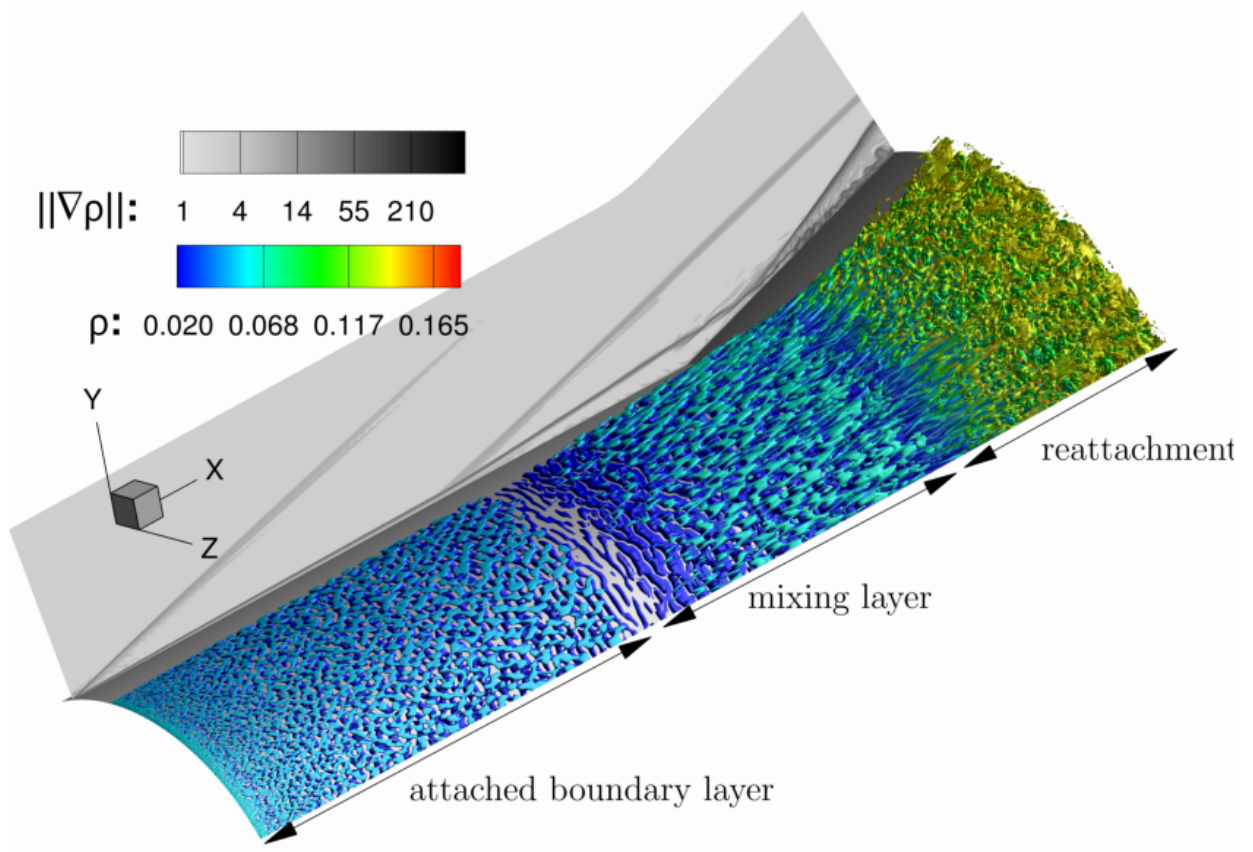


Figure 6.1: Isosurface of Q criterion ($Q = 9 \times 10^{-6} \frac{U^2}{\delta^2}$) coloured by density and numerical Schlieren visualisation for an instantaneous snapshot of the QDNS.

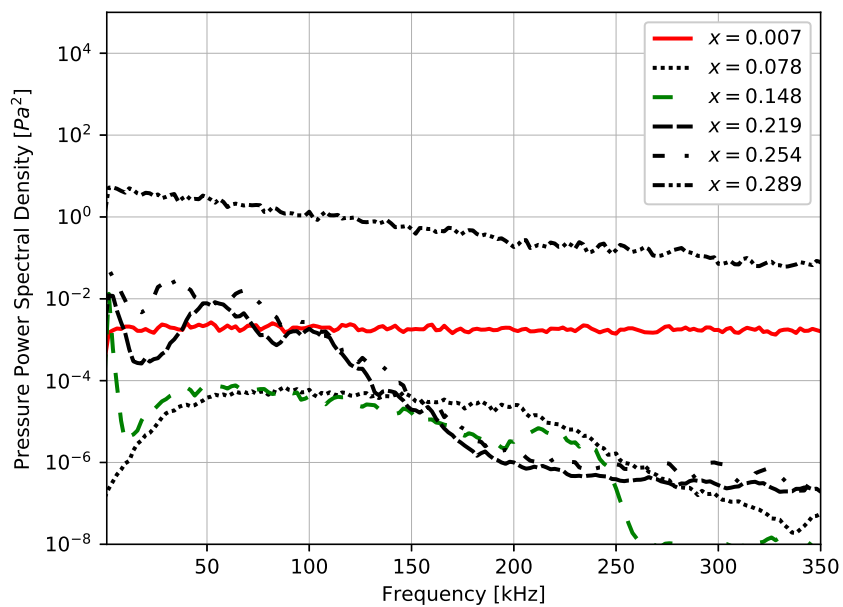


Figure 6.2: Power spectral density of wall pressure fluctuations at different longitudinal locations of the QDNS.

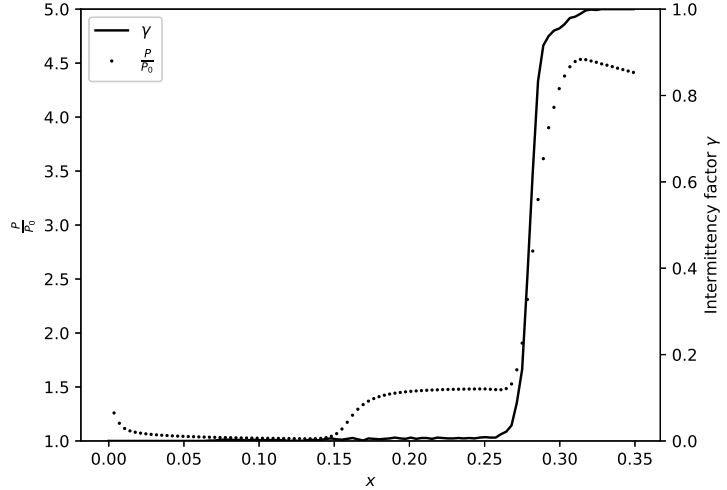


Figure 6.3: Intermittency factor and wall pressure distribution along the geometry showing that the transition is occurring near the reattachment point.

T_∞	86.6 K
M_∞	5
P_∞	1228 Pa
U_∞	933 m/s
T_{wall}	290 K
Re_θ	724
δ	1.975 mm
$\frac{\delta}{R}$	0.03
L_{sep}	129 mm

Table 6.1: Free-stream conditions and characteristic values for the simulation, the Reynolds numbers based on momentum thickness and displacement thickness are computed upstream of the separation point.

Grid size and resolution:	
n_x	353
n_r	102
n_θ	257
θ resolution	$\approx 0.23^\circ$
m resolution	6

Temporal sampling:	
Sampling rate	200kHz
Number of samples	1664
Number of samples in each realisation	128
Frequency resolution	1562.5Hz
N_r	26

Table 6.2: Numerical parameters for the SPOD.

2. the dynamics of the subdomain is quantitatively analysed through an energy map, as defined in section 3.2.3, giving the distribution of the fluctuation energy in the ω - m domain,
3. the structure of SPOD modes from the highest-energy parts of this map is discussed (see table 6.2, for the numerical parameters used for SPOD modes computation).
4. a resolvent analysis of the subdomain is carried out, and the results are compared to the SPOD analysis. In particular, the energy maps are compared to maps of μ_0^2 and c_0 to identify whether or not the high-energy structures result from a linear convective instability.

6.2 Study of the subdomains

6.2.1 Attached boundary layer

Boundary layer instabilities most likely play an important role in the transition process. For that reason, this section focuses on the attached boundary layer (*i.e.* the domain downstream of the interaction is discarded, focusing only on $X \in [0, 0.16]$ or $X/L \in [0, 0.63]$). This corresponds to the first of the three regions of interest defined in section 6.1.

First of all, a surface of constant Q-criterion extracted from the QDNS is presented in figure 6.4. The green cross-shaped patterns in the upper part of the boundary layer indicate that oblique first mode structures (both clockwise and counter-clockwise) are present. To a lesser extent, elongated azimuthal structures are also visible in the lower part of the boundary layer, which suggests the presence of second mode disturbances.

The fluctuation energy distribution in the (m, ω) domain presented in figure 6.5 confirms the importance of the first oblique modes. Energy linked to these structures is contained in the four diagonal branches of the diagram. They represent the majority of the fluctuation energy from the boundary layer.

Oblique modes appear on a wide range of frequencies (from 20kHz to up to 100kHz) and wavenumbers (from 20 up to 125) with peak amplification around $m = \pm 60$ and $f = \pm 40$ kHz. The broad-band nature of boundary layer instabilities shows that it was relevant to inject white noise rather than a specific forcing designed to focus on a given instability mode. It unveils the complexity of this flow, where a wide range of structures may develop, interact, and compete.

It is then interesting to look at the structure of the SPOD modes link to four of the most energetic (m, ω) -points associated with the four diagonal branches. As discussed in section 3.2.3, two points correspond to the same clockwise SPOD mode (m and ω of same sign) and the two others to

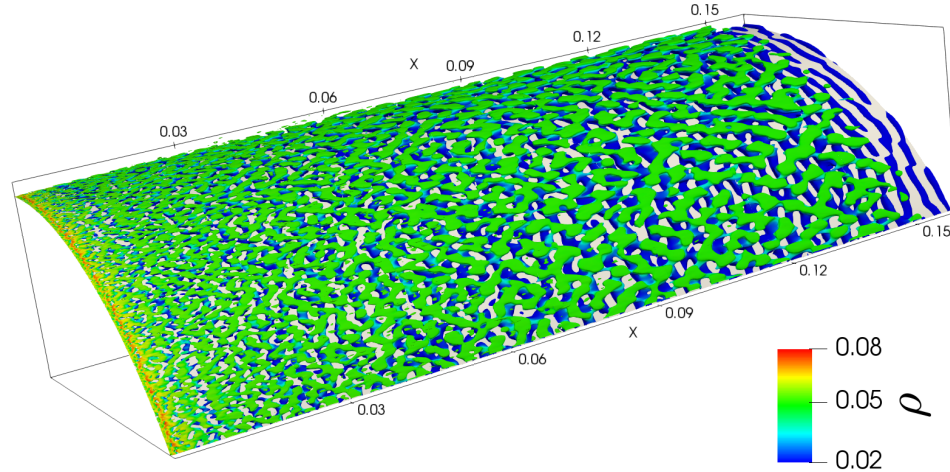


Figure 6.4: Isosurface of Q criterion ($Q = 2 \times 10^{-6}U^2/\delta^2$) coloured by density for the attached boundary layer from an instantaneous snapshot of the QDNS.

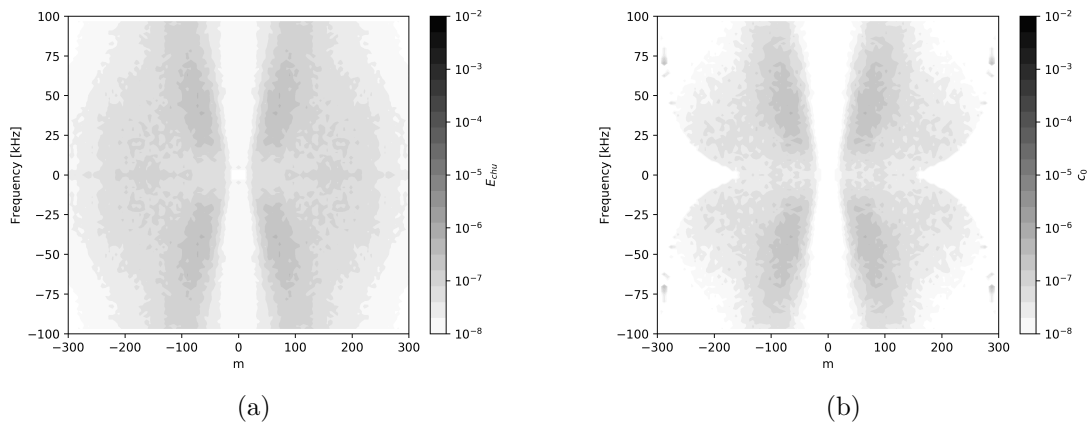


Figure 6.5: Map of (a) the distribution of the fluctuation energy from the QDNS (b) the c_0 coefficient for the dominant linear mechanism against frequency and azimuthal wavenumber for the attached boundary layer region.

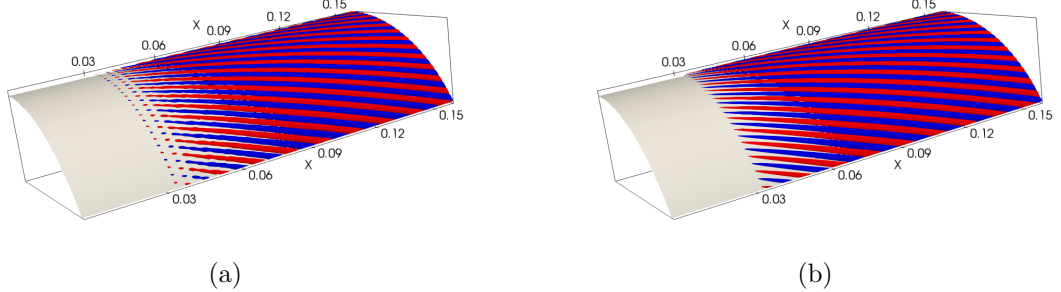


Figure 6.6: 3D reconstruction (isosurface of equal positive and negative density fluctuations) of (a) the leading SPOD mode ($r_0 > 92\%$), (b) the optimal response, for the attached boundary layer at $m = 72$ and $f = 51\text{kHz}$, showing oblique first mode structures.

the same anti-clockwise SPOD modes, which are a mirror symmetry of the former. Thus, only the structure of the clockwise leading SPOD mode is shown in figure 6.6(a), revealing that it is indeed an oblique mode. This leading SPOD mode accounts for more than 92% of the energy with respect to other lesser-ranked SPOD modes at the same frequency/wavenumber. This strong dominance of the first SPOD mode occurs for the whole energetic oblique branches from figure 6.5(a). Thus, other modes will neither be presented nor discussed.

As oblique modes are linearly amplified convective instabilities, the resolvent analysis should yield high optimal gain and a strong separation of singular values for the corresponding range of wavenumbers and frequencies (see section 3.3.2). The separation ratio of the first two largest eigenvalues is presented in figure 6.7(b), the largest eigenvalue is at least one order of magnitude larger than the second one in the zone of interest for the study of oblique modes. As expected, this zone also displays the highest linear amplification (see figure 6.7(a)) such that the energy distribution of figure 6.5(a) is very close to the maps of figure 6.7. The frequencies and wavenumbers of highest amplification match those of energetic structures that develop in the QDNS. The optimal response at the same wavenumber and frequency than the SPOD mode of figure 6.6(a) is shown in figure 6.6(b), and their structures seem identical. This similarity may be quantified by computing an ‘alignment coefficient’, defined as the modulus of the scalar product of the two normalised modes $|\langle \Psi, \psi \rangle|$ (the modes are normalised such that $\langle \Psi, \Psi \rangle = \langle \psi, \psi \rangle = 1$). If this value is 1, the modes are aligned and thus represent exactly the same structure, while a null alignment coefficient means that the modes are orthogonal and have nothing in common. This is commonly used to asses the correspondence of SPOD and resolvent response modes (Towne et al., 2018). The modes presented in figure 6.6 yield $|\langle \Psi, \psi \rangle| = 0.98$, which confirms that the observed oblique modes relate to a linear non-normal (convective-type) amplification mechanism, excited by the inlet white noise.

Other structures than oblique modes appear in the boundary layer: a wide zone of less-energetic fluctuations is visible in figure 6.5 close to the $\omega = 0$ axis. The SPOD analysis reveals that it corresponds to elongated streamwise structures, that will be called streaks (see figure 6.8). Note that these streaks are barely visible in the Q criterion isosurface as it does not allow for the visualisation of velocity deficit.

As there is no corresponding zone of amplification in the gain map (figure 6.7(a)), these structures do not stem from a strong linear amplification mechanism excited by the inlet white noise and may come from either a weak linear mechanism strongly excited by the injected noise (receptivity), or a non-linear interaction. As explained in section 3.3.2, the former hypothesis may easily be discarded by computing the coefficient c_0 which is presented in figure 6.5(b). For the (ω, m) couple linked to oblique modes, the c_0 map is very close to the E_{chu} map, however, for those linked to streaks, this coefficient is several orders of magnitude lower than the energy present in the QDNS. This result was actually expected since the apparition of these streaks relates to

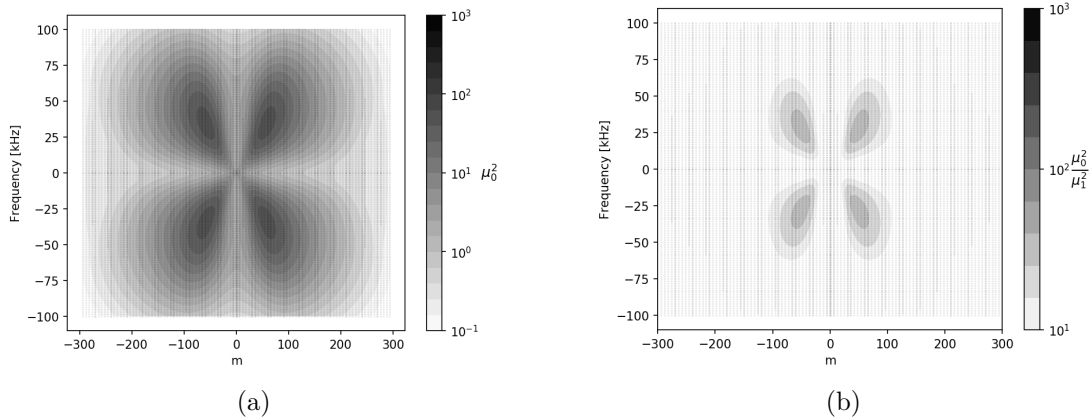


Figure 6.7: Map of (a) the gain (μ_0^2) from the resolvent analysis (b) the separation between the two first eigenvalues of equation (3.35) (μ_0^2/μ_1^2) against frequency and azimuthal wavenumber for the boundary layer region.

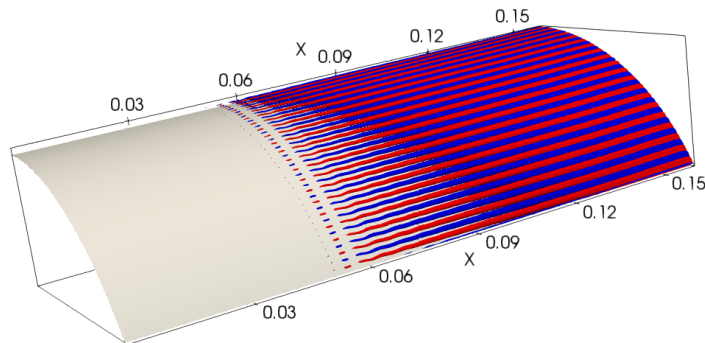


Figure 6.8: 3D reconstruction (isosurface of equal positive and negative density fluctuations) of the leading SPOD mode ($r_0 > 83\%$) for the attached boundary layer at $m = 120$ and $f = 1.5\text{kHz}$, showing quasi-stationary streamwise streaks.

a well-known non-linear mechanism. From the study of incompressible channel flow by Schmid and Henningson (1992), oblique modes of opposite frequencies (*e.g.* the clockwise rotating mode (ω, m) and the counterclockwise rotating one $(-\omega, m)$) are known to interact non-linearly to create streamwise stationary streaks $(0, 2m)$. This explains the diffused energetic zones between the opposed frequency oblique branch of the energy map (figure 6.5(a)), which result from the non-linear interaction of these branches. This interaction is linked to an oblique breakdown mechanism that has been widely studied, mostly for flat-plate boundary layer, for example by Fasel et al. (1993a), Chang and Malik (1994), Sandham et al. (1995), or more recently Franko and Lele (2014) and Franko and Lele (2013). Here, this non-linear interaction is causing the birth of low-energy streaks in the boundary layer which will play an important role in the transition process, as shown in the next section.

Lastly, axisymmetrical ($m = 0$) second mode disturbances are also predicted by the resolvent analysis (see figure 6.9(a) which presents the resolvent gain against frequency for axisymmetrical structures $m = 0$), with a local peak amplification at $f = 230\text{kHz}$ and a maximal associated gain less than half that of the most amplified oblique first mode (see figure 6.7(a) for the gain of the most amplified first mode). The optimal response associated with this maximal gain value is presented in figure 6.10 and displays the typical structure of second mode disturbances (Bugeat et al., 2019; Laurence et al., 2016). The low-intensity, high-frequency peak from the Power Spectral Densities (PSD) presented in figure 6.2 is a sign of those weaker instabilities. The peak visible on the green curve ($X/L = 0.588$, near the end of the boundary layer region) around $f = 230\text{kHz}$ confirms that the most amplified frequencies in the QDNS are matching the resolvent prediction.

Figure 6.9(b) presents the streamwise distribution of the energy of second mode instabilities as predicted by the resolvent analysis. The quantity dE_{chu} is computed by integrating the local Chu energy contribution of the optimal response mode along the gridlines in the wall-normal direction (the gridlines are not exactly perpendicular to the wall in the cylinder-flare junction zone due to the mesh construction) for each streamwise location. This is similar to what has been done by Sipp and Marquet (2013), or more recently by Bugeat (2017) and Bugeat et al. (2019). It is important to note here that the energy level presented in this figure relates to an eigenmode, which is defined up to a multiplicative constant by construction. Figure 6.9(b) shows that the second mode instability is strongly damped as soon as it enters the separated region, such that at the end of the mixing layer, and thus before the transition, it has reached negligible levels. This explains why past the separation point, the PSDs from figure 6.2 do not display any high-frequency peak. Therefore, the second mode is not considered to play a role in the transition scenario since it is virtually absent from the flow at the transition location. Note that Marxen et al. (2010) showed that lower frequency second mode instabilities might be further amplified in the separated region. However, in the present case, even if some of the lower frequency second mode instability are less damped, none of them are further amplified downstream of the interaction and thus all of them become several orders of magnitude less energetic than other modes. This difference with the results of Marxen et al. (2010) is probably due to the fundamental topology difference between the separated region as the recirculation region studied here is massive. Because of the damping of second mode instabilities, the computational and storage cost linked to a higher sampling frequency for the QDNS snapshots (that would allow the extraction of SPOD mode for second mode instabilities) is unnecessary and it was chosen as previously explained to use a sampling frequency of 200kHz.

The resolvent results in the boundary layer are consistent with the LST results in the literature. Even if the second mode can be locally more amplified than the first mode for a Mach 5 boundary layer, the present results should be compared with integrated values such as the N factor, which is often higher for the oblique mode due to the larger instability domain of the first mode (Adams and Kleiser, 1993): the first mode gets amplified earlier than the second mode, resulting in a

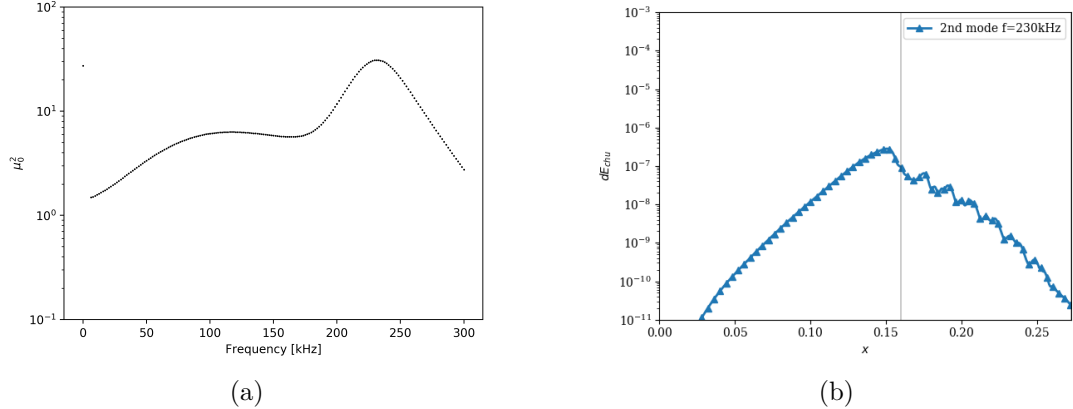


Figure 6.9: (a) resolvent gain against frequency for $m = 0$ showing the second mode peak (b) streamwise distribution of the energy predicted by the resolvent analysis for the second mode. The grey line represents the limit between the boundary layer and the mixing layer region. The amplitude of the linear prediction is arbitrary and only the longitudinal evolution should be considered.

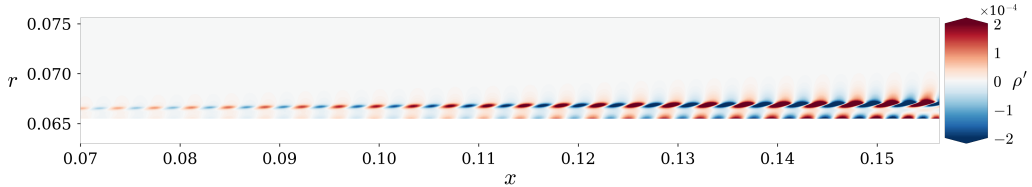


Figure 6.10: Optimal response (density fluctuation) for the attached boundary layer at $m = 0$ and $f = 230\text{kHz}$, showing second Mack mode structures.

higher amplitude despite a possible locally weaker amplification.

To conclude, oblique first mode structures are dominant in the boundary layer. They are due to a convective-type non-normal linear mechanism and are perfectly predicted by the resolvent analysis. They interact non-linearly to create low-energy quasi-steady streaks. Second mode instabilities are also present in the QDNS and predicted by the resolvent analysis, but of much lower energy.

6.2.2 Mixing layer

As it encounters the separation shock, the boundary layer is subject to an adverse pressure gradient and separates, creating a recirculation bubble. A mixing layer appears between the high-speed flow outside of the recirculation region and the reversed flow inside of it, changing the topology of the flow and marking the entry in the second region defined in section 6.1. This section focuses on the portion of the flow that is downstream of the separation shock but upstream of the reattachment point, *i.e.* $X \in [0.16, 0.28]$ or $X/L \in [0.63, 1.11]$. As such, as explained in section 3.3.2, the resolvent analysis spatially constrains the response to this region, but not the forcing, in order to account for the amplification of structures that have developed in the boundary layer.

Figure 6.11 presents an isosurface of Q criterion coloured by density for the mixing layer. Oblique mode structures are still visible, but they have a larger wavelength than those of the boundary layer. Quasi-axisymmetrical structures can also be seen near the wall and are either linked to convected second mode structures.

There are fewer small structures at the beginning of the mixing layer than at the end of the

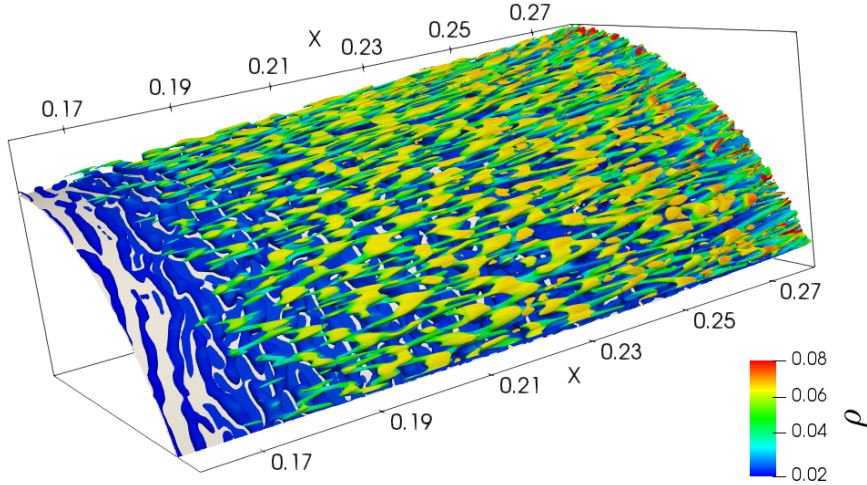


Figure 6.11: Isosurface of Q criterion ($Q = 9 \times 10^{-6}U^2/\delta^2$) coloured by density for the mixing layer from an instantaneous snapshot of the QDNS.

boundary layer, which may be seen more clearly in figure 6.1. This indicates that the separation region damps high-frequency instabilities coming from the boundary layer.

Figure 6.12 (a) presents the fluctuation energy distribution in the mixing layer. Consistently with the Q-criterion results, oblique modes are still present in the flow but they are of lower frequency/wavenumber than in the boundary layer region. The four oblique branches are indeed still visible but shorter: only structures below $f = 40\text{kHz}/m = 100$ have been amplified, which confirms the qualitative observation that the separation region filters a large part of high frequency fluctuations. Moreover, the oblique modes are not dominant anymore, due to the appearance of high-energy streaks around $f = 0\text{Hz}$ for wavenumbers up to $|m| \approx 200$.

Then, two points need to be addressed: the filtering of high-frequency oblique modes, and the appearance of high-energy quasi-steady streaks. The former point may be straightforwardly explained by the resolvent analysis. Figure 6.13 presents the results of the analysis for the mixing layer. Overall the results are comparable to what was observed in the boundary layer: oblique modes are still dominant, but compared to the boundary layer, the mixing layer mainly amplifies structures below $f = 50\text{kHz}$. Physically, this may be caused by the sudden increase of equivalent boundary layer thickness due to the separation, leading to a weaker wall-normal velocity gradient in this region. Therefore, the filtering property of the separation region is the consequence of the abrupt change of the topology of the flow, which shifts the frequency range of the linear amplification mechanisms towards lower values. Consequently, high-frequency structures coming from the boundary layer, which have transferred a part of their energy non-linearly to streamwise structures (see section 6.2.1) are not as amplified as they were in the boundary layer. Meanwhile, lower frequency oblique structures, such as presented in figure 6.14, start to be more strongly amplified when entering the separation region. Thus, the resolvent analysis yields again consistent explanations concerning oblique modes in the mixing layer. Once again, the alignment coefficient between the most amplified oblique mode and the corresponding SPOD mode such as presented in figure 6.14 is high: $|\langle \Psi, \psi \rangle| = 0.84$, which shows that the SPOD oblique modes match their resolvent counterpart.

Figure 6.15 presents the streamwise distribution of the energy of two oblique modes of interest both for (a) the SPOD mode in the QDNS and (b) the linear prediction by the resolvent analysis. In the same way as what was presented in figure 6.9, the quantities dE_{chu} is computed by

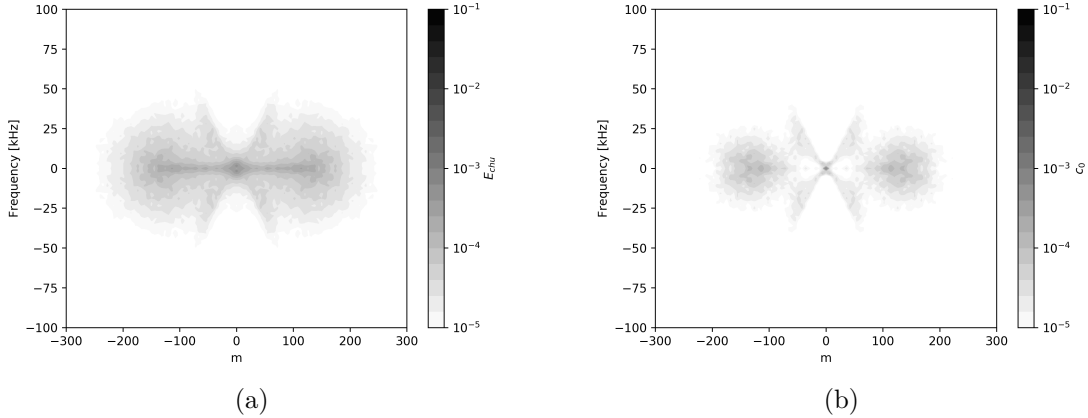


Figure 6.12: Map of (a) the distribution of the fluctuation energy from the QDNS (b) the c_0 coefficient for the dominant linear mechanism against frequency and azimuthal wavenumber for the mixing layer region.

integrating the local Chu energy contribution along the gridlines in the wall-normal direction for each streamwise location. Regarding the resolvent mode, the streamwise energy distribution dc_0 is computed in a similar way from the optimal response normalised based on c_0 (i.e. receptivity is taken into account) such that the curves from 6.9(a) can be quantitatively compared to 6.9(b). Figure 6.15(b) confirms the frequency filtering in the separated region: the linear amplification of low-frequency oblique modes (blue dashed line) becomes significantly stronger than that of high-frequency modes (plain orange line) in the separated region. This result is consistent with the observation from Marxen et al. (2010). However, unlike Marxen et al. (2010), there is a good agreement between the predicted linear energy growth of oblique modes in the separated region (figure 6.15(b)) and the actual growth in the QDNS (figure 6.15(a)), showing the advantage of global resolvent analysis against LST. This is due to the ability of the present linear stability study to account for both non-parallel effects and component-type non-normalities, which are the two main limitations of the study of Marxen et al. (2010) (the non-parallel effect most probably being the main cause of error for the oblique modes in the separated region). Finally, a similar amplification of the 2D first mode in the separated region to that discussed by Marxen et al. (2010) was also observed in the present study. It is not presented here as it is several orders of magnitude less energetic than the oblique modes.

Regarding the energetic streaks observed in figure 6.12(a) they become one of the most energetic structures in the mixing layer. This cannot be explained by the resolvent gain alone, which displays low values for quasi-steady structures (figure 6.13(a)). This means that existing linear mechanisms that may generate streaks are very weak.

Yet, the leading SPOD modes corresponding to the streaks, which dominate the flow for low frequencies, have a structure similar to the linear optimal responses at the same frequency/wavenumber. An example is presented in figure 6.16 for $m = 120$ and $f = 1.5\text{kHz}$. The two modes are globally similar, except for some small structures in the SPOD mode around $X = 0.26$, which are absent from the resolvent mode. This may be due to intermittent turbulent spots (the intermittency function is no longer zero in this region, see figure 6.3)) or to the presence of a nearby shock. The alignment coefficient is $|\langle \Psi, \psi \rangle| = 0.66$, which is lower than what was observed in the previous region of the flow. It is nonetheless still rather high and may indicate that the streaks are due to the weak linear amplification mechanisms mentioned above, that may lead to high-energy structure through receptivity processes. This may be investigated by computing the c_0 coefficient distribution in the (ω, m) -domain (see section 3.3.2), and comparing to the energy distribution of the fluctuations. Note that c_0 and E_{chu} are homogeneous quantities that can be quantitatively compared (see section 3.3.2).

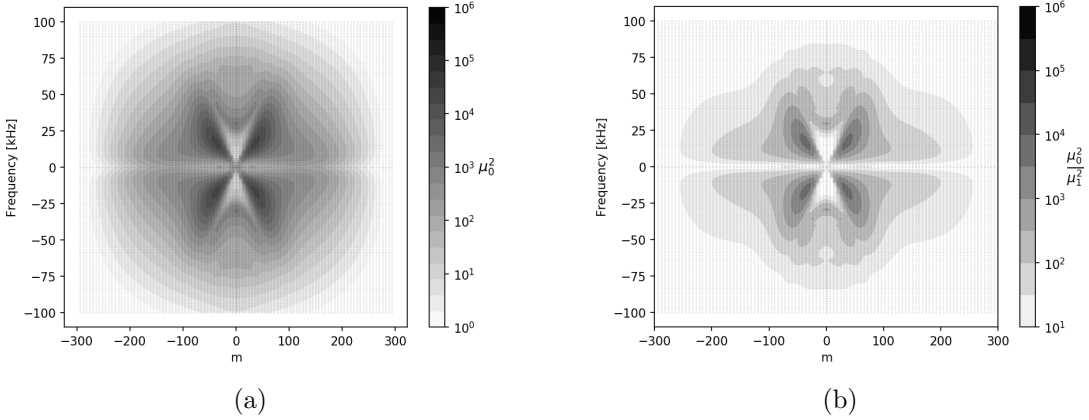


Figure 6.13: Map of (a) the gain (μ_0^2) from the resolvent analysis (b) the separation between the two first eigenvalues of equation (3.35) (μ_0^2/μ_1^2) against frequency and azimuthal wavenumber for the mixing layer region.

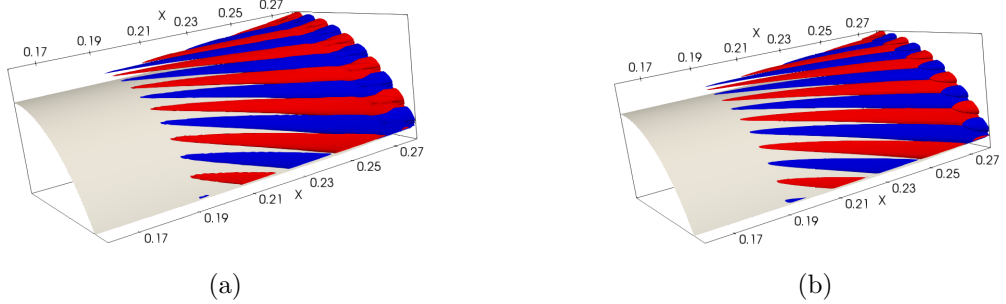


Figure 6.14: 3D reconstruction (isosurface of equal positive and negative density fluctuations) of (a) the leading SPOD mode ($r_0 > 87\%$), (b) the optimal response of the mixing layer at $m = 30$ and $f = 15$ kHz, showing oblique first mode structures.

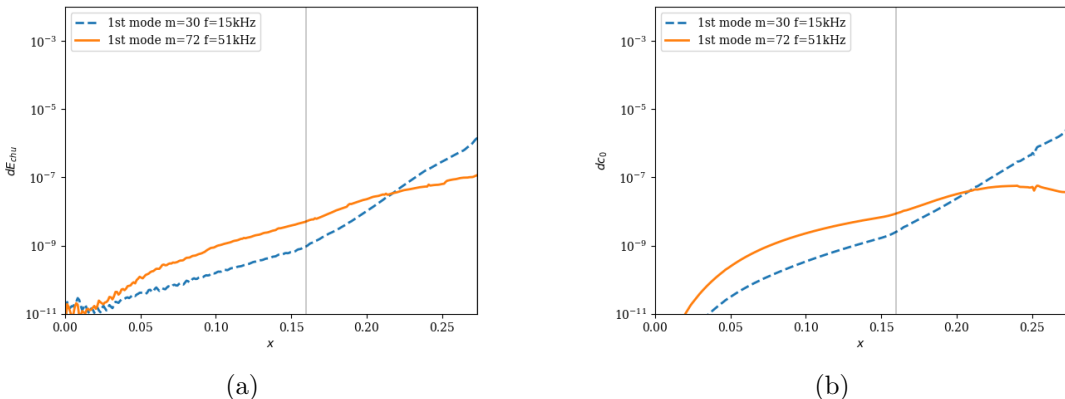


Figure 6.15: Streamwise distribution of the energy of two oblique modes of interest. Panel (a) shows the energy evolution for the SPOD modes extracted from the QDNS, (b) shows the energy evolution predicted by the resolvent analysis, the grey line represents the limit between the boundary layer and the mixing layer region. dE_{chu} and dc_0 can be quantitatively compared.

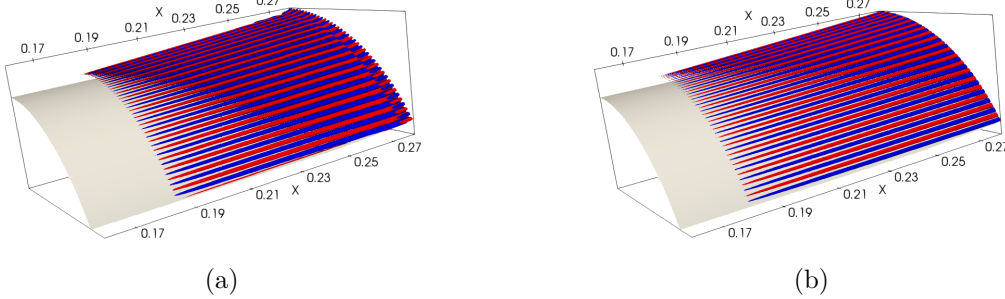


Figure 6.16: 3D reconstruction (isosurface of equal positive and negative density fluctuations) of (a) the leading SPOD mode ($r_0 > 83\%$), (b) the optimal response of the mixing layer at $m = 120$ and $f = 1.5\text{kHz}$, showing similar quasi-stationary streamwise streaks.

Figure 6.12 (b) presents the resulting projection map. Compared to the gain map (figure 6.13(a)), a high-energy region appears for the streaks up to $|m| = 200$ and low frequency. It is interesting to note that because of these discrepancies, contrary to the gain map, the c_0 coefficient map is very similar to the fluctuation energy map from the QDNS. This proves that the quasi-steady streaks are mainly the result of a weak linear mechanism, which is strongly excited either by the injected noise or by the non-linear forcing. As a result, due to this selective nature of the excitation, quasi-steady streaks become as energetic as oblique modes, despite their much lower amplification gain. The particular role of the inlet noise in this receptivity process may be ruled out by computing the coefficient c_r (see section 3.3.2), which was found several orders of magnitude smaller than c_0 and E_{chu} . Therefore, these structures are driven by the nonlinear forcing rather than directly created by the inlet noise. In particular, the nonlinear structures created upstream in the boundary layer play an important role. This may be underpinned by computing the optimal forcing (figure 6.17), which is located in the upstream part of the boundary layer. Additionally, even though they are not homogeneous to a forcing, it is interesting to observe that the elongated structures created in the boundary layer (figure 6.8) turn out to be very close to the optimal forcing exciting streaks in the mixing layer (figure 6.17). Finally, the c_0 -map reveals that above $|m| = 200$, the streaks are almost not excited anymore, which is consistent with the QDNS results where structures with $|m| > 200$ display very low levels of energy.

A linear streak growth triggered by the non-linear interaction of oblique modes was already observed for supersonic boundary layer by Laible and Fasel (2016), who concluded that the non-linear interaction of oblique modes acted as an "actuator" that forces component-type non-normal growth of the streaks, in the same way as it was described by Schmid and Henningson (1992) for incompressible channel flow. This mechanism is known as one of the fastest ways to transition in attached boundary layers according to the studies of Franko and Lele (2013). For the present configuration, the separation induces an even stronger non-normal growth of the streaks than in the boundary layer, making this scenario even more relevant.

To conclude, in the mixing layer, high-frequency oblique modes from the boundary layer have transferred their energy to streaks via the non-linear interaction described before and are, at best, only weakly amplified due to the effective thickening of the boundary layer linked with separation. Consequently, their relative intensity becomes very low. Some oblique modes of lower frequency continue to be linearly amplified and are thus present in the flow. But the most important finding is that the structures created by the non-linear interaction in the boundary layer are actually close to the optimal forcing that generates streaks in the mixing layer. Therefore, the flow in this region is dominated by quasi-steady streaks for wavenumbers up to $|m| \approx 200$. Non-linear interactions of oblique modes in the mixing layer may also contribute to the appearance of these streaks, although probably to a lesser extent.

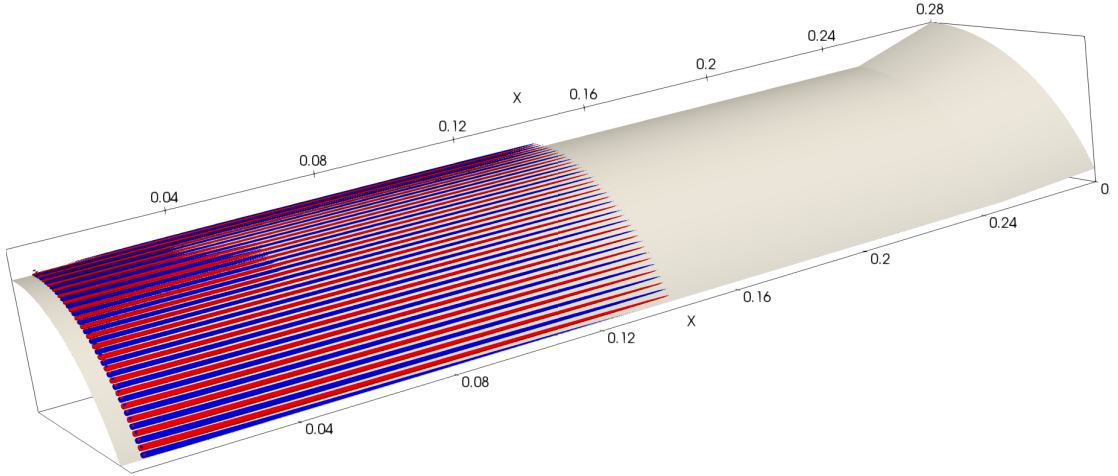


Figure 6.17: 3D reconstruction of an optimal forcing (isosurface of equal positive and negative density forcing) at $f = 1.5\text{kHz}$ and $m = 120$ corresponding to linear amplification of streaks developing due to the non-linear forcing in the mixing layer. Boundary layer region is shown as the forcing is mainly located upstream of the mixing layer.

6.2.3 Reattachment region

At some point on the flare, the mixing layer compresses, the flow reattaches, and the separation bubble no longer exists. That marks the entry in the third region of interest as defined in section 6.1, the reattachment region. This is where the heat fluxes are usually the highest, particularly in transitional cases. This region also contains the most energetic fluctuations. The reattachment region is studied in a similar way as the two previous regions by focusing on the region downstream of the reattachment (*i.e.* $X \in [0.28, 0.35]$ or $X/L \in [1.11, 1.39]$). Once again, for the resolvent analysis, the energy norm for the response only accounts for the reattachment region, but the forcing is not constrained.

Figure 6.18 presents an isosurface of Q criterion for the reattachment region. It reveals elongated streamwise structures at the beginning of the domain, which then breakdown creating smaller structures like hairpin vortices, a sign of transition towards a turbulent flow. The fact that the breakdown happens at reattachment is one of the main reasons for the peak of heat flux. As observed by Mayer et al. (2011) for boundary layer oblique breakdown, the point where the periodicity of the flow is lost (*i.e.* were the streaks breakdown) is the point where the skin-friction, and thus the heat-flux, is maximal.

The energy distribution presented in figure 6.19 (a) confirms that the flow is transitioning to turbulence as the energy is spread on a wide range of frequencies and wavenumbers, which is typically due to the breakdown of coherent structures into many smaller scale structures. This breakdown leads to a spread of energy from low to high frequencies and for $|m| \approx 300$ or lower. The energy map also shows that there are less significant levels of energy in coherent structures like streaks and oblique modes. Moreover, the energy levels involved are several orders of magnitude higher than those of the boundary layer (see figure 6.5) shows how intense the dynamics is in the reattachment region.

Let us now compare these results to the resolvent analysis. Figure 6.20 presents the resolvent results for the reattachment region: oblique modes display the highest gain values. However, the energy map from the QDNS (figure 6.19(a)) shows that they are far from being dominant in the reattachment region as there is no clearly defined energetic region for these structures. Beside oblique modes, a new secondary zone of amplification appears at frequencies and wavenumbers corresponding to already existing streaks. The local maxima of this zone agree well with the

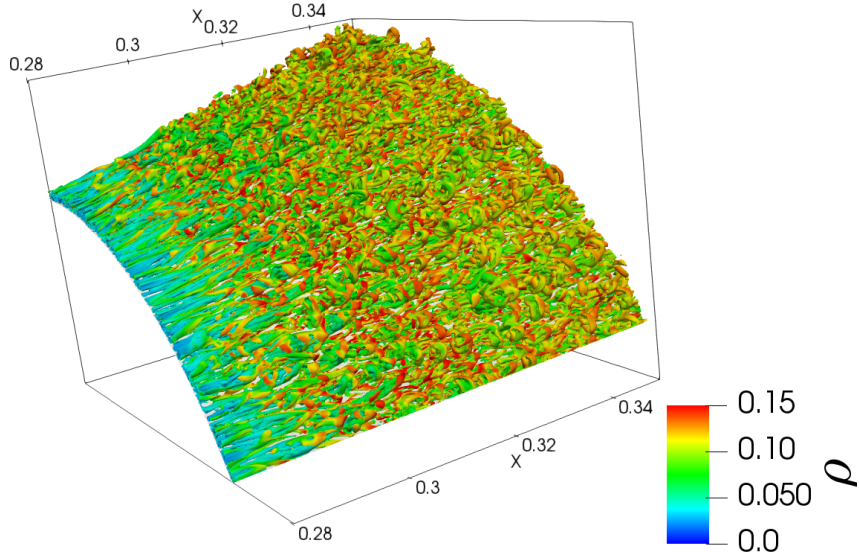


Figure 6.18: Isosurface of Q criterion ($Q = 9 \times 10^{-3} U^2 / \delta^2$) coloured by density for the reattachment on the flare from an instantaneous snapshot of the QDNS.

energy map of figure 6.19(a) (the maximal linear amplification of streaks occurs around $|m| = 120$). However, the energy map presents energy spread on a wider range of frequencies and wavenumbers than the gain map.

These discrepancies may be investigated following the same approach as in section 6.2.2 by computing a map of the c_0 coefficient in the (m, ω) domain (see section 3.3.2). Figure 6.19(b) presents the results of this analysis. As in the mixing layer, the forcing term plays a significant role in the selection of linearly amplified structures. It completely shifts the amplification map from an oblique-mode-dominated configuration to a streaks-dominated one. This is similar to the situation of the mixing layer: the strong linear mechanism for oblique modes is very weakly excited while streaks are nearly-optimally forced by higher-energy structures. Indeed, as shown in figure 6.21, the optimal forcing associated with streaks is once again located far upstream, and is rem-

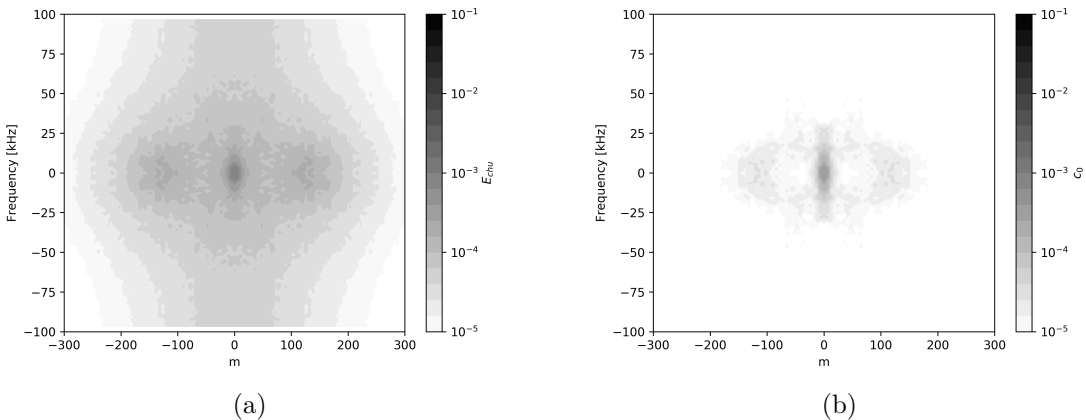


Figure 6.19: Map of (a) the distribution of the fluctuation energy from the QDNS (b) the c_0 coefficient for the dominant linear mechanism against frequency and azimuthal wavenumber for the reattachment region.

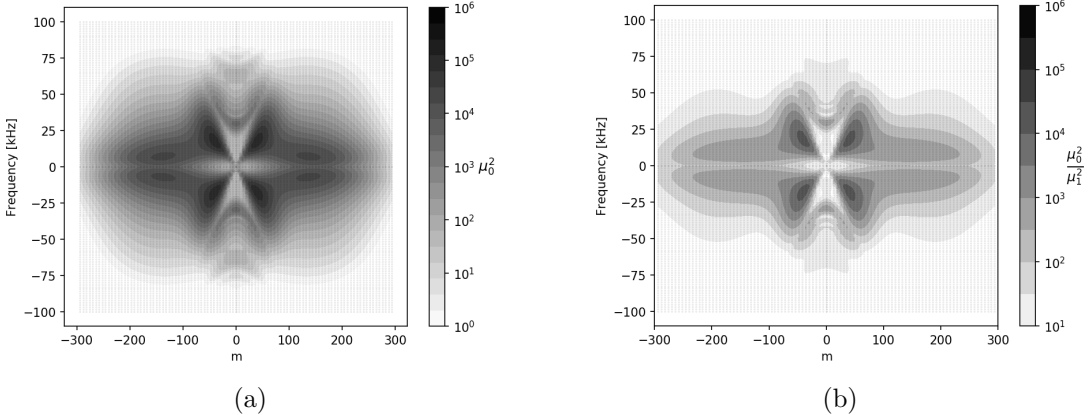


Figure 6.20: Map of (a) the gain (μ_0^2) from the resolvent analysis (b) the separation between the two first eigenvalues of equation (3.35) (μ_0^2/μ_1^2) against frequency and azimuthal wavenumber for the reattachment region.

inherent of the structures that developed through nonlinear interaction of oblique modes in the boundary layer. Thus, the dynamics of the boundary layer plays a critical role in the transition process, even though the boundary layer instabilities are around three orders of magnitude less energetic. The corresponding optimal response of a streak mode is compared to SPOD results for the QDNS in figure 6.22. Again, there is a good agreement between the predicted linearly amplified structures and those that develop in the QDNS. Another interesting point is that, contrary to the mixing layer region, the c_0 map for the reattachment region (figure 6.19 (b)) is quite different from the energy map from the QDNS (figure 6.19 (a)) and is lacking a lot of energy that is spread on a wide range of wavenumber and frequency. This is a sign that the coherent structures are breaking down. This breakdown implies a transfer of energy from the streaks to a multitude of other spatio-temporal scales associated with turbulence. This is confirmed by figure 6.23, which shows that the low-frequency dynamics at moderate $|m|$ values is dominated by one single SPOD mode associated with streaks. But as $|m|$ increases above approximately 200, there is almost no separation between the leading SPOD mode and others, which reveals the spatio-temporally uncorrelated (turbulent) nature of the flow. In such conditions, as explained by Towne et al. (2018), the resolvent analysis is expected to differ from the actual dynamics, since only a limited number of resolvent modes cannot characterize the dynamics anymore. This is confirmed by the alignment coefficient $|\langle \Psi, \psi \rangle| = 0.37$ (for $m = 174$, $f = 7\text{kHz}$) which is very low. An explanation for this low value can be found in figure 6.22. Even if the modes look very similar at the beginning of the region, the SPOD mode begin to meander as soon as we reach the turbulent zone. While the alignment coefficient at the beginning of the domain would be high as the linearly amplified structure is very similar to the one present in the QNDS, its value is plummeting in the downstream part of the region due to the breakdown. The same logic applies for all the energy spread on a wide frequency-wavenumber range in this region, as the energy is spread by the breakdown to turbulence and the flow is no longer dominated by a single dominant mechanism, the leading resolvent mode is unable to describe it correctly, causing the discrepancies between figure 6.19 (a) and (b). Even with these discrepancies, it is still interesting to notice that the linear amplification of streaks is increasingly stronger in the mixing layer and at the beginning of the reattachment region than in the boundary layer, due to an increasingly stronger linear mechanism. As previously discussed, oblique breakdown is already known to be one of the fastest ways to create turbulence in attached boundary layers (Franko and Lele, 2014; Franko and Lele, 2013; Laible and Fasel, 2016), the fact that linear mechanisms associated with streaks become stronger after the separation point makes it even more relevant for SBLI flow.

To summarize these findings, in the reattachment region, the streaks caused by a non-linear

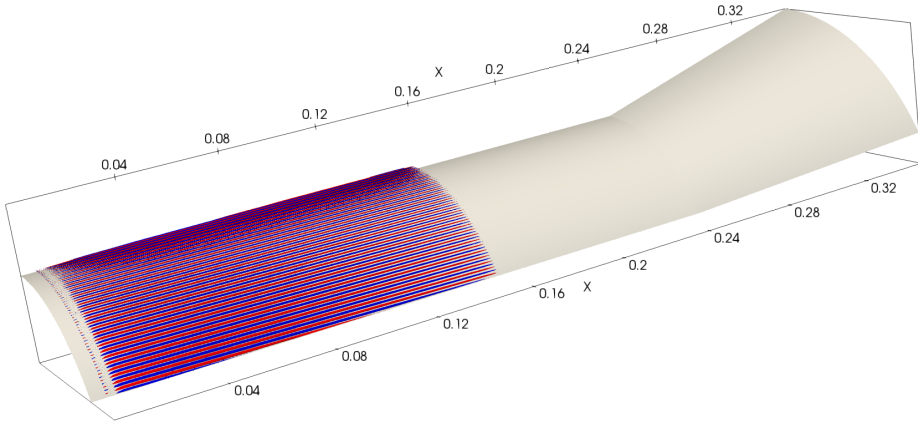


Figure 6.21: 3D reconstruction (isosurface of equal positive and negative density forcing) of the optimal forcing linked to streak amplification for the reattachment at $m = 174$ and $f = 7\text{kHz}$.

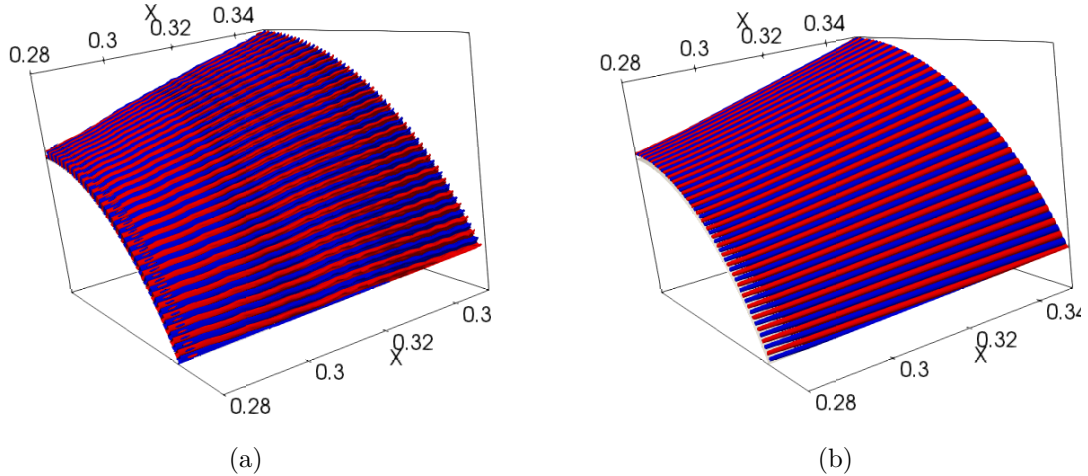


Figure 6.22: 3D reconstruction (isosurface of equal positive and negative density fluctuations) of (a) the leading SPOD mode ($r_0 > 86\%$), (b) the optimal response of the reattachment region at $m = 174$ and $f = 7\text{kHz}$, showing elongated streaks.

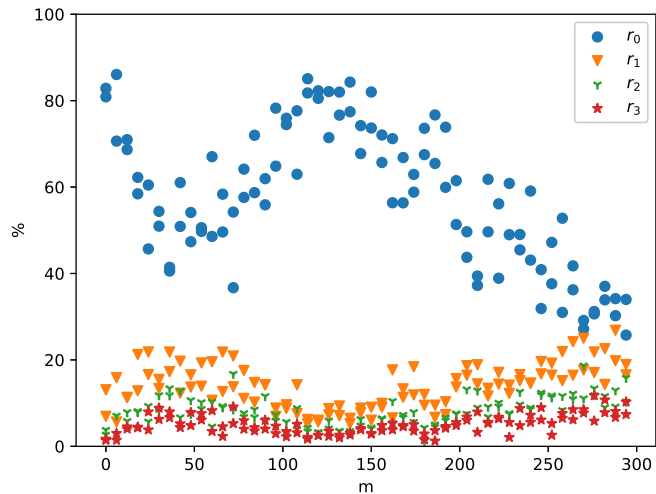


Figure 6.23: Percentage of energy contained in the first 4 SPOD modes for the reattachment at $f = 1.5\text{kHz}$ depending on azimuthal wavenumber.

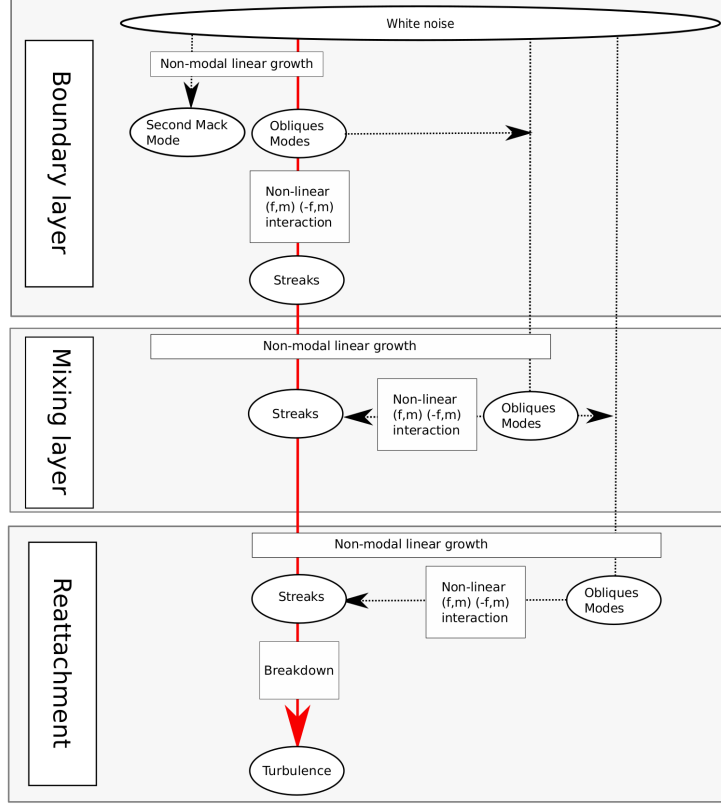


Figure 6.24: Proposed scenario for the transition process.

interaction in the boundary which are linearly amplified in the mixing layer are further amplified by a linear mechanism. Then, they quickly breakdown in the way described by Mayer et al. (2011) for the flat plate boundary layer as the tip of the streamwise structure lift up from the wall and break to turbulence.

6.3 Transition scenario

The findings of the previous section yields a transition scenario for the studied case. Even if the scenario is not new, as it is built on mechanisms that are well-known in the literature, it is the first time that it is studied in a complex configuration. Note that despite the generic broadband nature of the noise injected within the simulation that excites a wide range of mechanisms (see section 3.1.4), the scenario might differ for a flow subject to a different type of perturbations (for example, in the case of purely acoustic perturbations).

The scenario is presented in figure 6.24 and can be followed step by step:

1. Boundary layer
 - (a) Some white noise is injected in the boundary layer, it triggers the linear growth of two well-known instabilities over a wide range of frequencies and wavenumbers:
 - i. Second Mack mode instabilities.
 - ii. Oblique first mode instabilities , they become dominant due to their larger instability domain.
 - (b) The oblique modes interact non-linearly in the way proposed by Schmid and Henningson (1992), creating quasi-steady streaks over a wide range of wavenumber.

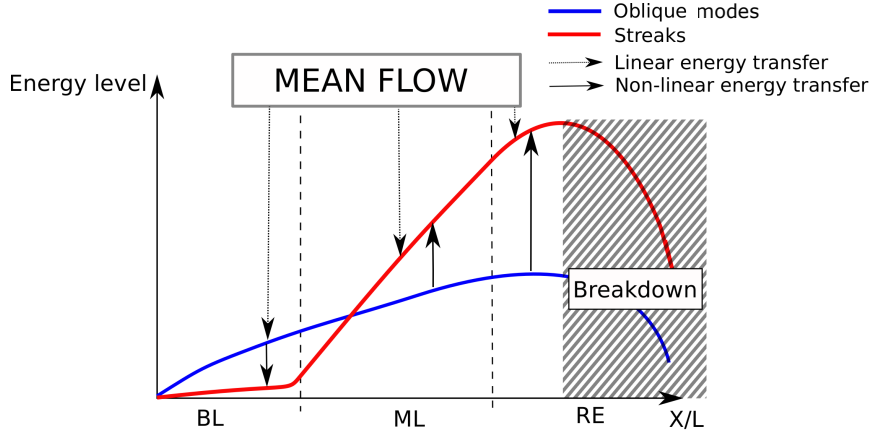


Figure 6.25: Energy transfer during the transition process.

2. Mixing layer

- (a) Oblique modes continue to be amplified (albeit for lower frequencies due to the thicker shear layer compared to the upstream boundary layer) and to interact non-linearly to feed energy to the streaks.
- (b) The non-linear forcing linked to streaks created in the boundary layer trigger a weak linear amplification mechanism in the mixing layer, making streaks the dominant structure in the flow.

3. Reattachment

- (a) The non-linear forcing linked to streaks created in the boundary layer continue to trigger a linear amplification mechanism in the reattachment region. The streaks finally break down, creating turbulent structures.

Energy transfers linked to that scenario are sketched in figure 6.25, which shows that the mean flow transfers energy to oblique modes (via a linear mechanism). These modes then transfer energy to streaks via a non-linear interaction. The mean flow also feeds energy directly to streaks, but as shown in figure 6.24, the non-linear interaction in the boundary layer is necessary to trigger this linear amplification mechanism. An important conclusion of the study is that even if the energy transfers in the boundary layer are of very low intensity when compared to energy transfers in other regions of the flow, the transition scenario is highly dependent on the low-energy structures that develop due to boundary layer instabilities.

This section draws a clearer picture of the dynamics of the Mach 5 transitional cylinder flare flow. Yet, it did not discuss from a physical viewpoint the nature of the linear amplification mechanism of streaks, which plays a central role in the overall dynamics of the flow. Even if good candidates for the linear amplification of longitudinal structures would be the centrifugal effect linked to Görtler instabilities (Benay et al., 2006; Murray et al., 2013; Navarro-Martinez and Tutty, 2005) or the lift-up effect such as pointed by Bugeat et al. (2019) (albeit only for boundary layer flow), a recent study by Dwivedi et al. (2019) tends to show that they are due to baroclinic effects. The work of Dwivedi et al. (2019) focuses on a laminar flow and does not address directly the question of transition, but nonetheless, it provides insights about the amplification mechanism of so-called 'reattachment vortices' in a hypersonic compression ramp flow. Their physical analysis, based on the study of the inviscid transport equations and particularly of the contribution of base flow gradients to the production of streamwise velocity, vorticity, and temperature perturbations, showed that the streamwise deceleration through the recirculation region caused the amplification of streamwise velocity perturbations, and that baroclinic effects were the main cause of the amplification of streamwise vorticity. Therefore, they concluded

that the linear amplification of these longitudinal vortical structure was due to the baroclinic effects.

6.4 Conclusion

To conclude this chapter, it was shown that the dominant transition mechanism for this case relies on the amplification of broadband first oblique modes in the boundary layer, beating the second mode growth because of their longer domain of instability. These oblique modes interact non-linearly to create streaks, such as already documented in many cases of supersonic and hypersonic transition (Fasel et al., 1993a; Franko and Lele, 2014; Franko and Lele, 2013; Mayer et al., 2011; Sivasubramanian and Fasel, 2011, 2016). Then, the non-linear forcing linked to those streaks trigger a linear amplification mechanism, either due to centrifugal, baroclinic, or the lift-up effect, in the mixing layer and reattachment region which leads to breakdown. Even if the breakdown is linked to linear amplification, the non-linear interaction of oblique modes was found to be essential for this transition scenario. The combination of both QDNS with SPOD and resolvent analysis has proven to be a highly efficient tool set to understand the physical mechanisms behind transition, especially when dealing with both linearly amplified instabilities and non-linear interactions.

The transition process presented is conjectured to be dominant for comparable (*i.e.* with high level of free-stream perturbations) high supersonic/low hypersonic flow.

Chapter 7

Numerical study of the effect of compressibility on the transition scenario

The chapter is dedicated to the numerical study of the impact of compressibility on transitional instabilities and the transition scenario presented in chapter 6. Quasi direct numerical simulation are conducted at transitional Reynolds number for Mach number of 4, 5, 6 and 7. A white noise is injected at the inlet of the simulations to allow the growth of convective instabilities. Results of the simulations are exploited with Spectral Proper Orthogonal Decomposition and compared to resolvent analysis. This allows to study and compare both linear and non-linear amplification mechanism for each Mach Number.

Contents

7.1	Introduction	122
7.2	Flow topology	123
7.3	Boundary layer instabilities	126
	Second Mack Mode	126
	First Oblique Mode	130
	Receptivity of first and second mode to the injected noise	132
	Streaks	132
7.4	Impact on the transition scenario	133
	Mach 4 case, boundary layer transition	133
	Mach 5-6-7 case, reattachment transition	134
	On the computation of second mode instability with AUSM schemes	134
7.5	Conclusion	135

7.1 Introduction

This chapter mainly focus on the presentation and the interpretation of QDNSs and resolvent analysis for the 4 flow conditions presented in table 7.1, those cases correspond to the same Reynolds number for different Mach numbers. The meshes used for this study correspond to the case F of table 3.2.

M_∞	4	5	6	7
T_∞	86.6 K	86.6 K	86.6 K	86.6 K
P_∞	1535 Pa	1228 Pa	1023 Pa	877 Pa
U_∞	746 m/s	933 m/s	1119 m/s	1305 m/s
T_i	364 K	520 K	710 K	935 K
T_{wall}	290 K	290 K	290 K	290 K
Re_L	1.95×10^6	1.95×10^6	1.95×10^6	1.95×10^6

Table 7.1: Free stream conditions and characteristic values for the 4 simulations.

Compared to the study presented in chapter 6, the noise is increased ($A = 2\%$), leading to smaller separated region for the Mach 5 case. A filtering of the noise (as described in section 3.1.4) was also used.

The goal of this chapter is to study the impact of the compressibility on the topology of the flow, the boundary layer instabilities and transition scenario. The study is split into 3 parts, first the topology of the flow is presented and the impact of compressibility on the flow is described. Then the linear (and non-linear) mechanisms causing the growth of instabilities in the boundary layer in each case are studied. To complete the study, the transition scenario of each case is briefly described.

It may be interesting to point out here that the interpretation of the results presented in this chapter may be a bit difficult, as the ratio of the adiabatic wall temperature to the actual wall temperature ($\frac{T_f}{T_w}$) is changing between simulations as the stagnation temperature is increased with the Mach number. This parameter is known to have a significant impact on the developing boundary layer instabilities. However, the present setup, which is keeping the static temperature constant, is a bit more representative of the different flow conditions that a vehicle may encounter when speeding up in flight.

7.2 Flow topology

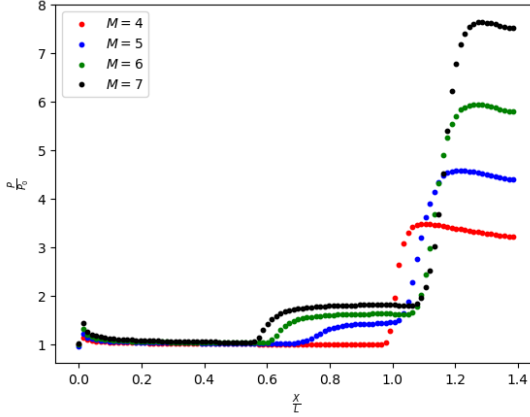


Figure 7.1: Mean pressure distribution along the geometry for each Mach number, showing the difference in flow topology and in particular in recirculation region size.

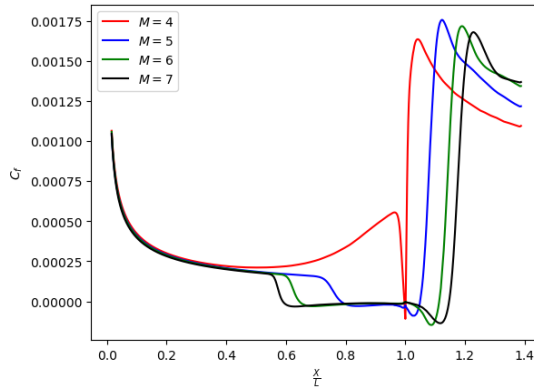


Figure 7.2: Mean skin friction coefficient along the geometry for each Mach number.

This section is dedicated to the study of the impact of compressibility on the topology of the flow. First, we can look the pressure distribution at the wall, as this allows to locate the separation and reattachment region and is widely used experimentally (Benay et al., 2006; Bur and Chanetz, 2009; Murray et al., 2013). Figure 7.1 presents the mean parietal pressure distribution for the 4 cases. This distribution shows the huge difference in flow topology caused by the increase in Mach number. While the Mach 4 case shows no noticeable mean separated region, the only pressure rise being due to the presence of the flare, the Mach 5 case starts to display a small pressure plateau before the reattachment region, which is due to the presence of a recirculation region. The Mach 6 and 7 cases show a large plateau of pressure upstream of the flare, proof of the presence of an important separated region. Those differences can be due to several physical mechanisms. First, as the Mach number increases, the shock caused by the flare will become stronger, causing a higher pressure gradient in the boundary layer and thus leading to stronger separation. This is confirmed by the results presented in figure 7.1 which underline that the pressure ratio through the shockwave is up to more than twice as high for the Mach 7 than for Mach 4 case. Another possible cause for this change of topology is the difference in the nature of the boundary layer itself. As already mentioned in the introduction, and previous chapters a laminar boundary layer will be more subject to separation than a turbulent one, thus if the boundary layer of the Mach 4 case transitions upstream of the interaction while the Mach 5, 6 and 7 cases does not, it can lead to the observed behavior of the flow.

Figure 7.2 presents the skin friction coefficient along the geometry for every case. It confirms the observation about the topology of the flow made from the pressure distribution as the recirculation bubble, linked with negative skin friction, is increasing in size for higher Mach number. However, a slight mean recirculation region is visible on the skin friction coefficient for the Mach 4 case, while it was not visible on the pressure distribution. While the friction peak for every-case is located on the flare at values higher than the turbulent one, which is expected (Benay et al., 2006), a big difference is visible for the attached boundary where the Mach 4 shows an increase in skin friction before separation while the other cases remain constant. This behavior is a sign of transition in the attached boundary layer (Benay et al., 2006).

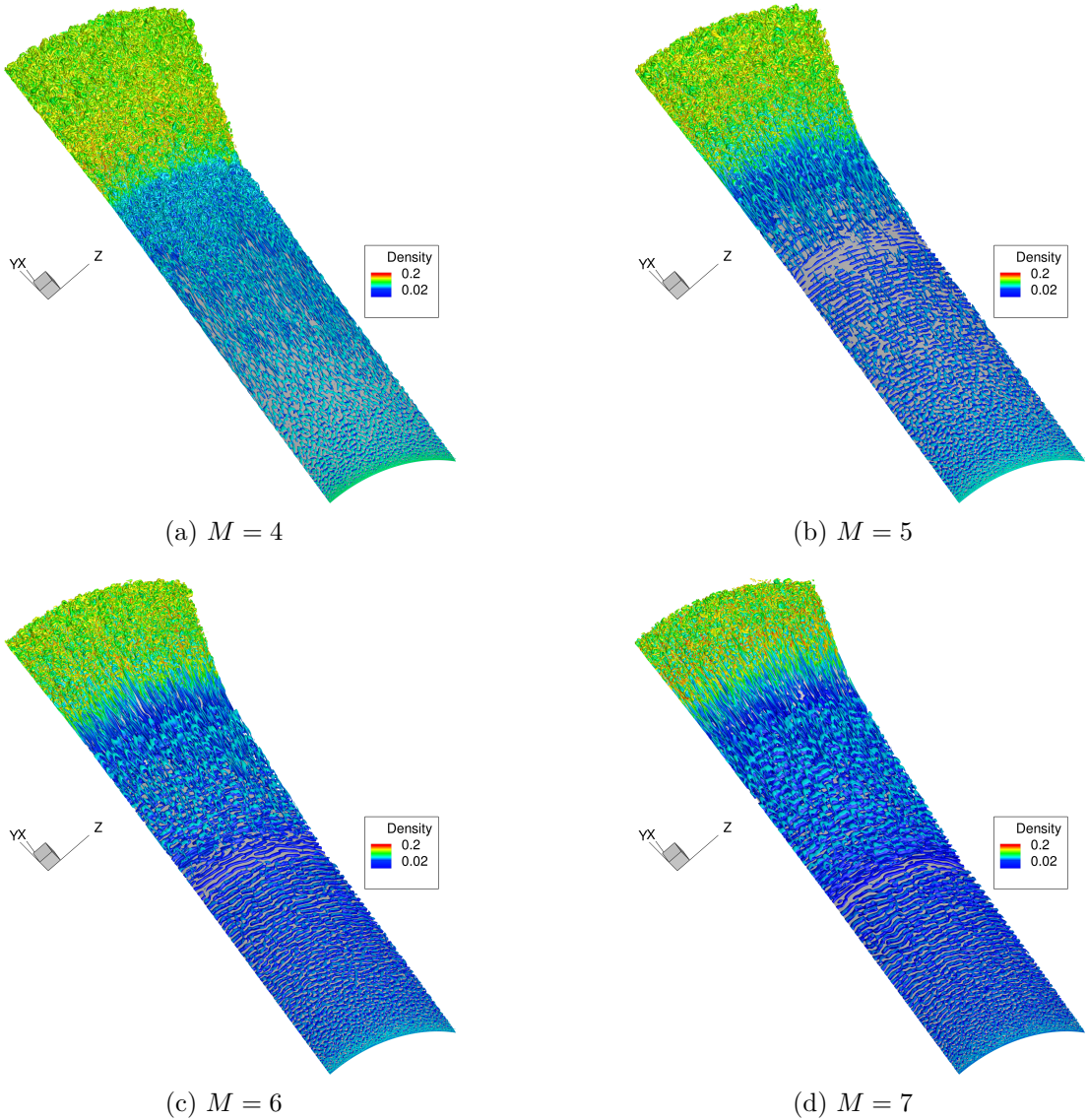


Figure 7.3: Isosurface of Q criterion from a snapshot of the simulation.

Figure 7.3 presents isosurface of Q criterion for each case. Those visualizations clearly show the change of topology of the flow, starting from no separation for (a), then increasing separation size as the Mach number increase in (b), (c), and (d). It is interesting to note that in all cases, turbulent structures (such as hairpin vortices) are observed downstream of the reattachment point. However, the way the transition is happening seems to be quite different between the cases: For the Mach 4 case (a), oblique structures are visible at the beginning of the boundary layer. When advancing downstream, streaky structures begin to dominate and then quickly lift

from the surface, creating hairpin vortices, which is a sign that the boundary layer is becoming turbulent.

For the Mach 5, 6 and 7 cases, the oblique modes are still present in the boundary layer, yet no more hairpin are visible. A new type of axisymmetric structure also appears in the lower part of the boundary layer. All three cases seems to be turbulent in the reattachment region. For the Mach 6 and 7 cases, conspicuously well-defined longitudinal structures are present in the reattachment and seems to be responsible for transition as they break down during the recompression.

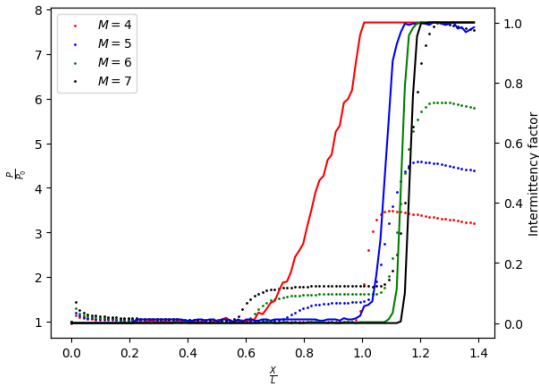


Figure 7.4: Intermittency factor and pressure distribution along the geometry for each Mach number, showing the change of transition onset location depending on the mach number.

The assumptions made from the Q criterion on the location of transition are confirmed by the intermittency function (see section 3.1.3) presented in figure 7.4. The results show first, and as expected, that the Mach 4 case is almost fully turbulent in the boundary layer upstream of the shock-boundary layer interaction as the intermittency factor rise to 1 before $\frac{X}{L} = 1$. At $\frac{X}{L} = 1$, γ gets to 1, meaning that the transition is completed and the flow downstream is turbulent. For the Mach 5, 6 and 7 cases, the scenario seems to be different, similarly to what was observed in chapter 5 and 6 the boundary layer encounter the separation shock when γ is still at 0, causing the separation. The intermittency does not rise in the mixing layer and everything happens at reattachment where the flow transitions brutally to turbulence. This is fully coherent with what was observed in the Q criterion figure 7.3 for the Mach 6 and 7 cases as they display well-organized flow in the boundary layer and mixing layer and turbulent spots brutally appears at the reattachment from the breakdown of streaks. For every case going through the reattachment shock leads to an intermittency of 1, a similar behavior was already observed by Sandham et al. (2014) for impinging oblique shock cases.

From the Q criterion and the intermittency function, two transition scenarios emerge:

1. Boundary layer transition for the Mach 4 case.
2. Transition in the reattachment region for Mach 5, 6 and 7 cases.

One of the main differences between the 4 cases is then the state of the boundary layer upstream of the interaction. This result highlights that the instabilities present in the boundary layer can have a noticeable impact on the topology of the flow and seems to be subject to changes when the compressibility increases. They thus need to be studied in details.

Grid size and resolution:	
n_x	704
n_r	102
n_θ	200
θ resolution	$\approx 0.3^\circ$
m resolution	6

Temporal sampling:	
Sampling rate	666.67kHz
Number of samples	1600
Number of samples in each realization	400
Frequency resolution	1666.67Hz
Number of realizations N_r	13

Table 7.2: Numerical parameters for the SPOD.

7.3 Boundary layer instabilities

To understand how the change in compressibility can lead to different transition scenarios, one can first study what happens in the boundary layer for each case. From the visualization figure 7.3, and going back to chapter 2, we can isolate 3 main categories of boundary layer instabilities that will be studied in details in the following: the second Mack mode, the first oblique mode, and the streaks.

For each instability, the same methodology will be employed:

1. The power spectral density of pressure probes along the attached boundary layer presented in figure 7.5 will be discussed with regard to recent experimental results.
2. Results from the resolvent analysis restricted to the boundary layer ($\frac{X}{L} < 0.5$), particularly the gain map presented in figure 7.6 will be studied to get information about the linear mechanism possibly causing the growth of the instability.
3. Energy distributions from the DNS presented in figure 7.7 will give information about the energy level of the instabilities in the DNS and will be directly compared to the resolvent gain. The projection coefficient map 7.8 will also be compared with the gain and the energy to get insight on the receptivity and the impact of the non-linear mechanisms.
4. SPOD modes linked to energetic instabilities extracted from the DNS will be compared to optimal response of the resolvent analysis.
5. Conclusions will be drawn on the origin of the instability and how it is affected by compressibility.

For the resolvent and SPOD, only the part of the domain comprising a boundary layer will be considered. The numerical parameters for the SPOD are presented in table 7.2.

Second Mack Mode

Let us first consider the second mode instabilities, which is supposed to be dominant for high Mach number boundary layers. The power spectral density distribution giving typical sign of the presence of second mode instability can be found in figure 7.5 ((c) and (d)). The peaks between 200 – 250kHz are characteristic of second mode instabilities (see the experimental results of Laurence et al., 2016 for instance). The PSD results show a stronger amplification for the Mach 7 case than for the Mach 6 one. The peaks also shift in frequency depending on the longitudinal position on the cylinder, the further from the leading edge, the lower the frequency.

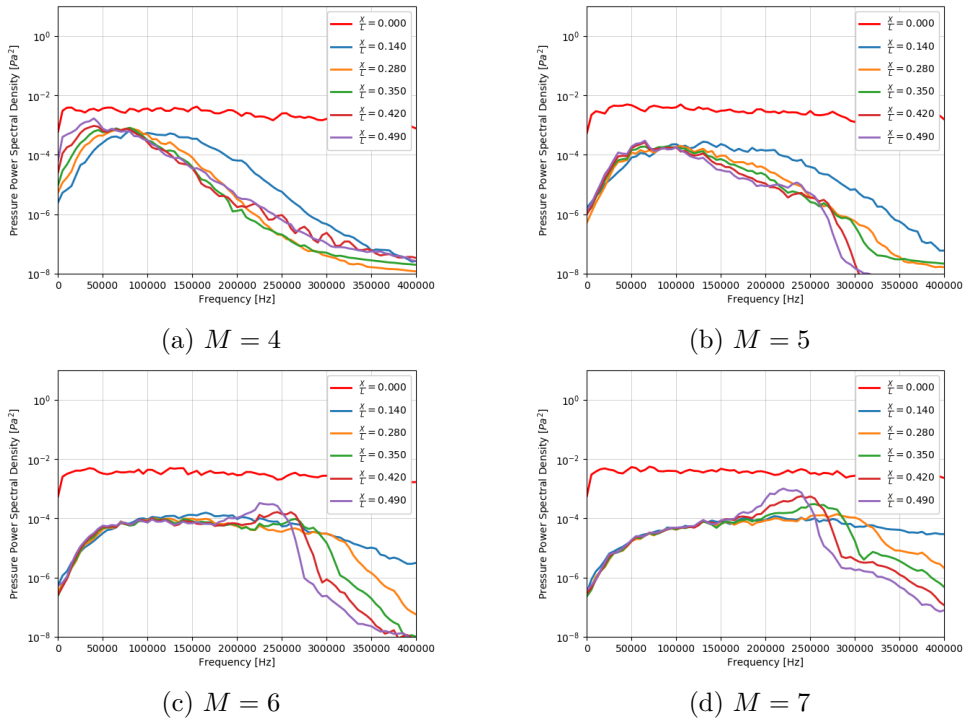


Figure 7.5: Pressure power spectral density for probes in the attached boundary layer along the cylinder.

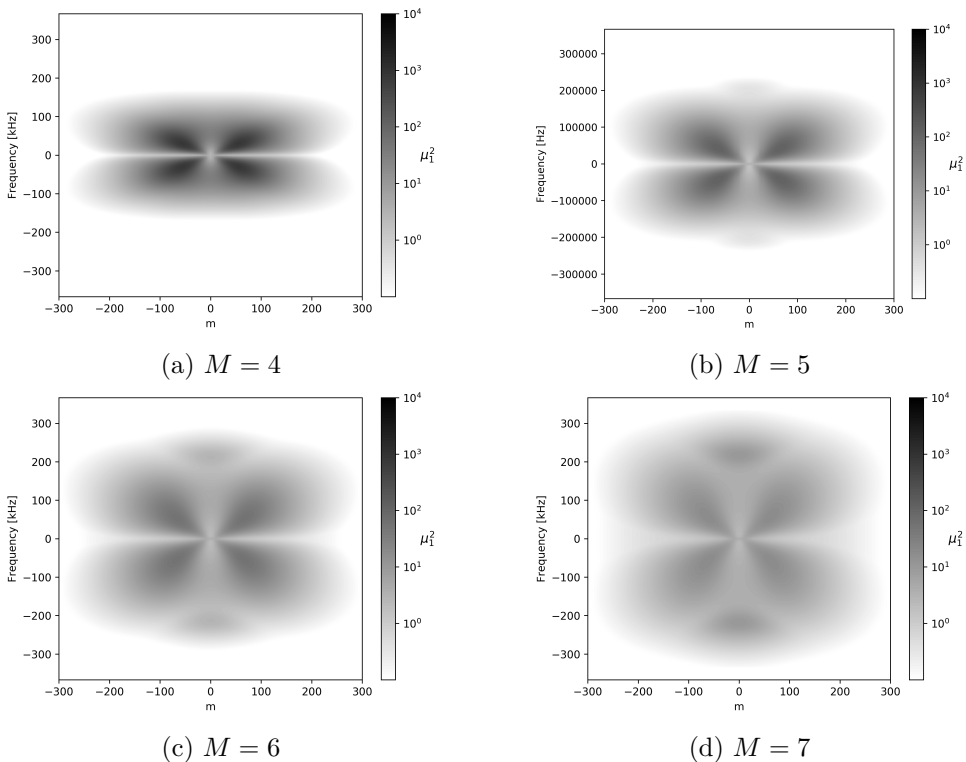


Figure 7.6: Resolvent gain for the boundary layer.

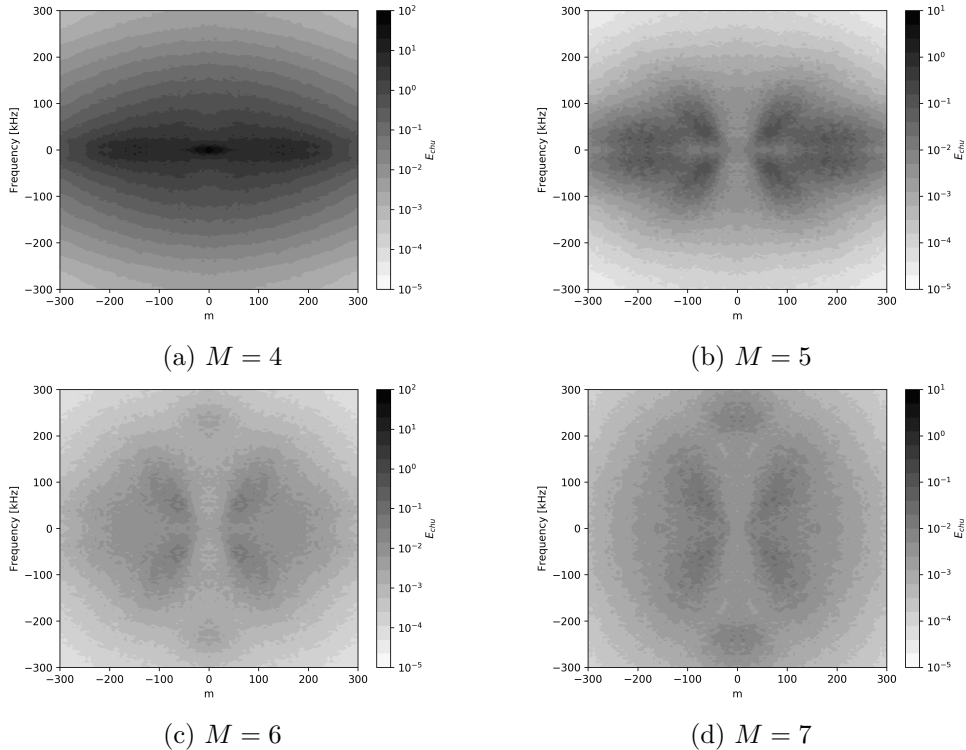


Figure 7.7: Map of the distribution of the fluctuation energy in the boundary layer from the DNS. Showing the zone where the fluctuations are the most energetic. The colormap is interpolated between background dots.

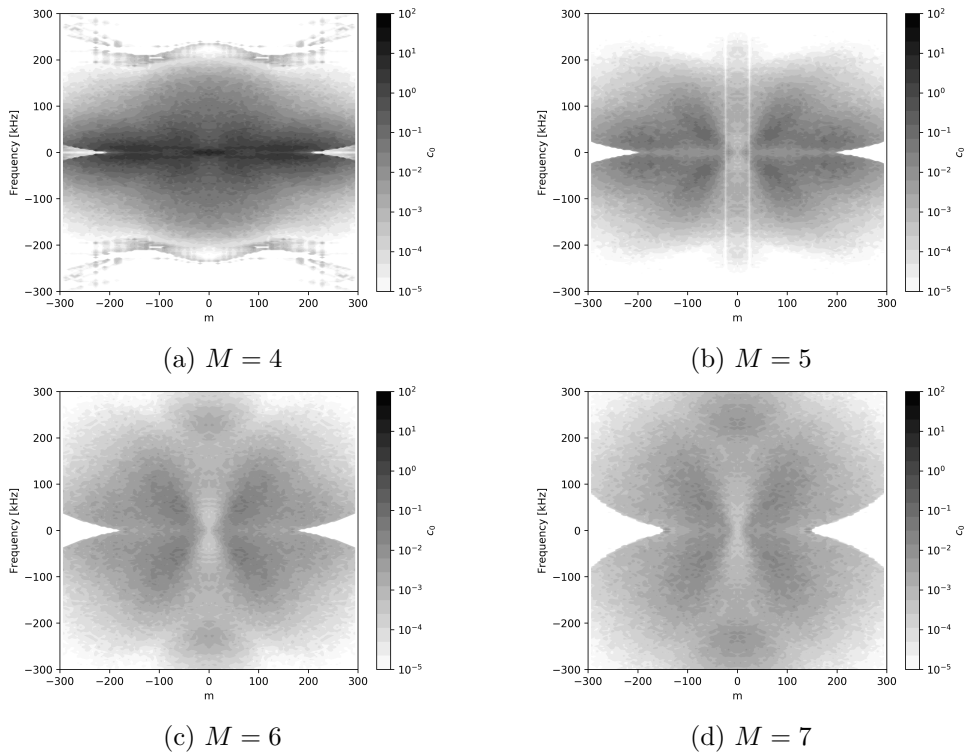


Figure 7.8: Map of the projection coefficient c_0 in the boundary layer region.

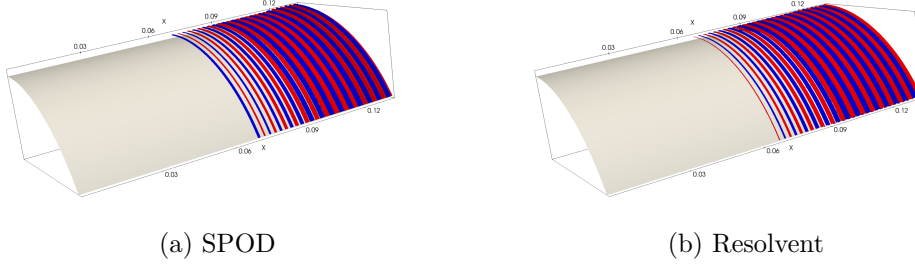
This behavior is due to the thickening of the boundary layer and is a standard feature of second mode. A slight amplification of second mode is also visible on the Mach 5 spectrum (b), while there is absolutely no high-frequency amplification for the Mach 4 case (a). It is also interesting to note that compressibility has no effect on the frequency of the second mode instability but only on the amplification rate, sensors located at the same position for the Mach 5,6,7 shows peaks roughly at the same frequency.

As already mentioned, the second mode is supposed to be a linear instability; thus the resolvent analysis should be able to predict it. The resolvent gain for the attached boundary layer of each case is presented in figure 7.6. Even if the predicted amplification is displayed on a frequency-wavenumber map, looking only at the amplification on the 0-wavenumber axis yields results in good accordance with the results of the pressure PSD presented in figure 7.5. For the Mach 4 case (figure 7.6), no amplification zone is present in the frequency range of second mode (200 – 250kHz). For the Mach 5 case, a slight gray zone start to appear in this range. This zone is getting darker as the Mach number increases, meaning that the linear mechanism gets stronger. This stronger amplification is linked with the displacement of the inflexion point. As the compressibility increases, the inflexion point moves away from the wall, leading to a stronger inviscid inflexional instability mechanism Özgen and KIrcallı, 2008. Considering the azimuthal wavenumber information shows that the second mode is as expected most amplified for a null wavenumber (axisymmetric structures) and then quickly decrease with an increasing wavenumber. These results were also found using LST by Özgen and KIrcallı (2008), which found that the second Mack mode amplification decreased rapidly when the instability angle increased. those results are also in good agreement with the original results of (Mack, 1975).

Energy distribution maps from the DNS are presented in figure 7.7 and can be compared to the resolvent gain maps. In the frequency range corresponding to the second mode, no energetic zone are visible neither for the Mach 4 case nor for the Mach 5 one. This is pretty coherent with PSD results, as the amplification for the Mach 5 case is only slightly visible for the Mach 5 case even with a logarithmic scale. For the Mach 6 case, a light spot appears on the same frequency-wavenumber range as the predicted amplification. This spot becomes clearly visible only for the Mach 7 case.

The leading SPOD mode and resolvent optimal response for the most amplified frequency presented Fig 7.9. They show structures that are perfectly similar, meaning that the resolvent analysis predicts the correct instability structures. As expected, it shows axisymmetric structures developing along the wall, which are typical of second mode structures. Those structures are pretty close from the ones visible in Q criterion of the boundary layer for high Mach number cases (figure 7.3). However, on the Q criterion, the structures are not perfectly axisymmetric (unlike the dominant SPOD mode, see figure 7.9) but are meandering. This is also predicted by the resolvent analysis and illustrated by the energy decomposition, as the energetic spots on the maps are not localized only on the $\omega = 0$ axis but are diffuse. This leads to non-axisymmetric second modes structures such as presented in figure 7.10 for $m = 6$. Those structure have a slight orientation angle and once again the SPOD mode and the resolvent response are very close, showing the good agreement between the linear prediction and the structures that actually grow in the DNS. The combination of all the linearly amplified axisymmetric and non-axisymmetric second mode structures present in the DNS can lead to structures such as seen in the Q criterion presented in figure 7.3.

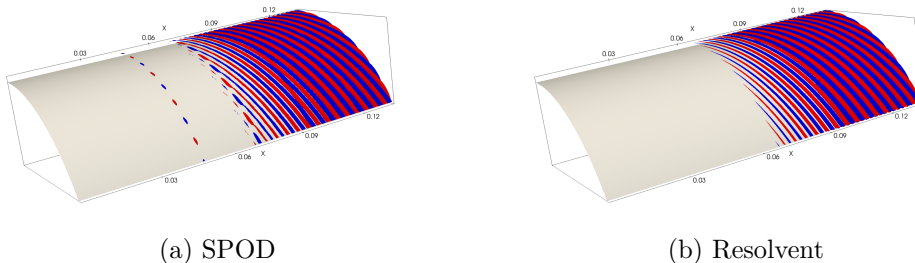
To conclude, for the second mode, compressibility increases the linear amplification. No second mode structures are present in the Mach 4 boundary layer, while the Mach 7 one has developed structures. Compressibility has no effect on the frequency nor the orientation angle of the second mode instability.



(a) SPOD

(b) Resolvent

Figure 7.9: SPOD mode (a) and resolvent optimal response for $m = 0$ and $f = 250\text{kHz}$, showing axisymmetrical second mode structures for the Mach 7 case.



(a) SPOD

(b) Resolvent

Figure 7.10: SPOD mode (a) and resolvent optimal response for $m = 24$ and $f = 250\text{kHz}$, showing non-axisymmetrical second mode structures for the Mach 7 case.

First Oblique Mode

Even if potentially of importance for high Mach number, second mode structures cannot be the cause of transition pre-reattachment in the low Mach number (4,5) cases as they are either not present or only slightly amplified. One other type of structure that has been identified in chapter 2 and seems to play an essential role in the transition for the Mach 4 case are the oblique first mode structures. Those structures are known from LST analysis to develop in compressible boundary layer Mack, 1975; Özgen and KIrcalı, 2008. Local stability results show that the critical Reynolds number for three-dimensional first modes (the oblique modes) at that mach number is always smaller than the critical Reynolds number of second mode instabilities (Özgen and KIrcalı, 2008). This could mean that the oblique modes could play an important role in all the cases presented here.

The identification of oblique first mode on parietal pressure is not straightforward. This is mainly linked to the fact that the first mode lies in the superior part of the boundary layer and does not create strong acoustic fluctuations, and explain why experimental results on hypersonic oblique modes are harder to find than on second mode instabilities. Parietal measurements are not sufficient anymore to accurately detect the instability. However, a low frequency amplification along the geometry is present for both PSD of the Mach 4 and 5 cases in figure 7.5 and could be linked to the oblique modes.

To get a better understanding of oblique modes and as they are known to be linearly amplified convective instabilities, one can look at the linear amplification predicted by the resolvent analysis figure 7.6. While the second mode was linked to the spot around $m = 0$ and $f = 230\text{kHz}$, the oblique modes are linked to the four oblique branches of the diagram as already discussed in chapter 6. A first interesting thing to note is that first oblique mode linear amplification is predicted for every case, which seems to be in accordance with the Q criterion figure 7.3. However, as the Mach number increases, oblique modes are amplified over a wider range of frequency (but in a similar range of wavenumber). While for the Mach 4 case, oblique modes are amplified

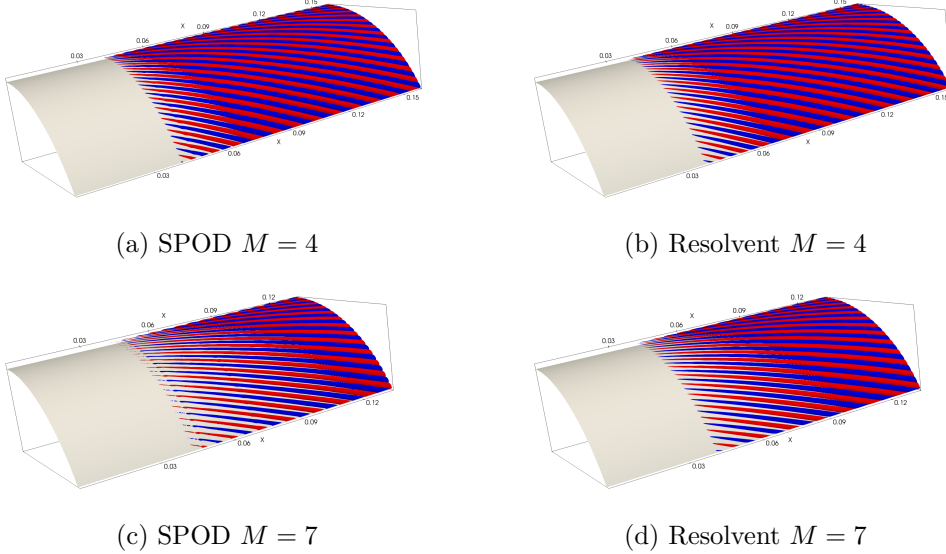


Figure 7.11: SPOD mode (a)-(c) and resolvent optimal response (b)-(d) for one of the most amplified oblique mode at Mach 4, $m = 78$, $f = 60\text{kHz}$ (a)-(b) and Mach 7, $m = 78$, $f = 90\text{kHz}$ (c)-(d).

M_∞	4	5	6	7
Wavenumber (m)	54	66	72	78
Frequency (f)	31, 6kHz	45kHz	62.5kHz	85.9kHz
Measured orientation angle (α)	65.6	67.5	67.7	67.6

Table 7.3: Characteristics of the most linearly amplified oblique mode in the boundary layer of each case.

mostly for $f < 100\text{kHz}$, for the Mach 7 case, they are amplified up to $f = 200\text{kHz}$. The first mode is also only amplified in its three-dimensional, or oblique, form (as there is no amplification of the branches for a null wavenumber); This is coherent with the results of Mack (1975) and Özgen and KIrcallı (2008), compressibility leading to an important decrease in amplification of two-dimensional first mode, even before reaching Mach 4.

Figure 7.7 presents the energy distribution from the DNS in the boundary layer. It is interesting to note that for the Mach 4 case, no zone corresponding to the first mode is visible on the map and that only a zone near the zero frequency axis emerge in a map where the energy is widely spread. This is simply because the boundary layer is transitioning, leading to a redistribution of the energy on a widespread spectrum by the turbulent cascade. The oblique branches corresponding to the linear amplification can be found on all other cases. For all of them, the energetic zone is in the same frequency-wavenumber zone as the predicted amplification.

Resolvent predicted structure and structures extracted from the DNS are presented in figure 7.11, it presents for the two extreme Mach number one of the amplified oblique mode. Once again, the structures present in the DNS are extremely close to the one predicted by the resolvent analysis. Even for the Mach 4 case where the energetic zone linked with first mode was not visible on figure 7.7, confirming the assumption that the first mode is present in the Mach 4 case but just not dominant in the boundary layer because of the transition (this will be further discussed in section 7.4)

In addition to that, no clear structural difference can be found between the Mach 4 and the Mach 7 oblique modes.

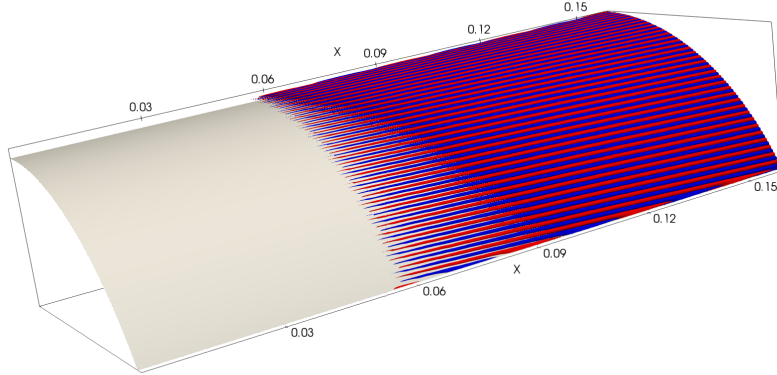


Figure 7.12: SPOD mode for energetic streaks at Mach 4, $m = 216$, $f = 20\text{kHz}$ in the laminar part of the boundary layer.

Table 7.3 presents the orientation angle of the most amplified oblique modes. This angle is measured from the leading SPOD mode of the most amplified oblique modes in the QDNS. The orientation angle is increasing between the Mach 4 and 5 cases, but then stabilize at a constant value of around 67° . This has been discussed by Özgen and KIrcalı (2008) who showed a Mach number independence for the most amplified wave direction past a Mach number of 4. They predicted a wavenumber of around 60° , which is coherent with the present results. Bugeat et al. (2019) also found a most amplified oblique at angle of around 70° for the supersonic ($M = 4$) boundary layer using resolvent analysis.

To conclude, first oblique modes are affected by compressibility as the amplification decreases with an increase in Mach number. The frequency range over which the oblique modes develop also increases. Apart from that, the oblique structures are present in every case and seems to be of importance in all of them. Apart from amplification, oblique modes are only slightly affected by compressibility in that range of Mach number, as the structures and orientation angle remain similar.

Receptivity of first and second mode to the injected noise

Now that the amplification of both the first and second modes has been discussed, it may be interesting to look at how the receptivity of those modes to the injected noise impact their growth in the simulations.

This can simply be done by comparing the gain map (figure 7.6) and the projection coefficient map (figure 7.8) for the two regions of interest (first and second mode region). Comparing qualitatively the maps, one can see that there is no significant discrepancies between the gain and the projection coefficient for those regions. From that observation, and with the assumption that non-linear terms do not impact first or second mode growth, one can conclude that the noise is not exciting preferentially any of those structures, which is comforting in the idea that it was designed correctly.

Streaks

The last type of structure that was spotted in the Q-criterion figure 7.3 and has to be studied is the streamwise elongated structure (streak). All the linear amplification region of the gain maps (figure 7.6) are already explained either by second mode or oblique first mode. Thus, no linear mechanism can be responsible for the energetic content of the streaks by itself. Yet, when looking at the energy distribution in the DNS for the “low” Mach number cases (4 and 5) figure 7.7 (a)

and (b), a highly energetic zone around the zero frequency axis for a wide range of wavenumber is clearly defined. An example of structure linked to that energetic zone is presented in figure 7.12. The fact that they develop in the QDNS, even if no linear amplification can directly cause them, means that they have to come from a non-linear mechanism (either totally or through the excitation of weak linear mechanisms, such as documented in chapter 6).

One can confirm the assumption that the streaks come from the non-linear excitation of weak linear mechanisms by looking at figure 7.8, which presents the projection coefficient. In the same way as what was presented in chapter 6, while there is no significant amplification of the streaks in the gain map 7.6, as soon as the non-linear forcing terms are considered, an amplification zone appears.

The streaks appear to be mostly amplified for the Mach 4 and 5 cases, where the oblique modes are sufficiently developed to lead to the apparition of clearly defined quasi steady streaks. However, the interaction also happens for the higher Mach numbers, the created streaks are simply not energetic enough to appear clearly on the energy distribution maps. Yet, energetic diffuse zones are still present between the diagonal branches of the map, which are a sign of non-linear interaction.

To conclude, streaks appears as the results of the non-linear interaction of oblique modes. In case where the oblique modes are sufficiently energetic, they become important structures of the boundary layer.

7.4 Impact on the transition scenario

Section 7.3 has shown how compressibility can affect the boundary layer instabilities. However, it is not clear how those differences can lead to the different transition scenario and flow topology described in section 7.2. This section aims at studying the amplification mechanism and interaction outside the laminar boundary layer to understand how transition is actually happening and how it is affected by the difference in boundary layer instabilities.

Mach 4 case, boundary layer transition

The fastest transition scenario is happening for the Mach 4 case. As seen in section 7.2, at the end of the attached boundary layer, the intermittency is already close to one. The study of the laminar part of the boundary layer has shown that oblique modes were the dominant linear instabilities and that they were responsible for the creation of streaks via a non-linear interaction.

For a “laminar” boundary layer, only a few types of instability are energetic, which leads to maps such as presented in figure 7.7 for the Mach 7 case with energy clearly contained in defined regions of the color map. In opposition, when the transition begins to happen, the structures break down and the flow is more and more disorganized, leading to a spread of the energy on a more diffused zone of the map such as visible for the Mach 4 map. However, even with the disorganization brought by the ongoing transition, there are still frequency-wavenumber couples that are more energetic than others. This is particularly true for a zone along the zero frequency axis, which is linked to streaks. When post-processed using SPOD, the structures linked to this region of the maps are similar to the one presented in figure 7.12. As already discussed, from figure 7.6 (a) no linear amplification seems to be able to contribute to those streaks. The map only shows a dominant mechanism for the amplification of oblique modes, with a gain several order of magnitude lower for the streaks. However, figure 7.8 (a) shows that when considering the non-linear forcing, a new region appears on the map for frequency around the 0 axis and a wide range of wavenumber. This shows that there is indeed a linear mechanism that amplifies the non-linearly created streaks. The results presented here shows that the non-linear interaction

is mandatory to trigger a linear amplification of streaks, as the linear mechanism alone is pretty weak. The map of projection coefficient is still quite different from the energy map in the DNS, this is expected as the flow is near turbulent, which is characterized by a lot of non-linear interaction and non-coherent structures (see Towne et al. (2018) for more details on the impossibility to represent a turbulent dynamic from a single resolvent mode). An illustration is that the leading SPOD mode for streaks in the “laminar” boundary layer contains more than 80% of the energy for that energy-wavenumber couple while the same leading mode for the full boundary layer (thus including turbulent part) represent only 40% of the energy while still being indisputably the dominant mode.

The scenario for the transition of supersonic boundary layer that could match the present case was proposed by Thumm (1991) and is linked to the scenario then described for incompressible channel flow by Schmid and Henningson (1992). It is also completely related to the scenario described in chapter 6. Again, after linear growth of oblique modes, a small non-linear energy transfer from oblique modes to streaks was enough to trigger a linear mechanism that would transfer energy from the mean flow to the streaks. This linear amplification would keep feeding energy to the streaks until they are sufficiently energetic and begin to lift from the surface, creating more complex structures such as hairpins and finally breaking down to create turbulence (Mayer et al., 2011). This kind of scenario was also studied recently by (Franko and Lele, 2013) and was found to be one of the fastest ways to create turbulence in high supersonic/hypersonic boundary layer.

The transition then happens when both mechanisms (linear and non-linear) have brought enough energy to the streaks to make them lift from the wall and break-down into turbulence. It is however not possible from the present results to know which mechanism is dominant in terms of energy, but the work of (Schmid and Henningson, 1992) shows that the non-linear transfers, even if essential for the scenario, are way less energetic than the linear one.

Mach 5-6-7 case, reattachment transition

The same transition scenario as the one presented in chapter 6 was drafted from the study of the 3 “high Mach number” cases (Mach 5,6,7). because of that, the results will not be presented in details here.

The main interesting conclusion that can be drafted from those results is that even with a strongly decreasing first mode amplification, and thus a decreasing non-linear excitation of the linear mechanism that amplifies streaks, this path to transition remains possible. While the transition scenario found here is consistent with other results on the subject such as those of Dwivedi et al. (2019), as the linear amplification mechanism may be the same as the one they are describing (*i.e.* a baroclinic effect, see section 2.1.1). However, this shows that the assumption that because the oblique modes are of low intensity the non-linear interaction cannot play an important role in the apparition of streaks may be incorrect and that in the same sense as what was proposed by Schmid and Henningson (1992), the non-linear stage is triggering a linear mechanism that would have been of greatly reduced intensity without it.

On the computation of second mode instability with AUSM schemes

It is important to note that in the simulations presented in this chapter, the second mode may be slightly underresolved. Resolvent gain presented in figure 7.13 shows how switching from a QDNS to a DNS type resolution impact the amplification of second mode waves. Using a QDNS grid leads to a slight underestimation of the second mode peak. The actual underestimation may be even more important, as the DNS grid is mostly refined in the turbulent region and not the boundary layer region. Some results may point to the fact that one could need as much as 50 points per wavelength to accurately predict the amplitude of the mode using AUSM(P) with

unlimited third order MUSCL reconstruction, due to the dissipation of the scheme. In fact, while around 10 points per wavelength seems to be enough to get the right perturbation profile, the growth rates seem to be way harder to converge.

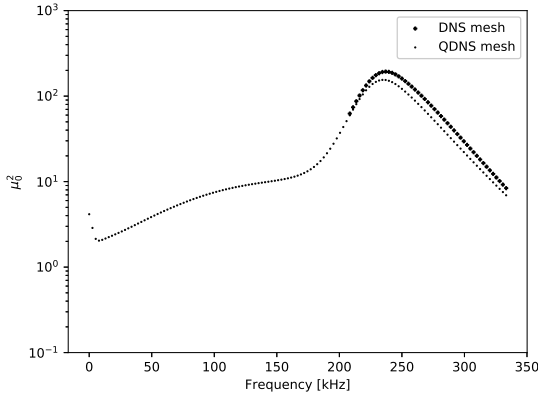


Figure 7.13: Grid convergence of the second mode gain for the Mach 6 case.

Because of that, for the Mach 7 case (and to a lesser extent, the Mach 6 case) one cannot conclude with complete confidence that the described transition scenario is the dominant one, as the second mode may actually be energetic enough to trigger other mechanisms. However, the study still allows to conclude that the scenario presented in chapter 6 is still relevant at Mach 7, we are just not assured that it will be the dominant one in those conditions. This however should not impact the conclusions drawn for the mach 6 case in chapter 5, the low perturbation (and hence the huge separation) lead to a boundary layer that develop over such a short distance that the second mode would have no chance to be involved in the transition process. The discussion about second mode for the Mach 5 case presented in chapter 6 also remains valid.

7.5 Conclusion

To conclude, the transition scenario presented in chapter 6 can occur for a wide range of Mach number. While the linear amplification of oblique first mode decreases with the increasing Mach number, leading to less non-linear seeding of the streaks, the linear mechanisms amplifying those streaks is strengthened by the compressibility, most probably because of the greater compression ratio at reattachment. While we cannot conclude on the dominance of this scenario in real conditions, it seems to be particularly relevant for separated compression ramp flow, even at high Mach number.

Chapter 8

Experimental results

The present chapter aims at presenting the results of the experimental campaign conducted in the R2ch facility. The campaign goal is to experimentally simulate a canonical transitional SBLI configuration to document the transitional instabilities and the change in topology of the flow. The study is a continuation of previous studies from Benay et al., 2006; Bur and Chanetz, 2009 and focus on the same geometry and overall similar flow conditions. The geometry is a cylinder of diameter $D = 131\text{mm}$ and length $L = 252\text{mm}$, followed by a 15° flare. The total length of the geometry is 350mm. The flow conditions for the runs that are going to be presented range from laminar flow at $Re_L = 4.0 \times 10^5$ to transitional flow for $Re_L = 1.14 \times 10^6$ with a ratio of more than 10 between the smallest and the largest Reynolds number presented. The main difference between the present study and already available results on that configuration from Benay et al., 2006 is the focus on the unsteady dynamics of the flow, with new unsteady measurements techniques such as described in chapter 4. The content of this chapter largely comes from an article that has been submitted for publication in the Experiments in Fluids journal.

Other Reynolds (from $Re_L = 2.0 \times 10^5$ to $Re_L = 2 \times 10^6$) and Mach ($M = 5$ and $M = 6$) numbers were explored during the experimental campaign to create a complete database. For the sake of conciseness, results from those runs are not presented in this chapter.

Contents

8.1	Flow topology	138
8.2	Streaks analysis	140
8.3	Shear-layer oblique modes	145
8.4	Conclusion	146

8.1 Flow topology

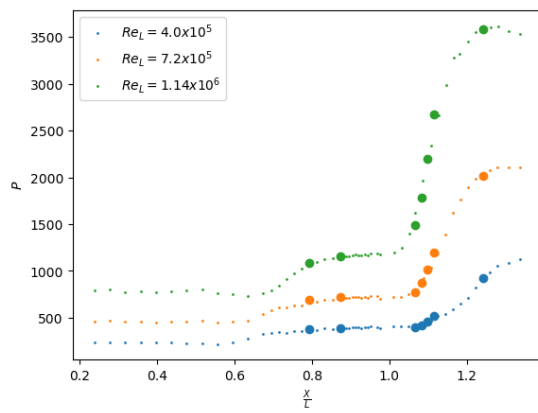
Let us first document the impact of the Reynolds number on the topology of the flow, and particularly on the recirculation region size. As the flow on this exact setup is already described in depth by Benay et al. (2006), only the information relevant to the present study will be presented in this section. Figure 8.1 presents the main indicators of the change in flow topology: time averaged wall pressure (a) and normalized pressure (b) distributions and mean (time and azimuthal average) heat-fluxes represented by Stanton number evolution along the model (c). As already documented by Benay et al., 2006 for a broad range of Reynolds numbers, the topology of the flow is strongly impacted by the Reynolds number change. First, the recirculation bubble, which is characterized by the pressure plateau after the first pressure rise, decreases in size while increasing the Reynolds number. The impact of the Reynolds number on the recirculation region size was also documented by Heffner et al., 1993 on a similar configuration. This reduction happens with both a downstream displacement of the separation point and an upstream displacement of the reattachment point. The upstream displacement of the separation point is well illustrated by figure 8.1(a) as the pressure rise caused by the separation happens sooner for lower Reynolds number. The downstream displacement of the reattachment point can be inferred from figure 8.1(c) and previous observation from Heffner et al., 1993, which have shown that the reattachment point position is located near the peak heat-flux position in transitional SBLI (according to Running et al. (2020) it is actually just upstream of the peak). The peak heat flux position is very clearly displaced downstream by a decrease in Reynolds number in the present experiments. Similar behavior of the separated region have also been documented numerically, albeit for increasing free-stream perturbations instead of Reynolds number, both for incompressible separated region (Marxen and Rist, 2010) and hypersonic SBLI separated region in chapter 3, showing that the transitional instabilities play an important role in the definition of the recirculation region size. Here, the same mechanisms can be at play, with transitional instabilities strengthened by the increase in Reynolds number instead of the increase in amplitude of the injected perturbations.

For all the cases presented here, the heat-flux peaks at a higher value than in the turbulent regime, which is typical of transitional flows. The transitional peak Stanton values on the flare, in the 10 – 25% higher than the turbulent Stanton value range, compares well with other experimental and numerical results (see for instance Benay et al. (2006), Heffner et al. (1993), Navarro-Martinez and Tutty (2005), and Vermeulen and Simeonides (1992)). The peak Stanton value of $St \sim 5 \times 10^{-3}$ is also coherent with the previous results of Benay et al. (2006). The displacement of the reattachment point and thus of the maximal heat-flux location is also illustrated by the heat-flux maps presented in figure 8.2.

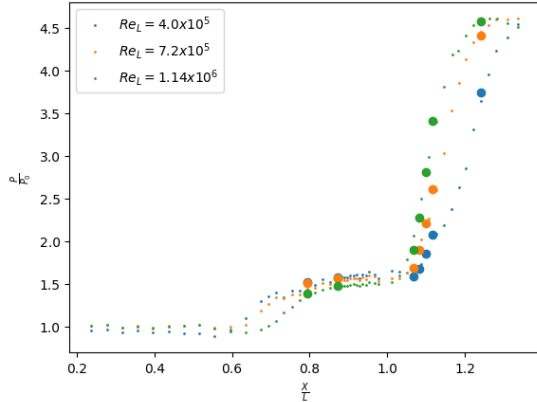
The evolution of state of the boundary layer on the flare for each case can be deduced from the results of figure 8.1; For the $Re_L = 4 \times 10^5$ case, at the end of the flare, the Stanton peak caused by transition is not over, meaning that the flow does not reach a fully turbulent state on the flare, and as such, the transition process is not fully over. For the two other cases, the Stanton number decreases after the transitional peak and reaches a steadily decreasing plateau on the flare, sign that the flow reaches a fully turbulent state.

It is worth to mention here that no clear evidence of SBLI unsteadiness was found in the present experiment, neither on full frame Schlieren imaging nor on the spectrums of pressure transducers located inside the bubble. Either there is not any low-frequency separated region motion or a very low amplitude one. As seen in chapter 5, the SBLI unsteadiness is also known to have a negligible impact on the transition process in noisy environment.

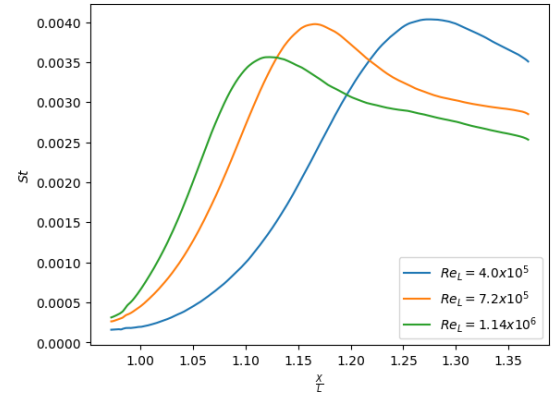
The next sections focus on the streaky pattern in the reattachment and the shear layer modes, on which the literature is more sparse.



(a)



(b)



(c)

Figure 8.1: Topology of the flow described by the mean wall pressure distributions (a)-(b) and mean Stanton number evolution (c).

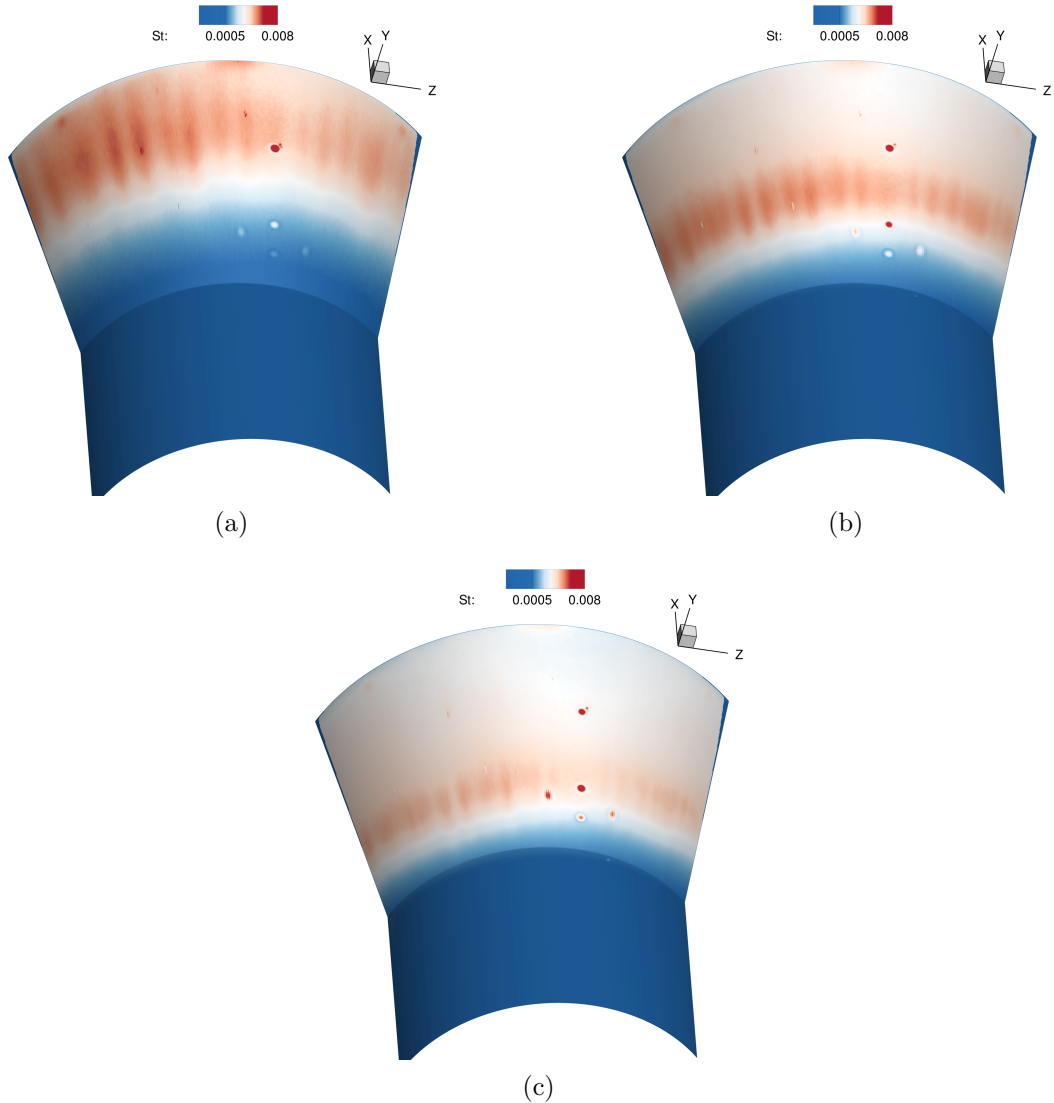


Figure 8.2: Mean Stanton number distribution from infra-red imaging for (a) $Re_L = 4 \times 10^5$, (b) $Re_L = 7.2 \times 10^5$, (c) $Re_L = 1.14 \times 10^6$.

8.2 Streaks analysis

A stated in the chapter 2, heat-flux striation is common in the reattachment region of SBLI and the origin of this phenomenon is still under debate.

The first interesting information to extract from the snapshots is the wavenumbers at which the streaks appear and how it depends on the Reynolds number. Looking at figure 8.2 already provides interesting information. For instance, the wavelength of the streaks seems to be decreasing along the intensity of the striation with an increase in Reynolds number. A similar trend was already described for laminar hypersonic SBLI by Aymer De La Chevalerie et al., 1997 as they noted a shift from high amplitude / low wavelength toward moderate amplitude and wavelength patterns with an increase in the Reynolds number. As the streaks break down and the flow become turbulent on the flare, the heat-flux striation disappear and is replaced by a uniform heat-flux distribution. Because of that, the length of the striated region is Reynolds number dependent: for the low Reynolds number case, the transition is never completed, and thus the streaks are visible from the reattachment point to the end of the model. For the high Reynolds number case, the streaks break-down to turbulence quickly and cause striation only on a small part of the model

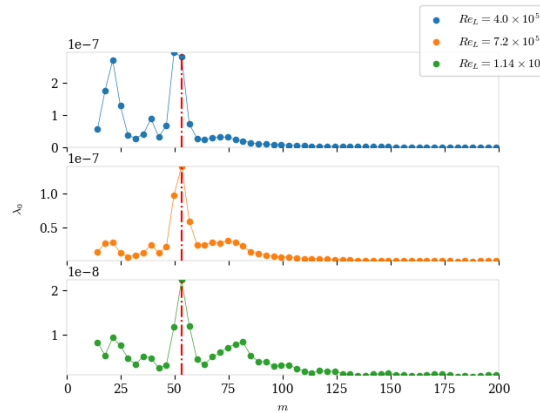


Figure 8.3: Energetic content of the streaky pattern against wavenumber for each Reynolds number. Computed from the azimuthal Fourier decomposition of infra-red images followed by POD (see 4.5.1)

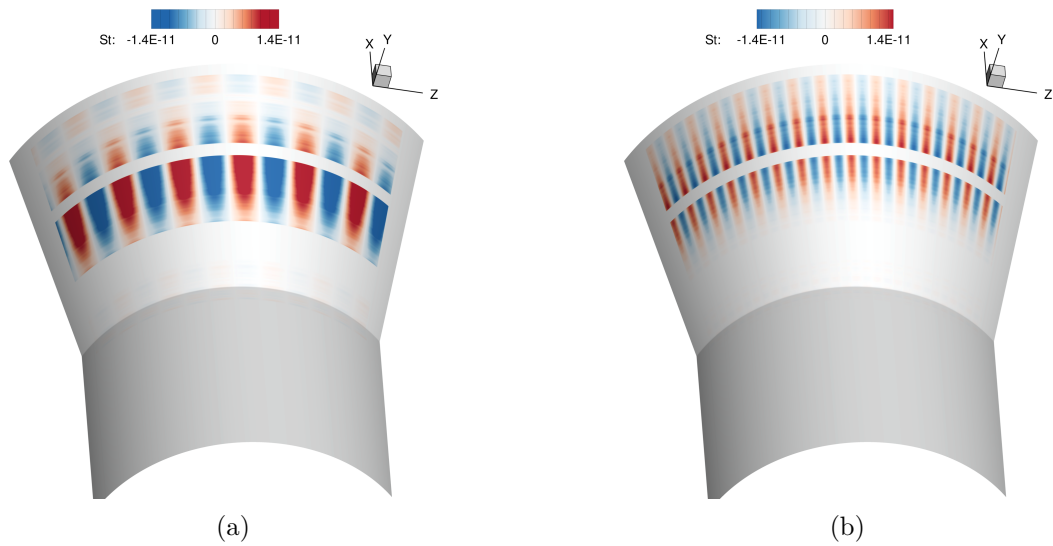


Figure 8.4: Reconstructed streaky pattern from most energetic modes at $Re_L = 4.0 \times 10^5$ (a) $m = 21$ and (b) $m = 57$. The masked bands correspond to region where the presence of PCB sensors makes the computation of the azimuthal Fourier decomposition impossible. The amplitude of the mode is arbitrary.

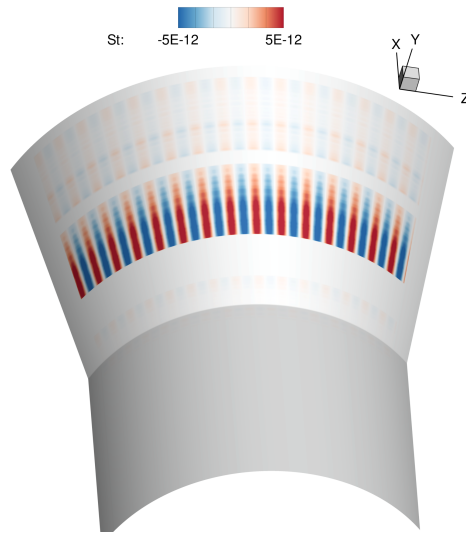


Figure 8.5: Reconstructed streaky pattern from most energetic modes at $Re_L = 7.2 \times 10^5$ ($m = 57$). The masked bands correspond to region where the presence of PCB sensors makes the computation of the azimuthal Fourier decomposition impossible. The amplitude of the mode is arbitrary.

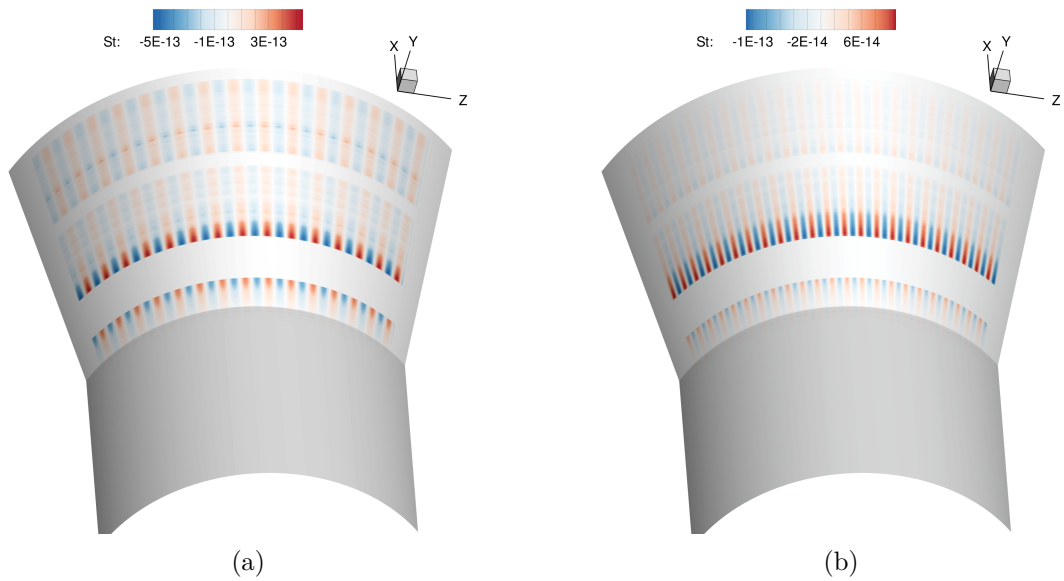


Figure 8.6: Reconstructed streaky pattern from most energetic modes at $Re_L = 1.14 \times 10^6$ (a) $m = 57$ and (b) $m = 81$. The masked bands correspond to region where the presence of PCB sensors makes the computation of the azimuthal Fourier decomposition impossible.

near the reattachment point. A similar behavior was also observed by Roghelia et al., 2017 for increasing ramp angle.

To get quantitative information on the dominant wavelength (or wavenumber), one can follow the procedure described in section 4.5.1 to post-process the instantaneous IR images.

Figure 8.3 present the energy of the leading POD mode against wavenumber for each Reynolds number. One has to be careful about the interpretation of the absolute value of λ_0 presented in this figure. The azimuthal decomposition cannot be computed in region where discontinuities are presents. Consequently, azimuthal slices of the images containing PCB sensors have to be masked. As the reattachment region position is dependent on the Reynolds number, the presence of the mask will lead to energetic levels in the spectrum that are not comparable from one Reynolds number to the others (as the maximum peak heat flux may be masked for the high Reynolds number case and not for the low Reynolds number case).

First, a peak at $m = 21$ is present in the low Reynolds number flow, this peak disappears when the Reynolds number increases. Then, another highly energetic peak appears at $m = 51$ for all the studied cases. The wavenumber of this peak is completely independent of the Reynolds number (and thus of the size of the separated region). Finally, a third energetic zone appears with the increase in Reynolds number for a large band of wavenumber around $m = 81$ which become more and more significant with an increase in Reynolds number.

Then, three different peaks have been identified of figure 8.3. Those peaks may be linked with different physical mechanisms. To get insight on the striation pattern they are linked with, figures 8.4, 8.5 and 8.6 presents the streak pattern linked with those peaks reconstructed from the leading POD mode. First figure 8.4 (a) present the pattern at $m = 21$, it displays a longitudinal "periodicity" of heat flux in addition to the obvious azimuthal one. The region of positive heat flux variation at reattachment is followed by a region of negative variation on the edge of the flare. Hildebrand et al., 2018 showed in their numerical work that global unstable modes presents in the recirculation region of transitional hypersonic SBLI could lead to such alternate pattern in the longitudinal direction, which lead us to the assumption that the mode at $m = 21$ is caused by such a global mode, the same behavior can also be seen on the mode R presented in chapter 5.

For the $m = 57$ pattern, which is presented 8.4 (b), 8.5 and 8.6 (a), the longitudinal pattern completely disappears, hinting that this mode may not be linked with the same physics. Dwivedi et al., 2019 and chapter 6, showed that convective modes do not display such pattern. As such, the mode at $m = 57$ could be linked to convective mechanisms. However, Cao et al., 2021 proved that non-linear saturation of unstable global modes could also lead to streaks which do not display any alternate pattern past reattachment. In that context, mode $m = 57$ could be either linked with convective, or non-linearly saturated global modes. The hypothesis that they could be caused by a centrifugal mechanism such as initially proposed by Benay et al., 2006 may be relevant in that case, as Görtler vortices can be extremely receptive to leading edge geometrical imperfection (Roghelia et al., 2017). This could explain why the wavenumber is not condition-dependent.

For the third amplification at high wavenumber ($m \sim 81$), the dominant mode at $m = 81$ for the $Re_L = 1.14 \times 10^5$ is presented in figure 8.6 (b), again it does not display any longitudinal pattern. There are two hints that point out to the fact that this mode could be a purely convective mode: first it displays energetic content over a wide range of wavenumber (which is often the case for convective modes that act as noise amplifiers) and second, it seems to be more and more dominant with an increase in Reynolds number.

This study has unveiled the presence of different types of striation patterns on the flare. It points towards the idea that multiple mechanisms could be at play in the creation of streaks. Some

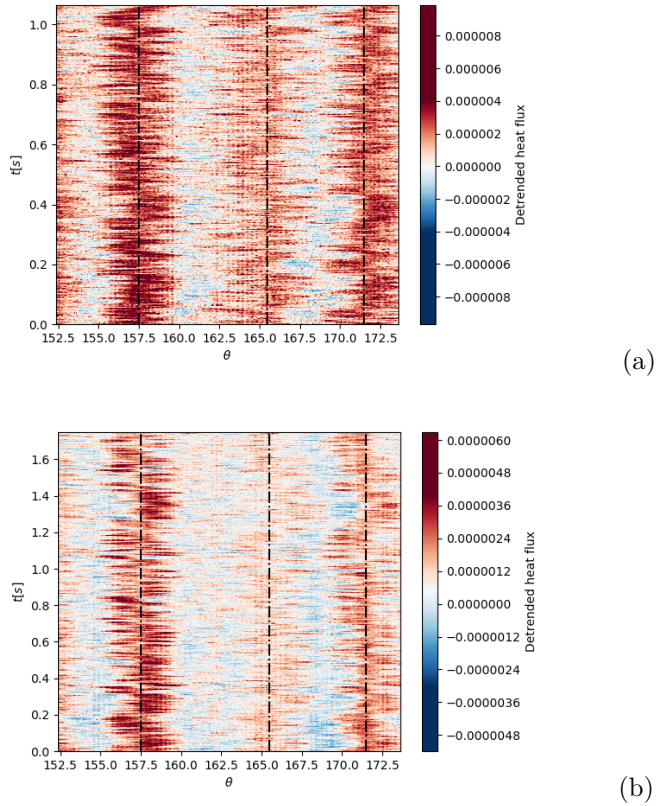


Figure 8.7: Time evolution of azimuthal heat-flux distribution measured with the infra-red camera at 1000Hz at $Re_L = 7.2 \times 10^5$ (a) and $Re_L = 1.14 \times 10^6$ (b) . The dashed lines represent the centerline of high-heat flux streaks.

partial evidences point out the fact that at least one of the mechanism is linked with a global unstable mode. There are also signs of the presence of convective amplification mechanisms.

Now that the dominant modes linked with streaks are identified, one would wonder about their temporal behavior. To get information on that behavior, IR imaging was conducted on reduced part of the model at higher sampling frequencies (972Hz, see section 4.5.1). Figure 8.7 presents the temporal evolution of the flux along an azimuthal line situated near the reattachment point for the Reynolds $Re_L = 7.2 \times 10^5$ run (a) $Re_L = 1.14 \times 10^6$ run (b). One can see the signature of the dominant streaks ($m = 51$), this signature is not constant in time but seems to be meandering. While the time resolution is not enough to accurately describe the full motion of the streaks, one can already draw some interesting conclusions from that. First, the streaks are not steady. However, they are not fully unsteady, and they seem to be moving only slightly around their mean position. They are neither rotating nor entirely changing position. This leads to similar (but improved) conclusion compared to the one previously obtained (Benay et al., 2006), while they were not wrong about the presence of "steady" streaky pattern on the flare, the oil flow visualization that they used did not allow to conclude on the small unsteadiness around the mean position measured in the present study. Another interesting information brought by the comparison of figure 8.7 (a) and (b) is that the centerline of the $m = 51$ streaks is Run and Reynolds-independent, which can only reinforce the hypothesis that they are linked with receptivity of geometrical imperfection of the model.

8.3 Shear-layer oblique modes

The last important features of the flow under study are the structures in the shear layer which are visible in the Schlieren images presented in figure 8.8. The images are relatively hard to interpret as the low density of the flow leads to very low contrast. However, one can still see that there seems to be some structures traveling in the shear layer that could be studied using SPOD, to get a better idea on the unsteady nature of the structure. It should be noted that compared to two-dimensional studies (Chuvakhov et al., 2017; Yang et al., 2012), our axisymmetric model minimize the integration effect of the Schlieren measurement and thus the spatial averaging of shear layer structures. Figure 8.9 shows the pre-multiplied energy content of the SPOD leading mode against frequency. The noise floor of the camera (which is constant with frequency) is displayed as a dotted line for each run, it shows that the increase in energy in the last part of the pre-multiplied spectra is only due to this constant noise floor. This information allows us to conclude that there is no physics that can be captured with those settings at higher frequencies (the motion blur caused by the $1\mu\text{s}$ exposure time acts as a low pass filters) and that the spectra are most probably free of aliasing. The spectra display broad peaks that span over more than $\sim 10\text{kHz}$, which frequencies increase with the Reynolds number.

The leading modes associated with the maximum energy of those peaks are presented in figure 8.10. For every case, the leading mode displays alternating oblique structures which are located in the shear layer on top of the bubble. When the Reynolds number increases, and as the frequency increases, the mode becomes of shorter longitudinal wavelength. From the SPOD results, one could make several hypotheses about the physics of this mode. First, the broad spectra points toward the fact that they originate from a convective mechanism and are subject to receptivity. From there, and giving their localization in the shear layer and their convective nature, one can make the hypothesis that they are compressible oblique supersonic shear-layer instabilities, which are well documented in the numerical literature (Foysi and Sarkar, 2010; Kudryavtsev and Khotyanovsky, 2005; Sandham and Reynolds, 1990). The frequency range of those instabilities is coherent with previous numerical results (see chapter 6) which documented such shear layer oblique convective modes in a similar case.

The leading mode also displays close to no signature in the near-wall region. So, one could expect that the pressure transducers will not be able to fully capture the dynamic of the mode. Figure 8.11 shows the pre-multiplied pressure power spectral density measured by a Kulite and a PCB sensor located at reattachment. First, the bandwidth of the Kulite sensor is very limited. the energetic content of fluctuations measured with the Kulite sensors starts to decrease before 10kHz while the one measured by the PCB is still increasing. As the bandwidth of the sensor is expected to be much less limited, thorough investigation was conducted to try to find the origin of this low-pass filtering characteristics. The acquisition system, the pressure reference regulation and the wiring were all tested and are not causing this loss of signal in the high-frequency region, which thus has to come from the sensors themselves and particularly from the protective screen, the resonant space between screen and sensitive cell or the integration of the sensor on the model. One might perform dynamic calibration of the sensor to check or qualify the real bandwidth. This may be caused by the operating conditions (very low pressure), or the way the sensor is mounted, but we cannot give a clear cause for this behavior. The PCB spectra is broadening towards high-frequency with increasing Reynolds number, showing sign that the flow is becoming turbulent for the two highest Reynolds number, which is in good accordance with the conclusion of section 8.1. For the lowest Reynolds numbers, a large peak is visible around 20kHz and is also visible on the spectra of the intermediate Reynolds number for slightly higher frequencies. Even if it is at higher frequencies than the oblique mode in the shear layer, this peak could be a trace of those structures as the frequency may increase at reattachment were the boundary layer is compressed. Figure 8.12 presents the pre-multiplied pressure power spectral density measured by a Kulite pressure transducer located inside the recirculation bubble. Given the limited bandwidth

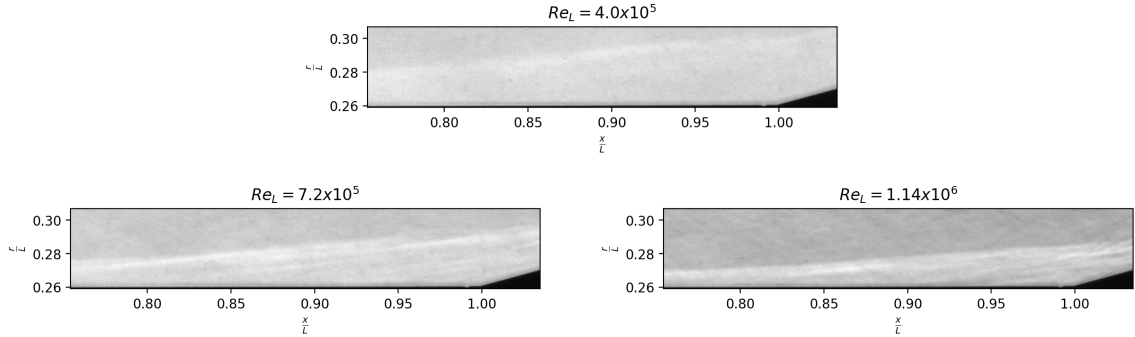


Figure 8.8: Instantaneous Schlieren images.

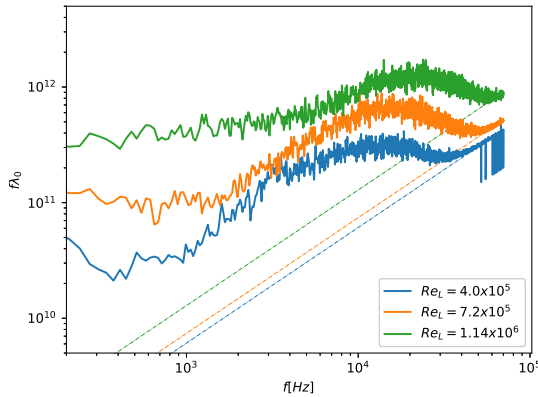


Figure 8.9: Pre-multiplied energy level λ_0 of the leading SPOD mode against frequency for all the Reynolds numbers. The dashed lines correspond to the noise floor of the camera.

of the sensor already discussed and the fact that the waves are traveling in the shear layer and not in the near wall region of the bubble, the interpretation of those spectra may be misleading. It is still interesting to note that there is a broad peak in the $1 - 10\text{kHz}$ range, with a frequency increasing with the Reynolds number.

The comparison with the SPOD results is not straightforward as the SPOD gives spectrum of the integrated energy while the sensor is more localized. Pixels near the sensors located in the bubble (the one at reattachment is not visible on the images) could be used to compute a localized version of the Schlieren spectra to give a good comparison, however, the signal-to-noise ratio is extremely low in that region and the resulting spectra impossible to interpret. Keeping those limitations in mind, one can still point towards the similarity between the Schlieren and pressure transducers spectrums, the peak is in a somewhat similar frequency range and the frequency increases with Reynolds number with both techniques.

To conclude, shear layer modes were identified using Schlieren imaging and seems to be the dominant instability in the shear layer on top of the bubble. Pressure transducers on the surface of the model bring no conclusive evidence of the existence of those modes, probably because the modes do not cause strong fluctuations in the near wall region.

8.4 Conclusion

To conclude, the IR imaging showed the presence of streaks in the reattachment region at different wavenumbers. The in-depth study of those streaks and comparison with numerical results from the literature brought conclusive evidence on the fact that they could be linked with dif-

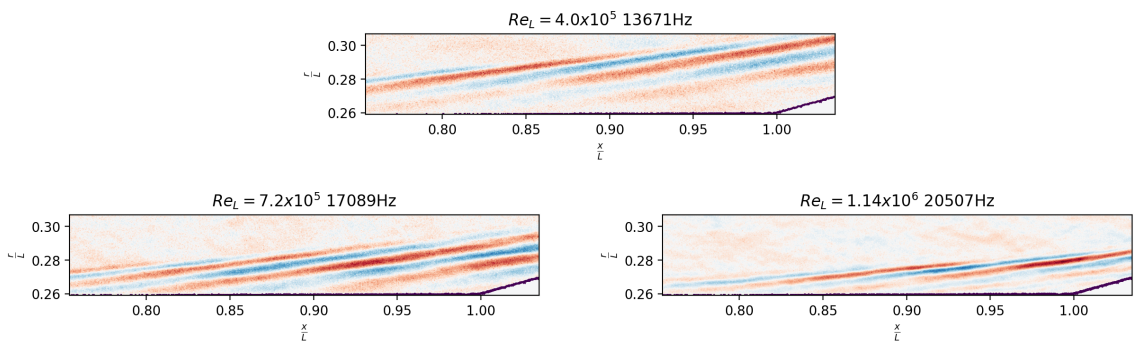


Figure 8.10: Most energetic leading SPOD mode linked with oblique shear layer modes for all the studied Reynolds number.

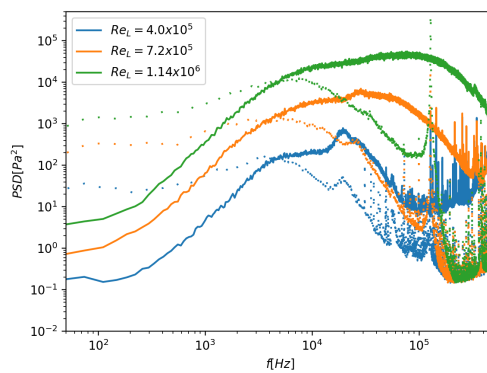


Figure 8.11: Pre-multiplied pressure power spectral density from the Kulite 4 sensor (dotted) and the PCB 1 sensor (line) on the flare for all the Reynolds numbers, showing the limited bandwidth of the Kulite sensors.

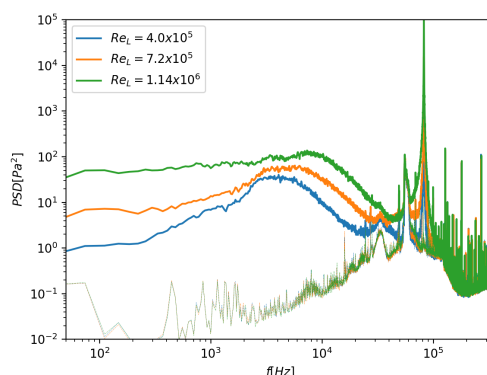


Figure 8.12: Pre-multiplied pressure power spectral density from the Kulite 2 sensor (line) and pre-run noise level (dashed) inside the recirculation region for all the Reynolds numbers.

ferent physical mechanisms, either linked with global or convective linear mechanisms. Mixing layer modes, identified as oblique supersonic shear layer structures, were identified using Schlieren imaging and are the dominant instability in the shear layer on top of the recirculation region. Those modes are found to have a very low-pressure signature at the wall, making their identification via pressure measurements complex. The role that the mixing layer modes and the streaks play in the transition process is still unclear, but the present study tends to show that either one of them or a combination of both may be at the origin of the transition. Precise numerical reproduction of those experiments would be necessary to accurately describe the transition process and to assess whether the constant-wavenumbers streaks are due to the leading edge geometry or to a physical mechanism that is fully independent of the Reynolds number.

Chapter 9

Numerical-experimental comparison

This chapter presents the results obtained when trying to numerically recreate some experimental results obtained in the R2ch facility. This includes first trying to understand and recreate free-stream fluctuations from the facility, and then computations which aim at getting a flow as similar as possible to the one observed during the experimental campaign.

Contents

9.1 Wind tunnel free-stream fluctuations	150
9.1.1 R1Ch runs	150
9.1.2 R2Ch runs	151
9.1.3 Possible improvement	151
9.2 Experimental results for the previously studied conditions	152
9.3 Numerical simulation of an experimental run	152
9.3.1 Simulation of the flow topology	153
9.3.2 Reproduction of the dynamics	155
Pressure fluctuations	155
Streaks	156
9.3.3 Conclusion	157

9.1 Wind tunnel free-stream fluctuations

As presented in chapter 2 and section 3.1.4, the measurements and modeling of wind tunnel (WT) free-stream fluctuations is a mandatory step to be able to accurately numerically reproduce WT experiments. While there is plenty of both experimental and numerical results in the literature on hypersonic transition, only few published articles manage to get a good agreement between the two means of investigation. This is mainly due to the difficulties linked with the reproduction of the free-stream fluctuations. This section focuses on the measurements using the cone presented in section 4.6 that have been conducted in the R1Ch and R2Ch facilities to get information about those fluctuations, and the first attempts to numerically reproduce the experiments that were conducted on the cylinder-flare model (see chapter 8). It also summarizes future work that may be conducted based on those results.

9.1.1 R1Ch runs

Due to facility availability, the free-stream measurement campaign was started in the R1Ch blowdown facility. The facility is overall very similar to R2Ch, albeit it is designed for lower Mach number (here a Mach 3 nozzle is used) and lower stagnation pressure and temperature. Another big difference is that the R1Ch facility underwent massive development in the early 2000 towards making it a quiet Mach 3 tunnel. This included the addition of a settling chamber upstream of the nozzle and a boundary layer suction at the throat of the nozzle (see Benay and Chanetz (2004)). In the runs presented in this chapter, the throat suction is not used, but the flow is still going through the settling chamber. So, we expect the flow in the R1Ch facility to be quieter than the flow in the R2Ch facility.

Table 9.1: Wind tunnel static pressure fluctuations measured with the 5° cone in the R1Ch facility.

Wind tunnel	M	P_i	T_i	P_{rms}
R1Ch	3	$1 \times 10^5 \text{ Pa}$	280K	7% _{oo}
R1Ch	3	$1.8 \times 10^5 \text{ Pa}$	280K	6% _{oo}
R1Ch	3	$2.7 \times 10^5 \text{ Pa}$	280K	6% _{oo}
R1Ch	3	$3.7 \times 10^5 \text{ Pa}$	280K	6% _{oo}
R1Ch	3	$4.8 \times 10^5 \text{ Pa}$	280K	7% _{oo}

A summary of the runs is presented in table 9.1, showing that at low stagnation pressure, R1Ch create surprisingly quiet flows, with mean static pressure root-mean-square fluctuations of around 7%_{oo}. Spectra of the measurements are presented in figure 9.1. The peak around 250kHz in the PCB spectrum is due to the resonance of the sensor and not to physical instabilities (see section 4.4), the rest of the signal is supposed to be due to the free-stream perturbations. Figure 9.1 shows that the actual free-stream fluctuations is not comparable to a white noise as the spectrum is not flat but biased towards low frequency.

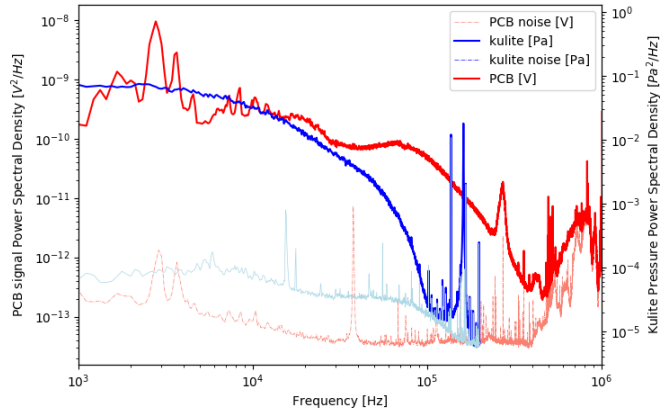


Figure 9.1: Spectra from the Kulite and PCB (B38 with an added layer of epoxy) sensors for a run in R1Ch at $M = 3$, $P_i = 2.7 * 10^5 \text{ Pa}$, $T_i = 280\text{K}$.

As the radiated noise from turbulent nozzle boundary layer is known to increase drastically with the Mach number (LAUFER, 1961). Runs have to be made at Mach 5 in R1Ch before concluding definitively on the impact of the settling chamber design.

9.1.2 R2Ch runs

Runs in the R2Ch have also been conducted and are summarized in table 9.2. They show that for transitional Reynolds numbers (similar to those of chapter 8), the free-stream pressure fluctuations amplitude does not vary with the stagnation pressure and remain close to 1.5%.

Table 9.2: Wind tunnel static pressure fluctuations measured with the 5° cone in the R2Ch facility.

Wind tunnel	M	P_i	T_i	P_{rms}
R2Ch	5	$1.29 * 10^5 \text{ Pa}$	408K	1.7%
R2Ch	5	$2.44 * 10^5 \text{ Pa}$	388K	1.5%
R2Ch	5	$6.43 * 10^5 \text{ Pa}$	532K	1.5%

9.1.3 Possible improvement

The free-stream measurement campaign represents a pilot study designed to assess whether a project can be launched at ONERA to get a better understanding of the hypersonic blowdown wind tunnels free stream flow. In the future, both numerical and experimental work will be planned:

- Numerical simulation of the flow around the cone subject to perturbations (or of new probes, as new probes design are not excluded yet) will be conducted to get an idea of the transfer function of the shock and boundary layer. Optimally, this should allow to use the inverse transfer function to get free-stream information from the measurements on the cone (see Schilden and Schröder, 2017 for instance). This step could also be conducted using the resolvent operator as a linear transfer function, if the non-linear effects of the shock and boundary layer on the perturbation are supposed small enough.
- More traditional measurements of the fluctuations, such as pitot probes pressure measurements (see Masutti et al., 2011 for instance) could be conducted to allow for easier comparison with other wind tunnels.

- To get information on other fluctuating quantities, velocity and temperature fluctuations measurement could be conducted using dual hot wires (with different overheat ratios to distinguish the velocity fluctuations from the temperature fluctuations, see Masutti et al., 2011).
- Density field high-frequency fluctuations measurements could also be conducted using Focused Laser Differential Interferometry (FLDI) setups (see for instance Fulghum, 2014).

In addition, it may be extremely interesting to have a reduced order model of the noise for injection in numerical simulations. This kind of model could be created starting from simple physical hypothesis on the form of the fluctuations such as proposed in the AVT-240 report (Paredes et al., 2018) (*i.e.* acoustic, entropic, vortical fluctuations of several frequencies/wavenumbers). The parameters of such models could then be optimized using data assimilation to match the experimental results on the cone. This would allow us to create inflow perturbations models that could be injected to reproduce the free-stream of the wind tunnel and that would not be case-dependent.

9.2 Experimental results for the previously studied conditions

While the stagnation conditions studied in chapter 5 and 6 are achievable in the R2Ch facility, as thoroughly discussed in this thesis, the injected noise chosen for those computations is far from being close (in shape or amplitude) to the free-stream noise of the facility. As stated in the previous chapters, the flow topology departs completely from the one studied experimentally. The decrease in perturbation level leads to the growth of the size of the separated region (see figure 3.3). This creates the topology discrepancies presented in figure 9.2. In that context, it makes little sense to try to compare the dynamics of both the numerically and experimentally simulated flows. Especially given the high impact of the separation on the transitional dynamics that was presented in chapter 6.

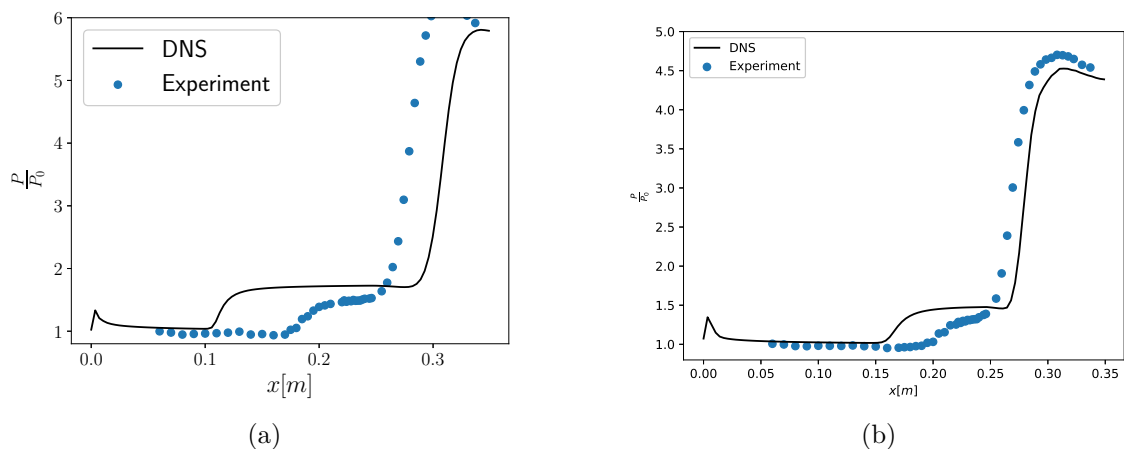


Figure 9.2: Comparison of the numerical and experimental results for operating conditions corresponding to $Re_L = 1.9 \times 10^6$ for (a) $M = 6$ chapter 5 (b) $M = 5$ chapter 6.

9.3 Numerical simulation of an experimental run

Given the conclusions of the previous section, a moderate Reynolds number run has been chosen to be studied numerically, the flow conditions are summarized in table 9.3. The chosen conditions offer numerous advantages:

- The Reynolds number is lower than on previous numerical study presented in this thesis

(while the mesh is kept the same, see 3.2), so we can be confident in the correct numerical convergence even for the smaller scale structures as the resolution get close to the DNS one, even in turbulent region.

- The pressure is still high enough to avoid numerical stability problems while injecting the white noise.
- The experimentally simulated flow still displays a large separated region.
- The frequency of the instabilities is in the range than can be measured using both the pressure transducers, and the V2640 camera.

M_∞	5
$T_{stagnation}$	547 K
$P_{stagnation}$	4.14×10^5 Pa
P_∞	783 Pa
Re_L	1.1×10^6

Table 9.3: Free-stream conditions and characteristic values for the experimental/numerical comparison.

Given the conclusions of chapter 5, a simulation on a 15° domain can then be conducted to try to recreate the experimentally simulated flow. This computation corresponds to the case G in table 3.2.

The injected noise for this simulation is a filtered version of the white noise as presented in section 3.1.4, the filter is a simple 3D kernel: the 3 directions of filtering being j, k and time, the kernel is a normalized 3D version of $[1, 2, 4, 16, 4, 2, 1]$.

The rms of the injected noise has then been chosen so that the topology of the simulated flow matches the experimental one, leading to a value of $A = 0.0074$ or 7.4% (see equation (3.10)).

9.3.1 Simulation of the flow topology

The first objective is to find out whether it is possible to recreate the flow topology found in the experiments with only a generic inlet noise, or if one needs a more complex noise with more physical insight coming from wind tunnel free-stream measurements.

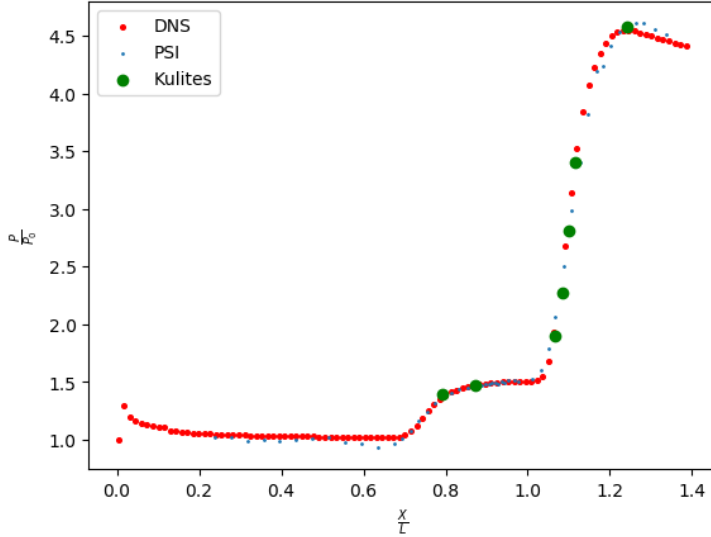


Figure 9.3: Comparison of the numerical and experimental pressure distributions, showing that the numerical simulation gives the same separation and reattachment point positions, in addition to correct pressure values on the whole extent of the domain.

After several attempts looking for the best possible level of white noise, a good agreement was found between the numerical simulation and the experiments for the pressure distribution along the geometry (see figure 9.3) for a noise level of $A = 0.74\%$ (one has to keep in mind that since the noise is filtered, the interaction with the numerical scheme will change, and thus this amplitude is not directly comparable to the one presented for unfiltered noises in previous chapters). The computation is not only fully able to predict the correct separation and reattachment points, but also the correct pressure level all along the geometry. This results alone is already encouraging, given the sensitivity of the separated region size to noise that was documented in chapter 6.

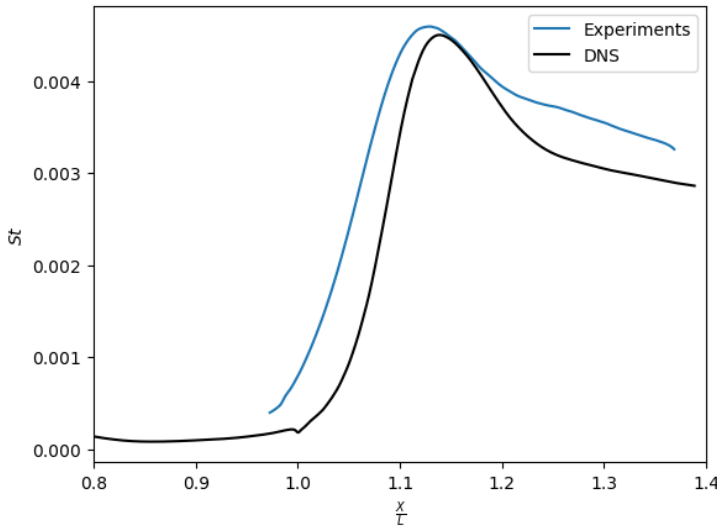


Figure 9.4: Comparison of the numerical and experimental heat flux distributions, showing that the numerical simulation predicts the correct heat-flux peak. The discrepancy in the reattachment position results from the fact that different runs are used for the pressure distribution measurement and the full frame heat-flux measurements, the small unwanted change in operating conditions of the wind tunnel and thus the Reynolds number leading to a small change in reattachment position.

However, as pressure is only an indicator of the fact that the computation can reproduce the overall topology of the flow, we have no information on if the transitional increase of heat-flux is correctly computed, sign that the same transitional process as the one happening in the experiment is accurately simulated. Figure 9.4 present the heat-flux distribution. First, the discrepancy in the reattachment position is because different runs are used for the pressure distribution measurement and the full frame IR imaging, the small unwanted change in operating conditions leading to a small change in reattachment position. The most important information in that figure is that the peak heat-flux is correctly predicted by the simulation, which is a good indicator that the transition process is accurately reproduced.

9.3.2 Reproduction of the dynamics

While the previous results show that the numerical simulation can predict the topology of the flow and the heat-flux peak caused by transition, they do not allow concluding on the accuracy of the simulated dynamics of the flow.

Pressure fluctuations

To assess whether the simulation can predict the correct dynamics, one can use the experimental pressure spectra computed from PCB and Kulite sensors data and compare them to spectra of numerical probes in the simulation. Figure 9.5 presents the experimental and numerical spectra from the turbulent region on the flare. It shows that the turbulent dynamics is correctly reproduced by the simulation.

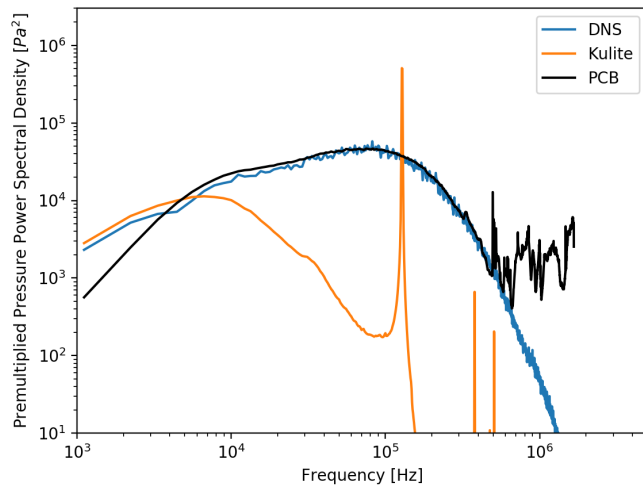


Figure 9.5: Comparison of the numerical and experimental (Kulite and PCB pressure transducers) pressure power spectral densities in the turbulent region on the flare $\frac{X}{L} = 1.1$.

Figure 9.6 presents the pressure fluctuations spectra inside the recirculation region. Figure 9.6 is complex to interpret for several reasons. First, one has to keep in mind the bandwidth limitations of the Kulite sensors discussed in chapter 8. Then, it seems like the experimental and numerical spectra have peaks at matching frequencies (two peaks around 100kHz); however, those peaks are in the resonance range of the sensor and cannot be attributed to instabilities with confidence. The only interesting information is that the energetic content for low frequency (around 10kHz) is higher in the experiment than in the simulation. This could point towards the idea that the white noise excitation does not reproduce accurately the wind tunnel perturbations, which tends to be mostly energetic at low frequency (Duan et al., 2019; Masutti et al., 2011).

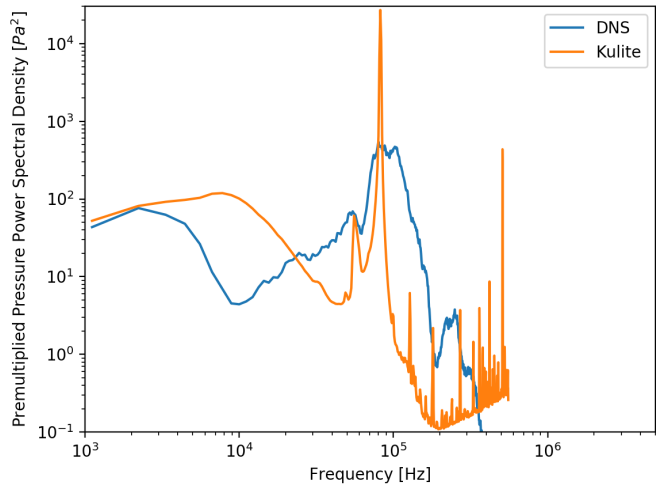


Figure 9.6: Comparison of the numerical and experimental (Kulite pressure transducer) pressure power spectral densities in the laminar bubble region $\frac{X}{L} = 0.87$.

Streaks

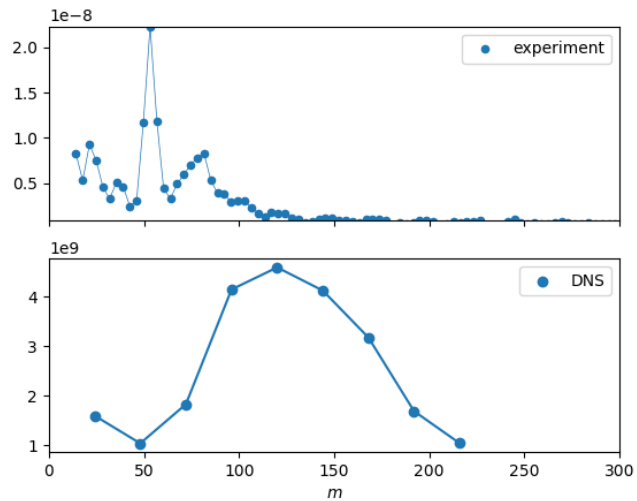


Figure 9.7: Comparison of the numerical and experimental energetic contents in the streaks against wavenumber (the amplitudes are arbitrary).

In addition to the pressure fluctuation spectra, a good comparison point between the numerical and experimental results is the wavenumber of the dominant streaks. Figure 9.7 presents the energetic content of the streaks against wavenumber for both the experimental and numerical simulation of the flow (see section 4.5.1 for more information on the methodology used to compute those spectrums). The computation fails to reproduce accurately the experiments. First, the peak around $m = 50$ is completely absent in the simulation. As explained in chapter 8, this could be because those streaks are linked with geometrical defaults in the model, which are not present in the simulation. Another hypothesis could be that those streaks are linked with non-linear saturation of lower wavenumber global modes (such as proposed by Cao et al. (2021)) which are not captured with the current numerical setup, which only covers 15° of the domain. Even for the large band peak that was attributed to convective mechanism in chapter 8, the simulation fails

to predict the correct wavenumber (the experimental peaks is centered around a wavenumber of about 75 while the numerical one is at twice the wavenumber, centered around $m = 150$). However, this could be explained by the inability of the infra-red imaging setup to capture such small streaks.

9.3.3 Conclusion

Preliminary work has been conducted on both the characterization of the free-stream disturbances present in the R1Ch and R2Ch wind tunnel and the numerical reproduction of experimental results. While the white noise injection used in previous chapters allows for accurate reproduction of the flow topology, it seems to be biased toward high-frequency and lead to the underestimation of the low-frequency content of the flow. The simulation was also not able to accurately predict the dominant streaks wavenumber, but it is unclear if that is due to limitations in the experimental measurements or in the simulation. This points towards the need to simulate a bigger azimuthal span of the domain to be able to conclude on the physics behind the streaks, as discussed in chapter 8.

The present chapter also allowed us to confirm what was already shown in chapter 5, a reduced domain of 15° is enough to accurately reproduce the topology of the transitional flow. However, it also raised questions on the limitations that this reduced domain can bring on the accurate prediction of the heat-flux striation in the reattachment region.

Given those encouraging preliminary results, future work should be conducted if one wants to fill the gap between the experimental runs in the R2Ch facility and the numerical simulations. First, a new campaign must be conducted in the R2Ch facility to gather more complete information on the flow. Then, a simple noise model designed to be injected in the simulations could be created from those data. This model could serve as a generic inflow condition for the simulations, which would match the free-stream of the R2Ch wind tunnel and thus allow to reproduce any experiments carried out in the wind tunnel.

Conclusions and perspectives

The interaction between a boundary layer and a shockwave at hypersonic speed and for transitional Reynolds number is studied both numerically and experimentally. The objectives are to understand the dynamics and the physical origin of:

1. The separated region unsteadiness.
2. The instabilities in hypersonic SBLI for a transitional flow regime.
3. The streaks observed in the reattachment region.

First, high-fidelity numerical simulations are conducted for different flow conditions. Results from those simulations are post-processed using Proper Orthogonal Decomposition and Spectral Proper Orthogonal Decomposition to extract coherent structures. Mean flows from the simulations are used to perform a global stability and resolvent analysis to study the unstable modes and non-normal linear amplification mechanisms present in the flow. An assessment of the information brought by the study of the Navier-Stokes operator linearized around the mean flow is presented, with a critical point of view on the interpretation of the growth rate of the eigenmodes and on the impact of non-linear terms on the resolvent optimal forcing. The comparison between the stability analysis and the simulations results provides insight on both the linear and non-linear mechanisms at play in the flow.

The recirculation region dynamics is found to be dominated by two coexisting large-scale modes, a quasi-steady one that expresses itself mainly by creating striation in the reattachment region and is caused by the interaction of two self-sustained instabilities. And an unsteady one linked with the separation and the mixing layer, causing a breathing of the bubble. The unsteady mode is driven by a feedback loop in the recirculation region, and it may also be relevant for other unsteady shock-motion already documented for shock-wave/turbulent boundary layer interaction.

The observed transition process is found to be completely uncorrelated with those recirculation region modes, which also contribute only marginally to the definition of the mean flow topology, and is dependent on the linear amplification of oblique modes in the boundary layer over a broad range of frequencies. These modes interact non-linearly to create elongated streamwise structures (*i.e.* streaks), which are then amplified by a linear mechanism in the rest of the domain until they break down in the reattachment region. The early nonlinear interaction is found to be essential for the transition process.

An experimental campaign has been conducted on the hollow-cylinder flare model in the R2Ch blowdown facility at a Mach number of 5 for different Reynolds numbers in the transitional regime. Unsteady wall pressure measurements are performed alongside heat flux measurements and high-speed Schlieren imaging. Methodological development on the use of unsteady pressure transducers is presented.

Using the same post-processing tools as in the numerical studies (POD and SPOD), two main phenomena were identified and documented: the oblique modes traveling in the shear layer above

the recirculation region and the streaks appearing in the reattachment region. New results illustrating the multiple physical origins of the streaks, either linked with globally unstable modes and convectively unstable mechanisms, were discussed and compared to the numerical results from this work and the literature.

Both the numerical and experimental study allowed to at least partially fulfil the 3 objectives cited here before :

1. The separated region unsteadiness has been documented for transitional SBLI and a hypothetical instability scenario has been proposed to explain the breathing of the bubble.
2. A transition scenario has been proposed.
3. At least 2 mechanisms leading to streaks have been discussed : a convective mechanism that can be seeded by oblique mode non-linear interactions and a global mechanism. There is also strong suspicion that Görtler vortices may be present in the experiments because of the leading edge geometry.

Finally, some preliminary work on the accurate numerical reproduction of the experimental runs has been presented. This represents one of the main perspective of this work, which unveiled both the importance and the complexity of numerical reproduction of experimental (and flight) free-stream conditions.

Future work should go in the direction of bridging the gap between numerical and experimental simulations of transitional hypersonic flows. This includes understanding and quantifying the perturbations causing transition both in flight and in the wind tunnel. Fine measurements of the free-stream fluctuations of R2Ch have to be conducted to numerically recreate the wind tunnel environment. Ideally, using data assimilation, one could even create a simple reduced order model, of the free-stream perturbations that is injectable in high-fidelity simulations. Naturally, this work on free-stream perturbations also leads to preliminary studies towards the hypothetical development of a quiet wind tunnel.

Additionally, the method used in this thesis, using high-fidelity simulation coupled with global linear stability analysis (and in particular resolvent analysis) has proven to be a powerful tool to study both linear and non-linear mechanisms at play in the transition process. It could be used on more complex geometries, such as the BOLT forebody, or even applied vehicles when the computing power will allow it.

Lastly, work could be conducted on the numerical methods to get a better stability - dissipation compromise, given how crucial it is to get low dissipation when one wants to study transition using second order accurate methods.

Résumé en Français

L'interaction entre une onde de choc et une couche limite en régime hypersonique et pour des nombres de Reynolds transitionnels est étudiée numériquement et expérimentalement. La configuration retenue pour l'étude est une géométrie de référence à l'ONERA (Benay et al., 2006; Bur and Chanetz, 2009; Vandomme, 2004) constituée d'un cylindre creux suivi d'une jupe à 15 degrés.

Le chapitre 1 présente l'étude, qui à pour objectif de documenter et d'analyser les phénomènes physiques liés à la dynamique de l'interaction, à la transition laminaire turbulente ainsi qu'à la striation présente dans les zones de recollement. Pour cela, des outils numériques ainsi qu'expérimentaux sont utilisés.

Ensuite, le chapitre 2 présente un aperçu de la littérature existante, tant sur le sujet de la dynamique des interactions onde de choc couche limite que sur la transition laminaire-turbulente en régime hypersonique. Les différents mécanismes physiques attendus sur la configuration étudiée sont identifiés et présentés.

Les outils liés à l'étude numérique sont présentés dans le chapitre 3, de multiples simulations haute-fidélité sont réalisées pour différentes conditions d'écoulement. Ces simulations sont post-traitées à l'aide de la décomposition orthogonale aux valeurs propres (POD) et de la décomposition spectrale orthogonale aux valeurs propres (SPOD) pour en extraire les structures cohérentes liées à ces phénomènes. Les champs moyens issus des simulations sont également utilisés pour conduire des études de stabilité globale ainsi que des analyses de résolvant afin d'étudier les modes instables et les mécanismes d'amplification linéaires présents dans l'écoulement. La comparaison des résultats issus des calculs haute-fidélité et de ceux issus des études linéarisées permet de conclure sur l'impact des mécanismes linéaires et non-linéaires sur l'écoulement.

Le chapitre 4 présente l'étude expérimentale qui est conduite sur la géométrie cylindre creux-jupe dans la soufflerie R2Ch à un nombre de Mach de cinq et pour une plage de nombres de Reynolds conduisant à la transition de l'écoulement. Les moyens de mesures de pressions instationnaires, de mesures de flux par thermographie infrarouge et de stroboscopies à haute vitesse sont présentés. Des développements méthodologiques sur la mesure de pression instationnaire sont proposés pour analyser des signaux à très hautes fréquences.

Le chapitre 5 présente des résultats numériques sur la dynamique de la zone d'interaction : la zone de recirculation est dominée par deux modes de grande amplitude. Le premier est un mode quasi stationnaire qui engendre de la striation dans la zone de recollement et qui est causé par l'interaction de deux modes instables de l'écoulement. Le second est instationnaire et lié au choc de décollement et à la couche de mélange, provoquant un mouvement de respiration de la bulle. Ce mode est lié à une boucle de rétro-action présente dans la zone de recirculation et pourrait potentiellement dépendre d'autres phénomènes déjà documentés dans le cadre d'interaction onde de choc/couche limite turbulente. La transition vers la turbulence est quant à elle complètement décorrélée de ces modes de bulle.

Ensuite, le chapitre 6 décrit le scénario de transition qui est dépendant de l'amplification linéaire

de premier mode oblique dans la couche limite attachée pour une large gamme de fréquences. Ces modes interagissent non-linéairement entre eux pour créer des structures allongées dans la direction de l'écoulement qui sont ensuite amplifiées par un mécanisme linéaire dans le reste du domaine jusqu'à ce qu'ils se brisent en aval du point de recollement pour créer de la turbulence. L'interaction non-linéaire en début de domaine semble essentielle pour ce scénario de transition.

Le chapitre 7 présente l'impact d'une montée en nombre de Mach sur ce scénario de transition. Bien que le second mode de Mack devienne de plus en plus amplifié, et donc présent, ce scénario reste inchangé.

Les résultats d'essais en soufflerie sont alors présentés dans le chapitre 8. Les essais ont permis d'observer deux principaux phénomènes dans la topologie de l'écoulement, à savoir des modes obliques qui existent dans la couche de mélange ainsi que des stries qui apparaissent sur la jupe dans la région de recollement. De plus, l'analyse des résultats montre que l'origine physique des stries est multiple, soit liée à des phénomènes globaux, soit à des mécanismes convectifs.

Finalement, un premier essai de comparaison quantitative entre des essais en soufflerie et des simulations numériques est présenté dans le chapitre 9. Ce chapitre montre qu'un modèle de bruit représentatif de celui présent à R2Ch est nécessaire pour pouvoir comparer quantitativement les expériences et les simulations dans les zones transitionnelles, ce qui représente une des principales perspectives de ce travail.

Bibliography

- Adams, N. A. (2000). "Direct simulation of the turbulent boundary layer along a compression ramp at $M = 3$ and $\text{Re}(\theta) = 1685$ ". In: *Journal of Fluid Mechanics* 420 (2000), pp. 47–83 (cit. on p. 19).
- Adams, N. A. and L. Kleiser (1993). "Numerical simulation of fundamental breakdown of a laminar boundary-layer at mach 4.5". In: *AIAA/DGLR 5th International Aerospace Planes and Hypersonics Technologies Conference, 1993*. 1993, p. 5027 (cit. on pp. 15, 22, 107).
- Agostini, L., L. Larchevêque, and P. Dupont (2015). "Mechanism of shock unsteadiness in separated shock/boundary-layer interactions". In: *Physics of Fluids* 27.12 (2015), p. 126103 (cit. on p. 89).
- Amestoy, P. R., I. S. Duff, J. Y. L'Excellent, and J. Koster (2002). "A fully asynchronous multifrontal solver using distributed dynamic scheduling". In: *SIAM Journal on Matrix Analysis and Applications* 23.1 (2002), pp. 15–41 (cit. on p. 45).
- Arnal, D. (1989). "Laminar-turbulent transition problems in supersonic and hypersonic flows". In: *Special course on aerothermodynamics of hypersonic vehicles* (1989), pp. 8.1–8.45 (cit. on p. 21).
- Arnal, D. and J.-C. Juillen (1977). "Etude de l'intermittence dans une région de transition de la couche limite". In: *La Recherche Aérospatiale* (1977), pp. 147–166 (cit. on p. 31).
- Aymer De La Chevalerie, D., A. Fonteneau, L. De Luca, and G. Cardone (1997). "Görtier-type vortices in hypersonic flows: The ramp problem". In: *Experimental Thermal and Fluid Science* 15.2 SPEC. ISS. (1997), pp. 69–81 (cit. on p. 140).
- Benay, R. and B. Chanetz (2004). "Design of a boundary layer suction device for a supersonic quiet wind tunnel by numerical simulation". In: *Aerospace Science and Technology* 8.4 (2004), pp. 255–271 (cit. on p. 150).
- Benay, R., B. Chanetz, B. Mangin, L. Vandomme, and J. Peraud (2006). "Shock wave/transitional boundary-layer interactions in hypersonic flow". In: *AIAA Journal* 44.6 (2006), pp. 1243–1254 (cit. on pp. 9–11, 19, 28, 33, 53, 100, 118, 123, 124, 137, 138, 143, 144, 161).
- Beneddine, S (2017). "Characterization of unsteady flow behavior". PhD thesis. ONERA, 2017 (cit. on pp. 44, 45).
- Beneddine, S., D. Sipp, A. Arnault, J. Dandois, and L. Lesshafft (2016). "Conditions for validity of mean flow stability analysis". In: *Journal of Fluid Mechanics* 798 (2016), pp. 485–504 (cit. on pp. 21, 36, 41–43).
- Benitez, E. K., J. S. Jewell, and S. P. Schneider (2021). "Separation bubble variation due to small angles of attack for an axisymmetric model at mach 6". In: *AIAA Scitech 2021 Forum*. 2021, pp. 1–23 (cit. on p. 51).
- Benitez, E. K., J. S. Jewell, S. P. Schneider, and S. Esquieu (2020). "Instability measurements on an axisymmetric separation bubble at mach 6". In: *Aiaa Aviation 2020 Forum*. Vol. 1 PartF. 2020, pp. 1–29 (cit. on p. 15).
- Berkooz, G., P. Holmes, and J. L. Lumley (1993). "The proper orthogonal decomposition in the analysis of turbulent flows". In: *Annual Review of Fluid Mechanics* 25.1 (1993), pp. 539–575 (cit. on p. 37).

- Berridge, D. C. and S. P. Schneider (2012). *Calibration of PCB-132 Sensors in a Shock Tube*. Tech. rep. NASA Langley Space Research Center, Purdue University, 2012, pp. 1–14 (cit. on pp. 10, 55).
- Bonne, N., V. Brion, E. Garnier, R. Bur, P. Molton, D. Sipp, and L. Jacquin (2019). “Analysis of the two-dimensional dynamics of a Mach 1.6 shock wave/transitional boundary layer interaction using a RANS based resolvent approach”. In: *Journal of Fluid Mechanics* 862 (2019), pp. 1166–1202 (cit. on pp. 29, 30).
- Brandt, L., D. Sipp, J. O. Pralits, and O. Marquet (2011). “Effect of base-flow variation in noise amplifiers: The flat-plate boundary layer”. In: *Journal of Fluid Mechanics* 687 (2011), pp. 503–528 (cit. on p. 21).
- Brear, M. J., F. Nicoud, M. Talei, A. Giauque, and E. R. Hawkes (2012). “Disturbance energy transport and sound production in gaseous combustion”. In: *Journal of Fluid Mechanics* 707 (2012), pp. 53–73 (cit. on p. 35).
- Bugeat, B., J. C. Chassaing, J. C. Robinet, and P. Sagaut (2019). “3D global optimal forcing and response of the supersonic boundary layer”. In: *Journal of Computational Physics* 398 (2019), p. 108888 (cit. on pp. 21, 35, 107, 118, 132).
- Bugeat, B. (2017). “Stabilité et perturbations optimales globales d’écoulements compressibles pariétaux”. PhD thesis. Paris 6, 2017 (cit. on p. 107).
- Bur, R. and B. Chanetz (2009). “Experimental study on the PRE-X vehicle focusing on the transitional shock-wave/boundary-layer interactions”. In: *Aerospace Science and Technology* 13.7 (2009), pp. 393–401 (cit. on pp. 10, 11, 28, 123, 137, 161).
- Butler, C. S. and S. J. Laurence (2021a). “Interaction of second-mode disturbances with an incipiently separated compression-corner flow”. In: *Journal of Fluid Mechanics* 913 (2021) (cit. on pp. 10, 53–55, 71).
- (2021b). “Interaction of second-mode wave packets with an axisymmetric expansion corner”. In: *Experiments in Fluids* 62.7 (2021), pp. 1–17 (cit. on p. 71).
- Cao, S., J. Hao, I. Klioutchnikov, H. Olivier, and C. Y. Wen (2021). “Unsteady effects in a hypersonic compression ramp flow with laminar separation”. In: *Journal of Fluid Mechanics* 912 (2021), A3 (cit. on pp. 19, 78, 80, 96, 143, 156).
- Chang, C. L. and M. R. Malik (1994). “Oblique-Mode Breakdown and Secondary Instability in Supersonic Boundary Layers”. In: *Journal of Fluid Mechanics* 273 (1994), pp. 323–360 (cit. on pp. 22, 107).
- Chu, B. T. (1965). “On the energy transfer to small disturbances in fluid flow (Part I)”. In: *Acta Mechanica* 1.3 (1965), pp. 215–234 (cit. on pp. 35, 37).
- Chuvakhov, P. V., V. Y. Borovoy, I. V. Egorov, V. N. Radchenko, H. Olivier, and A. Roghelia (2017). “Effect of Small Bluntness on Formation of Görtler Vortices in a Supersonic Compression Corner Flow”. In: *Journal of Applied Mechanics and Technical Physics* 58.6 (2017), pp. 975–989 (cit. on p. 145).
- Chynoweth, B. C., S. P. Schneider, C. Hader, H. Fasel, A. Batista, J. Kuehl, T. J. Juliano, and B. M. Wheaton (2019). “History and progress of boundary-layer transition on a Mach-6 flared cone”. In: *Journal of Spacecraft and Rockets* 56.2 (2019), pp. 333–346 (cit. on pp. 15, 16, 19).
- Clemens, N. T. and V. Narayanaswamy (2014). “Low-frequency unsteadiness of shock wave/turbulent boundary layer interactions”. In: *Annual Review of Fluid Mechanics* 46.1 (2014), pp. 469–492 (cit. on pp. 24, 25, 85).
- Comte, P. (1999). “Large-Eddy Simulations of Compressible Shear Flows”. In: *Recent Advances in DNS and LES*. Ed. by D. Knight and L. Sakell. Dordrecht: Springer Netherlands, 1999, pp. 1–12 (cit. on p. 19).
- Dalcin, L. D., R. R. Paz, P. A. Kler, and A. Cosimo (2011). “Parallel distributed computing using Python”. In: *Advances in Water Resources* 34.9 (2011), pp. 1124–1139 (cit. on p. 45).
- Debièvre, J. F. and P. Dupont (2009). “Dependence Between Shock and Separation Bubble in a Shock Wave Boundary Layer Interaction”. In: *IUTAM Bookseries* 14.6 (2009), pp. 331–341 (cit. on pp. 25, 89).

- Duan, L. et al. (2019). "Characterization of freestream disturbances in conventional hypersonic wind tunnels". In: *Journal of Spacecraft and Rockets* 56.2 (2019), pp. 357–368 (cit. on pp. 20, 155).
- Dwivedi, A., G. S. Sidharth, J. W. Nichols, G. V. Candler, and M. R. Jovanović (2019). "Reattachment streaks in hypersonic compression ramp flow: An input-output analysis". In: *Journal of Fluid Mechanics* 880 (2019), pp. 113–135. arXiv: 1811.09046 (cit. on pp. 19, 78, 118, 134, 143).
- Egorov, I. V., A. V. Fedorov, and V. G. Soudakov (2008). "Receptivity of a hypersonic boundary layer over a flat plate with a porous coating". In: *Journal of Fluid Mechanics* 601 (2008), pp. 165–187 (cit. on p. 16).
- Erengil, M. E. and D. S. Dolling (1993). "Effects of sweepback on unsteady separation in mach 5 compression ramp interactions". In: *AIAA Journal* 31.2 (1993), pp. 302–311 (cit. on p. 24).
- Estorf, M., R. Radespiel, S. P. Schneider, H. B. Johnson, and S. Hein (2008). "Surface-pressure measurements of second-mode instability in quiet hypersonic flow". In: *46th AIAA Aerospace Sciences Meeting and Exhibit*. 2008, p. 1153 (cit. on p. 15).
- Fasel, H., A. Thumm, and H. Bestek (1993a). "Direct numerical simulation of transition in supersonic boundary layers: oblique breakdown". In: *American Society of Mechanical Engineers, Fluids Engineering Division (Publication) FED*. Vol. 151. Publ by ASME. 1993, pp. 77–92 (cit. on pp. 22, 29, 107, 119).
- (1993b). "Direct numerical simulation of transition in supersonic boundary layers: oblique breakdown". In: *American Society of Mechanical Engineers, Fluids Engineering Division (Publication) FED* 151 (1993), pp. 77–92 (cit. on p. 22).
- Foysi, H. and S. Sarkar (2010). "The compressible mixing layer: An les study". In: *Theoretical and Computational Fluid Dynamics* 24.6 (2010), pp. 565–588 (cit. on pp. 16, 18, 145).
- Franko, K. J. and S. Lele (2014). "Effect of adverse pressure gradient on high speed boundary layer transition". In: *Physics of Fluids* 26.2 (2014), p. 24106 (cit. on pp. 22, 23, 29, 32, 107, 115, 119).
- Franko, K. J. and S. K. Lele (2013). "Breakdown mechanisms and heat transfer overshoot in hypersonic zero pressure gradient boundary layers". In: *Journal of Fluid Mechanics* 730 (2013), pp. 491–532 (cit. on pp. 22, 23, 29, 32, 107, 112, 115, 119, 134).
- Fulghum, M. R. (2014). "Turbulence Measurements in High-Speed Wind Tunnels using Focusing Laser Differential Interferometry". PhD thesis. 2014 (cit. on p. 152).
- Gallaire, F., M. Marquillie, and U. Ehrenstein (2007). "Three-dimensional transverse instabilities in detached boundary layers". In: *Journal of Fluid Mechanics* 571 (2007), pp. 221–233 (cit. on p. 26).
- Ganapathisubrama, B., N. T. Clemens, and D. S. Dolling (2007). "Effects of upstream boundary layer on the unsteadiness of shock-induced separation". In: *Journal of Fluid Mechanics* 585 (2007), pp. 369–394 (cit. on p. 24).
- Garnier, E., N. Adams, and P. Sagaut (2009). *Large Eddy Simulation for Compressible Flows*. Springer Science & Business Media, 2009, p. 276 (cit. on p. 29).
- Garnier, E., P. Sagaut, and M. Deville (2002). "Large eddy simulation of shockboundary-layer interaction". In: *AIAA journal* 40.10 (2002), pp. 1935–1944 (cit. on p. 29).
- Georgiadis, N. J., D. P. Rizzetta, and C. Fureby (2009). "Large-Eddy Simulation: Current capabilities, recommended practices, and future research". In: *47th AIAA Aerospace Sciences Meeting including the New Horizons Forum and Aerospace Exposition* 48.8 (2009), pp. 1772–1784 (cit. on p. 29).
- Gianetti, F. and P. Luchini (2007). "Structural sensitivity of the first instability of the cylinder wake". In: *Journal of Fluid Mechanics* 581.1 (2007), pp. 167–197 (cit. on p. 42).
- Görtler, H (1940). "Instabilität laminarer Grenzschichten an konkaven Wänden gegenüber gewissen dreidimensionalen Störungen". In: *ZAMM - Journal of Applied Mathematics and Mechanics Zeitschrift für Angewandte Mathematik und Mechanik* 21.4 (1940), pp. 250–252 (cit. on p. 19).

- Gromyko, Y. V., P. A. Polivanov, A. A. Sidorenko, D. A. Buntin, and A. A. Maslov (2013). “An experimental study of the natural noise in the Transit-M hypersonic wind tunnel”. In: *Thermophysics and Aeromechanics* 20.4 (2013), pp. 481–493 (cit. on p. 20).
- Grossir, G. (2017). “Xperimental Characterization of Hypersonic Transitional Boundary Layers”. In: *introduction to stability and transition analysis method SSEMIC*. Von Karman Institute for Fluid Dynamics. 2017 (cit. on pp. 53–55).
- Gudmundsson, K. and T. Colonius (2011). “Instability wave models for the near-field fluctuations of turbulent jets”. In: *Journal of Fluid Mechanics* 689 (2011), pp. 97–128 (cit. on p. 36).
- Hader, C. and H. F. Fasel (2018). “Towards simulating natural transition in hypersonic boundary layers via random inflow disturbances”. In: *Journal of Fluid Mechanics* 847 (2018) (cit. on pp. 20, 22, 32, 74).
- Hanifi, A., P. J. Schmid, and D. S. Henningson (1996). “Transient growth in compressible boundary layer flow”. In: *Physics of Fluids* 8.3 (1996), pp. 826–837 (cit. on p. 35).
- Heffner, K. S., A. Chpoun, and J. C. Lengrand (1993). “Experimental study of transitional axisymmetric shock-boundary layer interactions at mach 5”. In: *AIAA 23rd Fluid Dynamics, Plasmadynamics, and Lasers Conference, 1993*. 1993, p. 3131 (cit. on p. 138).
- Hernandez, V., J. E. Roman, and V. Vidal (2005). “SLEPC: A scalable and flexible toolkit for the solution of eigenvalue problems”. In: *ACM Transactions on Mathematical Software* 31.3 (2005), pp. 351–362 (cit. on p. 45).
- Hildebrand, N., A. Dwivedi, J. W. Nichols, M. R. Jovanović, and G. V. Candler (2018). “Simulation and stability analysis of oblique shock-wave/boundary-layer interactions at Mach 5.92”. In: *Physical Review Fluids* 3.1 (2018), p. 13906. arXiv: 1712.08239 (cit. on pp. 14, 19, 26, 79, 80, 91, 93, 96, 143).
- Hutchinson, P (1971). “Stochastic Tools in Turbulence”. In: *Physics Bulletin* 22.3 (1971), pp. 161–161 (cit. on p. 36).
- Joseph George, K. and R. I. Sujith (2011). “On Chus disturbance energy”. In: *Journal of Sound and Vibration* 330.22 (2011), pp. 5280–5291 (cit. on p. 35).
- Karban, U., B. Bugeat, E. Martini, A. Towne, A. V. Cavalieri, L. Lesshafft, A. Agarwal, P. Jordan, and T. Colonius (2020). “Ambiguity in mean-flow-based linear analysis”. In: *Journal of Fluid Mechanics* (2020). arXiv: 2005.05703 (cit. on p. 42).
- Kudryavtsev, A. N. and D. V. Khotyanovsky (2005). “Numerical Investigation of High Speed Free Shear Flow Instability and Mach Wave Radiation”. In: *International Journal of Aeroacoustics* 4.3 (2005), pp. 325–343 (cit. on pp. 16, 17, 145).
- Laible, A. C. and H. F. Fasel (2016). “Continuously forced transient growth in oblique breakdown for supersonic boundary layers”. In: *Journal of Fluid Mechanics* 804 (2016), pp. 323–350 (cit. on pp. 112, 115).
- LAUFER, J. (1961). “Aerodynamic Noise in Supersonic Wind Tunnels”. In: *Journal of the Aerospace Sciences* 28.9 (1961), pp. 685–692 (cit. on p. 151).
- Laurence, S. J., A. Wagner, and K. Hannemann (2016). “Experimental study of second-mode instability growth and breakdown in a hypersonic boundary layer using high-speed schlieren visualization”. In: *Journal of Fluid Mechanics* 797 (2016), pp. 471–503 (cit. on pp. 55, 107, 126).
- Le Sant, Y., M. Marchand, P. Millan, and J. Fontaine (2002). “An overview of infrared thermography techniques used in large wind tunnels”. In: *Aerospace Science and Technology* 6.5 (2002), pp. 355–366 (cit. on pp. 68, 69).
- Le Sant, Y. (2005). “An image registration method for infrared measurements”. In: *Quantitative InfraRed Thermography Journal* 2.2 (2005), pp. 207–222 (cit. on pp. 68, 69).
- Lehoucq, R. B., D. C. Sorensen, and C. Yang (2013). *ARPACK Users' Guid: Solution of Large Scale Eigenvalue Problems with Implicitly Restarted Arnoldi Methods*. Vol. 53. 9. Siam, 2013, pp. 1689–1699. arXiv: arXiv:1011.1669v3 (cit. on p. 45).

- Luchini, P., F. Giannetti, and J. Pralits (2009). "Structural Sensitivity of the Finite-Amplitude Vortex Shedding Behind a Circular Cylinder". In: *IUTAM Bookseries*. Vol. 14. Springer. 2009, pp. 151–160 (cit. on pp. 42, 85).
- Lugrin, M., S. Beneddine, E. Garnier, and R. Bur (2021a). "Multi-scale study of the transitional shock-wave boundary layer interaction in hypersonic flow". In: *Theoretical and Computational Fluid Dynamics* (Nov. 2021) (cit. on p. 77).
- Lugrin, M., S. Beneddine, C. Leclercq, E. Garnier, and R. Bur (2021b). "Transition scenario in hypersonic axisymmetrical compression ramp flow". In: *Journal of Fluid Mechanics* 907 (2021), A6. arXiv: 2009.08359 (cit. on p. 99).
- Mack, L. M. (1975). "Linear stability theory and the problem of supersonic boundary-layer transition". In: *AIAA Journal* 13.3 (1975), pp. 278–289 (cit. on pp. 15, 17, 129–131).
- Marquet, O., D. Sipp, L. Jacquin, and J. M. Chomaz (2008). "Multiple timescale and sensitivity analysis for the passive control of the cylinder flow". In: *5th AIAA Theoretical Fluid Mechanics Conference* 615 (2008), p. 221 (cit. on p. 42).
- Marquet, O., M. Lombardi, J. M. Chomaz, D. Sipp, and L. Jacquin (2009). "Direct and adjoint global modes of a recirculation bubble: Lift-up and convective non-normalities". In: *Journal of Fluid Mechanics* 622 (2009), pp. 1–21 (cit. on p. 26).
- Marxen, O., G. Iaccarino, and E. S. Shaqfeh (2010). "Disturbance evolution in a mach 4.8 boundary layer with two-dimensional roughness-induced separation and shock". In: *Journal of Fluid Mechanics* 648 (2010), pp. 435–469 (cit. on pp. 33, 107, 110).
- Marxen, O. and U. Rist (2010). "Mean flow deformation in a laminar separation bubble: Separation and stability characteristics". In: *Journal of Fluid Mechanics* 660 (2010), pp. 37–54 (cit. on pp. 33, 138).
- Mary, I. and P. Sagaut (2002). "Large Eddy Simulation of Flow Around an Airfoil Near Stall". In: *AIAA Journal* 40.6 (2002), pp. 1139–1145 (cit. on p. 28).
- Masutti, D., E. Spinoza, O. Chazot, and M. Carbonaro (2011). "Disturbance level characterization of a hypersonic blow-down facility". In: *41st AIAA Fluid Dynamics Conference and Exhibit* 50.12 (2011), pp. 2720–2730 (cit. on pp. 20, 151, 152, 155).
- Mayer, C. S., D. A. Von Terzi, and H. F. Fasel (2011). "Direct numerical simulation of complete transition to turbulence via oblique breakdown at Mach 3". In: *Journal of Fluid Mechanics* 674 (2011), pp. 5–42 (cit. on pp. 15, 22, 29, 32, 113, 117, 119, 134).
- McClellan, J. H. and T. W. Parks (1973). "A Unified Approach to the Design of Optimum FIR Linear-Phase Digital Filters". In: *IEEE Transactions on Circuit Theory* 20.6 (1973), pp. 697–701 (cit. on p. 40).
- McKeon, B. J. and A. S. Sharma (2010). "A critical-layer framework for turbulent pipe flow". In: *Journal of Fluid Mechanics* 658 (2010), pp. 336–382 (cit. on p. 41).
- Mettot, C., F. Renac, and D. Sipp (2014). "Computation of eigenvalue sensitivity to base flow modifications in a discrete framework: Application to open-loop control". In: *Journal of Computational Physics* 269 (2014), pp. 234–258. arXiv: 1401.1204 (cit. on p. 42).
- Morkovin, M. V., E Reshotko, and T Herbert (1994). "Transition in open flow systems – a reassessment". In: *Bull. A. Phys. Soc.* 39 (1994), p. 1882 (cit. on p. 14).
- Murray, N., R. Hillier, and S. Williams (2013). "Experimental investigation of axisymmetric hypersonic shock-wave/turbulent-boundary-layer interactions". In: *Journal of Fluid Mechanics* 714 (2013), pp. 152–189 (cit. on pp. 118, 123).
- Myers, M. K. (1991). "Transport of energy by disturbances in arbitrary steady flows". In: *Journal of Fluid Mechanics* 226 (1991), pp. 383–400 (cit. on p. 35).
- Narasimha, R (1990). *Modelling the transitional boundary layer*. 90-90. NASA, Langley Research Center, Institute for Computer Applications in Science and Engineering, 1990, pp. 1–24 (cit. on p. 31).
- Navarro-Martinez, S. and O. R. Tutty (2005). "Numerical simulation of Görtler vortices in hypersonic compression ramps". In: *Computers and Fluids* 34.2 (2005), pp. 225–247 (cit. on pp. 19, 118, 138).

- Nichols, J. W., J. Larsson, M. Bernardini, and S. Pirozzoli (2017). “Stability and modal analysis of shock/boundary layer interactions”. In: *Theoretical and Computational Fluid Dynamics* 31.1 (2017), pp. 33–50 (cit. on pp. 25, 85).
- Ockendon, H. (2001). *Viscous Fluid Flow*. Vol. 20. 1. McGraw-Hill New York, 2001, pp. 157–158 (cit. on p. 14).
- Özgen, S. and S. A. KIrcalı (2008). “Linear stability analysis in compressible, flat-plate boundary-layers”. In: *Theoretical and Computational Fluid Dynamics* 22.1 (2008), pp. 1–20 (cit. on pp. 15, 16, 129–132).
- Paladini, E., S. Beneddine, J. Dandois, D. Sipp, and J. C. Robinet (2019). “Transonic buffet instability: From two-dimensional airfoils to three-dimensional swept wings”. In: *Physical Review Fluids* 4.10 (2019), p. 103906 (cit. on pp. 42, 45).
- Paredes, P., M. M. Choudhari, F. Li, J. S. Jewell, R. L. Kimmel, E. C. Marineau, and G. Grossir (2018). “NATO STO AVT-240”. In: (2018) (cit. on p. 152).
- Péron, S., T. Renaud, M. Terracol, C. Benoit, and I. Mary (2017). “An immersed boundary method for preliminary design aerodynamic studies of complex configurations”. In: *23rd AIAA Computational Fluid Dynamics Conference, 2017*. 2017, p. 3623 (cit. on p. 28).
- Pickering, E., T. Colonius, P. Jordan, and A. Towne (2020). “Resolvent-based jet noise models: A projection approach”. In: *AIAA Scitech 2020 Forum*. Vol. 1 PartF. 2020, p. 999 (cit. on p. 80).
- Piponnai, S., J. P. Dussauge, J. F. Debièvre, and P. Dupont (2009). “A simple model for low-frequency unsteadiness in shock-induced separation”. In: *Journal of Fluid Mechanics* 629 (2009), pp. 87–108 (cit. on pp. 25, 85, 88).
- Priebe, S. and M. P. Martín (2012). “Low-frequency unsteadiness in shock wave-turbulent boundary layer interaction”. In: *Journal of Fluid Mechanics* 699 (2012), pp. 1–49 (cit. on p. 25).
- Reynolds, W. C. (1991). “Three-dimensional simulations of large eddies in the compressible mixing layer”. In: *Journal of Fluid Mechanics* 224 (1991), pp. 133–158 (cit. on pp. 18, 29).
- Robinet, J. C. (2007). “Bifurcations in shock-wave/laminar-boundary-layer interaction: Global instability approach”. In: *Journal of Fluid Mechanics* 579 (2007), pp. 85–112 (cit. on pp. 25, 79).
- Roghelia, A., P. V. Chuvakov, H. Olivier, and I. V. Egorov (2017). “Experimental investigation of Görtler vortices in hypersonic ramp flows behind sharp and blunt leading edges”. In: *47th AIAA Fluid Dynamics Conference, 2017*. 2017, p. 3463 (cit. on pp. 19, 143).
- Running, C. L., T. J. Juliano, M. P. Borg, and R. L. Kimmel (2020). “Characterization of post-shock thermal striations on a cone/flare”. In: *AIAA Journal* 58.5 (2020), pp. 2352–2358 (cit. on p. 138).
- Sandham, N. D., N. A. Adams, and L. Kleiser (1995). “Direct simulation of breakdown to turbulence following oblique instability waves in a supersonic boundary layer”. In: *Applied Scientific Research* 54.3 (1995), pp. 223–234 (cit. on p. 107).
- Sandham, N. D. and W. C. Reynolds (1990). “Compressible mixing layer: Linear theory and direct simulation”. In: *AIAA Journal* 28.4 (1990), pp. 618–624 (cit. on pp. 16, 19, 145).
- Sandham, N. D., E. Schülein, A. Wagner, S. Willems, and J. Steelant (2014). “Transitional shock-wave/boundary-layer interactions in hypersonic flow”. In: *Journal of Fluid Mechanics* 752 (2014), pp. 349–382 (cit. on pp. 29, 31, 125).
- Sawant, S. S., V. Theofilis, and D. A. Levin (2021). “Kinetic modelling of three-dimensional shock/laminar separation bubble instabilities in hypersonic flows over a double wedge”. In: *arXiv preprint arXiv:2101.08957* (2021). arXiv: 2101.08957 (cit. on p. 26).
- Schilden, T. and W. Schröder (2017). “Numerical analysis of high speed wind tunnel flow disturbance measurements using stagnation point probes”. In: *Journal of Fluid Mechanics* 833 (2017), pp. 247–273 (cit. on pp. 20, 151).
- Schilden, T., W. Schröder, S. R. C. Ali, A.-M. Schreyer, J. Wu, and R. Radespiel (2016). “Analysis of acoustic and entropy disturbances in a hypersonic wind tunnel”. In: *Physics of Fluids* 28.5 (2016), p. 056104 (cit. on p. 20).

- Schmid, P. J. and D. S. Henningson (1992). "A new mechanism for rapid transition involving a pair of oblique waves". In: *Physics of Fluids A* 4.9 (1992), pp. 1986–1989 (cit. on pp. 22, 29, 107, 112, 117, 134).
- Schmid, P. J. (2007). "Nonmodal stability theory". In: *Annual Review of Fluid Mechanics* 39 (2007), pp. 129–162 (cit. on p. 21).
- Schmid, P. J., M. F. De Pando, and N. Peake (2017). "Stability analysis for n-periodic arrays of fluid systems". In: *Physical Review Fluids* 2.11 (2017), p. 113902 (cit. on pp. 45, 46).
- Schneider, S. P. (2008). "Development of hypersonic quiet tunnels". In: *Journal of Spacecraft and Rockets* 45.4 (2008), pp. 641–664 (cit. on pp. 20, 32).
- Sidharth, G., A. Dwivedi, G. V. Candler, and J. W. Nichols (2018). "Onset of three-dimensionality in supersonic flow over a slender double wedge". In: *Physical Review Fluids* 3.9 (2018), p. 93901 (cit. on pp. 19, 26, 78–80, 91).
- Simon, B. J. (2017). "Active Cancellation of Tollmien-Schlichting Waves under Varying Inflow Conditions for In-Flight Application". PhD thesis. Technische Universität, 2017 (cit. on p. 14).
- Sipp, D. and A. Lebedev (2007). "Global stability of base and mean flows: A general approach and its applications to cylinder and open cavity flows". In: *Journal of Fluid Mechanics* 593 (2007), pp. 333–358 (cit. on p. 41).
- Sipp, D. and O. Marquet (2013). "Characterization of noise amplifiers with global singular modes: The case of the leading-edge flat-plate boundary layer". In: *Theoretical and Computational Fluid Dynamics* 27.5 (2013), pp. 617–635 (cit. on pp. 21, 107).
- Sirovich, L. (1987). "Turbulence and the dynamics of coherent structures. III. Dynamics and scaling". In: *Quarterly of Applied Mathematics* 45.3 (1987), pp. 583–590 (cit. on p. 71).
- Sivasubramanian, J. and H. F. Fasel (2011). "Numerical investigation of laminar-turbulent transition in a cone boundary layer at Mach 6". In: *41st AIAA Fluid Dynamics Conference and Exhibit* 14 (2011), pp. 26–35 (cit. on pp. 22, 119).
- (2016). "Numerical investigation of laminar-turbulent transition for a flared cone at Mach 6". In: *54th AIAA Aerospace Sciences Meeting*. 2016, p. 3557 (cit. on p. 119).
- Spalart, P. R. (2000). "Strategies for turbulence modelling and simulations". In: *International Journal of Heat and Fluid Flow* 21.3 (2000), pp. 252–263 (cit. on pp. 29, 30).
- Teramoto, S. (2005). "Large-eddy simulation of transitional boundary layer with impinging shock wave". In: *AIAA Journal* 43.11 (2005), pp. 2354–2363 (cit. on pp. 29, 31).
- Thumm, A. (1991). "Numerische Untersuchungen zum laminar-turbulenten Strömungsumschlag in transsonischen Grenzschichtströmungen". PhD thesis. University of Stuttgart, 1991 (cit. on pp. 22, 134).
- Touber, E. and N. D. Sandham (2009). "Large-eddy simulation of low-frequency unsteadiness in a turbulent shock-induced separation bubble". In: *Theoretical and Computational Fluid Dynamics* 23.2 (2009), pp. 79–107 (cit. on p. 85).
- (2011). "Low-order stochastic modelling of low-frequency motions in reflected shock-wave/boundary-layer interactions". In: *Journal of Fluid Mechanics* 671 (2011), pp. 417–465 (cit. on p. 24).
- Towne, A., O. T. Schmidt, and T. Colonius (2018). "Spectral proper orthogonal decomposition and its relationship to dynamic mode decomposition and resolvent analysis". In: *Journal of Fluid Mechanics* 847 (2018), pp. 821–867. arXiv: 1708.04393 (cit. on pp. 36, 71, 105, 115, 134).
- Turton, S. E., L. S. Tuckerman, and D. Barkley (2015). "Prediction of frequencies in thermosolutal convection from mean flows". In: *Physical Review E - Statistical, Nonlinear, and Soft Matter Physics* 91.4 (2015), p. 43009 (cit. on p. 41).
- Vandomme, L (2004). "Contribution à l'étude de l'interaction onde de choc couche limite transitionnelle en écoulement hypersonique à Mach 5". thèse de doctorat. ONERA, 2004 (cit. on pp. 10, 52, 53, 161).
- Vermeulen, J. and G Simeonides (1992). *Parametric studies of shock wave/boundary layer interactions over 2 D compression corners at Mach 6*. Tech. rep. VKI, 1992 (cit. on p. 138).

- Wu, M. and M. P. Martín (2008). “Analysis of shock motion in shockwave and turbulent boundary layer interaction using direct numerical simulation data”. In: *Journal of Fluid Mechanics* 594 (2008), pp. 71–83 (cit. on p. 85).
- Yang, L., H. Zare-Behtash, E. Erdem, and K. Kontis (2012). “Investigation of the double ramp in hypersonic flow using luminescent measurement systems”. In: *Experimental Thermal and Fluid Science* 40 (2012), pp. 50–56 (cit. on p. 145).
- Zhang, C. H., Q. Tang, and C. B. Lee (2013). “Hypersonic boundary-layer transition on a flared cone”. In: *Acta Mechanica Sinica/Lixue Xuebao* 29.1 (2013), pp. 48–54 (cit. on p. 55).
- Zhuang, Y., H. J. Tan, X. Li, F. J. Sheng, and Y. C. Zhang (2018). “Letter: Görtler-like vortices in an impinging shock wave/turbulent boundary layer interaction flow”. In: *Physics of Fluids* 30.6 (2018), p. 61702 (cit. on p. 19).

Titre : Etude de l'interaction visqueuse avec décollement en régime hypersonique

Mots clés : Transition, Interaction, Onde de choc, Couche limite

Résumé : L'interaction entre une onde de choc et une couche limite en régime hypersonique et pour des nombres de Reynolds transitionnels est étudiée numériquement et expérimentalement. La configuration retenue pour l'étude est un cylindre creux suivi d'une jupe à 15 degrés.

Afin d'étudier numériquement la dynamique de large amplitude de la zone de recirculation, les instabilités transitionnelles et les mécanismes causant l'apparition de stries dans la zone de recollement, de multiples simulations haute-fidélité sont réalisées pour différentes conditions d'écoulement. Ces simulations sont post-traitées à l'aide de la décomposition orthogonale aux valeurs propres (POD) et de la décomposition spectrale orthogonale aux valeurs propres (SPOD) pour en extraire les structures cohérentes. Les champs moyens issus des simulations sont également utilisés pour conduire des études de stabilité globale ainsi que des analyses de résolvant afin d'étudier les modes instables et les mécanismes d'amplification linéaires présents dans l'écoulement. La comparaison des résultats issus des calculs haute-fidélité et de ceux issus des études linéarisées permet de conclure sur l'impact des mécanismes linéaires et non-linéaires sur l'écoulement. La zone de recirculation est dominée par deux modes de grande amplitude. Le premier est un mode quasi stationnaire qui engendre de la striation dans la zone de recollement et qui est causé par l'interaction de deux modes instables de l'écoulement. Le second est instationnaire et lié au choc de décollement et à la couche de mélange, provoquant un mouvement de respiration de la bulle. Ce mode est lié à une boucle de rétro-action présente dans la zone de recircu-

lation et pourrait potentiellement dépendre d'autres phénomènes déjà documentés dans le cadre d'interaction onde de choc/couche limite turbulente. La transition vers la turbulence est quant à elle complètement décorrélée de ces modes de bulle et est dépendante de l'amplification linéaire de premier mode oblique dans la couche limite attachée pour une large gamme de fréquences. Ces modes interagissent non-linéairement entre eux pour créer des structures allongées dans la direction de l'écoulement qui sont ensuite amplifiées par un mécanisme linéaire dans le reste du domaine jusqu'à ce qu'ils se brisent en aval du point de recollement pour créer de la turbulence. L'interaction non-linéaire en début de domaine semble essentielle pour ce scénario de transition.

Une étude expérimentale est également conduite sur la géométrie cylindre creux-jupe dans la soufflerie R2Ch à un nombre de Mach de cinq et pour une plage de nombres de Reynolds conduisant à la transition de l'écoulement. Des mesures de pressions instantanées sont réalisées ainsi que des mesures de flux par thermographie infrarouge et des stroboscopies à haute vitesse. Des développements méthodologiques sur la mesure de pression instantanée sont proposés pour analyser des signaux à très hautes fréquences. Les résultats d'essais ont permis d'observer deux principaux phénomènes dans la topologie de l'écoulement, à savoir des modes obliques qui existent dans la couche de mélange ainsi que des stries qui apparaissent sur la jupe dans la région de recollement. De plus, l'analyse des résultats montre que l'origine physique des stries est multiple, soit liée à des phénomènes globaux, soit à des mécanismes convectifs.

Title : Study of the viscous interaction with separation in hypersonic regime

Keywords : Transition, interaction, Shock wave, Boundary layer

Abstract : The interaction of a shock-wave and a boundary layer at hypersonic speed and for several transitional Reynolds numbers is studied both numerically and experimentally. The configuration under study is a hollow cylinder followed by a 15-degree flare.

To numerically study the large-scale dynamics of the recirculation region, transitional instabilities and the mechanisms behind the apparition of streaks in the reattachment region, multiple high-fidelity numerical simulations are conducted for different flow conditions. Results from those simulations are post-processed using Proper Orthogonal Decomposition and Spectral Proper Orthogonal Decomposition to extract coherent structures. Mean flows from the simulations are used to perform a global stability and resolvent analysis to study the unstable modes and non-normal linear amplification mechanisms present in the flow. The comparison between the stability analysis and the simulations results provides insight on both the linear and non-linear mechanisms in the flow. The recirculation region dynamics is found to be dominated by two coexisting large-scale modes, a quasi-steady one that expresses itself mainly in the reattachment region and is caused by the interaction of two self-sustained instabilities. And an unsteady one linked with the separation shock-wave and the shear layer, causing a breathing of the bubble. The unsteady mode is driven by a feedback loop in the recirculation region, and it may also be relevant for other unsteady

shock-motion already documented for shock-wave/turbulent boundary layer interaction. The observed transition process is found to be completely uncorrelated with those recirculation region modes and is dependent on the linear amplification of oblique modes in the boundary layer over a broad range of frequencies. These modes interact non-linearly to create elongated streamwise structures, which are then amplified by a linear mechanism in the rest of the domain until they break down in the reattachment region. The early non-linear interaction is found to be essential for the transition process. An experimental campaign is conducted on the hollow cylinder-flare model in the R2Ch blow-down facility at a Mach number of 5 for several Reynolds numbers in the transitional regime. Unsteady wall pressure measurements are conducted alongside heat-flux measurements by infra-red thermography and high-speed Schlieren imaging. Methodological developments on the use of unsteady pressure transducers are presented in order to analyze high-frequency signals. Two main flow phenomena are identified and documented: the oblique modes traveling in the shear layer above the recirculation region and the streaks appearing on the flare in the reattachment region. Analysis of results illustrates that physical origin of the streaks is multiple, either linked with globally unstable modes and convectively unstable mechanisms.